School of Electrical Engineering, Computing and
Mathematical Sciences

Auxiliary affiliation

Exploring the southern pulsar population in image domain with the Murchison Widefield Array

Susmita Sett

This thesis is presented for the Degree of
Doctor of Philosophy
of
Curtin University of Technology

September 2023

To the best of my knowledge and belief this thesis contains no material previously published by any other person except where due acknowledgement has been made. This thesis contains no material which has been accepted for the award of any other degree or diploma in any university.

Susmita Sett

"*There's nowhere you can be that isn't where you're meant to be*"

— All you need is love, The Beatles

Acknowledgements

First and foremost, I owe every bit of this to my parents, who were always supportive of my decisions even if it meant I would be moving away from them for several years. They understood and respected my passion for astronomy and I will forever be grateful to them for everything.

My first move into the big, wide world, living on my own, was almost 10 years ago. It wouldn't have been smooth if not for the wonderful friends I got in the process and the wonderful times I spent in Bangalore. Special mention to Kshitishman, Akul, Rajat and Shankar for making my undergraduate days memorable. The next big move was to move countries all the way to Manchester. And what an experience it was! I owe my master's supervisors, Rene and Colin and the pulsar group for enlightening the spark of research in me. I am extremely grateful for the wonderful bunch of friends I got there for making me feel home away from home. Special thanks to MSc gang of Dirk, Shankar, Suheil, Tom, Tony, Tracy, David and also the hangout gang of Nialh, Dan, Dom, Eunseong, and the other Tom and Luke. You guys will always be family and Manchester will always have a piece of my heart.

Finally, I landed in Perth and started the journey of PhD. First and foremost, I do owe it to Manisha for encouraging me to move to literally the other side of the world. I am very grateful for the wonderful supervisors: Ramesh for always having wonderful ideas to work on, Marcin S. for being very patient and helpful in answering all my questions and listening to my thoughts and rants and Emil for always answering my questions and helping me with solutions (I will meet you

one day in person!). This wouldn't have been enjoyable without you all. Also thanks to the pulsar group, especially, Brad and Sammy for fielding my questions and making it a great learning experience.

Thanks to my panel chair over the years who have always made sure I am doing well and everything is on track. A very special mention to Cath, for always being there with me through thick and thin, as a friend, mentor and someone who inspires me to be a better person every day.

Obviously, it wouldn't be complete without the great PhD cohort, starting with the OG gang of Sandro, Mawson, Danica, Freya and Ben Q. The first six months of COVID wouldn't be bearable without you guys. And yes, we did procrastinate a lot! Jaiden for being very supportive during the final months of my Phd, hearing me rant about all the problems and for all the dad-jokes that eventually cheered me up. Thanks to Steve, Jishnu and Jun for making my working weekends at CIRA fun and eventful. Thankfully some of us are not here on weekends anymore. Thanks to Garvit for never letting me miss the feeling of having a brother by always being a looming shadow near my desk, wherever it is. I quite enjoy the presence. Thanks to Callan, for always keeping me on my toes and scaring me whenever he gets a chance. You have made me more vigilant of my surroundings. Thanks to Dylan, for all the Monday morning chats. I always look forward to Mondays because of you! Thanks to Tom for always being a good friend and I look forward to the rest of the time to come. My plots and work wouldn't be as good and easy-going if not for all the help from Nick and Chris, so a huge thank you to Nick and Chris. Thanks to Jordan for letting me annoy him so much and not shouting at me even once (yet). Thanks to Flora, for being Flora! You have been an amazing friend and a great co-conspirator in all my adventures. I don't know how we became such close friends but I am glad we did! Thanks to all the people that I did not mention by name but you are a part of this journey.

Finally, thanks to Leshan for being always supportive and listening to my

rants about work and PhD. Thanks to Anupa for always being ready for a trip. Its been great so far and I cannot wait for the next adventure to begin!

Abstract

Pulsars are unparalleled astrophysical tools for studying physics under intense gravitational magnetic fields and probing ultra-dense matter and relativistic plasma physics. Nevertheless, despite over five decades of intensive research, we still lack a fundamental understanding of the underlying mechanism responsible for pulsar radio emission. Even though pulsars were discovered at low frequencies ($\sim$81.5 MHz) and initially studied extensively at lower frequencies ($\lesssim$500 MHz), over the past several decades, they have been largely studied at higher frequencies ($\gtrsim$1 GHz), and mainly using single-dish radio telescopes. In the recent past, the combination of new and upgraded low-frequency aperture arrays and telescopes and advancements in signal processing have increased the interest in conducting pulsar observations at low radio frequencies ($\lesssim$300 MHz), a relatively unexplored parameter space. To fully realize the scientific potential of the next-generation radio telescopes, such as the Square Kilometre Array-Low (SKA-Low), it is therefore imperative to gain a more comprehensive understanding and study pulsar properties at low frequencies. This can be realised by existing SKA-Low precursor instruments, such as the Murchison Widefield Array (MWA). The MWA provides us with the flexibility to not only explore traditional beamformed pulsar searches but also to investigate complementary approaches such as pulsar searching in the image domain.

My thesis explores this complementary approach to detecting pulsars in the image domain using the Voltage Capture System (VCS) mode of MWA. The MWA VCS provides the unique capability of recording complex voltages from all

individual antennas (tiles) which provides maximum flexibility in data processing. For instance, the same VCS data can be imaged or beamformed and searched for pulsars in either Stokes images or through time series analysis respectively.

Traditional pulsar searches have primarily employed time-domain techniques that are generally sensitive to periodic pulses. However, these methods are susceptible to effects like scattering, eclipses and orbital motion (in the case of binary systems). At lower radio frequencies ($\lesssim$ 300 MHz), factors such as dispersion measure (DM) and pulse broadening due to multipath scattering become more prominent, reducing the detection sensitivity. Additionally, searching for pulsars at these frequencies requires extensive computational resources due to a very large number ($\sim$10000) DM trials. On the other hand, image domain searches for pulsars are not limited by scattering and/or DM and therefore this approach can extend the parameter space to regions inaccessible to traditional pulsar search techniques. Despite a loss in sensitivity for image-based searches (by a factor of $\sim$2 to 5 depending on the pulsar duty cycle), it has the potential to detect highly scattered or high DM pulsars that may be missed by beamformed searches.

A pipeline has been developed to produce 1-s images and average them to form full Stokes images using offline correlated MWA VCS data. This allowed developing methodologies to identify pulsar candidates from the Stokes I and V images based on pulsar observables. Steep spectrum was one such criterion, where sources with a spectral index of -1.2 or a steeper spectrum were selected. The second criterion was based on circular polarisation. After considering the leakage, a threshold of 7% was selected to produce a list of circularly polarised pulsar candidates. The third criterion was flux density variability. Light curves of variable sources were produced at timescales of 30 s, 60 s and 300 s based on the application of variability statistics such as the chi-squared value and modulation index. The criteria were also combined to reduce the number of candidates and produce a list of highly ranked pulsar candidates. These methodologies were tested on four observations ($\sim$2000 deg^2 sky). The candidates found in the observations were

beamformed and searched for pulsations. Furthermore, image and beamformed verification of known pulsars in the observations were also performed. This pilot survey demonstrated the feasibility of image-based pulsar detections and searches at low frequencies.

Subsequently, these methodologies were applied to perform a survey of the entire Galactic plane (using 12 MWA VCS observations, i.e. $\sim$6000 deg^2 sky) marking the first image-based pulsar census of the Galactic Plane using MWA VCS data. The known pulsars in the observed region of the sky were verified using both image-based and beamformed methods. This resulted in the detection of 83 known pulsars, with 16 pulsars found only in Stokes I images but not in periodicity searches applied in beamformed data. Notably, for 14 pulsars this is the first reported low-frequency detections. This underscores the importance of image-based searches in identifying pulsars that may be undetectable in time-series data, due to scattering and/or dispersive smearing at low frequencies. The imaging detections of the pulsars provided useful flux density measurements, which is important as flux densities at low frequencies are not readily available for a large number of currently known pulsars. Analyzing the spectra of detected pulsars after the addition of the low-frequency flux density measurements from this work demonstrates changes in the spectra for 15 pulsars. This highlights the importance of low-frequency flux density measurements in refining pulsar spectral models and investigating the spectral turnover of pulsars at low frequencies.

The application of image-based methodologies also produced a list of pulsar candidates, with the steep spectrum criterion, being the most promising one. Circular polarisation criterion can also be promising, if future improvements can be achieved in leakage characterisation. The resulting pulsar candidates were followed up using the very same MWA VCS data processed by forming tied-array beams in their direction and searched for pulsations. Due to a large number of initial candidates (of the order of several thousands), the criteria were combined to produce a short list of 154 candidates; 30 of the highest-ranked candidates were

followed up with the Parkes (Murriyang) Radio Telescopes, whereas five candidates with either a gamma-ray or X-ray counterpart and were also followed up with the upgraded Giant Metrewave Radio Telescope (uGMRT). Most of these turned out to be either double or extended radio sources in uGMRT imaging. This highlights the significance of a higher angular resolution for this kind of analysis. The Parkes follow-up (0.7-4 GHz band) did not reveal any pulsations for the candidates. However, it is possible that these sources may still be pulsars, but their detection could be unsuccessful due to propagation effects or emission geometry. Alternatively, they can be other known radio sources like Active Galactic Nuclei (AGN) or even a completely new category of Galactic radio sources.

In summary, the work presented in this thesis demonstrates that an image-based approach probes complementary part of the parameter space (i.e. sensitive to high-DM/ highly-scattered pulsars) to traditional periodicity searches, and therefore has the potential to reveal previously undiscovered pulsars. The work also underscores the importance of low-frequency flux density measurements for pulsars and the benefits these measurements offer in spectral modelling, which can be used for studies of pulsar emission and informing population models and survey simulations. Out of 110 pulsars that we were expecting to detect within the sensitivity limits of imaging with the MWA, we were able to detect 66 of them. Amongst these 66 pulsars, 16 of them were not detected in beamforming, which highlights the fact that imaging can in principle add more discoveries to those possible with beamforming searches alone. The success of this study emphasizes the application of image-based techniques in identifying pulsar candidates in low-frequency imaging and serves as a first step in improving future pulsar detection efficiency, not only for instruments like the MWA and for more sensitive future instruments like SKA-Low.

Contents

List of Figures

List of Tables

Chapter 1

Background and Introduction

1.1 Overview of pulsars

Pulsars are neutron stars with extremely strong magnetic fields that rotate rapidly, emitting bursts of electromagnetic radiation primarily detectable as a series of pulses in the radio frequency range. These extremely interesting objects are formed when a star with mass 8 to 15 solar masses ($M_\odot$) collapses in a supernova explosion. Pulsars have emerged as remarkable physical tools and have been used to verify theories such as general relativity and have several other scientific applications. The first pulsar, PSR B1919+21 was discovered in 1967, by Jocelyn Bell Burnell, a graduate student at the University of Cambridge at the time. This was a chance discovery, when she noticed a pulsed radio signal, repeating every 1.337s as shown in Figure 1.1 while studying quasars with the Interplanetary Scintillation Array at the Mullard Radio Astronomy Observatory. Due to the repeated detection of this unknown source at a fixed right ascension and declination, it was thought to be of astrophysical origin and dubbed as 'Little Green Men' or LGM 1. The lack of any parallax measurement indicated that the source was of extra-solar origin. This, along with several such detections, led to the discovery of the very first pulsar, PSR B1919+21 and a new class of astrophysical object, altogether (Hewish et al., 1968).

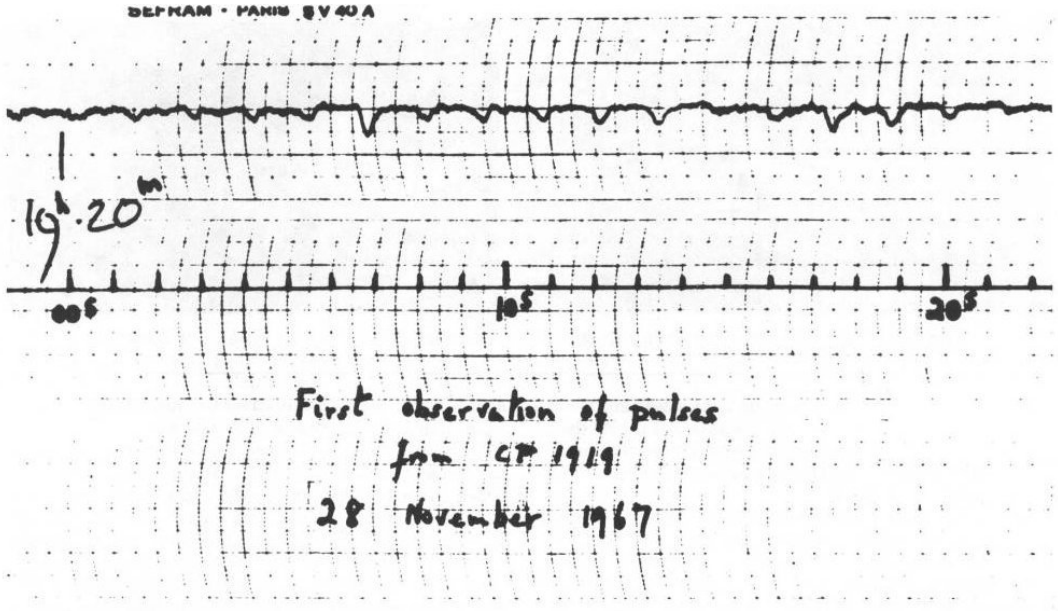

Figure 1.1: The first recorded signals from the first pulsar B1919+21. This was the confirmation signal for the periodicity of the incoming pulses and led to the discovery of pulsars (Hewish et al., 1968).

Two years after the discovery of neutrons, Baade & Zwicky (1934) proposed the existence of neutron stars. They suggested that after a core-collapse supernova of a star, the remnant is small, dense and consisting of neutrons. A simple equation of state was derived for such a remnant by Oppenheimer & Volkoff (1939), which was used to estimate the mass and radius and was mainly dependent on density and pressure. It was argued by Hoyle et al. (1964) that if such an object exists at the centre of the Crab Nebula, it should have a magnetic field of about 10^{10} G as a result of the conservation of magnetic flux from the progenitor. The hypothesis of an object with high magnetic field emitting radiation was confirmed by Pacini (1968) even before the discovery of pulsars and was suggested that such an object is the possible source of energy for the Crab Nebula. After the discovery of pulsars, Gold (1968) tried to establish a relationship between the pulsations observed and that of a magnetised, rapidly rotating neutron star. They suggested such a relationship can be established by measuring the lengthening of the period between the pulses. Even though, theories relating pulsars to vibrating white dwarfs were favoured at the time, the discovery of two short-

period pulsars, the Vela pulsar at 89ms (Large et al., 1968) and the Crab pulsars at 33ms (Lovelace et al., 1968) shifted the explanation to pulsars being neutron stars as the periods were too short for vibrating white dwarfs. This idea was further strengthened by the measurement of the increase in period of the Crab pulsar (Gold, 1969).

Since then the development of the field of pulsar astronomy has seen significant discoveries in the last few decades. The first binary pulsar, PSR B1913+16, also called the Hulse-Taylor pulsar was discovered in 1974 and was the first example of a pulsar in a binary system (Hulse & Taylor, 1975). It was also the first example of a double neutron star (DNS) binary system with a decaying orbit, leading to the first indirect evidence of gravitational waves. The discovery of such a complex system of objects helped in furthering studies in regards to models of stellar evolution and pulsar formation and was important for testing Albert Einstein's general theory of relativity. The next step would be to detect a binary system of a pulsar and black hole that would be of extreme significance for stellar evolution and for their potential application as probes of strong gravity. Discovering such exotic binary systems would open up new avenues of research.

The first millisecond pulsar, B1937+21, was discovered in 1982 (Backer et al., 1982), which led to the discovery of an entirely new class of pulsars with an increased degree of rotational stability and posed numerous challenges to models of pulsar formation and evolution. The first pulsar to be discovered in a globular cluster M28 was PSR B1821-24A (Lyne et al., 1987), followed by the discovery of PSR B0529-66 in the Large Magellanic Cloud (McCulloch et al., 1983). These discoveries significantly improved our understanding of the pulsar luminosity distribution and helped in probing the local Intergalactic medium (IGM). In 1992, Wolszczan & Frail (1992), discovered the first extrasolar planets around PSR B1257+12, and thus confirmed the existence of planets outside our Solar System. However, despite studies of pulsars for several decades, the physical and emission mechanisms of these objects are still not well understood, which has prompted

the search for more pulsars (Levin et al., 2018). Some of these systems are hard to detect using periodic searches. For example, a pulsar in a binary system will require high computational power to perform acceleration searches to detect the system. Therefore, ongoing efforts to improve existing detection techniques and explore complementary methods of pulsar search is an evolving area of research.

1.2 Fundamentals of pulsars and neutron stars

As previously discussed, a large amount of progress has been made with regard to the scientific understanding and applications of pulsars. Although many aspects of pulsar physics are not yet resolved, significant developments have been made in areas such as the structure and composition of the NS interior, details of pulsar emission mechanism etc (Losovsky, 2022). An overview of the basics of NS formation and the essential structure and properties of typical pulsars is described in the subsections below.

1.2.1 Formation

Typically, the formation of a neutron star starts with any star that is part of the main sequence and has an initial mass exceeding eight times the mass of the sun ($> 8M_{\odot}$). Beyond the main sequence phase, subsequent nuclear fusion processes lead to the development of a core rich in iron. Once all the nuclear fuel in the core is used up and the fusion ceases it completely relies on the degeneracy pressure for support. The accumulation of mass from the burning shell causes the core to surpass the Chandrasekhar limit ($1.4M_{\odot}$, Chandrasekhar, 1931). This leads to the further collapse of the core due to the diminished degeneracy pressure, resulting in an increase in temperature surpassing 5×10^9 K. At these extreme temperatures, high-energy gamma rays induce photo-disintegration, breaking down iron nuclei into alpha particles. With temperatures rising even higher, electrons and protons combine through electron capture to form neutrons, emitting a substan-

tial number of neutrinos in the process. When densities escalate to the point of nuclear density at 4×10^{17} kg m^3, a balance between the repulsive forces of the strong nuclear force and the pressure from neutron degeneracy counteracts the contraction. This phenomenon stops the inward fall of the star's outer envelope, causing it to be expelled outward due to the flux of neutrinos generated during neutron creation. This expulsion gives rise to a supernova, leaving behind a remnant known as a neutron star. However, if this remnant possesses a mass greater than approximately $3M_{\odot}$, it proceeds to undergo further collapse, culminating in the formation of a black hole.

1.2.2 Structure and measurable properties of pulsars

The structure and composition of neutron stars are not yet fully understood due to their complex nature and it extends to all current models of pulsar behaviour and phenomenology. Nonetheless, a simple pulsar model shown in Figure 1.2, referred to as the 'toy' or 'lighthouse' pulsar model, can be used to explain the basic characteristics of pulsars. In this model, the pulsar is represented as a rotating neutron star with a purely dipolar magnetic field, surrounded by vacuum and with a misalignment angle, α, between the magnetic and rotation axes. The magnetic lines are a combination of open and closed field lines, divided by the light cylinder, an imaginary surface at which an object (or magnetic field lines) co-rotating with the pulsar would move at the speed of light. The open field-line region determines the size of the emission beams pointed along the pulsar's magnetic axis.

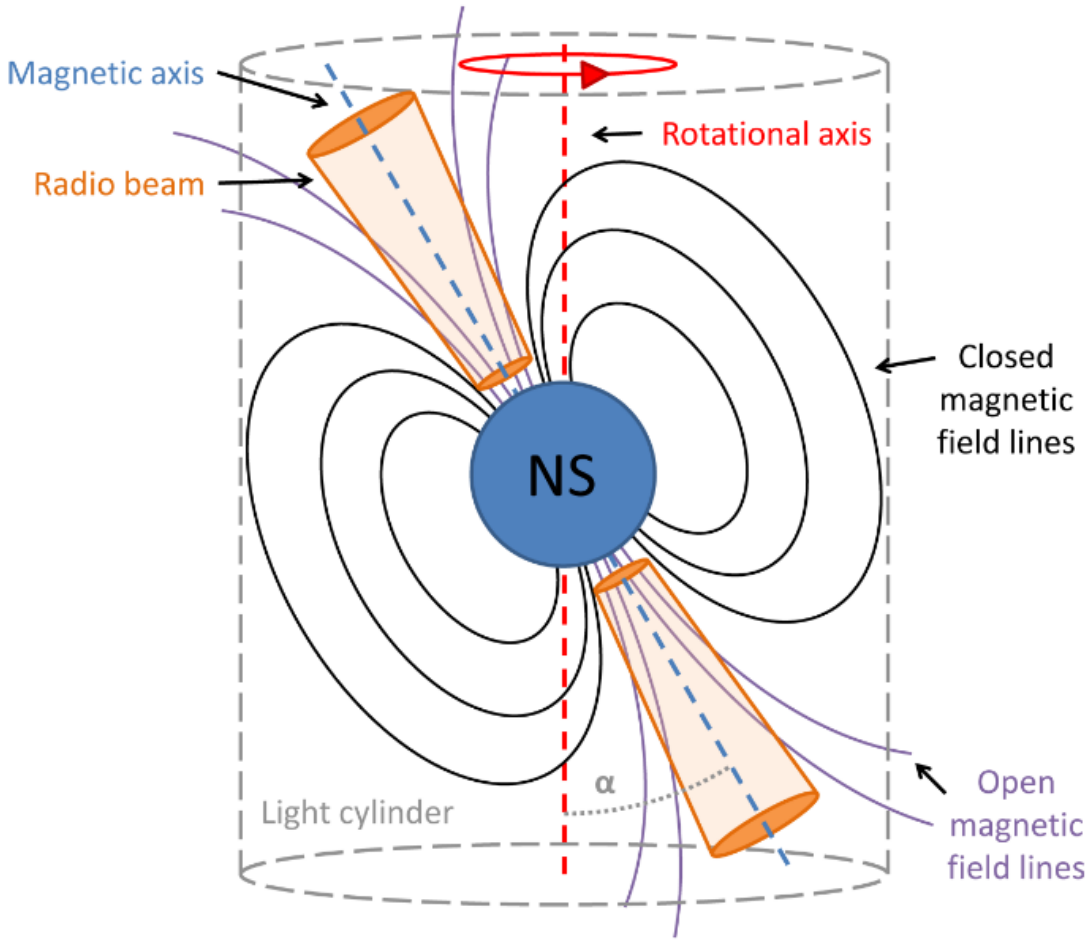

Figure 1.2: A simplified lighthouse (or toy) model of pulsars. This shows the relevant features such as magnetic field lines, light cylinder and the radio beam.

Based on the model described earlier and shown in Figure 1.2, the remainder of the section explores some of the main properties of pulsars.

The matter that makes up neutron stars is highly compressed and is very different from what can be studied in terrestrial laboratories. Therefore the theoretical calculations for the properties of neutron stars are uncertain. Reliable measurements of neutron star's radii, which could constrain their equation of state, are difficult to obtain. The neutron star's gravity causes redshifts in the thermal flux and temperature that is observed. Due to that, a distant observer

measures a temperature that is lower than the real surface temperature. The intrinsic R value is smaller than the corresponding radius, R_{obs} as follows:

$$R_{obs} = \frac{R}{\sqrt{1 - 2GM/Rc^2}} = \frac{R}{\sqrt{1 - R_s/R}}, \tag{1.1}$$

where M and R are the gravitational mass and radius of the star, c is the speed of light, G is Newton's gravitational constant and

$$R_S = \frac{2GM}{c^2} \simeq 4.2 \text{ km} \left(\frac{\text{M}}{1.4\text{M}_\odot} \right) \tag{1.2}$$

is the Schwarzschild radius.

A lower limit for the neutron star radius was derived by Lattimer & Yahil (1990) and Glendenning (1992) and is as follows:

$$R_{min} \simeq 1.5 R_S = \frac{3GM}{c^2} = 6.2 \text{ km} \left(\frac{\text{M}}{1.4\text{M}_\odot} \right) \tag{1.3}$$

An upper limit can also be obtained by requiring that the neutron star is stable against break-up due to centrifugal forces. For a neutron star rotating with a period P, the upper limit is,

$$R_{max} \simeq \left(\frac{GMP^2}{4\pi^2} \right)^{1/3} = 16.8 \; km \left(\frac{M}{1.4M_\odot} \right)^{1/3} \left(\frac{P}{\text{ms}} \right)^{1/3} \tag{1.4}$$

The conservation of angular momentum during the core collapse of the progenitor star and the contributions of the natal 'kick' imparted during the explosion itself cause the initial spin of a pulsar. The pulsar spin periods gradually increase over time as they lose rotational kinetic energy to emission processes such as magnetic dipole radiation, high energy emission and the formation of pulsar winds. This loss of energy, $\dot{E}$, is known as the spin-down luminosity and is defined as

$$\dot{E} = -I\Omega\dot{\Omega} = 4\pi^2 I \dot{P} P^{-3} \tag{1.5}$$

where $\Omega = 2\pi/P$ is the angular frequency, P is the pulsar period, $\dot{P} = dP/dt$

is the rate of spin-down and I is the pulsar's moment of inertia and can be defined as,

$$I = kMR^2 \tag{1.6}$$

where k is 0.4 for a sphere of uniform density and M is the mass. Assuming the canonical pulsar mass of $1.4M_{\odot}$ and radius of 10 km, the canonical moment of inertia can be calculated as $I \simeq 10^{38}$ kg m^2 and reduces Equation 1.5 to

$$\dot{E} \simeq 3.95 \times 10^{31} erg \text{ s}^{-1} \left(\frac{\dot{\text{P}}}{10^{-15}}\right) \left(\frac{\text{P}}{\text{s}}\right)^{-3}. \tag{1.7}$$

Magnetic dipole radiation is a process of the formation of electromagnetic waves from a rotating magnetic dipole. For a pulsar with a magnetic moment $|m|$ and angle α between the magnetic and rotational axes, the magnetic dipole energy loss can be defined as

$$\dot{E}_{dipole} = \frac{2}{3c^3}|m|^2\Omega^4 sin^2\alpha \tag{1.8}$$

Equating Equations, 1.5 and 1.8 gives:

$$\dot{\Omega} = \left(\frac{2|m|^2 sin^2\alpha}{3Ic^3}\right)\Omega^3. \tag{1.9}$$

On generalising Equation 1.9 to a power law and substituting for the pulsar's rotational frequency $\nu = 1/P$ results in:

$$\dot{\nu} = -K\nu^n, \tag{1.10}$$

where K is usually taken as a constant, and n is referred to as the braking index. For a pure magnetic dipole braking, from Equation 1.9, and the braking index is then, n=3. Differentiating and re-arranging Equation 1.10 we get

$$n = \frac{\nu\ddot{\nu}}{\dot{\nu}^2} \tag{1.11}$$

An estimate of n can be derived by measuring the value of $\dot{\nu}$ and $\ddot{\nu}$ for the pulsar and are typically possible for young pulsars with high rates of spin-down. However, timing noise and pulsar glitches can cause complications to such measurements.

An approximate pulsar age T can be derived by integrating Equation 1.10 and can be expressed in terms of pulsar period, P as

$$T = \frac{P}{(n-1)\dot{P}} \left[1 - \left(\frac{P_0}{P} \right)^{n-1} \right], \tag{1.12}$$

where P_0 is the birth period of the pulsar and $n \neq 1$. If a pure magnetic dipole braking (n=3) scenario is assumed, along with the assumption that the pulsar's birth period $P_0 \ll P$, then the characteristic age τ_c can be derived and defined as:

$$\tau_c \equiv \frac{P}{2\dot{P}} \simeq 15.8 \text{ Myr} \left(\frac{\mathrm{P}}{\mathrm{s}} \right) \left(\frac{\dot{\mathrm{P}}}{10^{-15}} \right)^{-1}. \tag{1.13}$$

While the characteristic age offers an initial approximation of a pulsar's age, it might not hold true for all pulsars, for example, millisecond pulsars (MSPs), that follow distinct evolutionary paths compared to the conventional spin-down model. They can appear to have a wide range of values of τ_c, some of which being greater than a Hubble Time, for example, PSR J1938+2012 (Stovall et al., 2016).

Having information on the previously mentioned parameters, one can also calculate the surface magnetic field of a pulsar. An expression for the surface magnetic field of a pulsar B_{surf} can be obtained assuming pure magnetic dipole braking as:

$$B_{surf} = \sqrt{\frac{3c^3 I P \dot{P}}{8\pi^2 R^6 sin^2\alpha}}. \tag{1.14}$$

Equation 1.14 is reduced to the following assuming the typical values for a canonical pulsar and $\alpha = 90°$

$$B_{surf} = 3.2 \times 10^{19}\mathrm{G}\sqrt{\mathrm{P}\dot{\mathrm{P}}} \simeq 10^{12}\mathrm{G}\left(\frac{\dot{\mathrm{P}}}{10^{-15}}\right)^{1/2}\left(\frac{\mathrm{P}}{\mathrm{s}}\right)^{1/2} \tag{1.15}$$

The calculation of the surface magnetic field should be done with caution and is best to take it as an order-of-magnitude estimate. Equation 1.15 is used to calculate the surface magnetic field of a pulsar, and it is found that the typical range is between 10^{11} to 10^{13} G. This range is consistent with the actual measurements obtained from the study of cyclotron processes in X-ray spectra of isolated and binary NS.

1.2.3 Observable properties of pulsars

In addition to the measurable characteristics of pulsars outlined in Section 1.2.2, there are several other properties that are generally consistent across the entire pulsar population, albeit with some variations in specific cases. The radio emissions observed from pulsars are thought to originate from the acceleration of charged particles along intensely magnetized field lines that surround neutron stars. Typically, pulsar magnetic fields are primarily dipolar, and these magnetic fields are inclined relative to the star's rotation axis. The emission beam becomes visible to observers when it sweeps across their line of sight, creating a phenomenon akin to a lighthouse beam. In cases where the magnetic axis and rotation axis are nearly perpendicular and their alignment is favourable for an observer, emissions from both magnetic poles can be detected. This results in pulses separated by approximately 180 degrees in pulse longitude, with the weaker of the two pulses known as the interpulse.

1.2.3.1 Pulse profiles and shapes

The integrated pulse profile is generated by averaging multiple rotations of a pulsar and illustrates the distinct probability distribution of when individual pulses occur in relation to the pulsar's rotation phase. This profile tends to remain con-

sistent for the majority of pulsars. Integrated pulse profiles can exhibit various shapes, spanning from simple, narrow, Gaussian-like shapes to intricate, broad profiles with multiple components. These diverse shapes can be accounted for by various models describing the geometry of the emission beam, as they aim to establish a link between the one-dimensional profile we observe and the three-dimensional structure of the beam.

The remarkable stability of the rotation of pulsars, along with their consistent emission profiles over extended periods (typically spanning minutes) positions them as exceptional astrophysical clocks. This is particularly true for millisecond pulsars, where their emissions exhibit such remarkable regularity that they can establish a time standard comparable to, or even surpass, the precision of Earth's finest atomic clocks (Rawley et al., 1987).

Due to the complex nature of the individual pulses, there is a significant variation of radio emission between rotations. This is a characteristic feature of all radio pulsar emissions. This variability can be seen in many forms, such as rotational phase shift, the difference in intensity or no observable emission for one or more rotations.

However, the integrated pulse profile for each pulsar, representing a cross-sectional cut through the pulsar's emission beam has a characteristic shape. The pulse shape of a radio pulse from a pulsar is determined by several factors including the geometry of the emission beam, the size of the beam, and the angle between the observer's line of sight and the beam centre. If the beam is not symmetrical or the angle between the line-of-sight and the beam centre is at an offset, the observed pulse shape can become distorted. Additionally, the shape of the emission beam can also affect the observed pulse shape, with wider beams leading to broader and less intense pulses. Understanding the pulse shapes can provide valuable information about the pulsar's emission mechanisms and geometry. Several models of the pulsar beam structure have been proposed to explain these different pulse profiles.

1.2.4 Pulse profile evolution with frequency

Most pulsars exhibit a frequency dependence in their observed pulse profiles, which means that the pulse shape changes with frequency. A possible explanation for this is that the emission is being produced at different regions of the magnetosphere, the pulse shape at different frequencies can provide information about the structure of the pulsar's magnetic field and the emission mechanisms responsible for the radio waves. These changes in the pulse shape can also be used to study the interstellar medium and how it affects the propagation of the pulsar signals.

For some pulsars, this change of profile with frequency can be explained using the radius-to-frequency mapping (RFM) model, which was first demonstrated via observations by Cordes (1978). The RFM model predicts that the low-frequency emission is emitted from the higher regions of the magnetosphere and the higher energy emission is from regions closer to the neutron star's surface.

This phenomenon can be ascribed to the fact that pulsar emissions result from the motion of ultra-relativistic charged particles along magnetic field lines. The emission frequency is contingent upon the local plasma conditions, which change with both time and altitude. Consequently, magnetic field lines exhibit wider opening angles at greater altitudes, resulting in low-frequency emissions that have a broader beam and a more extensive profile. Moreover, the emission height can be determined by calculating the separation angle of profile components using the RM model, as demonstrated in the work by Cordes (1978). Nevertheless, there are instances where the RM model fails to elucidate the pulse profiles of certain pulsars that do not display strong frequency evolution. In some of these pulsars, the opposite behaviour is observed: the profile narrows at lower frequencies, a phenomenon that the RM model cannot entirely account for.

A clear picture regarding the cause of the change in the profile with observing frequency as well as the physics of the emission mechanism and emission height of pulsars has not been fully explained yet. To further understand the emission

mechanism of pulsars it is important to study the cause of profile evolution with frequency. This can be realised by analysis of pulse profiles of a large sample of pulsars at low frequencies which is an ongoing effort. The existing low-frequency telescopes such as LOFAR, MWA and LWA, and upcoming facilities like SKA-Low will provide valuable inputs to these studies. Large observing campaigns of pulsars with these telescopes will help to measure pulse profiles at low frequencies and build a complete picture of the pulse profile dependency on frequency, which will ultimately lead to an explanation of pulsar emission mechanisms.

1.2.5 Flux density spectra

The mean flux density of pulsars is dependent on the observing frequency (Jankowski et al., 2018), and is a fundamental observable of pulsar emission with the potential to improve our understanding of the energy involved in the pulsar emission mechanism (Bhat et al., 2014; Bilous et al., 2016). Measurements of flux density play a vital role in calculating the pulsar luminosity function. This, in turn, provides insights into investigating the birth rates and the initial distribution of spin periods of the Galactic population of radio pulsars (Bates et al., 2013).

In many cases, the spectra of pulsars tend to follow a simple power law for the most part across the frequency range, given as

$$S_\nu = S_0 \left(\frac{\nu}{\nu_0}\right)^\alpha, \tag{1.16}$$

where S is the flux density, at an observing frequency, ν and α is the spectral index and S_0 is the flux density at ν_0.

Since the discovery of pulsars, a lot of work has been done to determine an average spectral index for pulsars that can be applied to the majority of the detected population of pulsars. Lorimer & Kramer (2004) from observation of 280 pulsars between 0.4 to 1.6 GHz, reported a mean spectral index of $\alpha = -1.6 \pm 0.3$, while more recently (Jankowski et al., 2018) reported a spectral index of $\alpha = -1.8 \pm 0.2$.

Even though most pulsars follow a simple power law, there are some categories such as magnetars that have a complex spectral behaviour. Moreover, at low observing frequencies, some pulsars tend to have a spectral turnover or a break in power law or two breaks (Jankowski et al., 2018). The spectral index is an important selection effect in pulsar searches and affects the derived population. For example, untargeted pulsar searches in large portions of the sky at higher frequencies are expected to detect pulsars with flatter spectra whereas lower frequencies tend to detect steep spectrum pulsars (Bates et al., 2013). Therefore, it is necessary to search for pulsars at a range of frequencies to understand the broadband spectral properties of the pulsar population (Lorimer et al., 1995). A large number of measurements spread across a range of frequencies provide better constraints in the spectral energy distribution (spectral fit).

Even though a simple power law seems to fit for the majority of pulsars (Equation 1.16, with multiple measurements at wide frequency ranges, some pulsars tend to deviate to other spectral fits such as simple power law with low-frequency turnover or a high-frequency cut-off. These spectral models used in Section 4.3.4 are explained in the following sections.

1.2.5.1 Simple power law

The simple power law is the most common spectral model and is linear in log space, taking the form of Equation 1.16.

1.2.5.2 Broken power law

The broken power law can be compared to two simple power laws differing at two spectral break frequencies. Generally, a sharp broken power law is used to fit pulsar spectra and is characterised by four parameters (Murphy et al., 2017). The model takes the form shown below,

$$S_\nu = \begin{cases} \left(\frac{\nu}{\nu_0}\right)^{\alpha_1} & \text{if } \nu \leq \nu_b \\ \left(\frac{\nu}{\nu_0}\right)^{\alpha_2} \left(\frac{\nu}{\nu_0}\right)^{\alpha_1 - \alpha_2} & \text{otherwise ,} \end{cases} \tag{1.17}$$

where ν_b is the spectral break frequency, α_1 and α_2 are the spectral indices before and after the break respectively.

1.2.5.3 Log parabolic spectrum

This model is mainly used to describe curved spectra of pulsars (Bates et al., 2013) and takes the form:

$$log_{10} S_\nu = a \left[log_{10} \left(\frac{\nu}{\nu_0} \right) \right]^2 + b \; log_{10} \left(\frac{\nu}{\nu_0} \right) + S_0, \tag{1.18}$$

where a is the curvature parameter and b is the spectral index for $a = 0$. The log parabolic spectrum is not used by default anymore due to other models being more appropriate for the fits.

1.2.5.4 Power law with low-frequency turnover

This model shows the power law turning over at low frequencies. This curve of the turn-over is useful in understanding the nature of pulsar emission mechanisms (Kijak et al., 2007). The model is described as below:

$$S_\nu = S_0 \left(\frac{\nu}{\nu_0} \right)^\alpha \; exp \left[\frac{\alpha}{\beta} \left(\frac{\nu}{\nu_{peak}} \right)^{-\beta} \right] \tag{1.19}$$

where α is the spectral index, ν_{peak} is the turnover frequency and $0 < \beta \leq 2.1$ is the factor that determines the smoothness of the curve. This low-frequency turnover of pulsars can be due to propagation effects. For example, free-free absorption (Malov, 1979) or induced scattering (Lyubarskii & Petrova, 1998) of the radio waves by the particles of the magnetospheric plasma.

1.2.5.5 Power law with high-frequency cutoff

This model is mainly based on the coherent emission model by Kontorovich & Flanchik (2013) and is often called hard cut-off model. At higher frequencies, the flux density tends to zero before a cut-off frequency. The model takes the form as follows,

$$S_\nu = S_0 \left(\frac{\nu}{\nu_0}\right)^\alpha \left(1 - \frac{\nu}{\nu_c}\right), \ \nu < \nu_c, \tag{1.20}$$

where α is the spectral index and ν_c is the cut off frequency.

1.2.5.6 Double turn-over spectrum

This model is a combination of a turn-over at low frequencies and a hard cut-off at high frequencies with an underlying power law. Due to the large number of parameters, this is not a preferred model. However, it is more physically motivated than the log parabolic model and has common parameters with other models. The model takes the form as follows:

$$S_\nu = S_0 \left(\frac{\nu}{\nu_0}\right)^\alpha \ exp\left[\frac{\alpha}{\beta}\left(\frac{\nu}{\nu_{peak}}\right)^{-\beta}\right] \left(1 - \frac{\nu}{\nu_c}\right), \ \nu < \nu_c \tag{1.21}$$

where α is the spectral index, ν_{peak} is the turn over frequency, ν_c is the cut-off frequency, $0 < \beta \leq 2.1$ is the turn-over smoothness.

All these models can be used to fit pulsar spectra with the number of fitted parameters depending on the specific model. The software used for this purpose is **pulsar_spectra** software (Swainston et al., 2022a) and is mainly used in Chapter 4.

1.2.6 Polarisation properties

The emission of pulsars is often polarised. The observation of radio pulsar polarisation and the longitude variation of its position range provided support to the polar-cap model of emission (Radhakrishnan & Cooke, 1969). However, the

origin of the circular component of polarisation still remains a mystery. Generally, circular polarisation is assumed to be formed between the source, defined as the surface of the last absorption and the observer but within the light cylinder radius (Jones, 2020).

The majority of pulsars show a significant amount of linear polarisation while some of them also show a certain amount of circular polarisation. The circular polarisation of pulsars is a good distinguishing factor from other radio sources. On average, the degree of linear polarisation is around 20 percent and can reach up to 100 percent for some pulsars (Han et al., 2009). The fractional circular polarisation degree on average is about 10 percent at 1.4 GHz (Johnston & Kerr, 2018). The circular polarisation can change with frequency for some pulsars. For example, von Hoensbroech & Lesch (1999) showed that the trend of circular polarisation increases with frequency for three pulsars. However, many other radio sources seen in radio images such as AGN can also be linearly polarised, whereas circular polarisation is not as common for AGNs and other astrophysical objects. Hence, circular polarisation is a good distinguishing factor between pulsars and other radio sources.

A polarised electromagnetic wave can be described by a defined set of four parameters first introduced by George Gabriel Stokes in 1852 (Stokes, 1851). The four Stokes parameters I, Q, U and V are defined as

$$s = \begin{bmatrix} I \\ Q \\ U \\ V \end{bmatrix} \equiv \begin{bmatrix} \mid E_x \mid^2 + \mid E_y \mid^2 \\ \mid E_x \mid^2 - \mid E_y \mid^2 \\ 2Re\left(E_x E_y^*\right) \\ -2Im\left(E_x E_y^*\right) \end{bmatrix} = \begin{bmatrix} E_x \mid^2 + E_y \mid^2 \\ E_x^2 - E_y^2 \\ 2E_x E_y cos\ \delta \\ 2E_x E_y sin\ \delta \end{bmatrix} \tag{1.22}$$

where E_x and Ey is the electric field that is obtained by the orthogonal linear feeds of the radio antenna, δ is the phase difference between the two orthogonal components, and x and y are perpendicular to z, the wave propagation direction.

The total intensity is represented as Stokes I and circular polarisation by

Stokes V for an observed source. **P**, the complex linear polarisation is calculated from the observed Stokes parameters, Q and U, and is given by

$$P = Q + iU. \tag{1.23}$$

The intensity of linear polarisation is given by

$$L = \sqrt{Q^2 + U^2} \tag{1.24}$$

The observed linear polarisation angle (P.A.), χ can be derived from the parameters and is defined as,

$$\chi = \frac{1}{2} arctan\left(\frac{U}{Q}\right) \tag{1.25}$$

The positional angle is determined by the direction of the magnetic field crossing our line of sight. When measured as a function of the rotational phase, it is expected to be of a S-shape, independent of observing frequency. It means that the P.A. will vary slower in the outer wings of the pulse profile than in the centre. This was first observed by Radhakrishnan & Cooke (1969), in their rotating vector model (RVM).

For this thesis, we are focused on the circular polarisation of pulsars (Stokes V), using it as a factor to distinguish between pulsar candidates and other radio sources in the field of view (FoV) of the radio telescope. Details about this work are given in Chapter 3.

1.2.7 Variation in intensity

Pulses display variability on timescales from seconds to days to years. This variability can be repeating or a one-off event. It has been studied for a long time with narrow fields of view in targeted investigations. Doing this blindly, at radio wavelengths, requires a wide field of view to complete it in a reasonable amount of time. Therefore, until recently, this was a capability of only X-ray

and γ ray satellites. Radio telescopes at lower frequencies provide a wider field of view. With new low-frequency radio telescopes such as the SKA-Low, being built in the radio regime, an exciting era of such transient detection is upcoming. Many observations now probe the lower frequency regime, from tens to hundreds of MHz, a previously unexplored range of frequencies.

Low-frequency transients can be divided into two classes, coherent and non-coherent emitters. Coherent emitters tend to display fast variability and are mainly detected in beamformed time series data, whereas, non-coherent emitters are slow variables and are usually detected by comparing several images of the same field.

Synchrotron radiation is the driving process behind the low-frequency incoherent emission process. This is when relativistic electrons are accelerated in strong magnetic fields, produced when large amounts of energy are injected into the ambient medium in jet sources and explosive events. The variability timescales of these sources are longer at low radio frequencies when compared to X-ray or γ ray energies due to the synchrotron self-absorption effects and the longer radiative lifetimes of particles to synchrotron emission. Inverse Compton cooling in radio plays a role limiting the timescale and brightness of incoherent radio sources, much like pair production does for compact gamma-ray sources.

For most pulsars, the average emitted flux density is constant when averaged over long time scales. However, the received flux density can be variable because of propagation effects such as diffractive and refractive interstellar scintillation. While diffractive scintillation causes variability on time scales of tens of minutes, refractive scintillation constitutes variations on the time scales of weeks to months. In this thesis, we focus on probing the diffractive scintillation, on timescales of seconds to minutes by producing light curves of sources at different timescales. The variability statistics that govern the selection of the sources are described in Chapter 3.

1.3 Propagation effects

The interactions of the radio waves from the pulsars with the interstellar medium (ISM) can cause several propagation effects which can affect the observed properties of pulsars. Some of the major effects include pulse dispersion, pulse scattering and scintillation. The underlying pulsar signal can be understood and studied in detail once these propagation effects have been accounted for. The effects are described in detail in the following subsections.

1.3.1 Pulse dispersion

Pulse dispersion is described as the delay in arrival time for pulses at lower frequency and was first observed in the first discovered pulsar, PSR B1919+21 (Hewish et al., 1968). This delay is because of the frequency dependence of the pulse's group velocity as it travels through the ionised components of the ISM. An example of such an effect is given in Figure 1.3

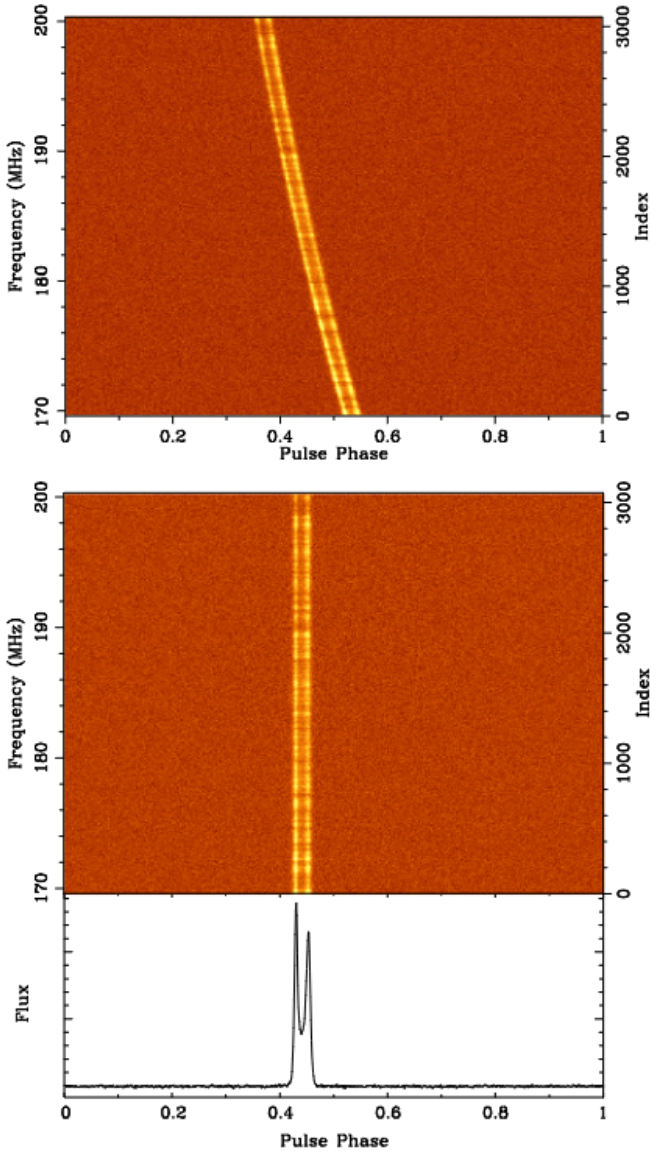

Figure 1.3: The flux density plotted as a function of pulse phase and observing frequency for PSR J1136+1551 (pulse period P=1.88s, DM=4.841 $pc\ cm^{-3}$. The frequency is centred at 185 MHz. The upper panel shows the dispersion of the incoming pulse from the ionised ISM, which causes the pulse to arrive at the lower band later than those at the higher band. The bottom panel shows the dedispersed pulse.

The dispersion measure (DM) is typically used to quantify the amount of dispersion affecting the pulsar's signal and is defined as the integral of the electron density of the ISM along the line of sight between the observer and the pulsar.

as

$$\mathrm{DM} = \int_0^{\mathrm{d}} \mathrm{n_e}\ \mathrm{dl}\ \mathrm{cm}^{-3}\mathrm{pc}, \tag{1.26}$$

where d is the distance to the pulsar and n_e is the electron density in units of cm^{-3}. The delay in arrival time between the higher and lower frequency components of the same broadband signal is related to the DM by

$$\Delta t \simeq D \times \left(\nu_1^{-2} - \nu_2^{-2}\right) \times \mathrm{DM} \tag{1.27}$$

where the dispersion constant $D \simeq 4.15 \times 10^6$ ms (Manchester & Taylor, 1972). As shown in equation 1.26, the DM value along a particular line of sight is approximately related to the distance to the pulsar and is dependant on the distribution of n_e throughout the Galaxy. Even though a crude estimate of n_e can be derived by assuming a constant value of $\simeq 0.03\ \mathrm{cm}^{-3}$ (Ables & Manchester, 1976), the actual Galactic distribution is not uniform. A better approach is to independently calibrate pulsar distances using HI absorption lines or parallax in order to construct elaborate models of the distribution. The well-established models that include more complexities of the Galactic structures, as well as identifiable local variations, are the NE2001 model (Cordes & Lazio, 2003) and YMW16 model (Yao et al., 2017).

1.3.2 Pulse scattering

Scattering caused by turbulence in the ISM can impact pulsar's radiation even though it may be spatially coherent at the point of origin. As a result of the turbulence, the incoming pulsar radiation bends along different lines of sight, hence modifying their path lengths. This is detectable as an offset in the pulse phase due to the modification of the arrival time of radiation as it reaches the observer. When the pulse phase is summed across the distribution function of potential paths a significantly broadened pulse profile is seen. This can be explained as

a result of the convolution of the 'true' pulse shape with a one-sided exponential decay function. The 1/e time constant of this exponential function is called scattering time, τ_s (Lorimer & Kramer, 2004).

Similar to DM, the amount and nature of scattering are also dependent on the distribution and behaviour of the ISM. One of the ways to determine the amount and nature of scattering is to assume a Kolmogorov spectrum of turbulence in the ISM (Armstrong et al., 1995a), in combination with a thin-screen model shown in Figure 1.4 (Scheuer, 1968). This reduces the scattering along the whole line of sight to a single screen halfway between the observer and the pulsar. This simple model works well for most pulsars but more sophisticated models are required for some specific systems.

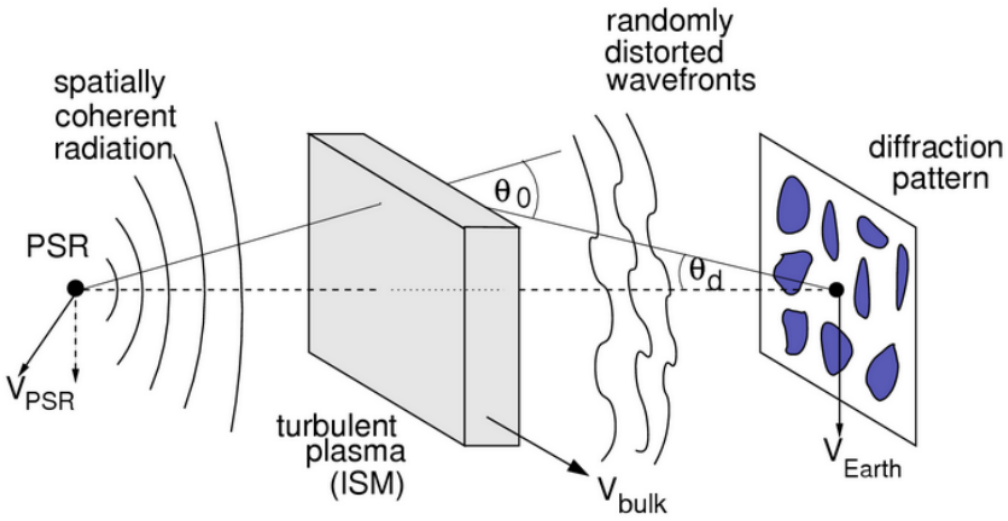

Figure 1.4: The thin screen scattering model. This shows that the pulsar emits spatially coherent radiation which is then randomly distorted by the turbulent ISM, leading to a diffraction pattern where θ_0 is the angle that the wave is bent and θ_d is the radius of the scatter-broadened image. This can be used to explain the scattering and scintillation of pulsars (Lorimer & Kramer, 2004).

Scattering can lower the overall signal-to-noise ratio (S/N) and hence make it hard to detect scattered pulses as shown in Figure 1.5. It can also prevent us from detecting features in the pulse profile that may provide additional information about the structure of the pulsar's emission region or improve timing

accuracy. According to the prediction of the thin screen model (Scheuer, 1968), the scattering time, $\tau_s \propto \nu^{-4}$, where ν is the observing frequency. It means that the scattering of the pulses is higher at lower frequencies, which may make the detection of pulsars at these frequencies harder. τ_s also correlates with DM (Bhat et al., 2004), such that higher DM pulsars experience increased values of scattering.

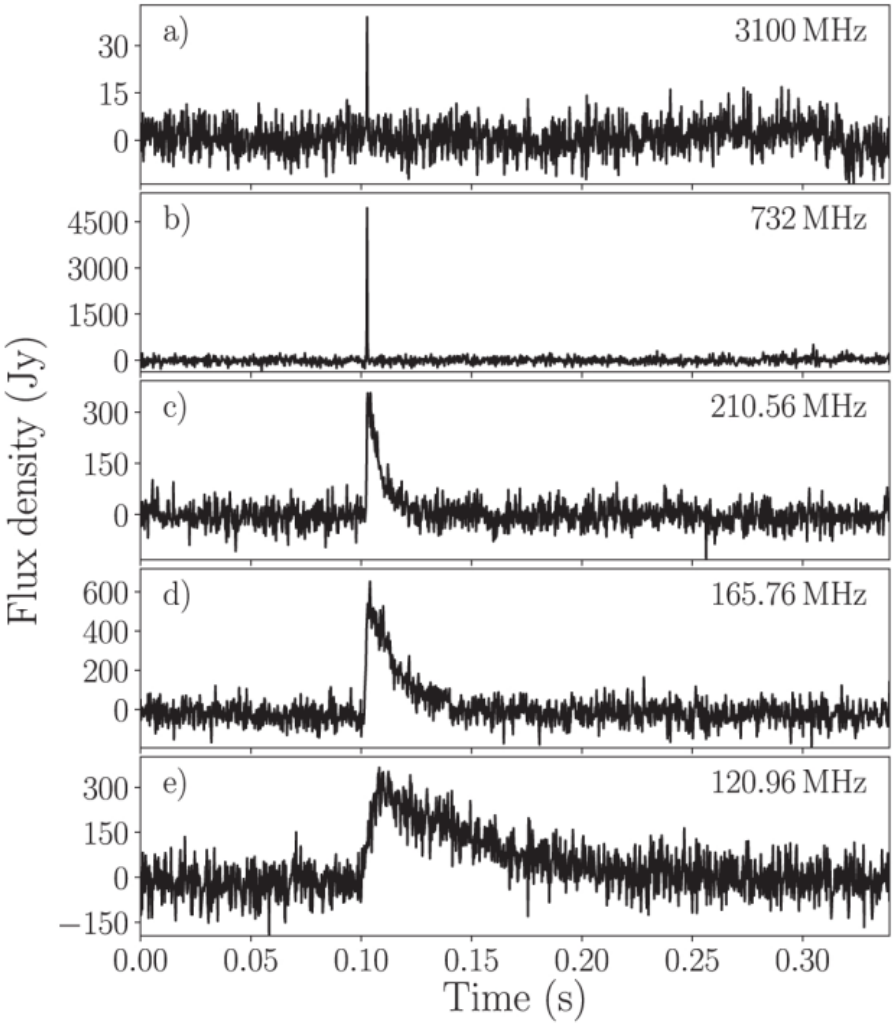

Figure 1.5: Simultaneous giant pulses of Crab pulsar at five observing bands. The effect of scattering is clearly visible as the exponential tail of the giant pulses gets more prominent with the decrease in frequency. (Meyers et al., 2017)

The minimum detectable flux density for the imaging interferometer is given

by:

$$S_{image} = f_{peak}\ \sqrt{N(N-1)}\ \sqrt{n_p t_{int} \Delta\nu}\ \frac{1}{SEFD_{tile}} \tag{1.28}$$

The minimum detectable flux density for periodic pulsar search is given by:

$$S_{periodic} = f_{peak}\ \sqrt{N(N-1)}\ \sqrt{n_p t_{int} \Delta\nu}\ \frac{1}{SEFD_{tile}}\ \sqrt{\frac{P-W}{W}} \tag{1.29}$$

where S_{image} and $S_{periodic}$ is the minimum detectable flux density via image-based searches and periodic searches respectively, f_{peak} is the peak flux density of the source, N is the number of baselines, n_p is the number of polarisations, t_{int} is the total integration time, $SEFD_{tile}$ is the SEFD for per tile, P is the pulse period and W is the pulse width.

We can see from the two equations that the for periodic pulsar search a factor of $\sqrt{\frac{P-W}{W}}$ is present which is not there in the equation for imaging interferometer. This is the pulsar period P and the pulse width W which we cannot record in image based searches. This factor leads to a loss of sensitivity for the image based searches. However, when the pulse period becomes almost similar to the pulse width due to scattering, image based searches are comparable or better than pulse searches.

Scatter broadening of the pulses is highly line-of-sight dependent and is much larger in the plane or towards the Galactic Centre compared to high $|b|$ sight lines. Bhat et al. (2004) provides empirical relations to guide the expected broadening times as a function of DM and frequency and is helpful in observing strategies. For example, the scatter broadening, $\tau_d \geqslant 100$ ms at DM $\geqslant 300 \mathrm{pccm}^{-3}$, for a line of sight as far off as $|b| \sim 5^{\circ}$ and 30° away from the Galactic plane. This also implies that at low frequencies, the search volume is largely limited to a few kiloparsecs in the plane. Therefore, it is harder to detect high DM pulsars at low frequencies especially along the plane or near the GC. However, image based pulsar searches are not affected by scattering and can be a useful alternative to detect any new bright, high DM pulsars that lie on the plane or near the GC.

1.3.3 Interstellar scintillation

The effect of ISM that is closely related to scattering is interstellar scintillation. It was first observed as strong modulations of observed pulsar intensity and can be compared to the optical 'twinkling of stars' when observed through the Earth's atmosphere (Lyne & Rickett, 1968). This effect can deter the detectability of a bright pulsar by 'scintillating-down' (Cordes, 2002). The scintillation bandwidth is the characteristic scale in frequency (ν_d) and scattering delay (τ_d) are are related to each other as below,

$$2\pi\nu_d\tau_d \sim 1, \tag{1.30}$$

where the scintillation bandwidth scales as,

$$\nu_d \propto \frac{1}{\tau_d} \propto \nu^4, \tag{1.31}$$

A scintle represents a region of increased flux density with a characteristic size of ν_d in the frequency regime and τ_d in the time domain.

Strong scintillation regime consists of two types of scintillation: diffractive scintillation (DISS) and refractive scintillation (RISS). DISS have scintillation timescales of ∼seconds and scintillation bandwidth, ν_d of $\sim$ 0.1 to 5 MHz and τ_{diff} of 1 to 100 min at ∼185 MHz and is mostly for low DM pulsars such as B0950+08 and J0437-4715. The timescale of DISS is highly frequency, direction and distance-dependent and is represented as,

$$\tau_{diff} \propto \nu^{1.2} d^{-0.6} \tag{1.32}$$

where d is the distance between the Earth and the pulsar. RISS is due to large-scale electron density variations and corresponds to timescales varying from days to months and scales as

$$\tau_{ref} \propto \nu^{-2.2} d^{1.6} \tag{1.33}$$

where τ_{ref} is the scintillation timescale.

The MWA can be used to make accurate measurements of these quantities using the dynamic spectrum method. For example, Bhat et al. (2004) observed DISS and RISS including drifts in the scintillation of PSR J0437-4715 as shown in Figure 1.6. Bhat et al. (2004) obtained $\nu_d \sim 1.7$ MHz and $\tau_{diff} \propto 260$ s at 185 MHz.

As seen in Figure 1.6, PSR J0437-4715 is an extreme example of the apparent flux density changing by an order of magnitude for low DM pulsars. As pulsars tend to scintillate down, it becomes harder to detect fainter pulsars and needs multiple observations spread across a long time to detect them successfully.

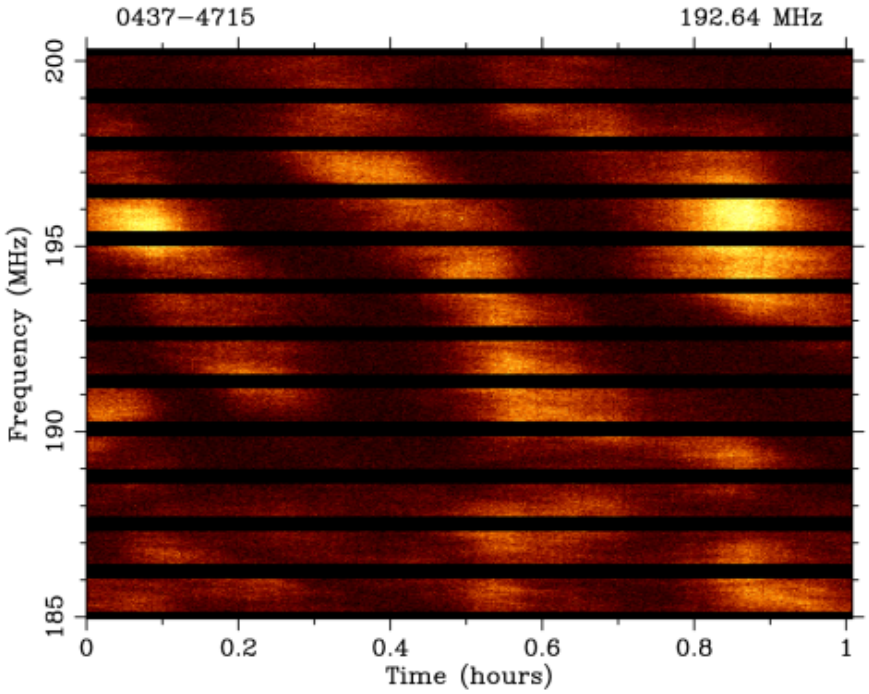

Figure 1.6: Dynamic spectra of PSR J0437-4715 from MWA observations for a time duration of 1 hr and a bandwidth of 15.36 MHz centred at 192.64 MHz. The gaps in frequency are the edge channels not recorded during the early days of VCS commissioning (Bhat et al., 2004).

1.4 The diverse population of pulsars

Pulsar emission is powered by the rotational kinetic energy of a neutron star. (Ostriker & Gunn, 1971). Hence, for isolated pulsars, there is a gradual increase in their rotational periods, P. The time derivative of the pulse period, $\dot{P} = dP/dt$, is also an important observable parameter and referred to as the spin-down rate. Both the parameters can be accurately determined from pulsar timing measurements. These measurements can be used to study the spin evolution of pulsars and are represented in the '$P-\dot{P}$' diagram as given in Figure 1.7. The '$P-\dot{P}$' diagram is essential in providing valuable insights into the evolutionary histories of the pulsar population as their 'trajectories' through this diagram describe changes in pulsar spin period and its derivative over their lifetime. The '$P-\dot{P}$' diagram can be thought of as an analog of the Hertzsprung-Russel (H-R) diagram, which tracks the evolution of conventional stars as a function of their luminosity and effective temperatures.

A 'typical' pulsar is expected to start its life in the upper left region of the diagram, with a short birth spin period. This region is rich in supernova remnant (SNR) associations (Staelin & Reifenstein, 1968; Camilo, 2002), serving as strong evidence for the young ages of the pulsars, as SNRs have a lifetime in the order of 10^4 years before they fade into the background interstellar medium (Frail et al., 1994). Over a timescale of $10^5 - 10^6$ years, the pulsar moves down the $P-\dot{P}$ diagram as it gradually spins down, before reaching the so-called 'death line' (Chen & Ruderman, 1993), after approximately 10^7 years. After passing this point, the electric potential drops below the limit required for the production of radio emission and the neutron star becomes undetectable as a pulsar. Multiple death lines have been theoretically predicted. However, a small number of pulsars (Zhang et al., 2000; Caleb et al., 2022) can be found in the so-called 'graveyard' region which exists beyond these lines, raising questions about the mechanism of radio emission of pulsars and challenge our current understanding of how the systems evolve.

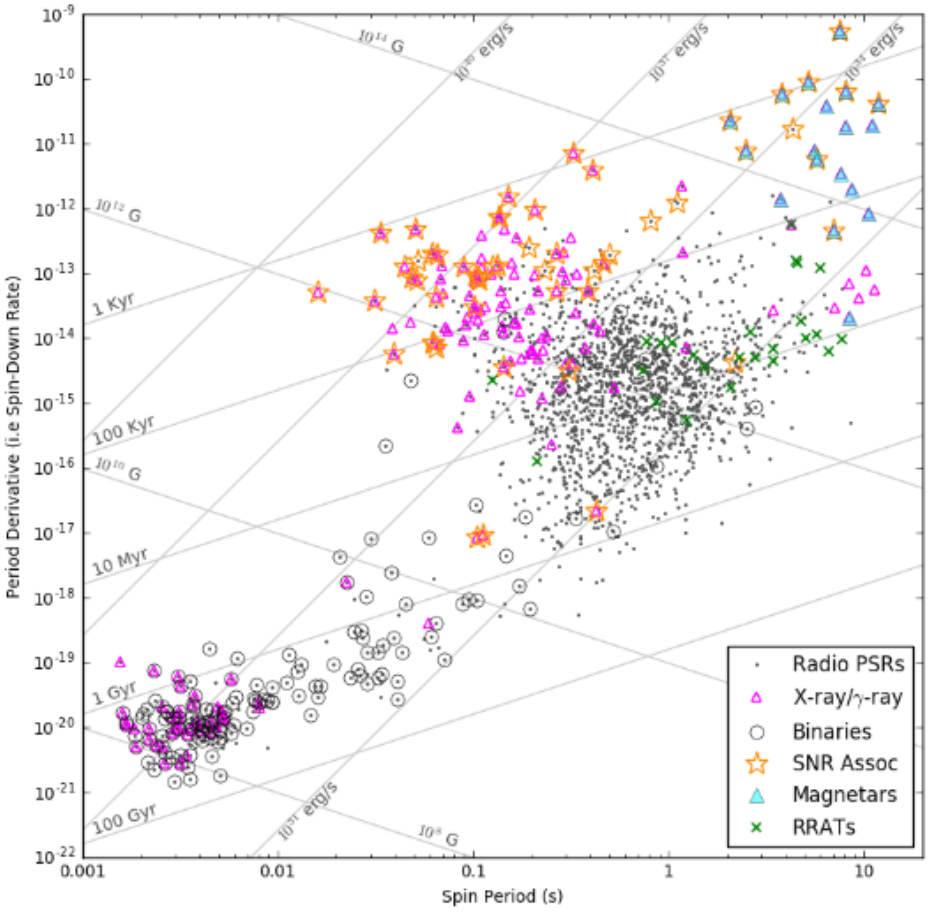

Figure 1.7: The period-period derivative diagram for pulsars encodes essential information about pulsar properties. The normal pulsars form a cluster of points in the middle of the plot, while the MSPs are in the lower left part of the plot. Magnetars, represented as blue triangles lie in the top right region of the plot. The plot also shows the X-ray or gamma-ray pulsars, binaries and supernova remnants associated with the pulsars. Lines of constant magnetic field, age and luminosity are also shown in the plot.

The subsections below describe some of the most important classes of pulsars that have been determined so far and focus on those most relevant to the science described in this thesis.

1.4.1 Millisecond and binary pulsars

Millisecond pulsars (MSPs) have extremely short spin periods (≤ 30ms), low spin-down rates and high rotational stability. MSPs typically have a low magnetic field strength of around $10^8 - 10^9$ G, distinguishing them from very young pulsars with short post-birth periods and higher magnetic fields. This difference can be easily seen in the $P - \dot{P}$ diagram as shown in Figure 1.7, with the MSPs forming a distinct 'island' towards the lower left corner of the $P - \dot{P}$ diagram.

MSPs are believed to be primarily formed in binary systems via the interaction of a normal (often non-active) pulsar with its stellar companion (Alpar et al., 1982). However, there are multiple evolutionary channels through which MSPs can be formed and it is possible that the evolution of every MSP is unique. A simplified diagram of different evolutionary paths of pulsars in binary systems is shown in Figure 1.8.

The formation of MSP begins with two main sequence stars, with one of them having sufficient mass to be the progenitor of a supernova (SN) explosion. This progenitor evolves faster than the companion and eventually explodes as a supernova, and forms a neutron star. If the mass of the progenitor star exceeds $30 M_\odot$ it can collapse into a black hole (BH) as a result of the SN explosion. This scenario is not considered as part of this thesis as it doesn't lead to an NS/pulsar. If the system is disrupted by the supernova, the two objects separate, which results in the formation of a young, isolated, neutron star. However, if the system remains undisrupted by the supernova explosion, as the remaining main sequence star evolves it eventually expands which leads to Roche-lobe overflow (RLO). This causes the outer layers of stellar material to be no longer gravitationally bound to the star. This material accretes onto the pulsar, resulting in the transfer of the angular momentum to the pulsar and eventually spinning up or 'recycling' the pulsar to very short rotational periods (Bisnovatyi-Kogan & Komberg, 1974). Such a recycled pulsar can become an MSP. The original pulsar can already be in a non-active state (i.e. in the 'graveyard' on the P-$\dot{P}$ diagram), but the

spin-up reactivates the emission mechanism and hence the term 'recycling'. The recycling process also leads to a decrease of the surface magnetic field of the MSP (Shibazaki et al., 1989) and results in a high degree of circularisation of the binary orbit due to the exchange of tidal forces between the pulsar and its binary companion (Phinney & Kulkarni, 1994). Recycling continues till an equilibrium point is reached between the inward gravitational pressure of the infalling accreted material and the outward radiation pressure of the NS (Bhattacharya & van den Heuvel, 1991).

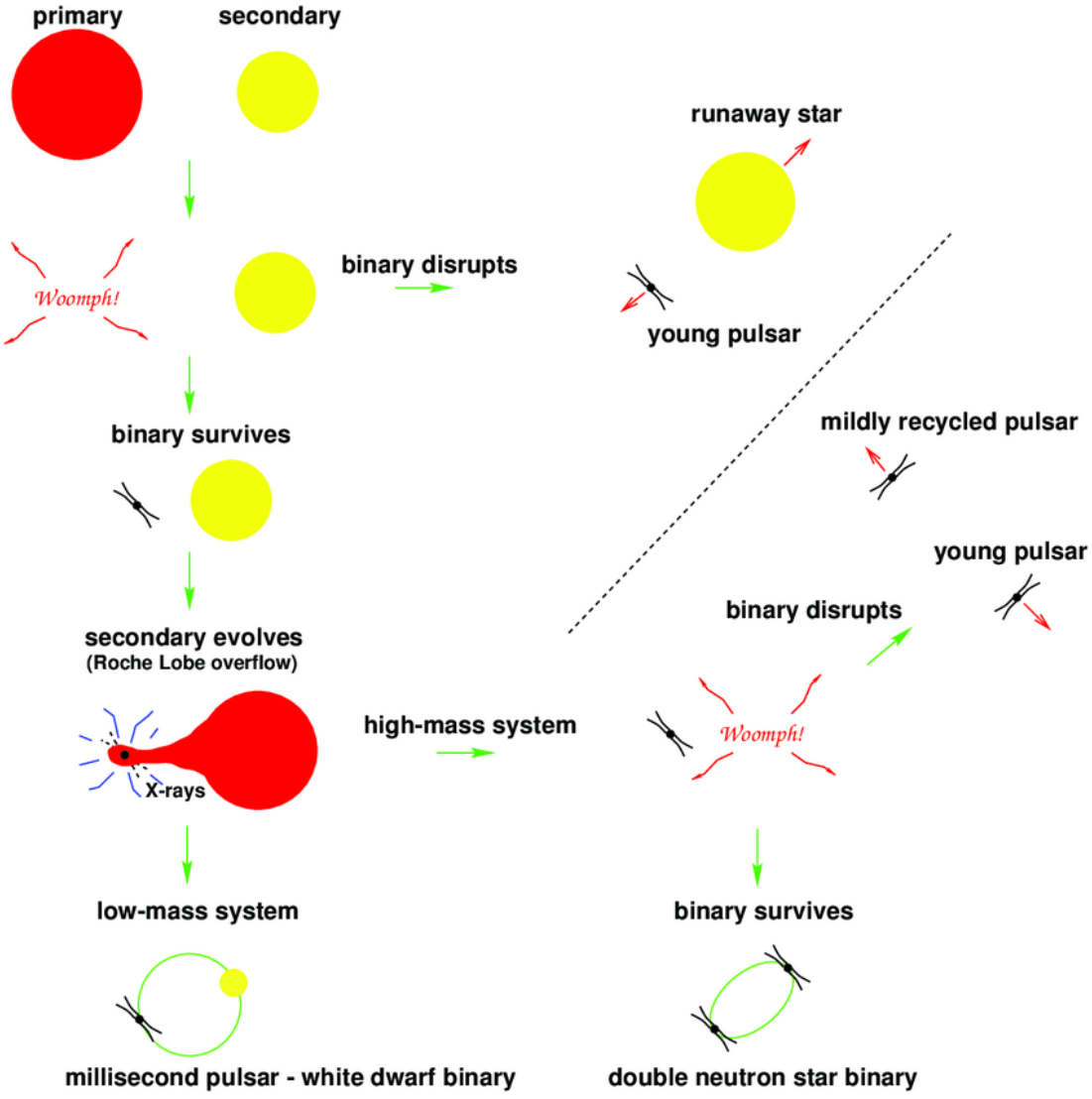

Figure 1.8: A simplified schematic of some major formation channels of pulsar binary systems.

The fate of the main sequence star as well as the binary system is dependent upon the companion's initial mass. If the companion is sufficiently massive to explode as a supernova, and the orbit is preserved it results in a double neutron star (DNS) system. As there is no further recycling in the system, the neutron star formed later may or may not be detectable as a pulsar by the time of its evolution. Alternatively, if the companion is not sufficiently massive to undergo a supernova, the accretion continues for about 10^8 years, until the companion star sheds its outer layers and becomes a white dwarf.

On the other hand, disruption of a binary system in the second supernova explosion can result in the formation of two isolated neutron stars. One of these NSs is fully or partially recycled. A small population of such isolated recycled pulsars has been observed. In an alternative scenario, a binary system does not reach the second supernova explosion, because the so-called 'black widow' MSP pulsar ablates its binary stellar companion, which also leads to an isolated MSP.

The detection of such systems using periodicity searches is rather hard and computationally expensive. One has to implement further parameters such as the acceleration searches to take into account the companion and the orbital period of the system. The estimation of an ideal acceleration search parameter space requires the prior estimates of the orbital period of the system, which is often poorly constraint. Therefore, alternative approaches such as detecting these pulsars as continuum sources in Stokes images is a good method of of discovering more such such pulsars.

1.4.2 Nulling, intermittent and mode changing pulsars

Some pulsars suddenly switch between emission on and off states, which is so-called 'nulling'. The first nulling pulsars, PSRs B0834+06, B1133+16, B1237+25 and B1929+10 were identified by Backer (1970). During the 'off' state, no pulsed emission is detected from the pulsars. While nulling pulsars have 'off' states of the timescale of the order of individual pulse periods to as long as several minutes,

intermittent pulsars are defined as pulsars with much longer 'on' and 'off' states ranging between hours to days and in extreme cases even years. The fraction of time when a pulsar is in its 'off' state is called a nulling fraction. It has been observed that the 'off' state may be accompanied by a change in the pulsar's spin properties (Kramer et al., 2006).

Mode changing is another phenomenon observed in pulsars, where a pulsar abruptly changes its pulsed emission between several discrete modes. It was first observed in the pulsar PSR B1237+25 and is described as the pulsar whose pulsed emission appears to be abruptly changing between multiple discrete 'modes'. Primarily, different modes have different pulsar profiles, but changes in the luminosity (Sobey et al., 2015), spin properties (Lyne et al., 2010) and other parameters may also be observed. All these phenomena are linked to the highly-ordered changes in the pulsar emission process, but they have not been fully understood yet and are an area of active research.

The recent work done by Janagal et al. (2023) on PSR J0026-1955, an independently discovered pulsar by the MWA as part of the SMART pulsar survey (Bhat et al., 2023a,b). This pulsar exhibits both subpulse drifting, where the radio emission from the pulsar appears to drift in the spin phase within the main pulse profile along with a change in pulsar mode as well as nulling episodes when the emission briefly ceases. This behaviour makes the pulsar a unique object which shows subpulse drifting, nulling and mode-changing behaviour. This and similar pulsars form the ideal cases for deeper studies of the complexities of pulsar emission physics and models. However, it is hard to detect such pulsars as the detectability of the pulsar depends on the accurate estimation of the on-and-off period of the pulsars. As traditional searches are dependent on the periodicity of the pulsars it may not be the best approach to search for them. Using image-based approach we can detect the pulsar irrespective of their on and off period (if they are bright enough to be detected in images in the off stage).

1.4.3 Magnetars

Magnetars refer to a particular class of neutron stars with exceptionally strong magnetic fields of the order of magnitudes of $B_{surf} \simeq 10^{14}$ to 10^{15} G. The existence of magnetars was proposed by Duncan & Thompson (1992). They are harder to detect in radio wavelengths than normal pulsars as they cease to produce radio emissions sooner after birth than normal pulsars. It was previously thought that pulsed magnetar emission was limited to high-energy wavelengths such as gamma and X-ray bands. However, Camilo et al. (2006a) observed bright linearly polarised radio pulses from XTE J1810-197 establishing that magnetars can be radio pulsars. Of the ∼30 magnetars currently known in our Galaxy and Magellanic Clouds, five have transient radio pulsations (Camilo et al., 2006b). Finding more magnetars that emit radio wavelengths will open a new avenue of research.

Strong magnetic fields result in rapid spin down of the rotational period which results in longer spin periods of magnetars between approximately 2 to 12 seconds (Olausen & Kaspi, 2014). The prevalent theory for the strong fields of magnetars was that it resulted from the magneto-hydrodynamic dynamo process in the turbulent, dense fluid that existed before the pulsar reached equilibrium (Thompson & Duncan, 1993). Another theory suggests that the magnetars result from the collapse of stars with unusually strong magnetic fields (Zhou et al., 2019).

1.4.4 Long period pulsars

Recent radio surveys have led to the discovery of a handful of pulsars with pulse periods significantly longer than the previously known population of pulsars. Three radio pulsars, PSRs J1903+0433 (Han et al., 2021) , J0250+5854 (Tan et al., 2018), J0901-4046 (Caleb et al., 2022) have been discovered recently with periods of 14s, 23s and 76s respectively. The lack of long-period pulsars can be caused by both intrinsic and observational biases. Due to the $P^{-0.5}$ dependence of the radius of the opening angle of the polar cap (Skrzypczak et al., 2018) narrow

radio beam of the long period pulsars may be missed by the observers' line of sight. One of the observational biases is the fact that most pulsar surveys spent only a few minutes of integration time per pointing, which only contains a few pulses from these long-period pulsars (Parent et al 2018). This makes it harder to detect such long-period pulsars via periodic searches and using image-based approaches may be more suited for searches for this kind of objects. The recent discoveries of long-period pulsars and transients open a new avenue of research. Detecting more and studying these kinds of objects will help us understand their progenitors and processes leading to their formation. Moreover, linking them with normal pulsars and other types of neutron stars can improve our understanding of pulsars and potentially other radio transients, such as repeating Fast Radio Bursts (FRBs).

1.5 Scientific applications of pulsars

Since their discovery pulsars have found multiple applications in astronomy. One of their most prominent and successful applications has been the verification of Einstein's theory of general relativity (GR; Einstein, 1915), which has been extensively tested with pulsars. Since its formulation in 1915, it has been subjected to multiple tests designed to investigate the extent of the theory's predictive power. Pulsars, especially those in binary systems provide an ideal test-bed for GR in the 'quasi-stationary strong-field regime (Wex, 2014), in which the masses involved move at speeds significantly lower than the speed of light while themselves strongly self-gravitating. Pulsars have been extremely successful in this kind of test as their regular clock-like pulsations and rotational stability allow for the extraction of precise information regarding the orbits and allow for probing of gravitational potential due to its impact on timing. Moreover, binary pulsars allow the testing of alternate theories of gravity such as the ones that agree with general relativity in the weak field regime but diverge from it in the strong field regime and may surpass the predictive power of general relativity under extreme

conditions.

Pulsars are galactic objects and the interaction of their polarised emission with the magnetised ionised interstellar medium (ISM) makes them excellent probes to study the properties and structure of the Milky Way. As we can accurately measure the dispersion measure of pulsars, they can be used to map the Galactic distribution of free electrons (Gupta, 2002). Furthermore, pulsar signals are also highly polarised. The magnetic field of the Galaxy acts as a Faraday screen rotating the position angle of linear polarisation by an amount proportional to the line of sight component of the magnetic field weighted by electron density. This rotation measure (RM) can be used to map the large-scale structure of the Galactic magnetic field which shows field-line reversals between some neighbouring spiral arms. Regular monitoring of pulsars can also be used to study the dynamics of the interstellar medium on small time and length scales.

A powerful technique used for most applications of pulsars is pulsar timing. It is the measurement of the arrival time of pulses emitted by the pulsar. Pulsar timing observations require the conversion of the observed arrival times to the Solar System barycentre (SSb) using a planetary ephemeris. This is very sensitive to small changes in the assumed position and allows us to determine the astrometric parameters of pulsars with exceptional precision.

Monitoring a large number of MSPs using the pulsar timing array (PTA; Verbiest et al., 2021), by measuring the small disturbances in arrival times caused by a "ripple" in the space-time due to passing gravitational waves can be used to search for correlated structures in the timing residuals of MSPs distributed across the sky, and can be complimentary to ground-based gravitational wave detectors such as LIGO, VIRGO in detecting low-frequency (nHz) gravitational waves. The most recent evidence of gravitational wave background was confirmed by using 15 years of data set from the pulsar timing arrays all over the world (Agazie et al., 2023).

These are just some of the applications of pulsars and they are undergoing

immense expansion with the planning and construction of the Square Kilometre Array (SKA) on the horizon. The significant increase in the number of new pulsar detections would allow us to study the Galactic electron density distribution and magnetic field structure in more detail, especially with the expected increase in the parallax measurements possible with the far greater sensitivity of the SKA (Keane, 2018).

1.6 Surveys

Most of the surveys that have led to the discovery of the majority of pulsars have been conducted at frequencies >400 MHz. However, low-frequency surveys (50-350 MHz) are becoming increasingly successful and have now come to the forefront for the preparation of the Square Kilometre Array (SKA). Various interferometric telescopes such as the Giant Metrewave Radio telescope and the Karl G. Jansky Very Large Array. The recent low-frequency surveys have also incorporated all-sky imaging surveys as a way of finding interesting sources, which can be pulsar candidates. One of the main advantages of low-frequency pulsar surveys is larger fields of view.

The recent advancements in low-frequency radio astronomy and high-performance computing (HPC) required to process significant amounts of data, enabled multiple pulsar discoveries, where candidates were identified in images and later confirmed with periodic searches. For example, at GHz frequencies, the discovery of a highly polarised, steep-spectrum millisecond pulsar in a deep image with the Australian Square Kilometre Array Pathfinder telescope (ASKAP; Kaplan et al., 2019) have demonstrated the rising potential of imaging surveys to detect new pulsar candidates. Another recent discovery of a circularly polarised variable radio source in the Large Magellanic Cloud (LMC) shows the potential to detect new pulsars (Wang et al., 2022). The work presented here builds on the existing high-time resolution capabilities of the MWA leveraged by the supporting HPC facilities in order to develop and demonstrate image-based methodologies leading

to new pulsar discoveries. In this work, we mainly use two surveys: GLEAM to verify the flux density of the sources detected as part of this work and RACS to determine the spectral index of the sources and to check the compactness of the sources detected. A brief description of these surveys is given below and their application is described in Chapter 3.

1.6.1 GLEAM

GLEAM, the Galactic and extragalactic all-sky MWA survey is the survey of the entire Southern radio sky at frequencies between 72 and 231 MHz (Wayth et al., 2015). Using the drift scan observing mode of the MWA, it reaches RMS of about 10 mJy/beam centred at 200 MHz, containing 307 455 radio sources (Hurley-Walker et al., 2017). The GLEAM survey catalogue is mainly used in this work as a flux density scale as a flux scale reference, as the flux densities of the sources identified in this work are cross-checked against the GLEAM source catalogue.

1.6.2 RACS

The Rapid ASKAP Continuum Survey (RACS; McConnell et al., 2020) is a precursor to the full sky survey that is planned to be conducted with the Australia SKA Pathfinder (ASKAP) telescope. It will image the whole Southern sky in the frequency range of 700-1800 MHz, with an instantaneous bandwidth of 288 MHz. The median RMS noise for the RACS Stokes I image is 250 μJy/beam and is one of the deepest surveys of the Southern sky to date. This work mainly uses the low band (central frequency of 888 MHz) of RACS and the Stokes I catalogue (Hale et al., 2021), in order to use RACS flux densities together with MWA flux densities measured in this work to calculate the spectral index and identify steep spectrum sources. The catalogue is generated from 799 tiles that has been convolved to a common resolution of 25″. Furthermore, its better spatial resolution of ASKAP (than the MWA) was used to check the morphology of the sources

and exclude extended sources - unlikely to be pulsars, which are unresolved (i.e. point sources).

1.7 Thesis: direction and scope

Since the initial discovery of the first pulsar in 1967 (Hewish et al., 1968), significant effort has been invested in the development of effective and highly sensitive algorithms to detect pulsars (Ransom, 2001). These techniques mainly focus on the time or Fourier domain to identify periodic signals in time series data (see Chapter 6 in Lorimer & Kramer (2004)). While these searches have been very successful and led to the discovery of more than ∼3000 pulsars (Manchester et al., 2005), they may not be very efficient in some parts of the parameter space. For example, pulsars with short orbital periods in binary systems or strongly scattered pulsars are more difficult to detect in time-domain searches. Acceleration searches or "jerk" searches have been developed to detect pulsars in binary systems, but they are computationally expensive for large surveys. Especially at low frequencies ($\leq$ 300MHz), time domain searches are time-consuming due to the large number of DM trials required to get promising detections. Moreover, at MHz frequencies, the arriving pulses are more affected by scattering leading to inefficiency of periodic searches at high DM values ($\gtrsim$250 pccm^{-3} for MWA).

A complementary approach is to identify pulsar candidates by forming interferometric images and identifying pulsar candidates based on pulsar properties, for example, steep spectral index, circular polarisation and variability. Even though this image-based approach to detecting pulsar candidates may not be as sensitive as time-domain searches, it is more likely to detect interesting sources such as highly scattered pulsars, and pulsars in exotic binaries, that may have been missed by previous time-domain searches. Image-based searches can enable discoveries of new pulsars in a new parameter space unavailable to standard time domain searches. Image based searches have aided the discovery of the first millisecond pulsar as a steep spectrum source (Backer et al., 1982), the first globuler

cluster MSP and the pulsar planets.

Identifying pulsar-like sources in the image plane has been successfully demonstrated with instruments such as the Giant Metrewave Radio Telescope (GMRT; Swarup et al., 1991; Roy et al., 2010) and the Australian Square Kilometre Array Pathfinder telescope (ASKAP). Frail et al. (2016) discovered six millisecond pulsars and one normal pulsar from Stokes I images from the all-sky survey with the GMRT by using the criteria of compactness and spectral index. Kaplan et al. (2019) has discovered a new MSP PSR J1431-6328 as a highly polarised, steep spectrum radio source from the deep image with ASKAP, which showed that image-based exploration could discover interesting new pulsars at high Galactic latitudes without the need for computationally expensive periodicity searches in all-sky surveys. Wang et al. (2022) also discovered a highly circularly polarised, variable, steep spectrum pulsar in the ASKAP Variable and Slow Transient (VAST) survey which further highlights the possibility of identifying pulsars, especially pulsars with unusual radio characteristics in radio continuum images.

The primary goal of this thesis is to investigate the efficiency of image-based pulsar searches with the Murchison Widefield Array (MWA; Tingay et al., 2013a; Wayth et al., 2018), and compare this kind of searches to traditional time-domain searches. This image-based approach leverages known pulsar observables in the low-frequency radio images from the Murchison Widefield Array's Voltage Capture System (MWA VCS) data. One of the advantages of using the MWA VCS data is the data processing flexibility that it provides; the same MWA VCS data can be processed to produce full Stokes images as well as be used for time-domain periodicity searches. This work focuses on using this data processing flexibility to identify pulsar candidates in images using three properties of pulsars, namely, steep spectral index, circular polarisation and variability and later verify their pulsations in the very same MWA VCS data and data from other telescopes.

Chapter 3 describes the pipeline developed to produce full Stokes images using MWA VCS data for the first time and the methodologies to identify pulsar

candidates and detect known pulsars in these images from four MWA VCS observations. This chapter is a pilot survey to test the pipeline and the efficiency of the methodologies and demonstrate the potential of using them to detect pulsar candidates at low frequencies and improve the efficiency of future pulsar discoveries with the MWA as well as with SKA-Low. These methodologies are then applied to 12 MWA VCS observations covering the Galactic Plane (GP) which is described in detail in Chapter 4. This chapter mainly discusses the observational details of the Galactic Plane image-based survey and discusses statistical analysis and consequences of detections and non-detections of known pulsars in the images. It also describes a spectral study of the pulsars detected in the image-plane and discusses the impact of additional flux density measurements from imaging at low frequencies on the spectral modelling of these pulsars. It also discusses reasons for the non-detections of the other known pulsars in image plane searches. The new pulsar candidates identified by the devised methodologies (Chapter 4) in images from the GP survey are described in Chapter 5. This chapter focuses on using known pulsars to verify the efficiency of the three developed criteria individually and their combinations. It also discusses the follow-up analysis of the candidates using the same MWA VCS data, and follow-up observations with GMRT and Parkes (Murriyang) radio telescopes. Since none of the pulsar candidates were confirmed as new pulsars, Chapter 5 also discusses the possibility of these sources being some other category of known radio sources or even a new class of radio objects. Finally, Chapter 6 summarises the main results of this work and addresses the current limitations and potential future work.

Chapter 2

Instruments and research methodology

Radio telescopes are used to detect radio waves from astronomical radio sources in the sky and consist of a specialized antenna and receiver. The amplitude and phase of the radio wave are used to characterise the visibility properties. Due to the Fourier transform nature of the relationship between sky brightness and visibility, visibility is sensitive to all regions of the sky to which the telescope responds. Radio astronomy has changed the way we view the Universe and has increased our knowledge of it by providing us with the possibility to explore parts that are not accessible by other parts of the electromagnetic spectrum. Radio waves can propagate through dense regions of the Universe, which are enveloped by clouds of dust and gas, unlike optical telescopes that rely on the visible part of the electromagnetic spectrum.

In this chapter, I have given a brief overview of the fundamentals of radio interferometry. I also discuss the telescopes used for the work presented in this thesis and the description of the methods used to obtain and process pulsar data from the three telescopes: the Murchison Widefield Array (MWA), the Parkes (Murriyang) Radio Telescope and the Giant Metrewave Radio Telescope (GMRT). Details specific to data sets used in the thesis are given in subsequent chapters

where the data itself is presented.

2.1 Instruments used

2.1.1 The Murchison Widefield Array

The Murchison Widefield Array (MWA; Tingay et al., 2013a) is the low-frequency precursor of the Square Kilometer Array (SKA) located at the Murchison Radio-astronomy Observatory (MRO) in Western Australia. The MRO is located in a radio-quiet zone and hence has a significantly low level of radio frequency interference (RFI), mostly caused by aircraft, communication devices and satellites. It can observe the Southern hemisphere sky in the frequency range of 70–300 MHz with a processing bandwidth of 30.72 MHz. The MWA Phase I was an aperture array interferometer with 128 tiles. Each tile was approximately 5 m $\times$ 5 m with 16 dual-polarisation dipole elements in a 4 $\times$ 4 grid. The dipole centres were separated by $\sim$ 1.1m each. The MWA Phase I is shown in Figure 2.1. The MWA Phase I tiles are randomly distributed with a resulting maximum baseline of $\sim$3 km, providing an angular resolution of $\sim$3 arcmin at an observing frequency of 150 MHz. It also has unparalleled survey efficiency due to its immense collecting area of $\sim$2752 m^2 and 610 deg^2 field of view.

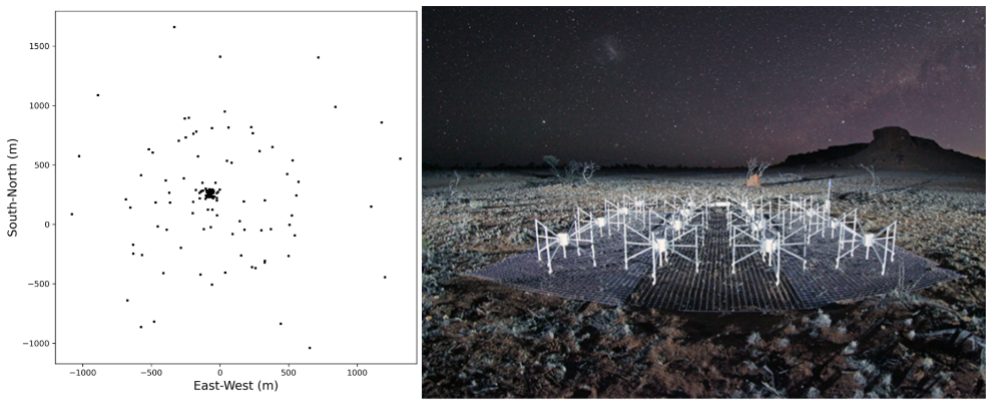

Figure 2.1: The left panel shows the MWA configuration of the tiles in Phase I and the right panel shows the image of an MWA tile (Tingay et al., 2013a).

An additional 128 tiles were deployed during the period of late 2016 and early 2017, leading to the MWA Phase II upgrade (Wayth et al., 2018), consisting of 256 tiles with baselines extending up to ∼6 km. The array is capable of switching between two types of configuration, namely, compact and extended. The compact configuration consists of 56 tiles in the core of the MWA, along with the 72 new tiles that are in two regular hexagonal configurations (Wayth et al., 2018). This configuration of the telescope is primarily used for the study of the Epoch of Reionisation (EoR) power spectrum, which is one of the main science goals of the MWA (Parsons et al., 2012). The compact configuration is also advantageous to pulsar surveys due to its functionality of large tied-array beams (due to shorter baselines and beam size of 23 arcminutes at 150 MHz), and eventually improving the survey speed. On replacing the 56 closely-spaced tiles with sparsely spaced ones, we get the extended configuration of the MWA Phase II. This is beneficial for high spatial resolution imaging (∼ 1.30' at 154 MHz) with a reduction in the expected classical confusion by a factor of ∼8 when compared with that of MWA Phase I (Wayth et al., 2018). The tile configuration of compact and extended MWA Phase II is shown in Figure 2.2. For the work presented in this thesis, we used a combination of Phase I and Phase II extended configuration observations.

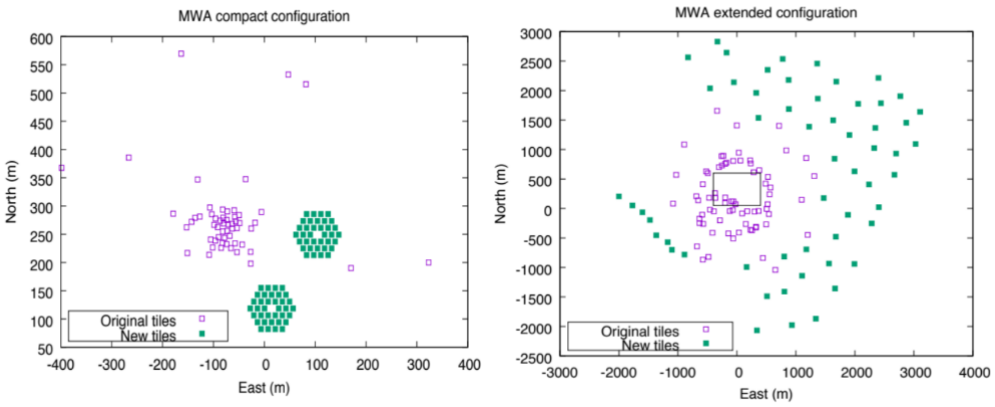

Figure 2.2: The left panel shows the tile locations for Phase 2 compact configuration. The right panel shows the extended configuration of Phase 2 (Wayth et al., 2018).

2.1.1.1 The Voltage Capture System

The MWA was initially envisioned as an imaging interferometer with its focus on detecting the signature of EoR, exploring Galactic and extragalactic radio sources in the Southern Hemisphere, searching for slow transient events and solar and space studies (Bowman et al., 2013; Beardsley et al., 2019). The output signal streams from the fine Polyphase Filter Banks (PFBs) are processed by the MWA correlator to produce cross-power spectra with a native time resolution of 100 μs and a frequency resolution of 10 kHz. This is the standard signal path of the MWA (Ord et al., 2015). Even though high-time resolution data products needed for pulsar studies, are not provided as a functionality for the standard MWA observing mode (so-called correlator mode), the flexibility of the signal path enables the acquisition of complex voltages from all MWA tiles.

The Voltage Capture System (VCS; Tremblay et al., 2015) enabled the MWA to record the high time (100 μs) and frequency (10 kHz) resolution 4-bit+4-bit complex voltage stream output from the fine PFB stage. This made it possible to use the MWA for high-time resolution studies such as searches for pulsars and fast radio bursts and solar science. The maximum recording time for one MWA VCS observation was 90 minutes for the old correlator due to the large data volume of VCS observations. With the new upgraded correlator, one can record multiple hours of data. For this thesis, observations with the old correlator are being used and hence the maximum time duration of the observations recorded is 90 minutes. Each observation is identified by 'OBSID', which is the GPS time when the observation commenced.

2.1.1.2 The MWA primary beam model

The beam response of the MWA tiles is complex as is shown in Figure 2.3. It is a function of the pointing position and the observing frequency (Sutinjo et al., 2015), such that the beam is larger at lower observing frequencies. When the telescope is pointed away from the zenith, a grating lobe, whose gain is stronger

than the normal side lobe and mimics the main beam in shape and sensitivity may arise. This effect generally comes into play at frequencies greater than 200 MHz. Several pulsars have been detected in these grating lobes for MWA VCS observations (Xue et al., 2017).

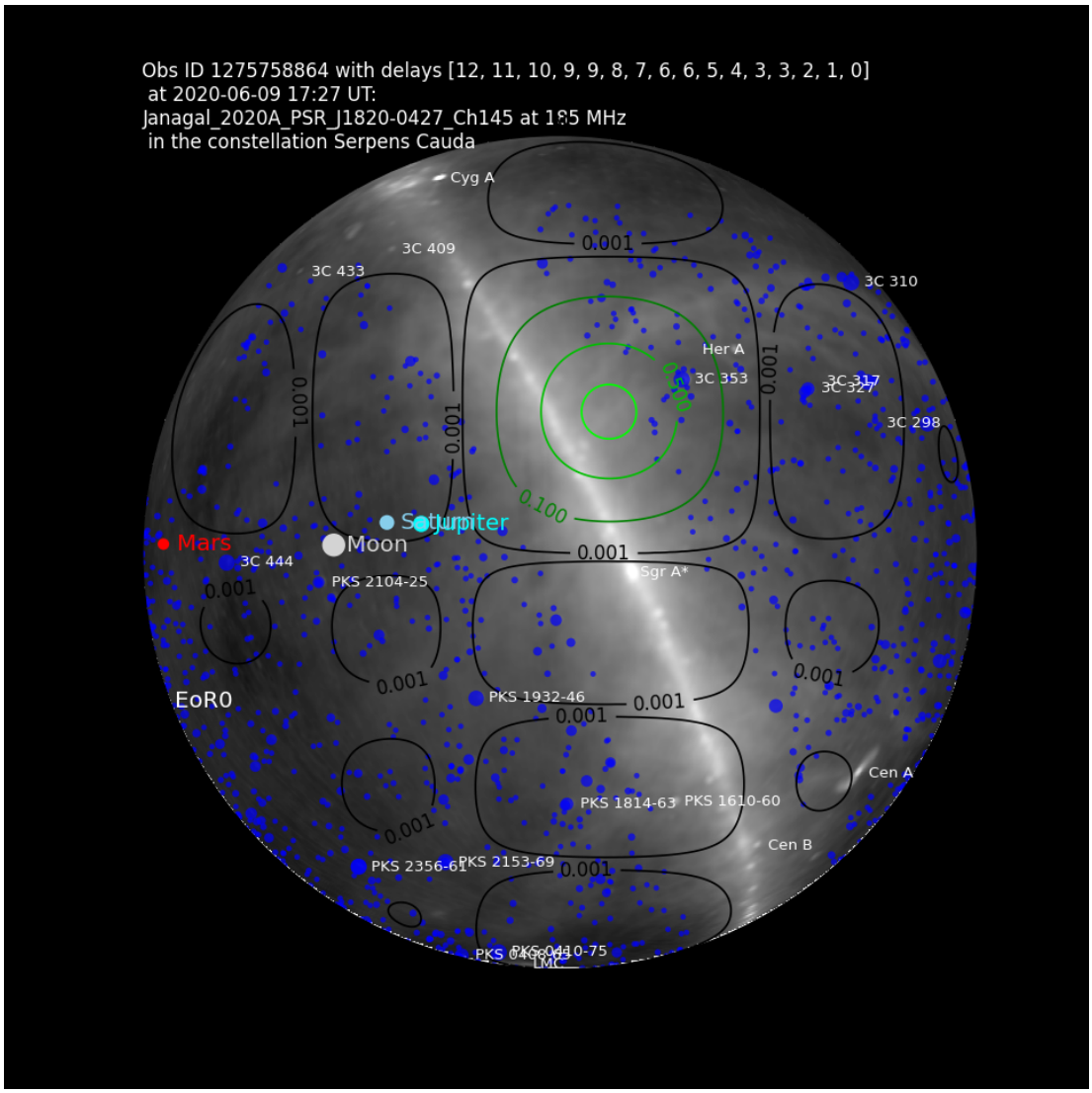

Figure 2.3: Primary beam and sidelobes for a MWA observation at 185 MHz. The green contours represent the primary beam of the MWA and the black contours are the sidelobes. The Galactic Plane is seen to be passing through the primary beam of the observation.

The MWA tile beam model is used in combination with an observation of a calibrator source to determine the direction-independent gain for each tile as a

Jones matrix. The resulting gain calibration can then be applied to observations of the target source. This is required to calculate Stokes IQUV and perform full polarimetry from measured visibilities or voltages in X and Y polarisations. Instrumental leakage between the Stokes parameters will be evident due to the differences between the beam model and the true beam (Sutinjo et al., 2015; Sokolowski et al., 2017; Lenc et al., 2017). The three types of available beam models with different levels of accuracy:

(1) The analytical beam model (Ord et al., 2010): This is the simplest beam model available, comprising of summation of 16 dual-polarisation Hertzian dipoles above an infinite ground screen.

(2) The Average Embedded Element (AEE) beam model (Sutinjo et al., 2015): This model has an improved accuracy than the previous analytical model. It describes the beam model of a tile as an average of 16 beam patterns of individual Bow-Tie dipoles within an MWA tile made with electromagnetics computational software called FEKO.

(3) The Full Embedded Element (FEE) beam model (Sokolowski et al., 2017): This is the most accurate beam model available to date. This comprises FEKO simulations of each of the 16 embedded elements and dual polarisation for each at every frequency.

2.1.2 Murriyang - The Parkes Radio Telescope

The Parkes radio telescope, Murriyang, has been one of the major radio telescopes in the Southern Hemisphere, operating for over 60 years. It is one of the leading pioneers of pulsar discoveries and has discovered more than 50% of pulsars known to date. The telescope is a classical paraboloid dish, 64 m in diameter. The dish is fully steerable and can point between 0–360 ° in azimuth and between $\sim$ 30–89 ° in elevation. To meet the varied observational requirements, the telescope has a wide range of receivers and backends, including the high time resolution modes which are beneficial for pulsar studies. The observable bands range from

0.7–22 GHz, with a corresponding system temperature between 20–150 K and gain between 1–2 KJy^{-1}. Previous multibeam receivers such as the 13-beam 20 cm receiver (Staveley-Smith et al., 1996) and the 7-beam "methanol" receiver (Green et al., 2009) have successfully performed multiple large-scale observations previously. This data can then be coherently dispersed in real time or generate data in the commonly called "search mode", which is a channelised filterbank data stream that can be processed offline. In recent years, the receiver system has been upgraded to a new ultra-wide-bandwidth low-frequency receiver (UWL, Hobbs et al., 2020) This thesis makes use of the UWL receiver which is described in detail in Section 2.1.2.1.

2.1.2.1 The Ultra-wideband Low-frequency receiver

The Ultra-wideband Low-frequency receiver (UWL), is the major addition to the Parkes receiver system that has enabled the continuous frequency coverage from 704 to 4032 MHz (Hobbs et al., 2020). The UWL receiver can be used to perform all types of pulsar observations such as fold-mode and search-mode as well as non-pulsar observations such as spectral line continuum, polarisation and even Very Long Baseline Interferometry (VLBI) observations. Given that the UWL band overlaps with that of ASKAP, it can also be used for high-time resolution and follow-up of ASKAP observations. This upgrade to the receiver system has been proven to be highly beneficial in performing ISM studies and other frequency-dependent phenomena.

2.1.3 The Giant Metrewave Radio Telescope

The Giant Metrewave Radio Telescope or GMRT, located around ~ 80 km north of Pune, India, is a steerable radio telescope operating in metre wavelengths (Intema et al., 2017). It consists of 30 fully-steerable parabolic dishes of 45 m diameter, spread over a 25 km baseline. The telescope forms a "Y" shape with the 14 dishes forming the central array and the 16 remaining dishes spread across

the other arm of the Y shape. Since being commissioned in 2002, the telescope has been used to study a variety of astrophysical phenomena from within the Solar System to the edge of the observable Universe. The legacy GMRT operated at five radio bands from 150 to 1450 MHz, with a bandwidth of 33.33 MHz. At the end of 2017, the GMRT was upgraded to uGMRT, and the details of the upgraded system are given in Section 2.1.3.1. The uGMRT is mainly used as part of this thesis work.

2.1.3.1 Upgraded Giant Meterwave Radio Telescope

Upgraded GMRT or uGMRT was commissioned at the end of the year 2017, and underwent major changes such as an increase in bandwidth (up to 400 MHz), an increase in dynamic range, improved channel resolution and a frequency coverage from 50 to 1500 MHz (Gupta et al., 2017). The upgraded system has the capability to provide four different beams with any combination of antennas, at a given phase centre. The signals can be combined either in an incoherent or a phased-array mode and can be used to perform simultaneous multi-frequency observations of pulsars. For the observations used in this work, we made use of Band3, which offers a continuous band between 300-500 MHz.

2.2 Radio interferometry

A visibility is the Fourier transform of the sky brightness distribution and provides us with information on the interferometric response of the telescope. Radio telescopes characterise the visibility properties by recording the amplitude and phase of the radio wave. Due to the Fourier transform nature of the relationship between sky brightness and visibility, a visibility is sensitive to all regions of the sky to which the telescope can respond. As radio waves can travel through dense regions obscured by gas and dust, they help us explore parts of the Universe that are not accessible at X-ray and optical wavelengths.

A single dish radio telescope's resolving power is given as $\approx 1.22\lambda/D$, where λ is the observing wavelength and D is the aperture diameter. The capability of single-dish telescopes to resolve sources in regions that are crowded with multiple structures is limited by the mechanical structure one can construct to hold the telescope. The biggest single-aperture telescope at present is the Five-hundred-meter Aperture Spherical Radio Telescope (FAST), with a diameter of 500 m and a resolution of $2.9^{'}$ in the L-band (Nan, 2006). The FAST telescope has been beneficial in performing useful science, however, the need for better resolution still exists. This need for better resolution led to the evolution of radio interferometry, where signals from multiple single radio telescopes distributed over large distances are combined together to essentially emulate one single telescope providing an extremely high angular resolution. The previous equation of resolving power for a single dish radio telescope is altered to $\approx 1.22\lambda/B_{max}$, where B_{max} is the maximum distance between the two antennas (baseline) for a radio interferometer. In the upcoming sections, I have given a brief overview of the fundamentals of radio interferometry.

2.3 Radio interferometry basics

Radio interferometers consist of several single radio telescope elements distributed over a few metres to thousands of kilometres like the MWA or even more, e.g., space VLBI. Advanced high-performance computing has enabled processing signals from a large number of antennas, increasing the collecting area and hence the sensitivity by manifolds. The basics of radio interferometry remain the same irrespective of its location, design or science goals. The detailed theory for the techniques in radio interferometry can be found in Clark (1999) and Thompson et al. (2001).

For radio interferometry we calculate the spatial coherence function of the incident electric field by combining the radiation collected by two or more antennas separated by some distance, often referred to as baseline (b). Under assump-

tions, it can be translated to the Fourier transform of the sky brightness. The sky brightness is affected by atmospheric and instrumental effects. However, we can invert it to calculate the distribution of the sky brightness, if the spatial coherence function is well sampled. This can then be used to generate an image of the observed sky.

Let us assume that we have N_e single antenna elements in a radio interferometer, then the number of independent pairs or baselines is given by $\frac{N_e(N_e-1)}{2}$ and does not include auto-correlations. If we include auto-correlations, then the number of baselines is given as $\frac{N_e(N_e+1)}{2}$. The quasi-monochromatic component is given by $E_\nu(r)$. For a time-varying electric field, $(E_\nu(r,t))$ created on a random pair of antennas by the source of interest, the quasi-monochromatic component, $E_\nu(r)$ is not the same for different pair of antennas. As given by Clark (1999), at frequency ν, the time-averaged cross-correlation (V) of the two electric fields, or visibilities, for antennas located at $\tilde{\mathbf{r_a}}$ and $\tilde{\mathbf{r_b}}$ can be defined as,

$$V_\nu(\tilde{\mathbf{r_a}}, \tilde{\mathbf{r_b}}) = \int \langle E_\nu(\tilde{\mathbf{r_a}})\, E_\nu^*(\tilde{\mathbf{r_b}}) \rangle \tag{2.1}$$

where E_ν^* is the complex conjugate of E_ν, and time averaging is denoted by $\langle\rangle$.

We can only obtain information on the structure of the astrophysical sources in two dimensions, as they are located at a large distance and have no information about their depth. A diagrammatic representation is shown in Figure 2.4.

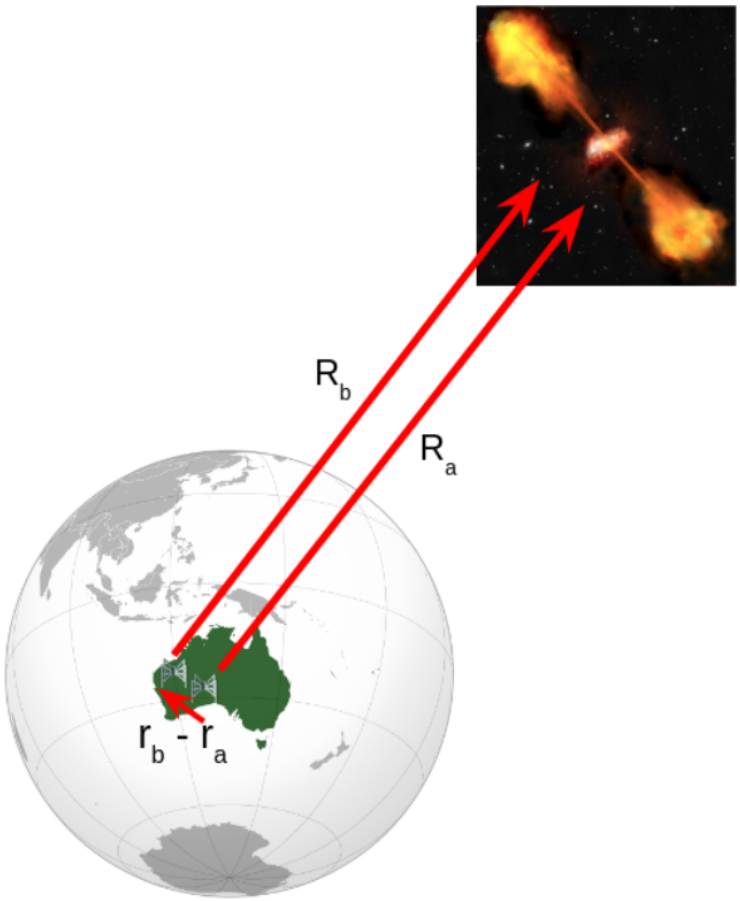

Figure 2.4: Representation of the geometry for interferometry in radio astronomy.

Another assumption that is made is that the intervening medium between the observer and the source is empty and there is no contamination from any additional source. The visibility function takes the below form under these assumptions,

$$V_\nu\left(r_a, r_b\right) \approx \int I_\nu\left(s\right) e^{-2i\pi\nu s.(r_a - r_b)/c} d\Omega \tag{2.2}$$

where I_ν is the observed intensity or surface brightness of a small area on the sky as shown in Figure 2.4 with a solid angle element $d\Omega$, where $d\Omega$ can be expressed as

$$d\Omega \equiv \frac{dl\ dm}{n} = \frac{dl\ dm}{\sqrt{1 - l^2 - m^2}}. \tag{2.3}$$

Equation 2.2 is called the van Cittert-Zernike Theorem (van Cittert, 1934; Zernike, 1938) and shows the visibility in terms of baseline length between two antennas and is the spatial coherence function. It can also be used to retrieve the surface brightness of the sky.

2.3.1 The measurement equation

Given that sources are located very far away from the observer (for example, the yellow star shown in Figure 2.5), we can assume that the radiation they emit travels to us in the form of a plane wave. When this radiation reaches antennas A and B (as shown in Figure 2.5), it does so at different times due to geometric delay. To account for this, the observers introduce time delays to the signals received by different components of the interferometer. These delays are added either through the use of software or physical cables.

The uv-plane (shown in Figure 2.5) can accommodate each of the interferometric visibilities. On this plane, the u and v axes are positioned perpendicular to the direction of the observed astronomical source, while the third axis, w, which is the direction of the observed source runs parallel to it. By projecting the baseline b (i.e., antenna spacing $= r_a - r_b$) onto the uv-plane, we can determine the values of u and v, which are measured in units of wavelength λ. A baseline on the UV plane can be defined as:

$$b = r_a - r_b = \lambda\,(u, v, w \equiv 0) \tag{2.4}$$

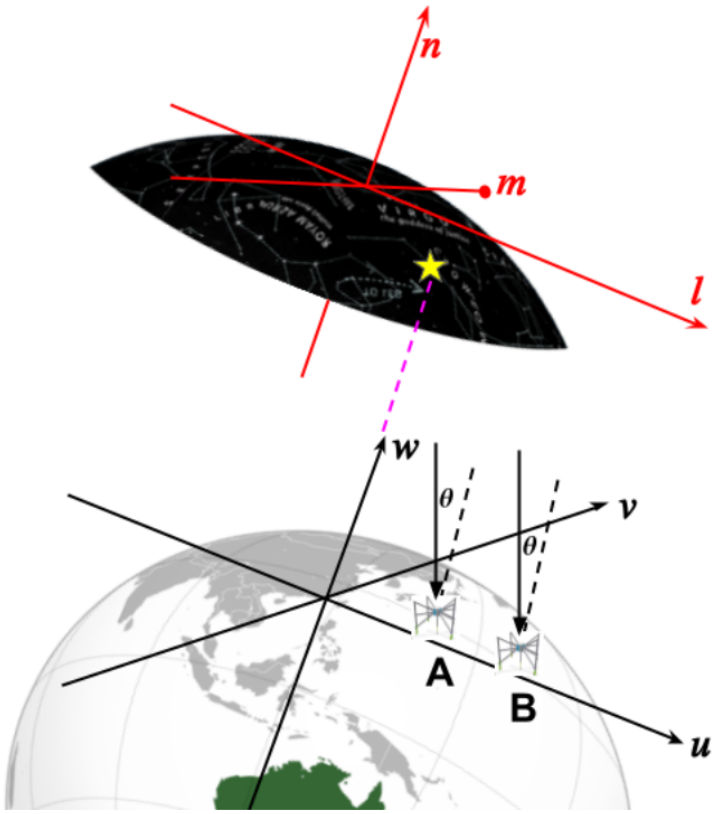

Figure 2.5: Coordinate system of the celestial sphere (red) and the baseline parameters (black).

We can then consider that the radiation is coming from a solid angle of the sky and hence is emitted in the form of a 2D plane, which sets w=0. A unit vector, s can then be defined in terms of its components as $l, m, n = \sqrt{1 - l^2 - m^2}$ where l, m, and n are direction cosines (see Figure 2.5). Substituting s with its direction cosine components, l, m, n in Equation 2.2 we get

$$V_\nu\left(u, v, w \equiv 0\right) = \int\int I_\nu\left(l, m\right) \frac{e^{-2\pi i(ul+vm)}}{\sqrt{1 - l^2 - m^2}} dl\ dm \tag{2.5}$$

For a small area of the sky, l and m will be extremely small and $\sqrt{1 - l^2 - m^2} \approx 1$. The observed visibility is attenuated by the normalised antenna response of the primary beam $A_\nu(s)$ and is now written as

$$V_\nu\left(u, v, w \equiv 0\right) = \int\int A_\nu\left(l, m\right) I_\nu\left(l, m\right) e^{-2\pi i(ul+vm)} dl\ dm \tag{2.6}$$

where w=0 and hence $V_\nu(u,v)$ is the complex visibility. $A_\nu(l,m)$ is the direction-dependent parameter and drops to zero when we move away from the pointing centre. Further derivation assumes that FoV is small, in which case the value of $A_\nu(l,m)$ can be calculated and enforces the earlier assumption that the emission is coming from a small patch of celestial sphere.

The inverse Fourier transform of the Equation 2.6 and then dividing by $A_\nu(l,m)$ can provide us with the true brightness of the source. The resulting quantity is the true sky intensity convolved with the Fourier transform of the uv-sampling function (described in Section 2.3.2). Performing deconvolution produces the true image of the sky.

However, in the case of interferometric arrays such as the MWA with a wide primary beam (i.e. wide FoV), Equation 2.6 without w≈0 is modified as

$$V_\nu(u,v,w\equiv 0) = \int\int A_\nu(l,m)\, I_\nu(l,m)\, e^{-2\pi i\left(ul+vm+w\left(\sqrt{1-l^2-m^2}-1\right)\right)} \frac{dl\ dm}{\sqrt{1-l^2-m^2}} \tag{2.7}$$

where the angular coordinate (l,m,n) defines a position in the celestial sphere and $n=\sqrt{1-l^2-m^2}$.

To image large fields of view, specialised algorithms are required, described in Sections 2.3.3 and 2.3.4.

We require the imaging algorithms described below to handle data from such wide FoV radio interferometers.

2.3.2 uv-coverage

The sampling of the uv-plane influences the retrieval of the true sky brightness. It is not possible to sample the uv-plane completely with an interferometer. A hole is left at the centre because there is a limit to how closely antennas can be physically placed and this limits sensitivity to structures of large angular extent (where required these short-spacings can be filled using single-dish data). A

sharp outer cut-off is defined by the longest baselines and this not only limits the available resolution but also results in increased sidelobes in the point source response.

The optimal uv-coverage of an ideal interferometer is a complex connection between sensitivity, FoV and cost, depending on the distribution of the baselines and the computational power required for the number of baselines for imaging. Furthermore, the uv-coverage required is different for different science themes and therefore the meaning of ideal uv-coverage is different. Therefore, the true brightness of the sky cannot be entirely recovered.

A sampling function ($S(b)$) is used to describe the limited uv-coverage which is important if we are trying to recover the true brightness of the sky through the Fourier transforms of our measurements. The sampling function can be written as

$$S(b \equiv (u,v)) = \sum_{m=0}^{M} \delta(u - u_m)\,\delta(\nu - \nu_m) \tag{2.8}$$

where M is the total number of baselines, and each Dirac-delta function represents a different baseline in the uv-plane.

2.3.3 W-Projection

This method as the name suggests projects the various W-terms onto the $w = 0$ plane, so that it is possible to use a two-dimensional Fourier transform to reconstruct the sky image which is easy to solve as well as computationally efficient (Cornwell et al., 2005). This is done to handle data from wide field-of-view interferometers (MWA in our case) and is discussed in more detail in Section 2.4.

Equation 2.7 can be rewritten in terms of the w-free term and w-term as

$$V_\nu(u,v,w \equiv 0) = \int\int A_\nu(l,m)\, I_\nu(l,m)\, e^{-2\pi i(ul+vm)} e^{-2\pi i w\left(\sqrt{1-l^2-m^2}-1\right)} \frac{dl\ dm}{\sqrt{1-l^2-m^2}} \tag{2.9}$$

The exponential component with the w-term can be represented as $G\left(l,m,w\right)$,

$$G\left(l,m,w\right)=\exp^{-2\pi iw\left(\sqrt{1-l^2-m^2}-1\right)} \tag{2.10}$$

Equation 2.9 can be rewritten as

$$V_\nu\left(u,v,w\equiv 0\right)=\int\int A_\nu\left(l,m\right)I_\nu\left(l,m\right)e^{-2\pi i(ul+vm)}G\left(l,m,w\right)\frac{dl\ dm}{\sqrt{1-l^2-m^2}} \tag{2.11}$$

and can be further simplified as

$$V_\nu\left(u,v,w\right)=\mathfrak{F}_{2D}\left[\frac{A_\nu\left(l,m\right)I_\nu\left(l,m\right)}{\sqrt{1-l^2-m^2}}G\left(l,m,w\right)\right] \tag{2.12}$$

where $\mathfrak{F}_{2D}$ is the 2-D Fourier transform operator and $\circledast$ represents convolution,

$$V_\nu\left(u,v,w\right)=\mathfrak{F}_{2D}\left[\frac{A_\nu\left(l,m\right)I_\nu\left(l,m\right)}{\sqrt{1-l^2-m^2}}\right]\circledast\,\mathfrak{F}_{2D}\left[G\left(l,m,w\right)\right] \tag{2.13}$$

$$V_\nu\left(u,v,w\right)=V_\nu\left(u,v,w=0\right)\circledast\,\mathfrak{F}_{2D}\left[G\left(l,m,w\right)\right] \tag{2.14}$$

$$V_\nu\left(u,v,w\right)=V_\nu\left(u,v,w=0\right)\circledast\,\tilde{G}\left(u,v,w\right) \tag{2.15}$$

The non-zero w-term can be presented as a convolution between the visibilities projected onto the $w=0$ plane and the convolution function $\tilde{G}\left(u,v,w\right)$, where the convolution function is the 2-D Fourier transform of the function $G\left(l,m,w\right)$, which can be defined as

$$\tilde{G}\left(u,v,w\right)=\int\int e^{-2\pi i(ul+vm)}G\left(l,m,w\right)dl\ dm, \tag{2.16}$$

$$\tilde{G}\left(u,v,w\right)=\int\int e^{-2\pi i(ul+vm)}e^{-2\pi iw\left(\sqrt{1-l^2-m^2}-1\right)}dl\ dm \tag{2.17}$$

After following, Cornwell et al. (2008), we can use the small angle approximation for Equation 2.17 and expand $\left[1-\left(l^2+m^2\right)\right]^{1/2} \approx \left[1-\frac{1}{2}\left(l^2+m^2\right)\right]$, to get

$$\tilde{G}\left(u,v,w\right) = \int\int e^{-2\pi i(ul+vm)}\ e^{\pi iw\left(l^2+m^2\right)}\ dl\ dm, \tag{2.18}$$

$$\tilde{G}\left(u,v,w\right) = \frac{i}{w} e^{-i\pi\left(\frac{u^2+v^2}{w}\right)} \tag{2.19}$$

We can then perform an FFT of the visibilities with a non-zero w-term in order to get a dirty image by using the following steps:

- Project the visibilities onto the w=0 plane
- Grid the visibilities using a gridding function and then perform an inverse FFT to obtain the so-called "dirty image"

The sampled visibility function $V_\nu^S\left(b\right)$ can be defined as a product of $V_\nu\left(b\right)$ and $S\left(b\right)$ as,

$$V_\nu^S\left(b\right) = V_\nu\left(b\right)\ \ S\left(b\right) \tag{2.20}$$

therefore,

$$I_{dirty}\left(s,\nu\right) = \mathfrak{F}\left[S\left(b\right)V_\nu\left(b\right)\right], \tag{2.21}$$

where $\mathfrak{F}$ is the Fourier operator and I_{dirty} is the dirty image, which is not the true image of the sky. The convolution of the sampling function and the spatial coherence function is the dirty image. The convolution theorem can then be used ($\mathfrak{F}\left[A,B\right] = \mathfrak{F}\left[A\right] \circledast \mathfrak{F}\left[B\right]$ where $\circledast$ is the convolution) to calculate its impact on the dirty image and then try to remove it,

$$I_{dirty}\left(s,\nu\right) = I_{true(s,\nu)} \circledast \tilde{S}\left(s\right), \tag{2.22}$$

where $\tilde{S}\left(s\right)$ is the Fourier transform of the sampling function.

From Equation 2.22 we see that when we directly Fourier transform our measurements from the uv-plane to the image plane, the recovered sky brightness is the true sky brightness convolved with $\tilde{S}(s)$, which is the dirty image. $\tilde{S}(s)$ is the dirty beam, and is the PSF (Point Spread Function) of the interferometer. To recover the true sky brightness, we require deconvolution, described in Section 2.4.3 to remove the artifacts generated due to incomplete sampling of the uv-plane. The algorithm used to deconvolve the data is described in detail in Section 2.4.3.1.

2.3.4 W-Stacking

Another important technique to handle the W-term (Offringa et al., 2015) is W-Stacking (Humphreys & Cornwell, 2011). It is an order of magnitude faster than W-Projection. For W-Stacking, the visibilities are gridded on different w-layers and w-corrections are applied after performing the inverse Fourier transform on the gridded visibilities (Offringa et al., 2015).

Taking Equation 2.7 and rewriting the right-hand side in terms of w-term independent and dependent components we get,

$$V_\nu(u,v,w_i) = \int\int A_\nu(l,m)\, I_\nu(l,m)\, e^{-i2\pi(ul+vm)} e^{-i2\pi\left[w_i\left(\sqrt{1-l^2-m^2}-1\right)\right]} \frac{dl\ dm}{\sqrt{1-l^2-m^2}} \tag{2.23}$$

For every given w-term (where $w_i \neq 0$), Equation 2.23 is a 2-D Fourier transform. Taking the inverse of the transform we get,

$$\frac{A_\nu(l,m)\, I_\nu(l,m)}{\sqrt{1-l^2-m^2}} = e^{i2\pi\left[w_i\left(\sqrt{1-l^2-m^2}-1\right)\right]} \int\int V_\nu(u,v,w_i)\, e^{i2\pi(ul+vm)} du d\nu \tag{2.24}$$

By integrating both sides of Equation 2.24 along the w axis between the minimum (w_{min}) and maximum (w_{max}) w value, it can be written as,

$$\frac{A_\nu\left(l,m\right)I_\nu\left(l,m\right)\left(w_{max}-w_{min}\right)}{\sqrt{1-l^2-m^2}}= \int_{w_{min}}^{w_{max}} e^{i2\pi\left[w\left(\sqrt{1-l^2-m^2}-1\right)\right]}\int\int V_\nu\left(u,v,w_i\right)e^{i2\pi(ul+vm)}dud\nu \quad (2.25)$$

Now the w values are discretized into N_w terms along the w axis and hence the integral changes into a summation. Equation 2.25 can be written as

$$\frac{A_\nu\left(l,m\right)I_\nu\left(l,m\right)\left(w_{max}-w_{min}\right)}{\sqrt{1-l^2-m^2}}= \sum_{n=0}^{N_w-1} e^{i2\pi\left[w\left(\sqrt{1-l^2-m^2}-1\right)\right]}\int\int V_\nu\left(u,v,w_i\right)e^{i2\pi(ul+vm)}dud\nu \quad (2.26)$$

It has been suggested by Offringa et al. (2014a) that the difference between two subsequent w values should be less than one radian,

$$\left|\delta w 2\pi\left(\sqrt{1-l^2-m^2}-1\right)\right| \ll 1 \quad (2.27)$$

The total number of w-layers required is,

$$N_w \gg 2\pi\left(w_{max}-w_{min}\right)max_{l,m}(1-\sqrt{1-l^2-m^2}) \quad (2.28)$$

The values of the right-hand side of the Equation 2.28 depend on the observation. The value of $w_{max}-w_{min}$ is determined by the wavelength, the coplanarity of the array and the zenith angle (Offringa et al., 2014a) and the value of the $max_{l,m}$ term depends on the angular size of the image (Offringa et al., 2014a).

In order to grid the visibilities, the w-values are changed by a small amount to match the w-value of the closest w-layer. The rounding off the w-values can create aliasing (leading to "ghost" sources) if the number of w-layers is significantly less than the required w-layers defined by Equation 2.28 (Offringa et al., 2014a). The number of w-layers should be set appropriately (see Equation 2.28) to limit the

effect of aliasing. After the visibilities are gridded, we perform an inverse FFT and apply a phase shift to the data to generate an image corresponding to a particular w-layer. The process is repeated N_w times to generate an image for every w-layer. Using Equation 2.26 the true sky image can be recreated as follows for every frequency channel,

$$A_\nu\left(l,m\right) I_\nu\left(l,m\right) = \frac{\sqrt{1-l^2-m^2}}{\left(w_{max}-w_{min}\right)} \sum_{n=0}^{N_w-1} e^{i2\pi\left[w_n\left(\sqrt{1-l^2-m^2}-1\right)\right]} \mathfrak{F}_{2D}^{-1}\left[V_\nu\left(u,\nu,w_n\right)\right] \tag{2.29}$$

where $\mathfrak{F}_{2D}^{-1}$ represents the two-dimensional inverse Fourier transform process.

2.3.5 Flagging

The visibilities corrupted by radio frequency interference (RFI) should be eliminated by flagging the affected data to get the true brightness of the source. Once the RFI is flagged, the data should be calibrated to correct for the effects by the instrument and the atmosphere. The following sections describe flagging and calibration in detail following the approach of Thompson (2017).

Flagging is the process by which one can go through the data, either manually or using automated algorithms to identify and then remove the corrupted data. The corruption of the data can be due to RFI, bad weather, damaged hardware such as broken antennas or dipoles, malfunction of hardware or software, memory failure and in a few cases can also be due to scheduling errors. If such bad data are not removed before further processing of data, it will limit us from accurately determining the actual response of the antenna and eventually result in incorrect calibration.

2.3.5.1 Flagging methods

RFI mitigation and flagging can be done at various stages, either in pre-correlation (hardware) or post-correlation (software) using various methods. When done in

pre-correlation, dedicated hardware such as extra antennas to remove sources of interference (Kocz et al., 2010) are used. Alternatively, a signal is used to estimate the interference and remove it from the data (Hellbourg et al., 2014). The other method is to search the data for anomalous bright bursts (RFI) in antenna, time and frequency space and discarded post-correlation (Offringa et al., 2012a) for further processing. The advantage of using software-based tools is that they can be applied to both archives as well as new data. The automatic flagging of visibility data using software-based tools is highly effective for continuum observations.

For this research, we use the **AOFLAGGER** software (Offringa et al., 2012b) for flagging RFI in the MWA data, PRESTO's RFI zapping routine for RFI removal in data from Parkes Radio Telescope and beamformed data from GMRT and CASA's FLAGDATA routine and manual flagging for GMRT phased array observations. After satisfactorily flagging the data and making it free from any spurious signals, the next step is calibration.

2.3.6 Calibration

The radio signal from the target source that we are interested in gets contaminated by the atmosphere as well as the instrument, resulting in the corruption of the signal. The recovery of the actual signal by removal of the instrumental errors as well as the atmospheric interference is called calibration. The calibration formalism can be mathematically realised as follows.

If we observed a source at a time t, the measured visibilities, $\tilde{V}_{ij}(t)$ for a pair of antennas with baseline ij, which is different from the true visibilities, $V_{ij}(t)$. In the case of an ideal interferometer, the measured and true visibilities are linear. However, in reality, the signal from the target source is affected by many things, such as beam response changing with elevation, time-varying atmospheric effects and even stochastic noise. The individual antennas have enough separation that there is no mutual coupling, so the response of one antenna does not impact the

other. The relation between the observed and the true visibilities can be defined as

$$\tilde{V}_{ij}(t) = G_{ij}(t) V_{ij}(t) + \epsilon_{ij}(t) + \eta_{ij}(t) \tag{2.30}$$

where $G_{ij}(t)$ is the baseline-dependant complex gain, $\epsilon_{ij}(t)$ is the baseline-dependant complex offset factor and $\eta_{ij}(t)$ is the contribution due to stochastic noise. $G_{ij}(t)$ can be further defined as the product of the two antenna-dependant complex gains $g_i(t)$ and $g_j(t)$

$$G_{ij}(t) = g_i(t) g_j^*(t) g_{ij}(t) \tag{2.31}$$

or

$$G_{ij}(t) = a_i(t) a_j(t) a_{ij}(t) e^{i(\phi_i(t) - \phi_j(t) + \phi_{ij}(t))} \tag{2.32}$$

where $a(t)$ is the antenna-dependant amplitude , $\phi(t)$ is the antenna-dependant phase factor and $g_{ij}(t)$, $a_{ij}(t)$ and $\phi_{ij}(t)$ are baseline dependent residual gains.

The antenna-dependant gains can be determined by using the observations of a standard calibrator source. In practice, two calibrator sources are observed, namely, flux (primary) and phase (secondary) calibrator. The flux density of the flux calibrator sources is well-established and constant in time. The same source can be used for delay and bandpass calibration. This is because it is typically bright so a channel-based response has sufficient signal to noise. The secondary calibrator source is used to determine the time-dependent amplitude and phase corrections. The secondary calibrator should be unresolved, bright and should have a highly constrained position and be close to the target source. The complex gains are calculated as a function of time and interpolated and/or extrapolated to the target source over the full observation. However, there may still be residual errors due to the spatial and timing differences between the source and calibrator observations which can be corrected by self-calibration described in Section 2.4.4.

2.3.6.1 Calibration techniques

The different techniques used in calibration are delay and bandpass calibration, flux calibration and time-dependent calibration. These are described below.

Delay and bandpass calibration: In an ideal observation, the antenna gains do not change over the bandwidth that is processed. However, inaccurate antenna timing and positioning can introduce inefficiencies in the correlator model. This can result in a linear phase gradient in the frequency domain, remaining constant over time, and referred to as a delay. This delay is observable in both the individual baseline measurements and the correlated visibilities. When performing continuum imaging and averaging frequencies, an uncorrected delay can lead to a loss of coherence in the continuous signal.

There are irregularities in the phase response and amplitude response as a function of frequency. The spurious frequency dependence on the measured visibility introduced by the instrument and the atmosphere needs to be determined and corrected. For continuum data, if these errors are not corrected, it results in a limited dynamic range and low signal-to-noise when frequencies are averaged. In order to correct these errors, we need to perform delay and bandpass calibration, where the calibration solutions are determined using a bright source observed for a short interval of time.

Flux calibration: The correlator merges signals from various antennas at specific frequencies to create visibilities. It deals exclusively with electronic voltages, considering their relative phase and signal strength. Consequently, it's crucial to correct the correlator results to derive the true flux density from the observed sky visibilities, accomplished through flux calibration.

In flux calibration, we map the instrumental response to the incoming radio emission to an established flux density scale. Flux calibration can be done most effectively by observing a standard flux calibrator to determine the antenna gain and then applying to our target source.

Time dependant calibration: Other factors that one takes into account are

the time-varying properties that arise due to dynamic conditions of the telescope such as receiver power level settings, receivers removal and corrupted baseband samplers. These effects can be corrected by applying a complex gain calibration. It also traces changes due to ionospheric conditions which are a particular hindrance at low radio frequencies, atmospheric phase and opacity, the troposphere and solar flares if applicable. For complex gain calibration, the calibrator sources should be unresolved, and have a constant flux density over the observation time as it allows the variation in gain to be directly calculated.

2.4 Interferometric techniques

2.4.1 Weighting

Weighting in the process of imaging is used to improve the dynamic range and the fidelity of the final synthesized image. Multiple factors are accounted for in weighting, namely, noise in the visibility represented by the data weights, UV locus of that weighting, e.g., a taper to change resolution, the convolution kernel that distributes the visibility to the UV plane during gridding and Fourier transforming to make the image of the sky.

Each sampled visibility data point is multiplied by a weight w_m before gridding and is defined as,

$$W(u,v) = \sum_{m=0}^{M} w_m \delta(u - u_m)\,\delta(\nu - \nu_m) \tag{2.33}$$

where $W(u,v)$ is the weighting function, which is introduced to improve the fidelity and dynamic range of the restored sky image. There are various weighting schemas for particular science cases which are described in the subsections below.

2.4.1.1 Natural weighting

The natural weighting scheme assigns a constant weight to each visibility, and is equivalent to the inverse noise variance on the particular visibility data point,

$$w_m = \frac{1}{\sigma_m^2} \tag{2.34}$$

where σ_m is the rms noise for the visibility point m.

This weighting maximizes the point source sensitivity in the sky image and in some way provides the natural resolution of the telescope. Natural weighting is most suited for extended source sensitivity as it up-weights the shorter baselines more than the longer ones.

2.4.1.2 Uniform weighting

For uniform weighting, the weights are equal to the inverse of the sampling density function and is defined as,

$$w_m = \frac{1}{\sigma_m^2 \rho_m \left(u_m, \nu_m\right)} \tag{2.35}$$

where ρ_m is the local density of the (u, ν) points.

This generally results in higher resolution while minimizing the sidelobe level. For MWA Phase I data, uniform weighting can reduce the sensitivity by almost a factor of two.

2.4.1.3 Robust weighting

A robust weighting scheme provides a good balance between natural and uniform weighting. While natural weighting reduces the noise level, uniform weighting suppresses the sidelobe. Robust weighting provides a trade-off between the two and changes smoothly from uniform to natural weighting as a function of robustness (R), which is a real value parameter (Briggs, 1995).

In use, the robustness parameter (R) varies from -2 to +2 and R=0 provides a good compromise between sensitivity and resolution.

2.4.2 Imaging and gridding

The visibilities can be considered to lie on a plane in the case of small field-of-view coplanar telescopes where $w \equiv 0$ and hence the term w can be ignored. In such a scenario, we can perform a two-dimensional inverse Fourier transform of the calibrated visibility to obtain a dirty image. A deconvolution algorithm is then applied to recover the true sky image.

However, the previous assumption does not hold true for radio interferometers with a wide FoV as we cannot approximate w=0. In order to handle the w-terms, we can use various approaches such as three-dimensional Fourier transform, warped snapshot, W-projection, W-stacking and W-snapshot. The methods broadly used as part of my PhD work are described in Section 2.3.1.

2.4.3 Deconvolution

Deconvolution is the process of reconstructing the accurate sky image (I_{true}) from the dirty image (I_{dirty}). For an observation with limited uv-coverage, a non-linear deconvolution technique is required to recover the actual sky brightness (Thompson, 2017). There are many algorithms one can use to perform deconvolution. The CLEAN algorithm, used as part of this work is described in the section below. A primary beam correction is also required to normalize the attenuated source fluxes in the recovered sky image.

2.4.3.1 The CLEAN algorithm

The CLEAN algorithm is one of the most commonly used processes for deconvolution (Högbom, 1974). It makes an assumption that there are only point sources in the image field and applies an iterative procedure to obtain a list of intensities

and positions of the point sources which are called 'CLEAN' components. These 'CLEAN' components form the model image.

For Hogbom CLEAN (Högbom, 1974), at every iterative stage a scaled point dirty beam, i.e. a scaled point spread function is subtracted from the dirty image at the highest peak position. The magnitude and position of the subtracted point sources gets added to the list of CLEAN components and form the model image. The iterative process is repeated until the number of iterations exceeds the defined maximum number or the brightest point source in the residual image is below the specified threshold. The final dirty image, also called the residual image should not contain any sources but should be noise-like. The 'CLEANed' image, or the recovered image can be produced by convolving the most recent stacked 'CLEAN' components with an idealised 'CLEAN restoring beam' and then adding with the residual image.

For computational efficiency, Clark (1999) proposed a more efficient CLEAN algorithm based on Fast Fourier Transform (FFT), operating in uv-space and including both major and minor cycles. In this process, the full dirty beam is not used, but rather a small section of the dirty beam including the highest exterior sidelobe is selected during a minor cycle. The point sources are then determined if the magnitude of the sources is higher than the maximum exterior sidelobe. A standard CLEAN is then executed using the dirty beam fraction and the selected point sources in the dirty image. The process of CLEAN-ing continues until there are no other elements to be selected in the dirty image. The model image (CLEAN components) is Fourier transformed to the uv-space and then subtracted from the visibilities.

Yet another modified version of the Clark CLEAN algorithm is introduced by Schwab & Cotton (1983), where CLEAN components are subtracted from the degridded visibility data (degridding reconstructs the visibility data from a given image model). This reduces gridding errors and eliminates aliasing noise. Cornwell et al. (2008) introduced a new version of CLEAN called multi-scale

CLEAN, where the large-scale structure emission is deconvolved first and the finer details are deconvolved in the later iteration process.

2.4.4 Self Calibration

As discussed in Section 2.3.6, we do not know the true structure or the surface brightness of the target field. So, for initial calibration of the visibilities, a standard calibrator must be observed to calculate and transfer the gains to the target field. Ideally, one would have calibrator observations nearly at the same time and close to the target of interest such that we are measuring the same section of the ionosphere. However, in some cases, the calibrator observations are different from the target source in pointing and time, and hence we are looking at a different section of the ionosphere, which reduces the effectiveness of the calibration. In order to handle these calibration errors, it is also important to have a good model of the field.

The main focus of self-calibration is to determine the actual complex antenna gains in the direction of the primary sources at the time of observations. It is an iterative process where the initial starting point is the model of the source itself, which can be iterated over to improve the complex antenna gain solutions with each iteration. In self-calibration, the difference 'S', between the measured visibilities ($\tilde{V_{i,j}}$) and the model visibilities ($\hat{V_{i,j}}$) is minimised by the least-squares approach (Cornwell et al., 2008) as follows,

$$S = \sum_{k} \sum_{i,j,i\neq j} w_{ij}(t_k) \left| \tilde{V}_{ij}(t_k) - g_i(t_k) g_j^*(t_k) \hat{V}_{ij}(t_k) \right|^2 \tag{2.36}$$

where $w_{ij}(t_k)$ are the weights corresponding to the baseline $i-j$ at a particular time t_k and g_i and g_j are the antenna dependant complex gains. The antenna gains $g(t)$ are determined by dividing measured visibilities with the initial model, which are then used to further calibrate the visibilities according to

$$S = \sum_{k} \sum_{i,j,i \neq j} w_{ij}(t_k) \left| \hat{V}_{ij}(t_k) \right|^2 \left| X_{ij}(t_k) - g_i(t_k) g_j^*(t_k) \right|^2, \tag{2.37}$$

where X_{ij} is the ratio of observed to model visibilities and is described as,

$$X_{ij}(t) = \frac{\tilde{V}_{ij}(t)}{\hat{V}_{ij}(t_k)} \tag{2.38}$$

If the model is accurate then X_{ij} is not dependent on u and v but proportional to the antenna gains. The gain for each integration period can be determined. The process is repeated till it converges and has no improvement, and an intensity map is created. Self-calibration cannot be used if the source structure is complex to model and/or the source is not bright. It also shows limitations if the total number of variables is greater than the number of independent visibility measurements (Cornwell et al., 2008).

2.5 Tied-Array Beamforming

Tied-array beamforming is used in this work to process the data to form beams and search for pulsars using periodicity searches. A detailed description of tied-array beamforming for the MWA is given in (Ord et al., 2019). An overview of the algorithms is given in this section.

2.5.1 Delay and gain calibration

We can calculate the phase correction for a channel n, with centre frequency ν_n of antenna j as $\phi_{j,n} = 2\pi\Delta t_j \nu_n$. The interferometric fringe pattern on the sky changes as the earth rotates and changes the array's projected baseline. The delays can be recalculated frequently to increase sensitivity by measuring how the fringe changes with time (fringe rate). For a maximum MWA frequency of 300 MHz and maximum baseline of 5 km, the maximum fringe rate for MWA Phase II is ~ 1 rad s^{-1}, which is enough to de-cohere the beam and hence the

delays are recalculated every second.

Gain calibration is used to determine the instrumental response of the interferometer. The incoming electric field has a phase turn due to the complex gain of each antenna. This phase turn de-coheres the sum of the antenna signals. This needs to be compensated so that they are on the same relative or absolute, amplitude and phase scale. As the antennas do not have a calibrated noise diode, they cannot be calibrated individually and hence have to be treated as an interferometer when calibrating. One of the ways to calibrate is to observe a nearby calibrator field and correlate the voltages to form visibilities, from which the calibration solution can be obtained.

The antenna-based complex gains can be described using the Jones matrix formalism. For every field vector, e, the complex gain that affects it can be represented as the Jones matrix, J_j, where j is each antenna. The resulting antenna voltage, ν_j is as follows,

$$\nu_j = J_j e \tag{2.39}$$

The real-time system or RTS (Mitchell et al., 2008) software calibrator can be used offline to produce an estimation of the complex gains by iteratively removing residual visibilities and correcting for ionospheric effects starting with the brightest sources. RTS corrects for direction-dependent ionospheric effects but this is not effective when the calibrator source is at a different part of the sky or observed at a different time than the target source. Hence, calibration using dedicated calibration observation is standard practice to obtain good calibration solutions. Direction-dependant calibration at low radio frequencies such as that of the MWA takes into account the bulk of the ionospheric shift into the gain calibration but does not correct for residual ionospheric offsets.

2.5.2 Beam formation

The MWA telescope can point at different sources electronically without physically moving any telescope parts. The observed voltage beam can be calculated as (Ord et al., 2019),

$$e' = \sum_{j}^{N_A} \nu_j J_j^{-1} exp\left\{-i\phi_{j,n}\right\}, \tag{2.40}$$

where ν_j is the complex voltage from each tile, J_j^{-1} is the inverse of the complex gain of the direction-independent calibration estimated by the RTS, $exp\left\{-i\phi_{j,n}\right\}$ is the direction-dependant delay compensation and N_A is the number of tiles.

The beam is then calculated for both polarisations and then transformed to the four Stokes parameters as follows:

$$I = \left[e'_x {e^*}'_x - \frac{1}{N_A^2}\sum_{j}^{N_A} e'_{j,x} {e^*}'_{j,x}\right] + \left[e'_y {e^*}'_y - \frac{1}{N_A^2}\sum_{j}^{N_A} e'_{j,y} {e^*}'_{j,y}\right] \tag{2.41}$$

$$Q = \left[e'_x {e^*}'_x - \frac{1}{N_A^2}\sum_{j}^{N_A} e'_{j,x} {e^*}'_{j,x}\right] - \left[e'_y {e^*}_y - \frac{1}{N_A^2}\sum_{j}^{N_A} e'_{j,y} {e^*}'_{j,y}\right] \tag{2.42}$$

$$U = 2 \times Re\left[e'_x {e^*}_y - \frac{1}{N_A^2}\sum_{j}^{N_A} e'_{j,x} {e^*}_{j,y}\right] \tag{2.43}$$

$$V = -2 \times Im\left[e'_x {e^*}'_y - \frac{1}{N_A^2}\sum_{j}^{N_A} e'_{j,x} {e^*}'_{j,y}\right] \tag{2.44}$$

The four Stokes parameters can be used to perform an analysis of the pulsar's rotation measure and the linearly and circularly polarised components of its pulsed profile. If a large number of beams are generated for large pulsar surveys, only Stokes I (Equation 2.41) is calculated as it is sufficient to detect pulsars. After the formation of the beam for the source we are interested in, we can search

it using pulsar search techniques described in Section 2.6.

2.6 Pulsar searching

Once the beam is formed for the MWA and GMRT, as described in Section 2.5, we can use the pulsar search software, PRESTO (Ransom, 2001) to search for pulsars. This section describes the underlying algorithm of the search software and is also applicable to the search mode data collected from the Parkes Radio telescope. A typical pulsar search pipeline is shown in Figure 2.6 and a detailed description of the different steps involved in the process is given below.

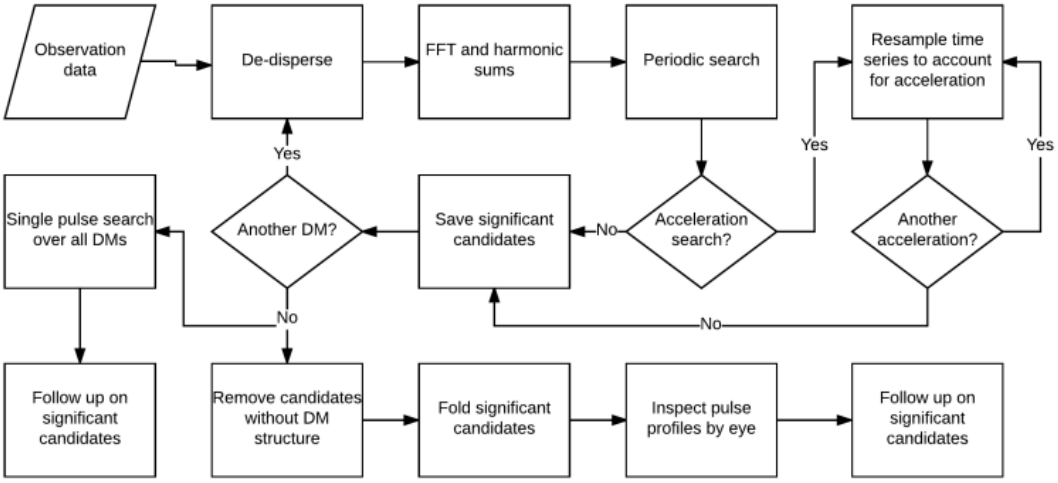

Figure 2.6: A common pulsar search pipeline. The steps are discussed in detail in the following sections. (Lorimer & Kramer, 2004).

To discover new pulsars, we need to search the sky for pulsations of an unknown period and DM. The two most common pulsar search strategies are (1) blind searches, where a large area of the sky is searched (Bhat et al., 2023a) which is similar to the approach taken with MWA blind searches and forms the basis of Chapter 3 and 4 and (2) targeted searches where we can target a list of sources that are suspected to be new pulsars and this approach is taken in the work described in Chapter 5. Blind pulsar surveys are the most common and used to find

new pulsar candidates whereas targeted searches are aimed at confirming pulsar candidates.

The three common types of search techniques to detect pulsars are periodic, acceleration and single pulse searches. For this thesis, we mainly focus on periodic and acceleration searches. The first step is to dedisperse the data to form a large number of time series for a specified DM range. This is mainly done to correct for propagation effects and is described in Section 1.3.1. These several time series are then searched for pulsations. The Fourier transform is the most common method of searching for regular pulses in time series data. The harmonics of the principal signal are summed to increase the signal-to-noise ratio (S/N) to increase the chances of detecting faint signals. The best candidates are then folded and inspected to confirm if they are due to real pulsars or not. The aforementioned process is described in detail below.

2.6.1 Dedispersion

Correcting for the effects of dispersion on the signal is important to increase the sensitivity of the observation and hence detect more pulsars. The most common method of dedispersion is incoherent dedispersion and is described in Section 2.6.1.1. Another important consideration for dedispersing is the choice of dispersion step which is explained in Section 2.6.1.2.

2.6.1.1 Incoherent dedispersion

Incoherent dedispersion consists of shifting each frequency channel in time such that the dedispersed signal aligns forming a vertical line in time across all frequency channels. However, we cannot completely get rid of dispersion within the frequency channel as shown in Figure 2.7, resulting in dispersion smearing which needs to be considered when deciding the DM step size. In cases where the frequency bandwidth is much smaller than the observing frequency ($\delta\nu \ll \nu$) Equation 1.27 can be written as,

$$t_{DM} \approx 8.3 \times 10^6 ms DM \frac{\Delta\nu}{\nu^3} \tag{2.45}$$

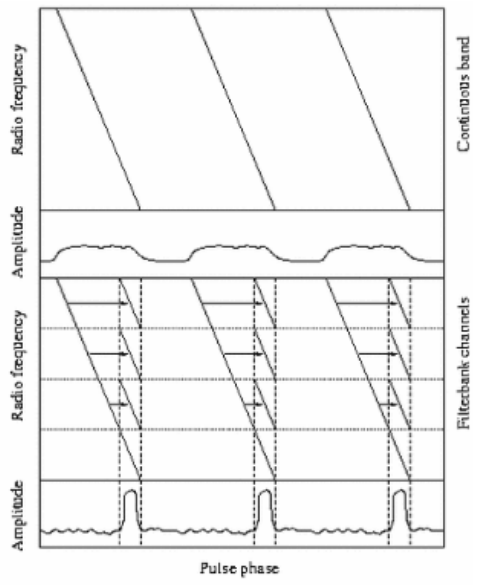

Figure 2.7: The theoretical diagonal DM of a pulsar. The top panel shows the raw pulsar signal in frequency and time. The second panel shows the resulting broadened pulse profile if the raw data is folded without correcting for dispersion. The third panel illustrates the process of incoherent dedispersion. There is still existing dispersion within the frequency channel due to finite frequency resolution. The pulse profile appears broadened when the dispersion exceeds the time resolution. (Lorimer & Kramer, 2004)

2.6.1.2 DM step size

The DM of the new pulsars is unknown hence a range of DM values needs to be searched. The sensitivity of the pulse profile decreases as the dispersion smearing gets larger than the time resolution. Thus, this has to be considered when deciding on the DM step size for the search. Another factor that needs to be considered when deciding the DM trials is the compromise between computational efficiency and search sensitivity. If we choose a large number of DM trials, it is computationally expensive to perform an FFT and search for pulsation for the large number of DMs in the chosen range. On the other hand, the DM steps should

not be too big such that the pulsar signal gets broadened and hence undetectable.

We have to decide the acceptable DM smearing for an incorrect DM to decide on a DM step (DM_{step}). A smearing factor, i_{smear} is defined, which is the limit for the time bin across which smearing is allowed. It can be expressed as,

$$i_{smear} t_{samp} = t_{DM} \tag{2.46}$$

where t_{samp} is the time resolution, t_{DM} is the dispersion smearing. The default value of i_{smear} is 3, but is dependant on the expected pulse width of the pulsars and the time resolution of the telescope.

The maximum smearing caused by an incorrect DM selection should be less than $i_{smear} t_{samp}$ and a corresponding DM_{step} to do so can be calculated as

$$DM_{step} = 4.15 \times 10^{-6} t_{DM} \frac{\nu^3}{\Delta\nu_{band}} \tag{2.47}$$

where t_{DM} is the dispersion smearing, ν is the central frequency and $\Delta\nu_{band}$ is the total frequency bandwidth in MHz. An ideal DM plan takes everything into account such that a high-significance signal is detected at a correct DM within the limitations of computational support available.

The DM step size and number of DM trails are decided by using the pulsar processing software. Typically for MWA frequency, the following plan is followed:

2.6.2 Fourier transform

The periodicity of the time series can be analysed by taking the Fourier transform of the time series and investigating in the Fourier frequency domain. For a set of N data points and dedispersed time series T_j the discrete Fourier transform (DFT) can be calculated as,

$$F_k = \sum_{j=0}^{N-1} T_j exp(-2\pi ijk/N) \tag{2.48}$$

DM_{min} (pc cm^{-3})	DM_{max} (pc cm^{-3})	DM_{step} (pc cm^{-3})	N_{DM}	d_s	Δt_{eff}	N_{sub} (ms)
1.0	12.2	0.02	560	1	0.1	4
12.2	24.4	0.03	406	2	0.2	6
24.4	48.8	0.06	406	4	0.4	16
48.8	97.6	0.11	443	8	0.8	32
97.6	195.2	0.23	424	16	1.6	64
195.2	250.0	0.46	119	16	3.2	64

Table 2.1: Typical dedispersion plan for MWA where columns 1 and 2 denote the ranges in dispersion measure, between DM_{min} and DM_{max}, with a DM step-size of DM_{step}, resulting in N_{DM} trial DM values. The downsampling factor is denoted by d_s, i.e. the factor by which the temporal resolution is averaged to yield a net resolution Δt_{eff}. N_{sub} is the number of frequency channels to partially shift to a nominal DM before being dedispersed, which results in fewer calculations.

where $i = \sqrt{-1}$. The bin width for the resulting Fourier frequency series is 1/T where T is the length of the observation. The DFT is not generally used but a more computationally efficient Fast Fourier Transform (FFT) is used which uses $N\ logN$ operations as compared to the DFT that uses N^2. Pulsar surveys use FFT for the entire time series to maximise the sensitivity of the search.

2.6.3 Search techniques

This section describes the two search techniques that are used in this work to detect pulsars in traditional pulsar search techniques.

2.6.3.1 Periodic search techniques

Periodic searches are effective in detecting pulsars that are isolated, i.e. not in a binary system. It searches for peaks in power in the Fourier space and is not computationally expensive.

2.6.3.2 Acceleration search techniques

Acceleration search techniques are most effective in detecting pulsars in binary systems. However, such systems are difficult to detect as the power smears into

nearby frequency bins due to the Doppler effect. In order to take this into account one needs to resample the time series as,

$$\tau(t) = \tau_{\circ}(1 + V_r(t)/c) \tag{2.49}$$

where $V_r(t)$ is the radial velocity, c is the speed of light, $\tau(t)$ is the time interval in the pulsar frame and $\tau_{\circ}$ is used for normalisation. Keplerian parameters need to be taken into account to accurately recover full sensitivity. This is a coherent search and is not practised due to the required high computational power.

When the observation time is much smaller than the binary orbital period, a constant acceleration can be assumed such that $V_r(t) = a_r t$, which reduces the computational requirements by reducing the parameter space to be searched. A potential improvement of such a search is given in Figure 2.8.

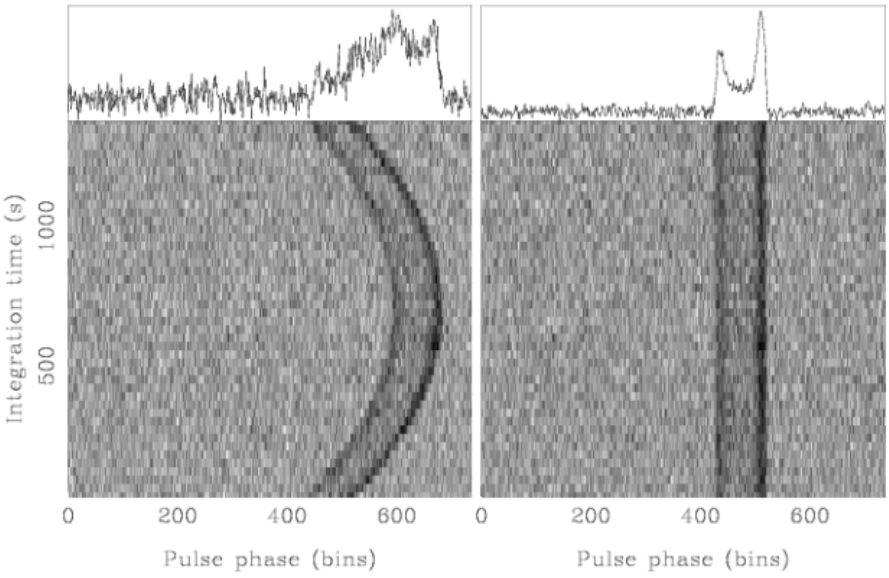

Figure 2.8: Left: A folded pulse profile of binary pulsar PSR B1913+16 from 22min observation with Arecibo without any correction for acceleration. Right: The same time series when corrected for an orbital acceleration of -16 ms^{-2} (Lorimer & Kramer, 2004).

2.6.4 Candidate selection and folding

On completion of the periodic and acceleration searches, a candidate list consisting of numerous pulsar candidates is generated. The candidates are compared to pure Gaussian noise to determine the "goodness" of the candidate. The DM and the shape of the S/N ratio over adjacent DM bins for a candidate can help determine if the candidate is a true pulsar, noise or RFI. DM=0 for a candidate signifies that the signal has not travelled through any ISM and is likely caused by terrestrial RFI. True pulsars generally have a characteristic curved shape when the S/N ratio and DM are compared. A random noise signal is not expected to have this shape and hence is used to filter out any noise and RFI.

Periodic candidates that are above an S/N threshold and have the expected curve characteristic are "folded". Folding of the candidates means averaging the observation over the pulsar's period to add pulses coherently to create a bright pulse profile that is characteristic of pulsar detection and to increase the S/N for an assumed pulsar period. This leads to a large number of folded profiles having to be classified (or assessed) by humans or using machine learning. A folded PRESTO plot of PSR J0908-1739 detected in MWA data is shown in Figure 2.9.

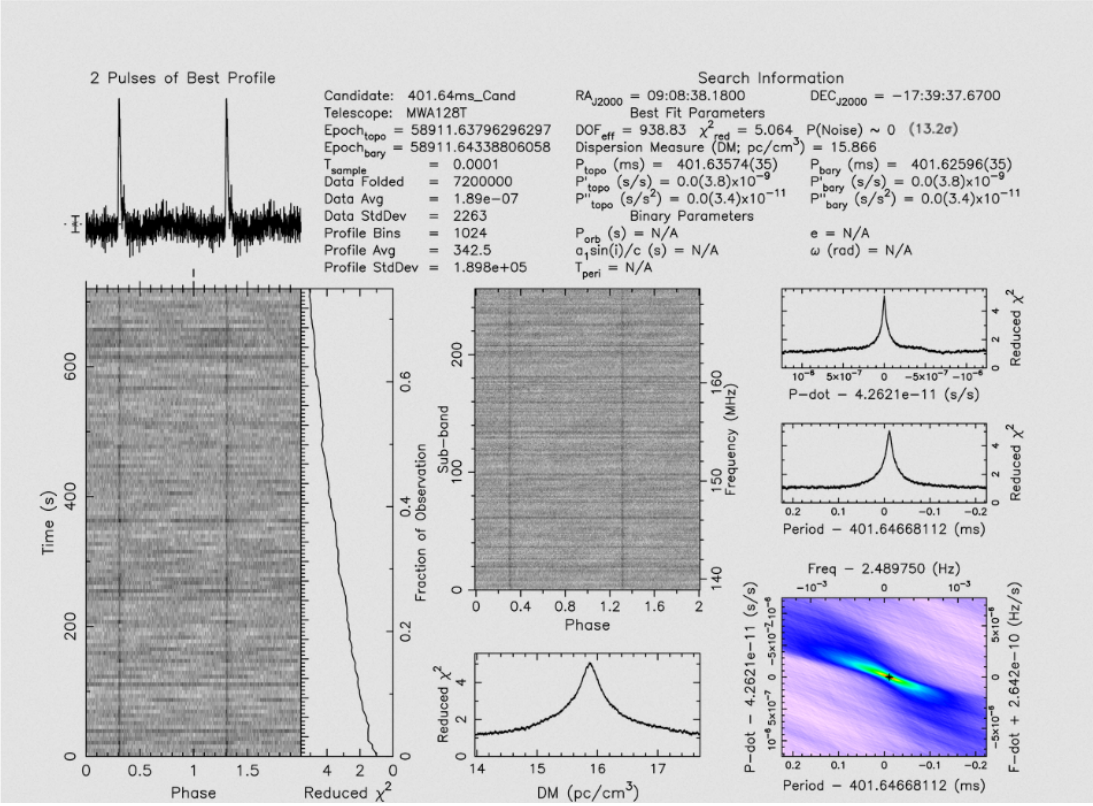

Figure 2.9: PRESTO result of searching and folding for PSR J0908-1739.

2.6.5 Candidate follow up

Once a pulsar candidate is detected with high confidence it cannot be immediately confirmed as a new pulsar. The pulsar candidate is then followed up using additional observations from the same telescope, in our case more MWA follow-up of the candidates or other telescopes such as the Parkes Radio Telescope and the Giant Metre-wave Radio telescope. The detailed process of follow-up of and further analysis of the pulsar candidates is described in Chapter 5.

2.7 Imaging of the MWA and GMRT data

This section describes the procedure of imaging the data collected using MWA VCS and GMRT.

2.7.1 Imaging MWA data

The MWA VCS data can be processed in multiple ways providing maximum data flexibility: creating a sensitive tied array beam for a particular source position, creating an incoherent beam with reduced sensitivity but observing the entire FoV and correlating offline which reduces the time resolution but improving sensitivity to form wide-field images. For this thesis, imaging and tied-array beamforming are used. Tied-array beamforming has been described in 2.5. This section focuses on the imaging aspect of the data.

Before one can process an observation, it needs to be downloaded from the MWA All-Sky Virtual Observatory (MWA ASVO; Sokolowski et al., 2020) server using a specified observation ID (OBSID). The observation has raw voltages, which then need to be correlated offline to form visibilities (Ord et al., 2015). Once the data are correlated, it can be used to generate full Stokes images.

MWA does not have any fixed number of pointings and does not track objects. Hence, the telescope needs to be re-pointed every few minutes depending on the observation, to take into account the Earth's rotation. This means that the MWA primary beam also changes in accordance with the change in the pointing. The x-GPU correlator (Ord et al., 2015) is used to produce visibilities at 1-s time resolution for imaging.

The steps to create the MWA images from correlated visibilities are as follows:

• The observation is calibrated using a bright, non-variable calibrator source such as Hydra A, Pictor A or Centaurus A. The calibration solutions for the MWA are obtained from the Murchison Widefield Array All-Sky Virtual Observatory (MWA ASVO) database of calibration solutions (Sokolowski et al., 2020). In-field calibration is not effective as the MWA sky model for the Galactic Plane is not present. A good calibration solution is obtained by flagging the bad phase and amplitude data that may corrupt the ultimate images. Multiple rounds of flagging are performed to get the best calibration solution. The final calibration solution is then used for the processing of the data.

• COTTER (Offringa et al., 2015) (described in Appendix A.1) is then used to convert the visibilities into a CASA measurement set. It also flags the channels affected by radio frequency interference (RFI) by using the in-built software AOFlagger (Offringa et al., 2012a). Briggs (1995) robustness parameter R=-1 is used to weight the visibilities. Imaging is performed using WSCLEAN (Offringa et al., 2014a) which applies w-corrections using the W-stacking method as described in Section 2.3.4. We created 8192 × 8192 pixel images at 1s time resolution with a pixel size of 0.2 arcmin.

• The 1s images have an rms noise level of 30 to 40 mJy/beam at 154 MHz in the extended configuration close to the Galactic Plane. Given the high rms noise, it is extremely difficult to detect a relatively faint ($\sim$ 30 mJy/beam) point source with high confidence ($> 5\sigma$). In order to detect fainter sources and increase the signal-to-noise ratio we stack the 1s snapshot images to produce a mean image for the whole observation. The stacking of the images reduces the rms noise to almost 5 mJy/beam (away from the Galactic Plane), making it easy to detect sources that are as faint as 25 mJy/beam at 5σ confidence. Alternatively, the 1s snapshot images are also averaged together at different timescales to search for variable sources. Further processing of such sources is described in Chapter 3.

2.7.2 Imaging GMRT data

For imaging of GMRT data, the software that is used in this thesis is Common Astronomy Software Application (CASA; McMullin et al., 2007), which takes the raw visibilities in the measurement set format as input. The final data products that are used in this work are the sky images produced for the candidates. The details of the candidates and the subsequent analysis are described in Chapter 5.

The first step is the use the *ugmrt* package in CASA to convert the visibilities to a CASA measurement set that can be used for the processing. Once that is done, the next step is to flag problematic antennas and the edges of the band where the gains are very low. The short baselines are also flagged as we are

not interested in extended emission of the sources and are mainly focused on compact objects. The task used for this purpose is $flagdata$ in CASA. Once, the first round of flagging is done, we can perform an initial calibration. The detailed process of calibration is described in Section 2.7.2.1.

2.7.2.1 Initial calibration of GMRT data

This initial calibration calculates the frequency and time-dependent antenna gains. Two calibrators, namely, flux calibrator and phase calibrator are used. The flux calibrator is usually a point source with a known spectrum so that one can use it to set the absolute flux density scale and calibrate the frequency-dependent antenna gains. The phase calibrator is also a point source that is close to the target source and is used as the complex antenna gains change with pointing direction. The phase calibrator's flux density is obtained using the flux calibrator and then the former is used to find the relative antenna gains as a function of time. As the frequency-dependent antenna gains are stable over several hours, observing the flux calibrator a few times during the whole observation is sufficient. However, the phase calibrator needs to be observed multiple times as the antennas go out of phase every 45-50 minutes.

The first step is to insert the known model for the flux calibrator which is done by using the task $setjy$ in CASA. A delay calibration is then performed with respect to a reference antenna using the *gaincal* routine of CASA. A small part of the band is selected and *gaincal* is used to find the time-dependent antenna gains (g_t) for this band. The values obtained from *gaincal* are then applied on the full band and then the frequency-dependent part of the gain (g_ν) is calculated using *bandpass*. Once we correct for the bandpass, the full band is used to recalculate the antenna gains for both flux and phase calibrators. The actual flux density of the phase calibrator is obtained using CASA's $fluxscale$ that compares the gain for both calibrators.

The gains calculated are applied to the calibrators using CASA's task *applycal*.

The corrected visibilities after the application of the gains are examined and more flagging of RFI is done if necessary. The above calibration and flagging is repeated till the calibrated visibilities of the calibrator sources show no or minimal sign of RFI. The final gains are then applied to the target sources and the process of initial calibration ends.

2.7.2.2 Imaging and self-calibration

Before we image the target sources, another round of examination and flagging of RFI is done for the calibrated target source visibilities. It is common practice to average the data over a few channels to reduce the data volume and processing overload. The final frequency resolution should be such that no bandwidth smearing occurs even at the edges of the final sky map. After averaging over the channels, a final round of flagging of the RFI is done if necessary. This is to remove any bad data that may have been missed previously. The final flagged and calibrated target visibilities are now used to make the final sky maps for the target sources. CASA task *tclean* is used to deconvolve the data till satisfactory sensitivity and image quality is achieved. The details of the analysis performed using these images are given in Chapter 5.

Chapter 3

Methodologies to detect pulsars in high time resolution images using the Murchison Widefield Array

3.1 Introduction

For decades, searching for pulsars have been performed using time-domain search techniques which are highly sensitive for detecting periodic pulses. This approach has been extremely successful and led to majority of pulsar discoveries (Manchester et al., 2005). However, the sensitivity of these techniques is negatively affected by factors such as binary eclipses, orbital motion and scattering. Especially at low radio frequencies, dispersion measure (DM), smearing and multipath scattering become dominant factors resulting in lesser number of detections. At these frequencies, traditional pulsar searches are also more time consuming and computationally expensive due to the large number of DM trials required at low frequencies. The necessity for performing acceleration searches to detect pulsars in tight binaries also increase the processing time. An alternative strategy to

search for bright pulsars is to exploit the high time resolution data of interferometers such as the Murchison Widefield Array (MWA; Tingay et al., 2013a; Wayth et al., 2018) to produce continuum images, find pulsar candidates in the image domain and verify them using high-time resolution time-series formed from the very same data. This kind of image-based pulsar candidate searches can potentially reduce the computational resources and processing time when compared to traditional Fourier-domain periodicity searches.

Many attempts have been made to search for pulsars in radio continuum surveys. Although many of them were unsuccessful, the first ever millisecond pulsar discovered, J1939+2134, was initially identified in radio continuum images as an unusual compact source with a steep spectrum (Backer et al., 1982). Furthermore, image-based methods have been gaining momentum in the recent years. For example, the discovery of a highly polarised, steep-spectrum millisecond pulsar in a deep image with the Australian Square Kilometre Array Pathfinder telescope (ASKAP; Kaplan et al., 2019) have demonstrated the rising potential of imaging surveys to detect new pulsar candidates[1]. Another recent discovery of a circularly polarised variable radio source in the Large Magellanic Cloud (LMC) shows the potential to detect new pulsars (Wang et al., 2022).

The primary difficulty in the searching for pulsars in image domain is that the observational data are averaged in time and hinder the ability to extract a pulsar profile from time series. The primary challenge, then, is to distinguish interesting pulsar candidates from other unresolved point radio sources. Such differentiation between pulsars and unresolved radio sources can be done using properties that are characteristic to pulsars.

One such metric is the steepness of the average spectrum. It has been successfully employed to discover new pulsars that were otherwise missed via traditional pulsar searching techniques (Frail et al., 1994). This technique has proved to be highly beneficial in targeted observations (Hyman et al., 2019) as well as large

[1]Continuum sources are considered candidates until confirmed by standard pulsar searches.

sky surveys (Frail et al., 2018). In addition to spectral index methods, Dai et al. (2016) demonstrates the identification of probable pulsar candidates whose scintillation time-scales and bandwidths are comparable to the time and frequency resolution of the instrument. Another approach is to search for sources that have a high degree of circular polarisation. Previously, a handful of pulsars have been discovered using a combination of spectral properties and linear polarisation (Navarro et al., 1995), but there has not been large-scale surveys including circular polarisation until Lenc et al. (2018). While some steady circularly polarised emission has been seen from sources like flare stars (Lynch et al., 2017b), chromospherically active binaries like cataclysmic variables (Mutel & Morris, 1988), the majority of polarised sources seen in large scale surveys are pulsars (Lenc et al., 2018). MWA surveys of linearly polarised sources and pulsar searches were also conducted by Riseley et al. (2018, 2020). Several other surveys are currently ongoing, such as a search for pulsars associated with polarised point sources using LOFAR, which detected 2 new pulsars (Sobey et al., 2022) and a circular polarisation survey for radio stars with the ASKAP, resulting in 37 pulsar detections, despite them only looking for flare stars (Pritchard et al., 2021).

In this paper, we present methodologies for finding pulsar candidates in the MWA offline-correlated observations, test their efficiency by detecting known pulsars, and making an attempt to detect new pulsar candidates. Section 2 describes the instrument and the observation details. Section 3 describes the data analysis and the metrics applied to the acquired data. Section 4 summarises the results of the data analysis and discusses the implications for the MWA and other low frequency telescopes such as the MWA.

3.2 Observations and data processing

3.2.1 Observations

The MWA is a low-frequency Square Kilometer Array (SKA) precursor telescope, operating in the frequency range of 70-300 MHz, located at the Murchison Radio-astronomy Observatory (MRO) in Western Australia. It is the only radio telescope operating at these frequencies able to access the entire southern sky, making it complementary both to similar low-frequency telescopes in the Northern Hemisphere, such as the Low Frequency Array (LOFAR; van Haarlem et al., 2013), as well as high-frequency telescopes in the Southern Hemisphere, such as the Parkes Radio Telescope (Murriyang). Pulsar physics is one of the key science drivers for the MWA (Beardsley et al., 2019). Despite being less sensitive than LOFAR, the combination of a large FoV and an extremely radio-quiet environment makes the MWA ideal for undertaking pulsar searches at frequencies below 300 MHz.

In this paper we consider archival data collected with the Phase I and II configuration of the MWA which we use to demonstrate image-based methods for pulsar searches. In 2018, the 128-tile array with a maximum baseline of $\sim$ 3km (Phase 1) (Tingay et al., 2013a) was upgraded to provide a maximum baseline of 5.3km with 256 tiles (sets of 4x4 cross-dipole antennas). The Phase II upgrade increased the angular resolution by a factor of ~ 2 and the sensitivity by a factor of ~ 4 as a result of reduction in the classical and sidelobe confusion (Wayth et al., 2018). Originally envisioned as an imaging telescope, requiring only time-averaged tile cross-correlation products ("visibilities"), it was eventually upgraded to enable the capture of raw complex voltages from each tile with the development of the Voltage Capture System (VCS; Tremblay et al., 2015). The VCS records high-time and frequency resolution voltage data (100 μs / 10 kHz), which provides the opportunity to process the data in different ways and maximise data flexibility. Since pulsar flux densities at low-frequencies can vary significantly from day to

Obs Name	OBSID	Project Code	MWA Phase	Dur(min)	Freq (MHz)	Main use
A	1276619416	G0071	PIIE	90	184.96	Formulating method 1 and 2
B	1150234552	G0024	PI	80	184.96	Formulating method 3
C	1148063920	G0024	PI	45	184.96	Independent verification of all methods
D	1274143152	D0029	PIIE	20	154.24	Independent verification of all methods

Table 3.1: Observations processed and analysed as part of this chapter. PI represents MWA Phase I Array and PIIE represents MWA Phase II Extended Array. The main application for the observations are given in the table. The first 2 observations were mainly used to establish the criteria and the thresholds required to detect highly significant pulsar candidates. The other two observations were used to independently test the methodologies and determine the efficiency of the different methods.

day, being able to find pulsar candidates in images formed from the MWA VCS data, and vet them by beamforming the very same data is a very powerful technique unique to the MWA.

The maximum MWA VCS observation duration used here is ∼90 minutes and the central frequency ranges from 154 MHz to 185 MHz. Table 3.1 shows the observations that are processed and analysed as part of this paper. Along with the observation IDs and corresponding project code, details of the telescope configuration at the time of the observation, duration of the observation, the central frequency of the observation and the main application of the observation in this paper are mentioned in the table.

3.2.2 Data processing

The raw complex voltages from the MWA antennas (i.e. "tiles") are correlated offline using xGPU software correlator (Clark et al., 2013) to produce "visibilities" at 1-s time resolution. These are then processed with COTTER (Offringa et al., 2015), which converts data into the CASA measurement set format (McMullin et al., 2007) and applies calibration in the conversion process. It also eliminates the channels affected by radio frequency interference (RFI) by using the in-built software AOFlagger (Offringa et al., 2012a). Calibration solutions

for the observation are downloaded from the MWA All-Sky Virtual Observatory (MWA ASVO; Sokolowski et al., 2020). Images in instrumental polarisation (XX, YY, XY, YX) are formed using WSCLEAN (Offringa et al., 2014b) with a Briggs weighting of -1. These images were then converted to Stokes I, Q, U and V images using the MWA "fully" embedded element beam model (Sokolowski et al., 2017). The image sizes were 8192×8192 pixels or 4096×4096 pixels, depending on the observation. Individual 1s images were averaged together to produce mean full Stokes images which were then used for further analysis. A block diagram showing the above described steps of the imaging pipeline is given in Figure 3.1.

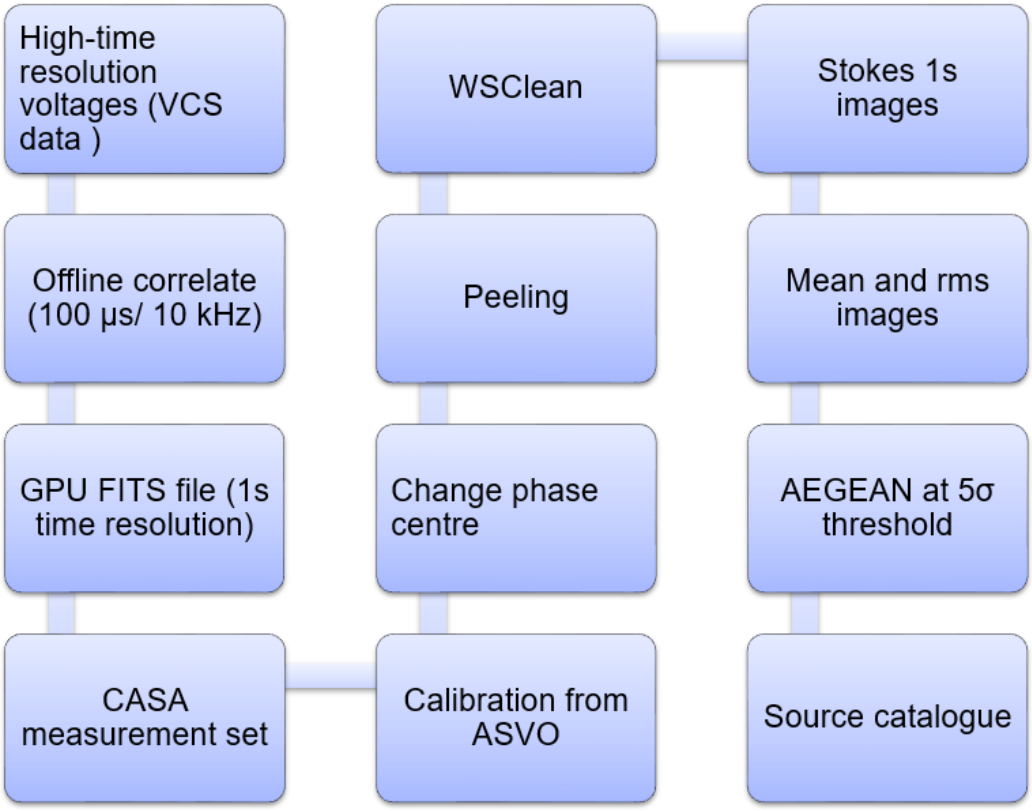

Figure 3.1: Block diagram of the imaging pipeline, which shows the different steps taken to get the resulting Stokes image. It follows from obtaining the raw voltages, offline correlating and producing measurement sets. WSClean is then used to create the images and apply calibration, ultimately producing Stokes images for every timestamp. These images are then averaged to form the mean Stokes images.

A cutout of a mean Stokes I formed from observation A is shown in Figure 3.2. It shows a region of the Galactic Plane passing through the centre of the image along with a supernova remnant which causes significant increase in the noise in that region. The other sources are a combination of stars, active galactic nuclei, known pulsars and other radio sources. The mean rms of this image is 5 mJy/beam and increases by almost a factor of 4 near the Galactic Plane and the edge of the image. Almost 9000 radio sources are detected at 5σ threshold in the whole image, where σ is the mean standard deviation of the noise. These sources are then used in the methodologies described in Section 3.3.

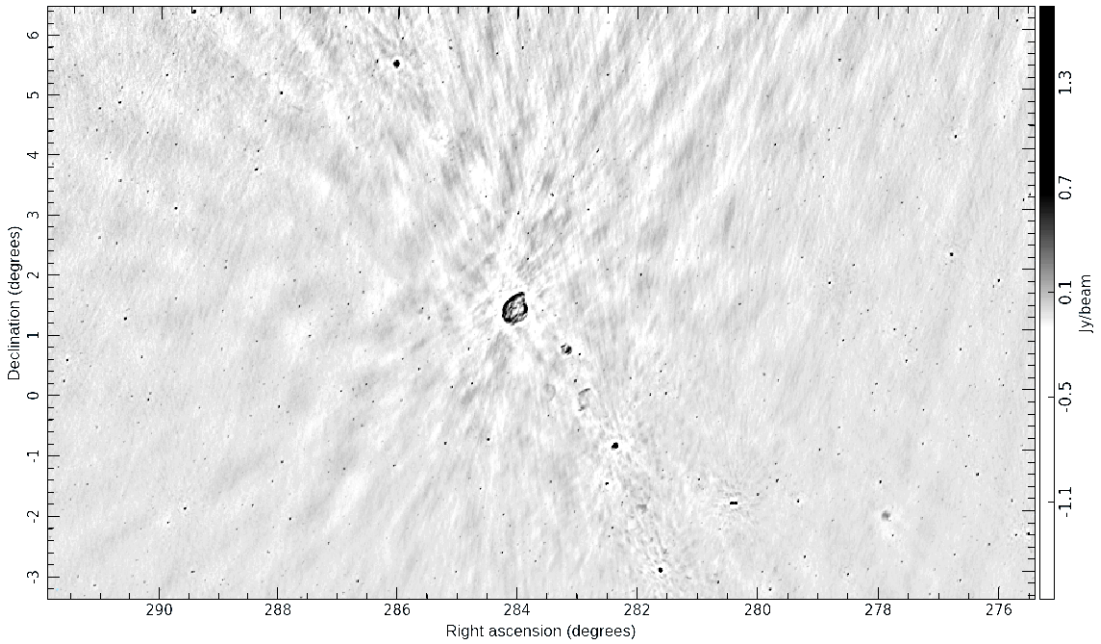

Figure 3.2: Stokes I mean image cutout of Observation A. It shows the Galactic Plane in the centre of the image. The average rms in the image is ∼5 mJy/beam, with a factor of 4 increase near the Galactic Plane and edge of the image. We can also see a variety of extended sources, such as supernova remnants as well as point sources which are a combination of already known pulsars and other radio sources.

The radio source-finding and extraction software, AEGEAN (Hancock et al., 2012, 2018) was then used to identify sources from the mean Stokes I and V images and create a catalogue of sources above a 5σ threshold which are then analysed to produce a list of promising pulsar candidates. The individual 1s images were

also averaged together to produce light curves at various time resolutions such as 300s, 60s and 30s. This can be helpful in detecting sources that are variable in time and hence can be promising pulsar candidates.

3.3 Methodologies developed to detect pulsar candidates

In the following subsections we describe the methodologies that we have developed and implemented in order to assess the efficiency on known pulsars and also attempt to discover pulsar candidates.

3.3.1 Steep spectrum

Pulsars are known steep-spectrum radio sources, with an average spectral index of -1.6 ± 0.2 (Jankowski et al., 2018). The first millisecond pulsar, PSR J1939+2134 was discovered due to the steep spectral properties of the continuum source, 4C 21.53W (Backer et al., 1982). The first discovery of a pulsar, PSR J1824-2452A in a globular cluster was made possible due to its steep spectrum (Lyne et al., 1987). Since then, there have been a handful of target searches aiming to detect steep spectrum sources as pulsars, e.g. Damico et al. (1985), Kaplan et al. (2000a) and Crawford et al. (2000) targeted 18, 16 and 92 sources, respectively, but found no pulsations. While the surveys mentioned above were sensitive enough to detect the associated pulsars with high significance, the available observing frequencies could have affected the detection results for some of the targets. With the advancement in computing resources, such surveys can be re-conducted using techniques such as acceleration searches to detect exotic systems and may be more fruitful. At radio frequencies, the spectral behaviour of many pulsars can be described by a power law, where the spectral index calculated from flux density measurements S_a and S_b, at two different frequencies ν_a and ν_b,

$$\alpha = \frac{\log\left(\frac{S_a}{S_b}\right)}{\log\left(\frac{\nu_a}{\nu_b}\right)}. \tag{3.1}$$

For our methodology, we have used the Rapid ASKAP Continuum survey (RACS; McConnell et al., 2020; Hale et al., 2021) as our counterpart catalogue to calculate the spectral index. The RACS survey is the first large sky survey covering the southern sky below declinations +41° using ASKAP (Hotan et al., 2014). The central frequency of the survey is 887.5 MHz and is one of the deepest radio surveys of the southern sky at these frequencies. The flux densities of the sources from RACS in combination with the flux densities from our images can be used to calculate spectral indices of the sources detected in both images or upper limits on spectral indexes for the sources detected only in MWA images. Since pulsars are known for their steep spectra, it is a compelling case to search for radio pulsations of sources exhibiting a steep spectral index. The results of applying a spectral index cutoff to the sources in the images are described in Section 3.4.4.1. Given the angular resolution difference between MWA and ASKAP, cross-matching with RACS is also a good way to eliminate any other extended sources which may have been pre-selected due to lower spatial resolution of the MWA (∼a few arcmin).

3.3.2 Circular polarisation

Until Lenc et al. (2018), most of the all sky surveys have been conducted using total intensity, i.e., Stokes I. As only a fraction of the sources present in the total intensity image emit in circular polarisation, it is useful in lowering the classical confusion limit (Lenc et al., 2017). Greater sensitivity can be obtained for instruments such as the MWA which is confusion limited in total intensity (Tingay et al., 2013b). This is extremely helpful for sources that are highly circularly polarised; with a trade-off in sensitivity for sources that are not. The advantage of this is that most sources are generally weak in circular polarisation

and hence will not contribute to side-lobe confusion, as a result reducing the need for deconvolution, making image processing easier. A smaller number of sources compared to Stokes I images also reduces the number of candidate pulsars significantly. This method has demonstrated its potential to detect pulsars by the discovery of a highly polarised millisecond pulsar by ASKAP (Kaplan et al., 2019), which would be otherwise missed by traditional searches due to its wide profile and high DM. We implement the method of looking for sources that are highly polarised in Stokes V images in an attempt to detect any potential pulsar candidates. This method will be highly effective in detecting sources that may be below the noise threshold in Stokes I images but are highly circularly polarised ($>$ 7%) (Lenc et al., 2018, 2017) and hence very bright in Stokes V images. Further details of this method are discussed in Section 3.4.4.2.

3.3.3 Time variability

One of the easiest ways to confirm if a promising candidate is a pulsar or not is to perform a periodicity search and fold the data at the best-fit period and DM. However, at lower frequencies, sources may suffer from significant scattering and dispersion lowers our sensitivity of periodicity searches using high time resolution data. Having images of the field at short timescales for the whole observation opens up a new avenue to detect pulsar candidates. It focuses on how the flux density of the sources vary with time. For example, the ASKAP Variables and Slow Transients (VAST) Pilot project (Banyer et al., 2012) and the LOFAR Transients key science project (Swinbank et al., 2015) have used this methodology to look for transients. Producing light curves essentially requires a priorised fitting for the sources for all the images and construct a light curve from the measured flux density values. This method can be efficient tool for detecting pulsars that may have high degrees of variability on timescale of seconds. The application of this method to the images obtained from our observation is discussed in detail in Section 3.4.4.3.

3.4 Verification of the methodologies on MWA data

The methodologies described above have been developed and tested on observation A and B (refer to Table 3.1 for details). On successful completion of the testing, they have been independently applied to observations C and D (from Table 3.1) to verify their efficiency in detecting possible pulsar candidates.

We use Stokes I and V images which are of particular interest in the analysis of observation A. The images are 8192 $\times$ 8192 pixels, with pixel size $\sim$ 3 arcmin/pixel, resulting in 40 $\times$ 40 degree images. The rms noise levels in the image for observation A are around 5 mJy/beam (Stokes I) and 3 mJy/beam (Stokes V) in the centre of both the images. The sources are extracted using AEGEAN (Hancock et al., 2012, 2018) with a mean cutoff of 5σ, where σ is the local root-men-square noise level near the source. The mean Stokes I image is complex with over 9000 sources including diffuse emission and several extended structures as shown in Figure 3.2. These sources are then used to cross-match with a pulsar catalogue as well as choose promising pulsar candidates, the details of which are discussed in the sections below.

3.4.1 Noise characterisation

Along with the source catalogues for the Stokes images, AEGEAN also creates maps of the rms noise (σ) in each image. The σ values vary across the image due to a combination of several factors. This includes adjacency to bright sources and unmodelled extended emissions, which are prevalent near the Galactic Plane. The mean σ value across the whole field of observation is 5 mJy/beam while it changes to 20 mJy/beam near the Galactic Plane. There is also a significant increase near the edge of the images ($\sim$ 30 mJy/beam) where the beam response

of the MWA decreases. Due to this variation of the noise across the whole image, the flux density detection thresholds for the sources should be defined locally and dependent on the location of the source in the image. For example, a 40 mJy source is easily detectable with a 5σ significance away from the Galactic Plane. However, the same source will not be bright enough to be detected at the edge of the image where the threshold is significantly higher.

3.4.2 Comparison with the ATNF catalogue

The Australian Telescope National Facility (ATNF) pulsar catalogue (Manchester et al., 2005) contains $\sim$ 3000 pulsars. Around 700 pulsars are present in the 3dB (half power point) beam of this observation. We expect to detect 42 of them at 5σ threshold when we take into account the local σ around the sources. Out of the 42 expected detections, we were able to detect 21 pulsars in imaging which is reasonable considering the more complex environment and the realistic details of the data and processing. Three of the pulsar non-detections can be attributed to their spectral turnover at low frequency as highlighted by Jankowski et al. (2018). The other 18 non-detections were due to the location of these pulsars near the Galactic centre or the edge of the image. The 21 detected pulsars were also folded with PRESTO (Ransom, 2001) in order to verify their detections using standard methods. Only 11 out of 21 were detected via PRESTO. This can be explained by the DM cutoff of $\sim$250 pc cm^{-3} for the MWA beyond which the detection sensitivity is highly reduced when dealing with time series data. The pulsars detected via imaging (black circles) and traditional search methods (orange circles) are shown in Figure 3.3. The blue dotted line indicates the flux density threshold for image based searches for this observation, the red dashed line indicates the approximate DM cut-off for traditional searches with the MWA. The green shaded region highlights where image-based searches can be more successful than traditional searches, especially at low frequencies. In the figure, we can see that even though there are more pulsars detected via traditional searches,

image-based searches probe a parameter space that is inaccessible to traditional searches.

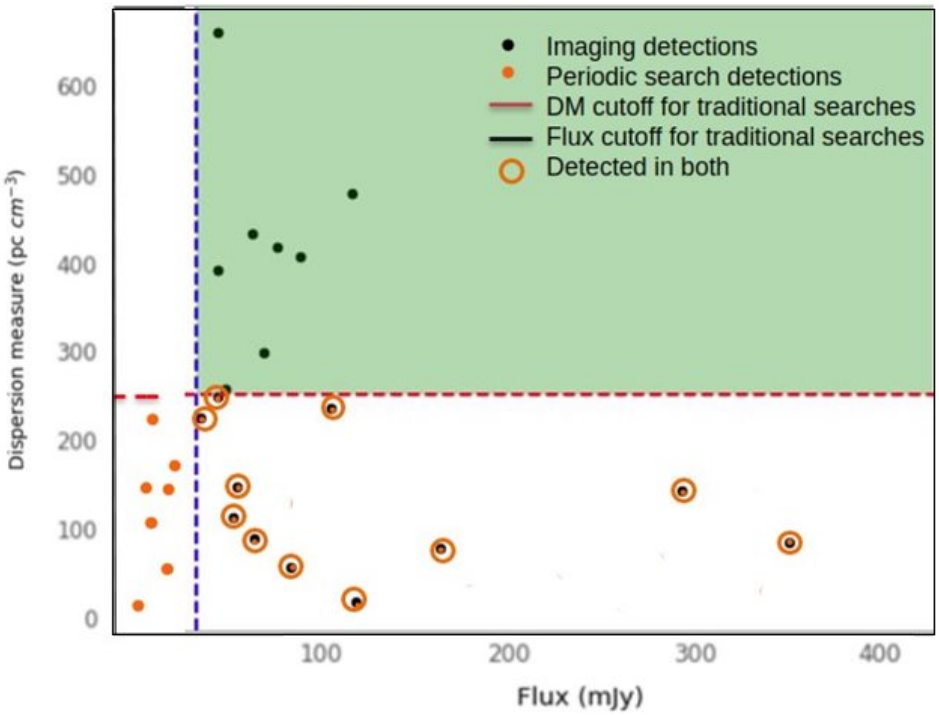

Figure 3.3: The above figure shows the parameter space that is exclusively accessible to low-frequency image-based pulsar search techniques, shaded in green. The black dots indicate the image-based pulsar detections and the orange dots represent the detection of pulsars via traditional techniques at low frequencies. The blue dashed line shows the mean flux density threshold of observation A for detection of sources above 5 σ (25 mJy). The red dotted line is the DM threshold (250 pc cm^{-3}) of traditional search techniques for MWA frequencies beyond which the sensitivity decreases significantly.

3.4.3 Comparison with RACS catalogue

3.4.3.1 Cross-matching known pulsars

Out of the 21 pulsars detected in the test MWA image (Observation A), 19 of them were detected in a Stokes I RACS image. Of the 2 pulsars not present, one is associated with a supernova remnant, SNR G21.5−0.9. A possible reason

for the non-detection of the other pulsar, PSR J1822−1400, could be very steep spectral index of −2.25 (Manchester et al., 2005, ATNF catalogue).

3.4.3.2 Cross-matching all sources

On cross-matching our catalogue with the RACS all-sky catalogue, we find ∼ 8000 sources that are present in both the catalogues and 342 sources that are present only in MWA catalogue at 5σ confidence level. Along with the sources that satisfy our criteria, these 342 sources are also of interest to us as potentially intriguing sources for follow up. We further reduce this number by excluding extended sources as pulsars are generally point sources. The ratio of the integrated flux over source in the image (S_I) to peak flux of the source in the image (S_P), both calculated by AEGEAN, is used to select the point sources such that sources where $S_I/S_P > 1.5$ are considered to be extended. This compactness criterion is based on the similar criterion in the GaLactic and Extragalactic All-sky Murchison Widefield Array (GLEAM) catalogue (Hurley-Walker et al., 2017) and is applied to the sources present in both catalogues as well as the sources present in MWA catalogue only. The ratio as a function of the signal to noise ratio (SNR) of the sources calculated using the source catalogue is shown in Figure 3.4. The blue points (∼ 6700) are the excluded extended sources and the red points (∼ 1600) are the compact sources taken into consideration for further analysis on application of the compactness criterion. This subset of sources is used for further analysis as described in Section 3.4.4.

3.4.4 Testing of the methodologies

3.4.4.1 Spectral Index

Observation A (refer to Table 3.1) is predominantly used for the examination of the first criterion. On successful verification of the criterion, it is then independently applied on observations C and D. The process begins by first selecting sources with a steep spectrum, by calculating the spectral index using Equation

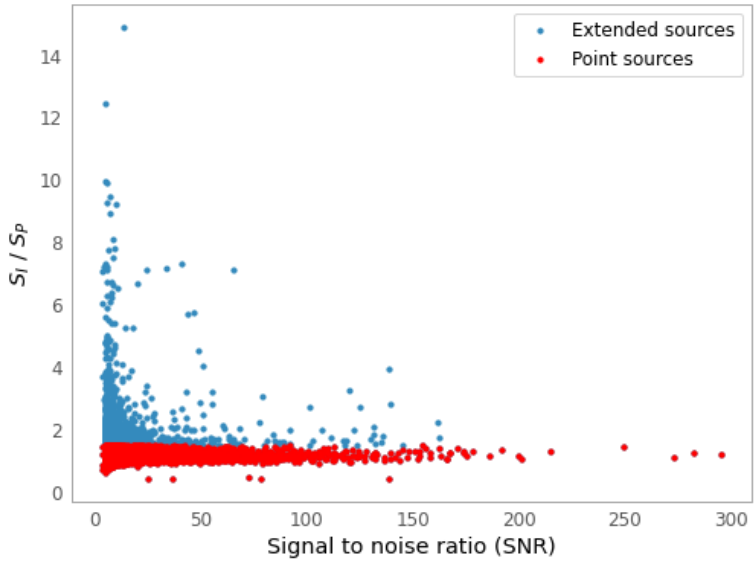

Figure 3.4: Ratio of integrated flux to peak flux of the sources in MWA images (S_I / S_P) as a function of SNR of the sources. The criterion for the source to be a point source was chosen to be the ratio S_I / S_P < 1.5. Based on this criterion all the point sources are shown in red ($\sim$ 1600) and the extended sources are in blue ($\sim$ 6700).

3.1 for the sources present in both MWA and RACS catalogues. Furthermore, for the sources that are present only in the MWA Stokes I images, an upper limit on the spectral index is calculated using the local σ from the RACS noise map (5σ for RACS). A recent study of spectral indices of 441 radio pulsars suggests the mean of the spectral index distribution is -1.8 $\pm$ 0.5 (the uncertainty given here is the weighted standard deviation) for 79% of pulsars following a simple power law spectrum (Jankowski et al., 2018). Taking this into account along with error margins, a spectral index cutoff of -1.2 is selected, such that sources steeper than -1.2 are considered as steep spectrum sources and used for further analysis. While 29% of the known pulsar population exhibit spectra flatter than -1.2 (Swainston et al., 2022a), the steeper cutoff is more likely to find those that were missed by previous surveys at higher frequencies while also reducing false positives from other source types e.g. steep spectra AGN. This cut-off may be

relaxed in future (allowing shallower power laws) if additional robust filtering criteria are developed in order to reduce the number of false positives.

The distribution of the spectral indexes of the sources and the applied cutoff are shown in Figure 3.5. Application of the criterion resulted in a subset of $\sim$ 300 sources that are steep spectrum. Out of these sources, 19 are already known pulsars. Figure 3.6 shows the pulsars that satisfy the criterion of steep spectrum sources. It also shows the two pulsars that were excluded due to criterion not being satisfied. One is in a supernova remnant and was excluded on application of the compactness criterion. The other pulsar, PSR J1834-0010 has a spectral index of -0.9 which is not steep enough to pass the criterion. The $\sim$ 300 sources that are considered steep according to our criterion were checked for pulsar-like emission by forming a tied-array beam on each of the sources and performing a PRESTO (Ransom, 2001) based search up to a DM of 500 pc cm^{-3} with minimum DM steps of 0.02 pc cm^{-3} and maximum of 0.5 pc cm^{-3}. No pulsations from the sources were found in the beamformed data other than the 19 known pulsars in the sample. However, as mentioned before the sensitivity of MWA is significantly reduced at DMs above 250 pc cm^{-3}. Therefore, deeper searches with a higher DM range with a high-frequency instrument may enable the identification of pulses from these sources.

3.4.4.2 Circular polarisation

A catalogue of sources from the Stokes V image is generated by running AEGEAN on the Stokes V inverted image and the original Stokes V image. The combination of the catalogues from both the processes is used as the Stokes V source catalogue. The second criterion of circular polarisation uses the sources from Stokes I and V images of observation A to select potential pulsar candidates based on their circular polarisation. Unfortunately, the positive detection of pulsar candidates is hindered by instrumental leakage, even when leveraging the most advanced MWA primary beam model used for this analysis (Sokolowski et al., 2017). Lenc et al.

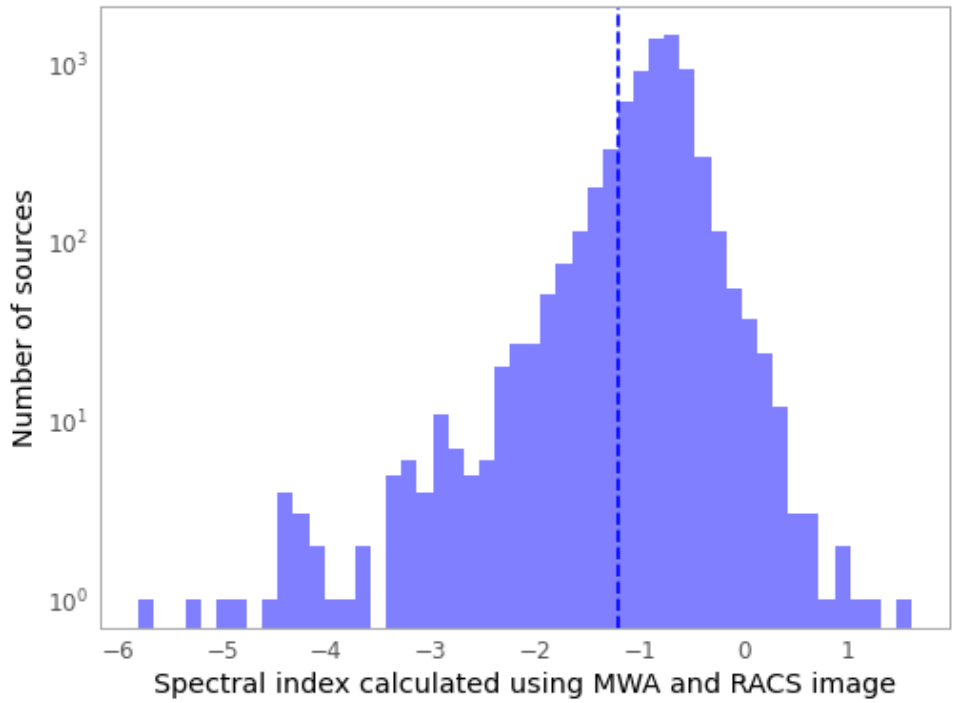

Figure 3.5: Distribution of the spectral index of the sources detected in the MWA image of observation A. It can be seen that most of the sources have spectral index between -1 and 1. The blue dotted line shows the spectral index cutoff threshold used in this analysis.

(2017) showed that such polarisation leakage can be mitigated in drift-scan observations by modelling the leakage pattern across the beam and then subtracting it. A similar approach has been taken in this analysis to deal with the leakage for the observations. For observation A, the Stokes V sources are crossmatched with Stokes I catalogue sources and the median leakage in 5° radius around each source is then calculated. This is then subtracted from the measured Stokes V flux density to suppress any residual leakage resulting in a more robust estimate of the source SNR and fractional polarisation. A distribution of fractional polarisation, V/I, of sources in the image for observation A is shown in Figure 3.7. The acceptable threshold for fractional polarisation according to literature (Lenc et al., 2018, 2017) is $\sim$ 7 %. This threshold is taken after subtraction of the

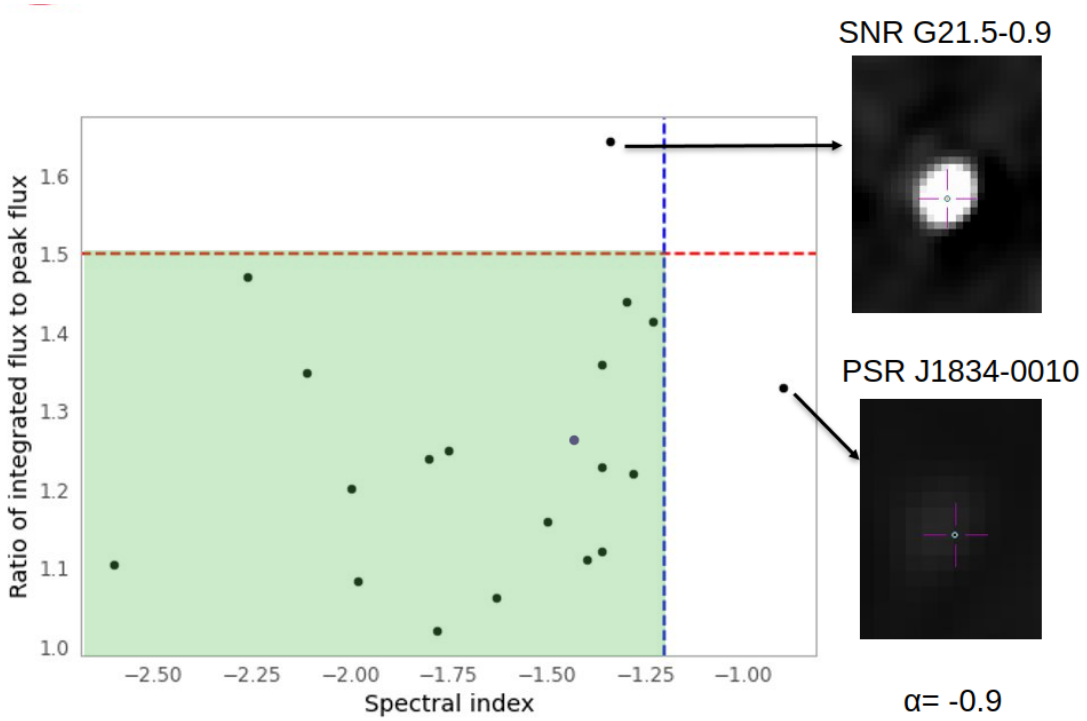

Figure 3.6: Pulsars that are detected in imaging and the ones that satisfy the criterion of steep spectrum. The blue dashed line shows the spectral index cutoff and the red dashed line signifies the compactness cutoff applied to the sources. The green region shows the parameter space that the combination of the compactness and spectral steepness criteria can probe in imaging domain .

mean leakage in nearby sources. Application of the threshold reveals 4 sources that satisfy this criterion. According to the European Pulsar Network (EPN) database, 9 pulsars in this field are circularly polarised. These 4 sources that satisfy our threshold with $V/I > 0.07$, are a subset of the 9 pulsars that are circularly polarised. Out of the 5 non-detections, one pulsar, PSR J1823-1115, shows a sign reversal in the mean pulse profile of Stokes V polarisation and the other 4 (highest absolute value of 15 mJy/beam) are below our detection threshold in Stokes V image ($\sim$ 35 mJy/beam). No other interesting pulsar candidates were detected in this image using this method. Further investigation in better removing the polarisation leakage is required in order to detect potentially interesting pulsar candidates.

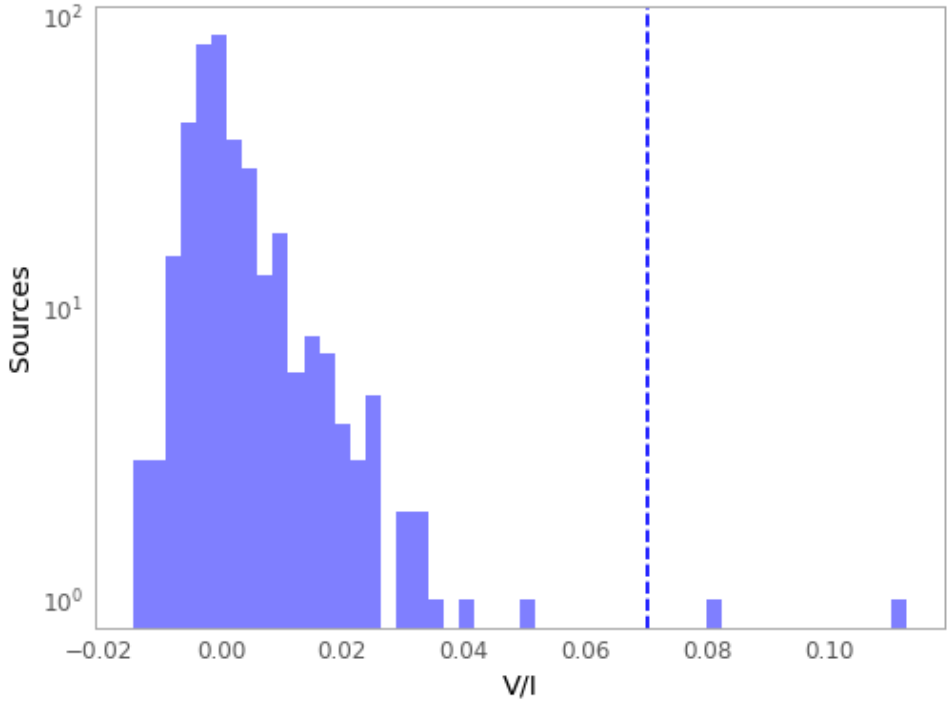

Figure 3.7: Distribution of fractional polarisation of the sources after the removal of non-physical leakage around the sources. The blue dashed line shows a fractional polarisation threshold of 7% from the existing literature. The 4 sources with $|V/I| > 0.07$ are known to be circularly polarised pulsars according to the European Pulsar Network (EPN) database.

3.4.4.3 Variability

The previously defined characteristics are not exclusive to pulsars and may be selecting other type of sources for example, flare stars and M-dwarfs (Lynch et al., 2017b,a). Even though the luminosities of pulsars are relatively stable when averaged over long time-scales (Taylor, 1991; Matsakis et al., 1997) , the received flux density can be modulated by propagation effects such as refractive and diffractive scintillation, e.g., Armstrong et al. (1995b). While diffractive scintillation causes variability on time-scales of tens of minutes, refractive scintillation constitutes variations on the time-scales of weeks to months. Depending on the cadence of the observations using the MWA, we explore the variability timescales of 300s, 60s

and 30s, probing diffractive interstellar scintillation specifically. This is done by generating light curves of the possible variable sources. These sources are selected based on variability statistics (equations. 3.2, 3.3, 3.4) such as how significant the variability is (significance) and the percentage of variability of (modulation) the pixel (or the source) when compared to its surrounding. The statistical quantities described below are are for a specific image pixel (function of (x,y) position of the image), but this dependence was dropped for brevity.

For each pixel, the reduced χ^2 (significance) statistic is defined as

$$\chi^2 = \sum_{i=1}^{n} \frac{(S_i - \bar{S})^2}{\sigma_i^2}, \tag{3.2}$$

where n is the number of images, S_i is the flux density of a pixel in image i, σ_i^2 is the variance within the images (Bell et al., 2016b). $\bar{S}$ is the weighted mean flux density defined as

$$\bar{S} = \frac{\sum_{i=1}^{n} \left(\frac{S_i}{\sigma_i^2}\right)}{\sum_{i=1}^{n} \left(\frac{1}{\sigma_i^2}\right)} \tag{3.3}$$

In combination with the χ^2 test, we also calculate the modulation index of the source/pixel that is used to quantify the degree of variability of the source when compared to its surrounding sources. The modulation index (m) is defined as

$$m\ (in\ \%) = \frac{\sigma_S}{\bar{S}} \tag{3.4}$$

where σ_S is the standard deviation of the flux density of the pixel and $\bar{S}$ is the mean flux density of the pixel (Bell et al., 2016a). The correlation between χ^2 and modulation index as shown in Figure 3.8 is used to determine specific threshold for the different timescales for every observation. A threshold is chosen such that the number of candidates to be checked via beamforming does not exceed 1000. For the observations analysed as part of this paper, the thresholds are similar

given that it is from the same instrument with similar noise characteristic of the image. For observations which are significantly different, this threshold has to be determined such that the candidate sources to beamform on is not extremely high.

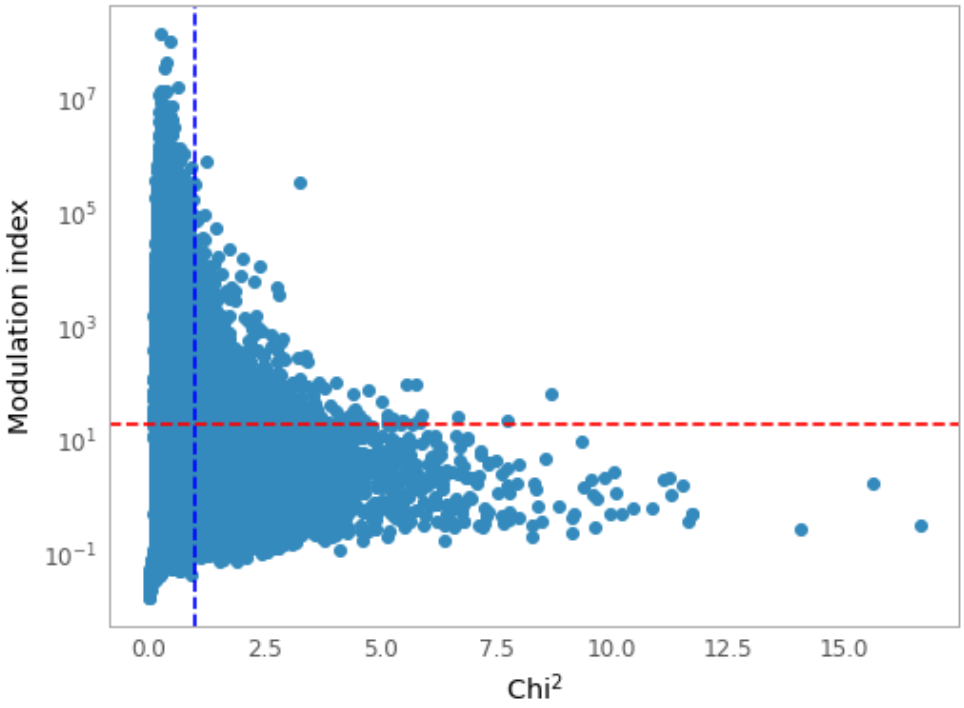

Figure 3.8: Correlation between χ^2 and modulation index for images with 30s cadence for observation B. The blue dashed line indicates the χ^2 threshold of 1 (for this case). In order to reduce the storage and CPU requirements, these sources are further subjected to a threshold of 20%, denoted by the red dashed line, for modulation index. The light curves for only sources ($\sim$ 250 sources) satisfying both threshold are saved for further assessment. These light curves are then visually investigated to determine its ranking in terms of variability and searched for pulses.

A test of the above described formalism was done on observation B (see Table 3.1) consisting of two known pulsars, PSR J0034-0521 and PSR J0034-0721, the latter of which is variable on short timescales (McSweeney et al., 2017). This test was a sanity check, performed to determine if the variable pulsar would satisfy

our criterion without any prior information as one of the variable candidates with high significance. As an initial test case, a χ^2 threshold of 1, was applied to the observation, resulting in a list of $\sim$ 5 candidate pixels in a small window around the test pulsar, PSR J0034-0721. Three out of the 5 candidate pixels corresponded to that of the pulsar. The other 2 candidates, when searched using PRESTO did not yield any pulsar like signals. The same analysis was then extended to the whole image, using the same threshold, which resulted in $\sim$ 250 candidates. A careful inspection of the light curves reveal one variable source whose pixel position is coincident with that of the variable pulsar PSR J0034-0721. Furthermore, a distinct variability on timescale of 300s is observed for J0034-0721 when compared to the light curve of the pixel position corresponding to that of J0034-0534 as shown in Figure 3.9. The χ^2 for this pixel is 1.6 with a modulation index of 30%, satisfying our threshold of χ^2. This demonstrates that any source which is at least as variable as J0034-0721 should be easily detected using the criterion of light curve extraction. The variability procedure is then applied to observations C and D as described in Section 3.4.5.

3.4.5 Application of the methodologies to other observations

Two observations are used to independently test the formulated methodologies and corresponding criteria to determine the success rate of detecting pulsar candidates. In this section, we describe the results obtained when the test is performed on the observations C and D.

3.4.5.1 Observation C

Processing of this observation was performed as described in Section 3.2.2 to produce Stokes I and V images. The images produced for this observation were 4096 $\times$ 4096 pixel with 0.5 arcmin/pixel resolution, resulting in 35°x 35°images. The σ for this observation was 30 mJy/beam (Stokes I) and 10 mJy/beam (Stokes V)

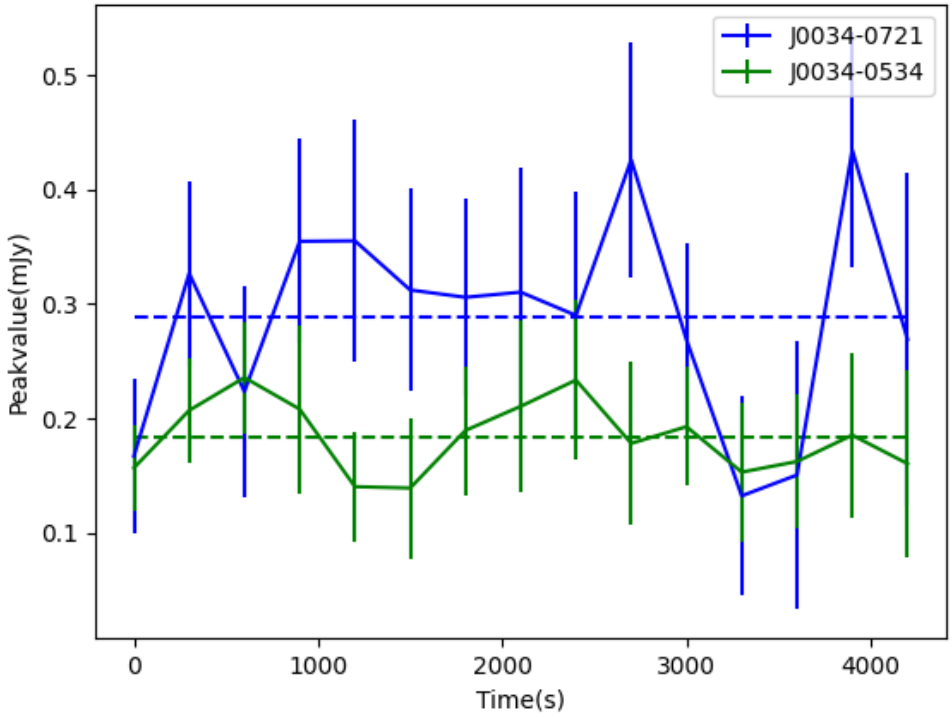

Figure 3.9: Light curves for PSR J0034-0721 (blue) and PSR J0034-0534 (green) for 300s timescale averaged images for the whole observation. For this test, our χ^2 threshold is 1 and the threshold on modulation index (m) is 20%. The blue light curve has a χ^2 of 1.6 and has a modulation index of 30%, whereas the green curve is approximately constant and has a χ^2 of 0.8 and modulation index of 10%. While the pixel corresponding to the blue curve will be easily selected as a candidate on application of our criterion, the pixel for the green curve will not satisfy our threshold. This supports the variability of J0034-0721 as stated in the literature and indicates that our criterion is indeed useful for detection of true pulsar candidates.

and increases almost by a factor of 3 at the edge of the image. AEGEAN (Hancock et al., 2012, 2018) was used with a threshold of 5σ to extract sources from mean image resulting in $\sim$ 1100 sources in Stokes I image. On the application of the compactness criterion, the extended sources are discarded from further analysis, reducing the number of sources to $\sim$ 800. On performing a similar comparison to the ATNF catalogue as described in Section 3.4.2, a total of 335 pulsars were present in the 3dB (half power point) beam. We expect to detect

52 pulsars at 5-σ level, after inspecting the local standard deviation of the noise near the pulsars. 23 out of the 52 pulsars were detected both in beamforming and image based searches while an additional 5 were detected only in imaging and 7 only in beamforming.

The non-detections in beamforming were because the pulsars were at a high DM where the scattering at low frequencies is significant enough to deter the detections. Four of the non detected pulsars in imaging were associated with supernova remnants and hence were not in the analysis when the compactness criterion is applied. One possible reason for the remaining non detections was the pulsar flux density being lower than the mean flux density threshold and hence not bright enough for it to be detected in imaging. Another possible reason for the non detection may be the turnover of pulsars, which is more dominant at lower frequencies.

Out of the 28 pulsars detected in MWA imaging, we are able to detect 27 in RACS Stokes I image. The possible reason for the non detection of PSR J1935+2154 could be its association with a supernova remnant, G57.2+0 (Kothes et al., 2018). This is because of the increase in the noise confusion as the pulsar is present in the supernova remnant.

Out of the compact sources present in our Stokes I catalogue, $\sim$ 500 are present in RACS all-sky catalogue. Around $\sim$ 350 sources are present only in MWA catalogue and are of high significance to us. The spectral index of the sources present in both catalogues is calculated using equation 3.1. The upper limit of the spectral index is calculated for the sources present in only MWA catalogue. The spectral index threshold of -1.2 as established in Section 3.4.4 is applied to both the subsets of sources. A total of $\sim$ 100 sources have a steep spectrum. 27 of the 100 sources are already known pulsars. The one excluded pulsar has a spectral index of -1.0 and hence does not satisfy our criterion. The remaining steep spectrum sources were beamformed and searched for pulsar-like signal. None were confirmed as pulsar candidates.

The second criterion was applied to the Stokes I and V catalogues sources in the similar way as described in Section 3.4.4.2 after the subtraction of instrumental leakage. When this criterion for selecting polarised sources as defined in Section 3.4.4 was applied, 2 sources are independently detected above the threshold, which can be associated with 2 pulsars. However, the EPN database shows that 4 pulsars should be detected in the Stokes V image. The non-detection of the other 2 pulsars can be attributed to the flux density of the pulsars (highest absolute value is 25 mJy/beam) being below the noise in the Stokes V image (∼40 mJy/beam). No other polarised sources above the threshold were detected in this observation. A reduction of Stokes V leakage will improve the sensitivity of this criterion.

In order to select sources which are variable in nature and could possibly be interesting pulsar candidates, we generated mean images for timescales of 300s, 60s and 30s. The χ^2 vs modulation index maps for three above mentioned timescales is used to set a threshold for χ^2 such that we produced light curves for only candidates that are most probable to be pulsar candidates. For this observation, a χ^2 threshold of 1, and modulation index threshold of 20% is applied, resulting in $\sim$ 550 candidates. Given that the number of light curves produced after the application of the variability statistics is manageable, the light curves were visually inspected by me to confirm the variability and a corresponding position in RA and DEC was calculated using the pixel coordinates of the light curve. As the variability statistics are not entirely reliable, the light curves which were not truly variable were discarded from any further analysis. The positions of the satisfactory light curves were used to perform a pulsar search to confirm if any of these are real pulsars.

3.4.5.2 Observation D

Stokes I and V images were again produced following the procedure laid out in Section 3.2.2. The images are 8192 × 8192 pixels with 0.3 arcmin/pixel resolution,

creating images that are $\sim$ 40°x 40°. The noise in this image varies from 15 mJy/beam at the centre of the images to 30 mJy/beam at the edge of the image in Stokes I. For mean Stokes V image, $\sim$ 2 mJy/beam at the centre of the image and increases by almost a factor of 5 at the edges of the image. The source catalogue for the mean images was produced using AEGEAN and consists of $\sim$ 5000 sources. The removal of the extended sources from the catalogue resulted in $\sim$ 4000 sources. According to the ATNF pulsar catalogue there are 12 pulsars in the field. Ten out of 12 are detected in imaging. The 2 pulsars are not detected due to the local noise of the pulsars being high as both the pulsars are at the edge of the image.

Around $\sim$ 3800 sources are present in both RACS and MWA catalogue. The spectral index for the sources present in both the catalogues and the upper limit of the spectral index for sources present in only MWA catalogue is calculated using equation 3.1. Application of the spectral index threshold mentioned in Section 3.4.4 results in a total of $\sim$ 250 sources that have steep spectral index. Out of 250 sources, 5 are known pulsars. The rest of the sources are beamformed and searched using the MWA pulsar search pipeline to detect any signal. We were not able to confirm any candidates as pulsars.

The sources from the Stokes I and V catalogues were then crossmatched and the fractional polarisation is calculated for the sources. After the removal of artifacts and leakage, we apply the fractional polarisation criterion and detect 5 real circularly polarised sources. Out of the 5 circularly polarised sources, Three of them are already known pulsars. The two other sources have been searched via traditional searches but no pulsations have been found. Five pulsars in this observation are expected to be circularly polarised based on EPN database. The 2 non-detected pulsars (highest absolute value is 10 mJy/beam) are below the detection threshold for the Stokes V image for this observation ($\sim$ 32 mJy/beam).

The variability criterion was then applied at the timescale of 300s, 60s and 30s. A χ^2 of 1 and modulation index threshold of 20% was enforced, resulting in $\sim$

Obs Name	Pulsars		Spectral Index		Polarisation		Variability	
	Expected	Actual	Expected	Actual	Expected	Actual	Expected	Actual
A	42	21	42	18	9	4	N/A	N/A
B	10	8	10	7	2	1	1	1
C	52	28	52	27	4	2	N/A	N/A
D	12	10	12	5	5	3	N/A	N/A

Table 3.2: Table shows the expected vs actual pulsar detections on application of the methodologies described in the paper. The last columns of observation A, C and D are empty as there are no variable pulsars in the field and hence the criterion of variability is not applicable for these observations.

1000 candidates. All candidates were searched using standard pulsar techniques, but none of the candidates displayed pulsar like emission.

The independent application of the criterion to the two observations helped in understanding the efficiency of the methodologies in selecting pulsar candidates. It also provided us with a context of the number of sources that one may expect from the different criterion and that increasing thresholds could be one possible way of reducing the number of candidates. Table 3.2 shows the expected and actual pulsar detections when the methodologies are applied to the four observations. The potential reasons for various non detections of known pulsars are stated in the Sections 3.4.4 and 3.4.5. Table 3.3 shows the initial number of candidates for the four methodologies when applied to the four observations. It is clear that the circular polarisation criterion produces significantly fewer candidates, which is possibly driven by our lack of full understanding of the polarisation leakage in the MWA images. More effort in understanding this issue and formulating a more robust threshold is required for greater success of the criterion. On the other hand, variability criterion produces a high number of candidates which may result in considerable amount of false positives. One must be careful when determining the threshold for χ^2 and modulation index in order to produce a greater number of true pulsar candidates. Lastly, the spectral index criterion, seems to generate a manageable number of candidates that can be followed up using periodicity or single-pulse searches while being computationally inexpensive.

OBS Name	Observation ID	Spectral Index	Circular polarisation	Variability	Total number of candidates	Candidates after combining criteria
A	1276619416	300	1	150	451	7
B	1150234552	150	1	250	401	4
C	1148063920	100	2	550	652	5
D	1274143152	250	5	1000	1255	4

Table 3.3: Table shows the total number of candidates when the four methodologies have been applied to the 4 observations. The last column shows the final candidates after combining the criteria like spectral index and circular polarisation and spectral index and variability.

3.5 Discussion

Even though there are lots of pulsars in the field of view of the observations, the number of pulsar detections in imaging is affected by the sensitivity of the images, reducing the number of pulsar detections in the imaging space. We also performed a comparison of the number of pulsars that were detected in imaging space and the detections of the same pulsars when searched for periodic signals using PRESTO. We can clearly deduce that the high DM pulsars are not detected when we perform a periodic search. For example, in observation A, PSR J1835-0643, was detected at $\sim 5\sigma$ in Stokes I image, but was not detected when a periodic search was performed due to its high DM of $\sim$ 473 pc cm^{-3}. Another reason for the non detection of the pulsars in periodic searches is the effect of scintillation and scattering. For example, PSR J1833-0338, in observation A Stokes I image was detected at $\sim 10\sigma$ via imaging as well as periodic searches. The expected detection significance for the pulsar is $\sim 30\sigma$ for periodic searches based on its flux density. Due to the scattering timescale of the pulsar ($\sim$ 0.7s) being close to its period ($\sim$ 0.6s), it suffers from scattering which degrades the detection sensitivity of the pulsar when searching using PRESTO and was hence was detected at a lower significance in periodic searches. On the other hand, there are pulsars such as PSR J1801-0357 that are detected by periodicity searches and not in image-based searches due to its flux density being lower than the flux density detection threshold for imaging. Overall, image-based searches target pulsar

candidates that may have been missed by traditional searches due to scattering or high DM. Any such pulsar candidates need to be followed up with high frequency telescopes such as the Parkes radio telescope (Murriyang) or uGMRT.

Another advantage of image-based pulsar candidate searches over traditional pulsars searches is the notably reduced time and resources that image based searches take to produce a list of pulsar candidates. If we perform a periodicity search for every pixel in our image, i.e. 10 million pixels, it would take 40 million CPU hours to obtain pulsar candidates. However, on applying the methodologies, we reduce the number of follow-up processing steps to a more tractable ~ 500 per observation.

3.5.1 Criterion 1 - steep spectrum

The first criterion focuses on candidates that have spectral index < -1.2. We were able to successfully detect most of the pulsars in the Stokes I images which satisfy our criterion. However, we did not detect any new pulsar candidates via this method. The steep spectrum sources detected in this criterion may be other categories of extragalactic sources, such as extended emissions from radio halos and relics in merging galaxy clusters and do not have a pulsar like signal and hence not detected via PRESTO searches. It may happen that sources that are not detected as pulsars via PRESTO-based searches are indeed pulsars but not detected due to high scattering and hence cannot be confirmed by using only the MWA data. This may be the case for the non detections when the field of view is dominated by the Galactic Plane and hence is more prone to scattering and have a larger sample of high-DM pulsars. Such candidates need to be observed with telescopes operating at higher frequencies. For cases of off-Galactic plane observations, the non detections may be caused due to the pulsar not being beamed towards us or may have some behaviour similar to nulling or intermittent pulsars in which case the observations have to be well-timed to be capturing the pulsar in on-mode to have a successful detection.

Overall, selecting an ideal upper limit of the spectral index that increases the fraction of pulsars detected without any prior bias while minimising the fraction of false detections of background radio sources is essential for success of this criterion. In this paper, we have used a spectral index threshold of -1.2 for selection of sources. By doing so, we were able to detect $\sim$ 90% of the pulsars detected via imaging in all the observations along with an average of $\sim$ 200 new pulsar candidates that are steep spectrum for each observation. Doing similar analysis with a higher threshold, for example, $\alpha = -3$, would result in significantly less candidates but at the expense of detecting fewer known pulsars. Ideally, a threshold that is able to redetect the maximum number of pulsars as well as generate a manageable number of candidates is preferred, hence, our threshold of $\alpha < -1.2$, seems appropriate for the future processing of much larger set of MWA observations.

3.5.2 Criterion 2 - circular polarisation

We also examined the Stokes I and V images to detect candidates that may be circularly polarised. Around 50% of the circularly polarised pulsars in the observation were detected as candidates without any prior knowledge about their polarisation. However, we were not able to detect any potential pulsar candidate with high significance via this method when the fractional polarisation threshold was applied. Compared to total intensity, the number of candidates resulting from the application of this criterion is lower by almost an order of magnitude. Selection of an appropriate threshold for candidates to be considered circularly polarised is beneficial to detect genuine Stoke V polarised sources and pulsar candidates. Moreover, any candidate that is circularly polarised but not a pulsar is likely to be objects of scientific interest. For dipole based instruments such as the MWA, the instrumental leakage, where emission from Stokes I leak into other Stokes parameters has to be better understood. This leakage significantly affects the detection of circularly polarised pulsars and increases the number of

false detections. Even with the improvements in calibration and the model of the primary beam, errors are still be present due to the imperfections of the model and the MWA dipoles itself. In Section 3.4.4 we describe the process of fitting a surface to the fractional polarisation of the sources for the observations, in order to account for the leakage and detect true pulsar candidates. However, further reduction of the leakage will be necessary to reduce the threshold and increase sensitivity of this criterion.

3.5.3 Criterion 3 - Variability

Another aspect of pulsar candidate selection tested is by taking advantage of the variability of the sources in different timescales. This method mainly focuses on detecting pulsar candidates that may be missed by traditional searches due to their nulling behaviour or scintillation. We were able to detect the variable pulsar, PSR J0034 − 0721 in the test observation as a pulsar candidate with high significance. Extracting light curves for every single pixel of the image will result in $\sim$ 1 million candidates, which is a large number of candidates per image to follow up. In order to limit the number of candidates to a few hundreds, we apply a threshold of χ^2 and modulation index as described in Section 3.4.4 by analysing the correlation between χ^2 and modulation index for every timescale we process. Even with those reductions in place, it is still not feasible to follow up on all the candidates with other telescopes. The benefit of leveraging the MWA VCS data means that all of them can be searched using products from the same telescope and observation. The other alternative is to check if these candidates satisfy the other two criteria, and ranking the candidates according to the number of criteria satisfied. This set of candidates ($\sim$ 10) can then be followed up with other telescopes. Unfortunately, we were not able to detect any pulsar-like candidates. One of the reasons for the non-detections could be that the sources are variable on longer timescales than the ones that are chosen for the observations. It may also be that the variable sources are not pulsars

but part of other variable populations such as flare stars. The lack of detection could also be related to the constraints on our periodicity search using PRESTO at MWA frequencies. It should be noted an improved understanding of imaging artifacts produced while imaging with the MWA is required in order to distinguish between true variable sources and sources that appear to be variable but are in fact spurious detections.

3.6 Conclusions and Future Work

Overall, the three methods have been successfully curated and tested on the observations given in Table 3.1. We have a detection efficiency of 50% for both method I (steep spectrum) and II (circular polarisation), while method III (variability) was tested on a small number of test sources all of which were successfully retrieved, after the relevant pulsars for each observation were taken into account. A thorough analysis of the candidates resulting from the application of the above methodologies to the observations was performed. All candidates were searched using MWA beamformed data, however we were not able to detect any pulsar signal. The larger number of initial candidates ($\sim$ 100) were reduced by combining the different methodologies to produce a list of 20 candidates, which can then be followed up with higher frequency telescopes. Care must be taken while combining the criteria as we may be missing interesting sources that may not necessarily satisfy more than one criteria.

Another way to reduce the number of candidates can be optimisation of the thresholds for all the criteria. This is an ongoing project and will be informed by processing a larger number of MWA VCS observations. Overall, it is demonstrated that we were able to detect a large fraction ($> 50\%$) of the pulsars expected to be found as well as a selection of new pulsar candidates for the observations. It is also important to understand the instrumental beam response of the instrument being used as any errors in the beam model will result in leakage. For example, effects such as "beam squint" affect radio telescopes with off-axis

feeds such as the (E)VLA (Uson & Cotton, 2008), and may also be relevant to the future low-frequency telescopes such as SKA-Low. This is useful in informing pulsar search methodologies with the MWA, and suggests that the SKA-Low will be a powerful telescope to find pulsar candidates in continuum images.

These three image-based detection methods outlined here will be applied to ~ 50 MWA observations in an attempt to make the first image-based detection of pulsar with the MWA. The success of this pilot project demonstrates the potential of using image-based methodologies to detect pulsar candidates at low frequencies and improve the efficiency of future pulsar detections with the MWA as well as the SKA-Low.

Chapter 4

Image-based Galactic plane pulsar census

4.1 Introduction

Even though pulsars were discovered by observing their pulsed emission at a very low radio frequency of 81.5 MHz (Hewish et al., 1968), most of the pulsars to date, for the last few decades, have been discovered and studied at frequencies $\gtrsim$ 1 GHz. Especially, the large population of Galactic pulsars still remain relatively unexplored at low frequencies ($\lesssim$500 MHz). The main effects that make pulsar studies at low frequencies more difficult are the frequency-dependant effects such as scattering ($\propto \nu^{-4}$, Bhat et al., 2004), increase in the system temperature due to diffuse Galactic continuum emission ($\propto \nu^{-2.6}$, Lawson et al., 1987) and the spectral turnover of pulsars at low frequencies. Despite these effects, multiple Galactic Plane (GP) surveys have been conducted in an effort to discover new pulsars and study the known Galactic pulsar population (Manchester et al., 2001; Sanidas et al., 2019; Hessels et al., 2008; Bhat et al., 2023a). With the advancements in instrumentation and computing, studying pulsars at low frequencies is once again coming back to the forefront. Recently upgraded or constructed telescopes such as the GMRT (Swarup et al., 1991; Roy et al., 2010), LOFAR (van

Haarlem et al., 2013) and the MWA (Tingay et al., 2013a; Wayth et al., 2018) are contributing to the study of pulsars in the low-frequency regime.

Studying pulsars at low frequencies will help us better understand the physics of pulsar radio emission and the interstellar medium (ISM). Moreover, given that the vast majority of catalogued pulsars lack reliable flux density measurements below 400 MHz, studying more pulsars at low frequencies is needed for better constraints on the modelling of spectral distributions at these frequencies. Studying the radio spectra of pulsars can help in planning surveys of the Galactic pulsar population with the Square Kilometer Array (SKA).

While the time domain search procedures have been successful in detecting a lot of the GP pulsars (Manchester et al., 2001), pulsars such as sub-millisecond period pulsars or highly scattered pulsars are more difficult to detect. High scattering at Galactic latitudes have also affected the detection of many of the Fermi unidentified sources with pulsar-like properties in the GP. Some algorithms that explore a wider parameter space have been developed (for example, acceleration searches Ransom, 2001) but they are computationally expensive for all-sky surveys. Continuum images have been considered an effective way to detect known pulsars and pulsar candidates. These image-based efforts have resulted in discoveries of many interesting sources, for example, PSRs J1431-6328 (Kaplan et al., 2019), J0523-7125 (Wang et al., 2022). The advantage of searching for pulsars in continuum images is that the emission is unaffected by period, scattering or orbital modulation which is beneficial for GP surveys. Such image-based GP surveys are advantageous in detecting known pulsars for the first time at low frequencies, which may have been missed by previous traditional surveys due to scattering being more dominant ($\propto \nu^{-4}$). For instance, the first-millisecond pulsar (MSP) was initially detected as an unusually steep and scintillating continuum source and then confirmed by a targeted pulsar search (Backer et al., 1982). Therefore, similar image-based surveys at low frequencies can be highly effective in overcoming the dispersion and scattering effect that limits the horizon

of detections using periodicity searches at low frequencies.

The study of pulsars at low frequencies can be used to inform pulsar population studies, which play an important role in estimating the yields of future surveys (Xue et al., 2017; Keane, 2018). The MWA is the low-frequency precursor telescope to the SKA. Therefore, pulsar observations in the same observing environment and at the similar frequencies are necessary to prepare for pulsar science with the SKA-Low.

In this chapter, we present the first attempt at using archival MWA Voltage Capture System (MWA VCS) data covering the dense region of the GP to perform an initial low-frequency image-based pulsar census in the Southern Hemisphere.

4.1.1 Science goals and motivation

Several surveys of the Southern sky such as the GLEAM survey covering the entire Southern radio sky at frequencies between 72 and 231 MHz (Wayth et al., 2015) have been done. The drift scan observations of the GLEAM survey were able to reach a sensitivity of 10 mJy/beam, producing a catalogue of radio sources that can be used for further discoveries. The next generation of the GLEAM survey, GLEAM-X (Ross et al, 2023 in prep) is currently ongoing and is expected to reach down to a sensitivity of 1-2 mJy/beam.

These surveys have also been utilised to study the pulsar population. Studies of the low-frequency spectral energy distribution of pulsars using the continuum images from the GLEAM survey were realised for 60 radio pulsars (Murphy et al., 2017). Their analysis provided reliable flux density measurements and helped in improving the spectral modelling of pulsars. Similar studies were performed to explore the variability of pulsars by Bell et al. (2016a) and circular polarisation of pulsars by Lenc et al. (2017). The method of detecting pulsars using the ISM and variance imaging was also investigated by Dai et al. (2016). An initial census of Southern pulsars with the MWA VCS using incoherent beamforming and searching was performed by Xue et al. (2017). This work also resulted in

the first low-frequency detections of 10 pulsars and forecasted that a survey with SKA-Low could potentially detect around 9400 pulsars. The currently ongoing large pulsar survey with the MWA, the Southern-sky MWA Rapid Two-metre (SMART) pulsar survey (Bhat et al., 2023a,b) has detected 4 new pulsars and is expected to detect much more. The SMART survey would also provide a complete census of the known Southern sky population of pulsars (in the time domain) and will be beneficial in informing future pulsar surveys with the SKA-Low.

With the SKA on the horizon, there is an increased need to study and understand the pulsar population. This work is the first attempt to perform an image-based pulsar census of the dense region of the GP using MWA VCS Phase II data. As the detectable pulsar population is solely guided by the known population of pulsars at any given time, therefore it is important to explore all new avenues and refine our knowledge of the known pulsar population. This work contributes to this knowledge by detecting some of the pulsars for the first time at frequencies lower than 300 MHz. More detection of pulsars, especially at low frequencies will be useful to address some of the broader questions surrounding the neutron-star population. This work also explores the new parameter space available to image-based pulsar search strategies and provides insights into the efficacy of such methodologies developed as part of this work.

An underlying goal of this work is to provide better and more reliable flux density measurements leading to improved spectral modelling for pulsars that do not have any low-frequency flux density measurements. Finally, conducting a full Galactic census of pulsars is a high-priority science objective for the SKA (Keane, 2018) and this work will also serve as a reference survey for future deeper image-based surveys at low frequencies such as those planned with the SKA-Low. The initial success of this work is the first step towards the greater goal of detecting new pulsars using low-frequency image-based pulsar searches. As the MWA is the official low-frequency precursor for the SKA-Low, the lesson learned from this work will be useful in informing future SKA-Low image-based pulsar surveys.

This chapter discusses the GP survey using MWA VCS Phase II archival observations and the details of the pulsars detected in this work. It also focuses on the flux densities of these pulsars measured in the Stokes I images and the application of these measurements to improve the spectral energy distribution of pulsars. On the other hand, the new pulsar candidates identified in this survey using methodologies described in Chapter 3 and the efficiency of the criteria to select pulsar candidates are discussed in Chapter 5.

4.2 Observations and data processing

This work uses 12 MWA VCS Phase II observations as shown in Figure 4.1. Their duration ranges between 30 minutes to 90 minutes with a central frequency of 184 MHz. The details of the observations are given in Table 4.1 and are marked from A to L. The total amount of data processed as part of this work is $\sim$ 450 TB and corresponds to 6000 deg^2 of the sky. These observations are used to form full Stokes images using the procedure described in Section 4.2.1, which leads to the detection of known pulsars and identification of new pulsar candidates. The mean RMS reached for the Stokes I images of the 12 observations ranges between $\sim$ 5 mJy/beam and 8 mJy/beam.

The same data is also used to confirm image detections of known pulsars and follow up the candidates by beamforming the original VCS data and searching for pulsations. Using the Pawsey supercomputing systems (mainly the Garrawarla supercomputer dedicated to processing MWA data), processing an hour of observation to produce full Stokes images takes about 12 hours. Forming a beam and searching for pulsations using the same one-hour data, for a single pointing (single source) takes about 5 hours. This demonstrates the large volume of data captured by VCS and the large amount of time and resources required to process all the observations.

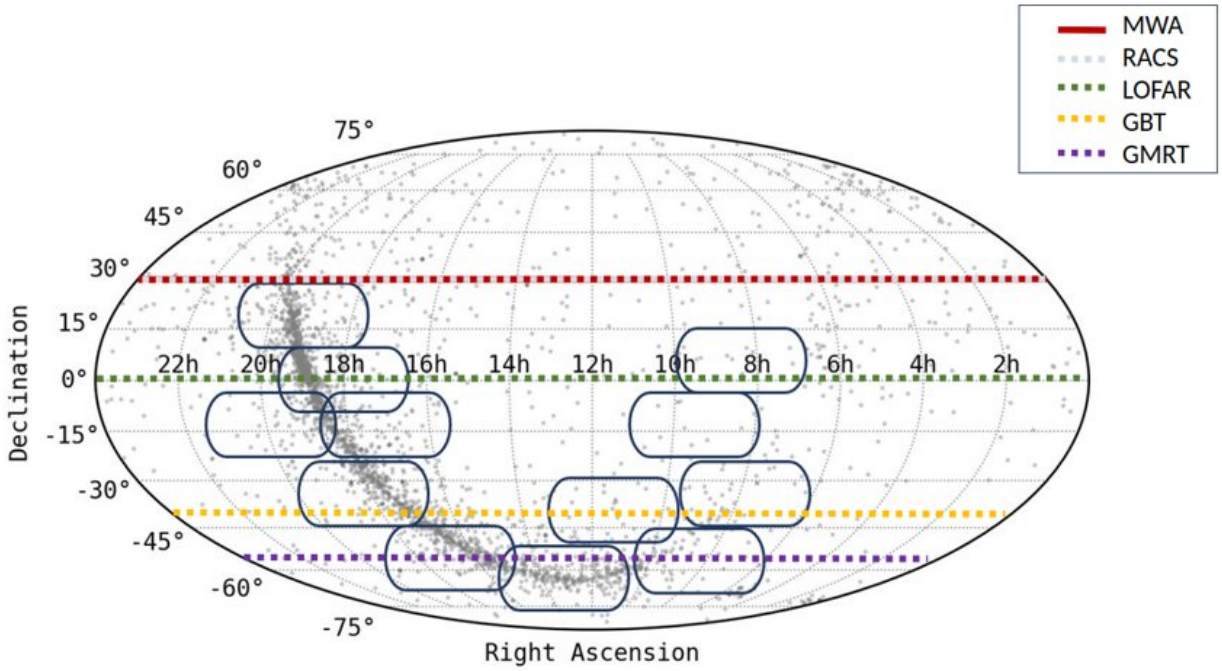

Figure 4.1: The MWA VCS observations processed as part of this work are shown in blue and the details of the observations can be found in Table 4.1. The grey points indicate the known pulsars recorded in the ATNF catalogue (Manchester et al., 2005). The red bold line is the part of the sky available to the MWA and the dotted green, yellow and purple line shows the sky that is visible to LOFAR, GBT and GMRT respectively.

4.2.1 Imaging

The raw voltages from the MWA antennas are processed by the xGPU software correlator (Ord et al., 2015) to produce visibilities with a temporal resolution of 1 second. The resulting data are then fed through COTTER (Offringa et al., 2015), which converts them into the CASA measurement set format and applies calibration, and flags channels affected by radio-frequency interference (RFI) using the AOFlagger software (Offringa et al., 2012a). Calibration solutions are obtained from the MWA All-Sky Virtual Observatory (MWA ASVO; Sokolowski et al., 2020). Images in instrumental polarisation are created using WSCLEAN

Obs Name	OBSID	Duration (s)	Mean RMS (mJy/beam)	N_{src}	N_{psr}	N_{3db}
A	1286617815	1800	8	1094	4	23
B	1284634952	5400	5	9490	7	78
C	1285498952	5400	5	9459	7	86
D	1275758864	5400	6	4296	6	102
E	1206977296	3600	6	4126	6	110
F	1200918320	3600	5	5388	8	123
G	1244457047	5400	5	9453	12	150
H	1195038136	3600	6	1002	7	130
I	1206201016	3600	5	1035	8	92
J	1287796112	1800	5	1028	6	54
K	1240826896	3600	5	3626	9	41
L	1239460849	1800	8	968	3	11

Table 4.1: The details of the 12 observations processed as part of this work, duration, mean RMS achieved for the Stokes I image. The survey covered the dense region of the Galactic plane with declination south of $< 30°$ and right ascension range >7h and <21h. It also shows the number of pulsar detections (column N_{psr}), the total number of pulsars in the 3dB (half power point) beam (column N_{3db}) and the total number of sources (column N_{src}) extracted using AEGEAN for each Stokes I image before the application of any criteria is also shown in the table.

(Offringa et al., 2014b) with a Briggs weighting of -1 and then transformed into Stokes I, Q, U, and V images using the MWA's "fully" embedded element beam model (Sokolowski et al., 2017). The images are 8192×8192 pixels with pixel size of 0.2 arcmin, corresponding to $\sim 35° \times 35°$ images. The individual 1-second images are averaged to produce mean full Stokes images, which are subsequently used for further analysis. The details of the processing pipeline can be found in Chapter 3. An example of on and off GP Stokes I image is shown in Figure 4.2 and 4.3 respectively. The pulsars present detected in the cutout of the images are shown in white circles. The Stokes I images from the other observations are shown in A.2. Figure 4.4 shows the cutout of Stokes V images for the pulsars detected in Stokes V images from this work.

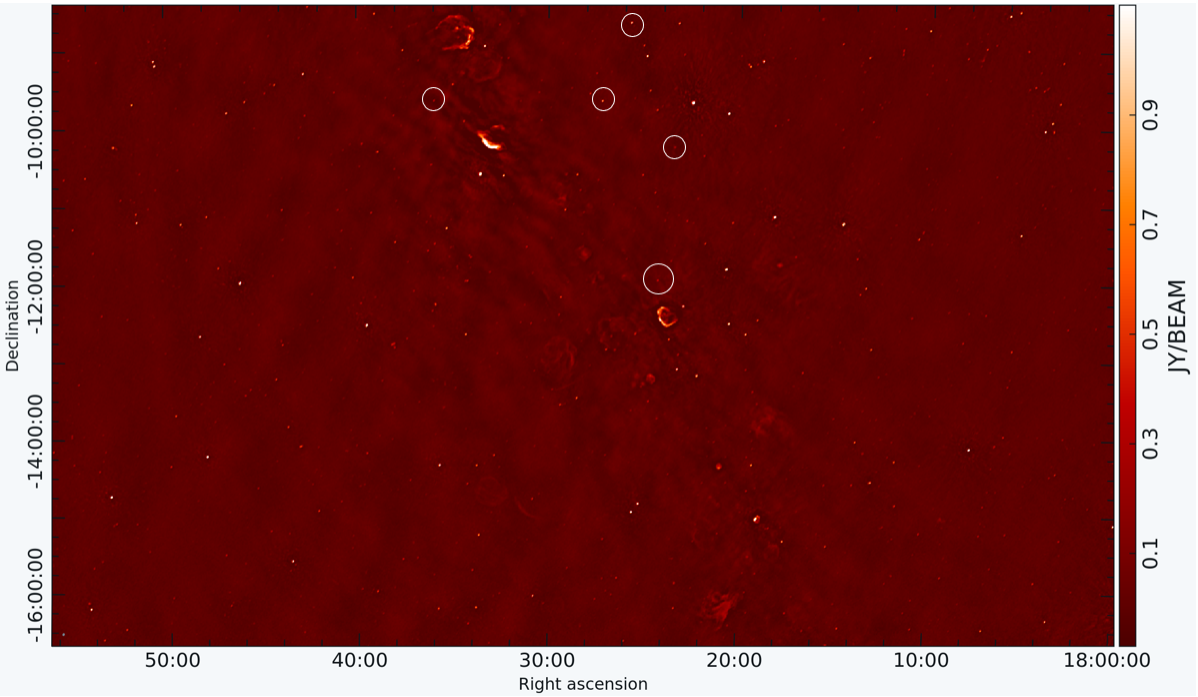

Figure 4.2: Stokes I image cutout of the on Galactic Plane observation. The pulsars detected in this part of the sky are circled in white. The mean RMS for the image is 5 mJy/beam. The Galactic supernova remnants can be seen in the middle of the image. Every single dot in the image corresponds to a source, the information of which is extracted using source extraction software, AEGEAN. The RMS of the image increases as we go closer to the Galactic Plane or at the image edges due to high confusion noise and lower sensitivity respectively.

The source finding software, AEGEAN (Hancock et al., 2012, 2018), was used to detect and extract radio sources from the mean Stokes I and V images. A catalogue of sources that exceeded a 5σ threshold was created and analysed to generate a list of potential pulsar candidates. The pulsar candidates were chosen based on three criteria, namely, steep spectrum, circular polarisation and variability.

4.2.2 Pulsar spectra fitting software - pulsar_spectra

Measurements of flux densities are important for detailed spectral analysis and furthering our understanding of pulsar radio luminosities. A recent version of the ATNF pulsar catalogue shows that the pulsar flux densities are well studied

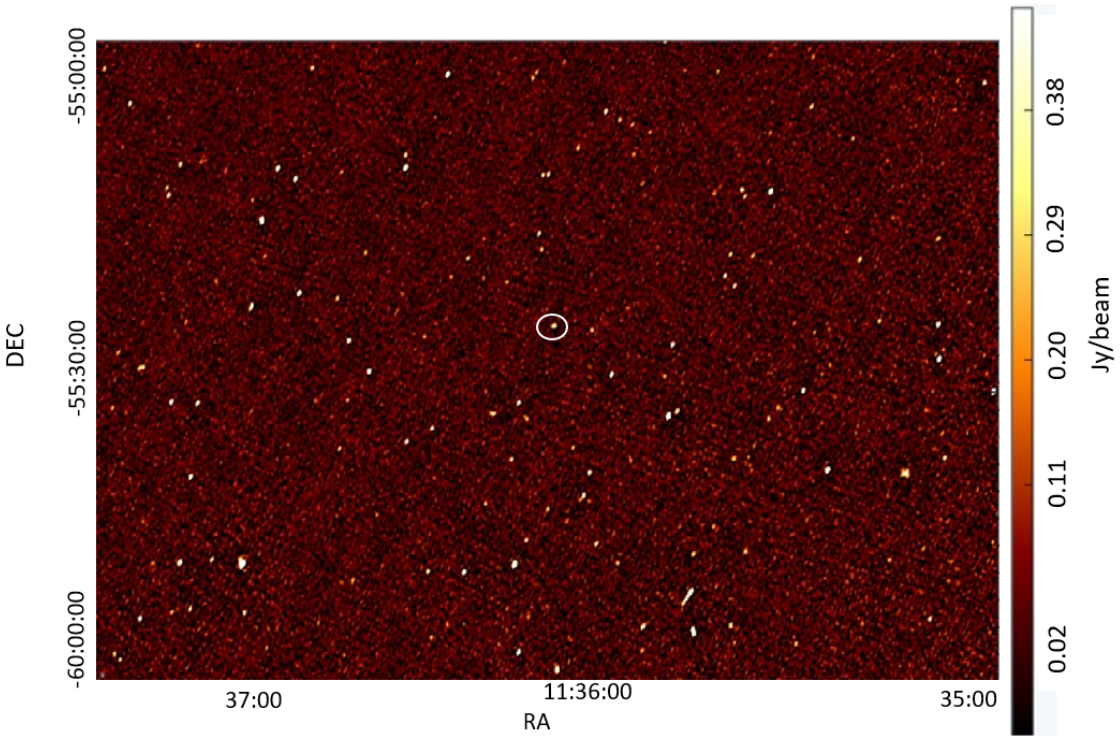

Figure 4.3: Stokes I image cutout of the off Galactic Plane observation. The mean RMS for the image is 6 mJy/beam. As the Galactic Plane is not in the image, the RMS of noise is much lower due to significantly lower confusion noise. The number of sources in the off-GP image is lower, which makes the source finding and processing easier and faster. The pulsar in the field is circled in white. As this is an off-GP field the number density of pulsars is less compared to an on-GP field.

between 400 MHz to 1.4 GHz as most of the pulsars were discovered at those frequencies. However, they are not studied as extensively at frequencies $\leq$400 MHz. The main reason for this is because obtaining accurate flux density measurements is challenging as pulsars tend to scintillate due to the interstellar medium leading to fluctuations in flux density from a factor of two to an order of magnitude. This effect is more dominant at low frequencies and is dependent on their Galactic latitude and instrumental parameters of the telescope such as observing bandwidth and integration time. The other factor that makes it hard to obtain reliable spectral models is that the currently catalogued data were taken with different instrumental backends and different systematic errors. Even though many accurate flux density measurements have been taken over the last several decades,

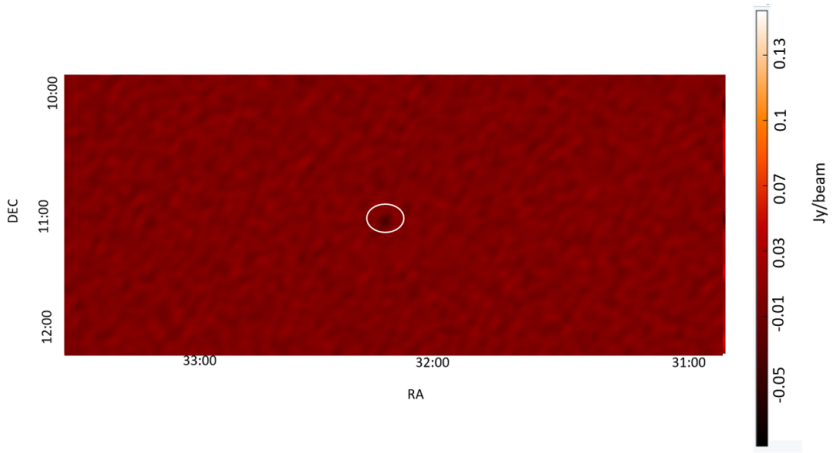

(a) PSR J1932+1059

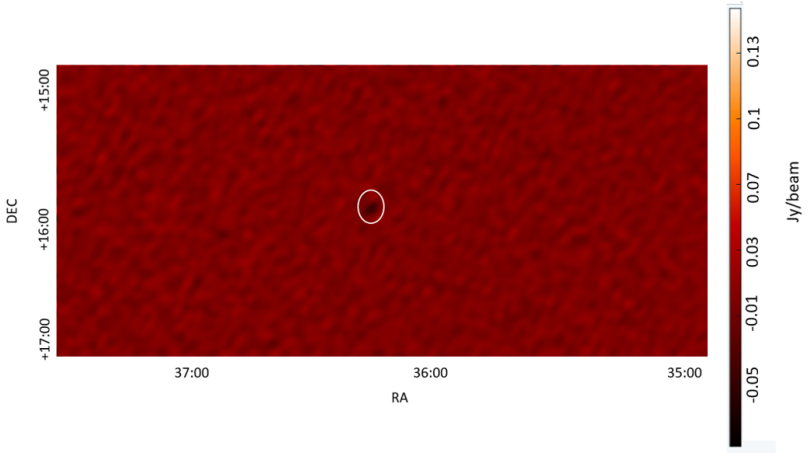

(b) PSR J1136+1551

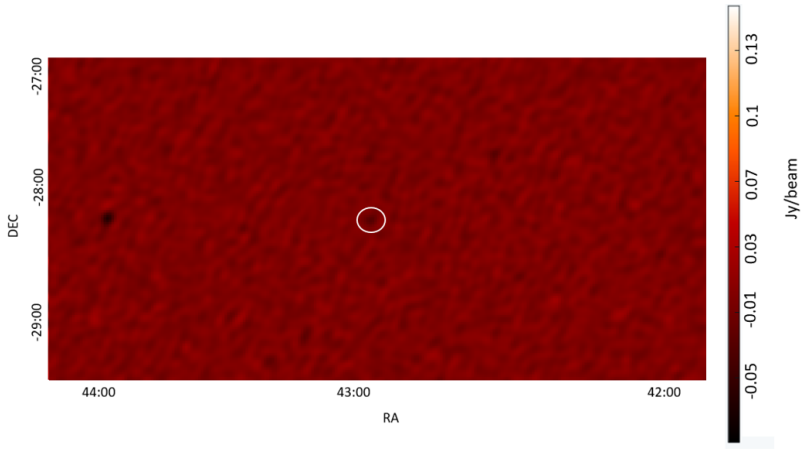

(c) PSR J0742-2822

Figure 4.4: Stokes V cutout for the pulsars that show a negative sign for Stokes V detection. The corresponding Stokes V flux density is given in Table 4.2.

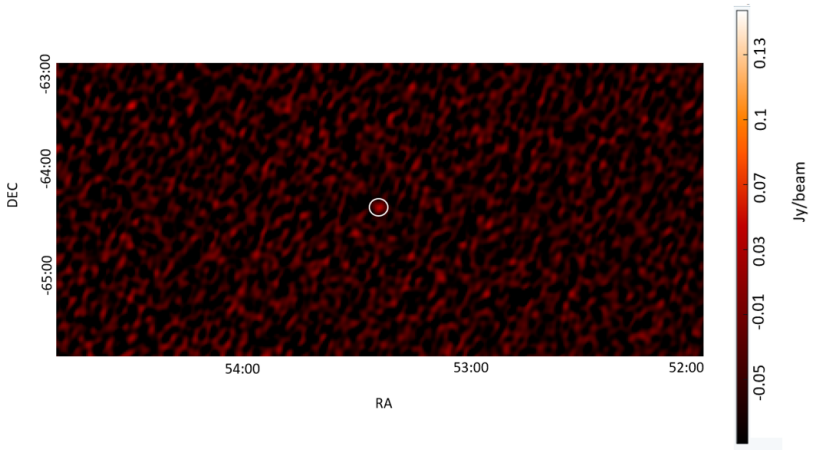

(d) PSR J1453-6413

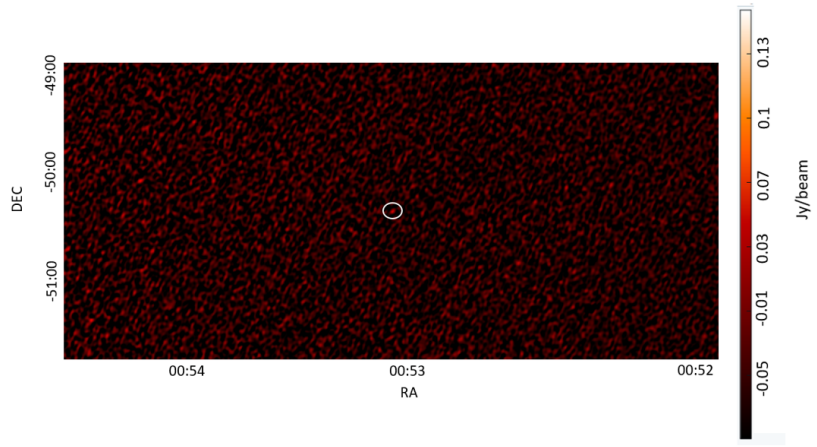

(e) PSR J1600-5044

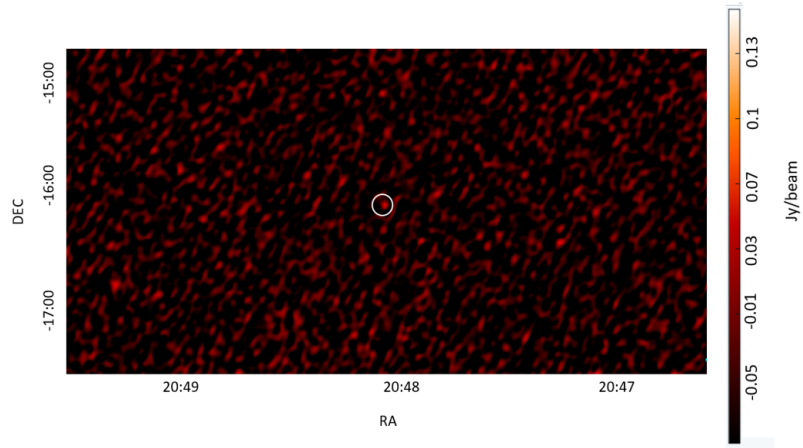

(f) PSR J2048-1616

Figure 4.4: Stokes V cutout for the pulsars that show a positive sign for Stokes V detection. The corresponding flux density for the Stokes I detection is given in Table 4.2 and 4.3.

there is no catalogue that records all this information. Furthermore, there is no theoretical model for the spectra of the pulsars and no single model that can accurately fit the wide variety of pulsars' spectra.

Jankowski et al. (2018) studied the spectral properties of 441 pulsars observed with the Parkes radio telescope at centre frequencies of 728, 1382 and 3100 MHz, providing a systematic and uniform sample of pulsar flux densities. The data was then combined with spectral data from the literature to derive the spectral properties of the pulsars and fit different spectral models to the combined data in a robust manner. The spectra of the pulsars needed to have at least four flux density measurements at four different frequencies to ensure sufficient spectral coverage and better constraints of the spectral fits. The Akaike information criterion (AIC) was used to decide on the best-fit model. AIC measures the amount of information about the data retained by the model without over-fitting. The model that results in the lowest AIC was selected as the best-fitting model.

Based on the method described in Jankowski et al. (2018), a spectral fitting software, **pulsar_spectra** was developed by Swainston et al. (2022b). The **pulsar_spectra** software contains an open-source catalogue of flux density measurements from several publications and uses this information to fit the best spectral model for a given pulsar. The **pulsar_spectra** software also reduces the effect of underestimated uncertainties on outlier points and prevents the skewing of the model fit by using the Huber loss function defined as:

$$H(T) = \begin{cases} \frac{1}{2}t^2 \text{ if } |t| < k \\ k\,|t| - \frac{1}{2}k^2 \text{ if } |t| \geq k \end{cases} \tag{4.1}$$

where t is the residual (i.e. the difference between the model and the measurement) and k is the threshold that defines the points that are considered as outliers (Huber, 1964).

Currently, the software can incorporate five different spectral models based on the work done by Jankowski et al. (2018). The five spectral models used in

pulsar_spectra are described in detail in Section 1.2.5. The software is written in Python and can be easily installed. It has multiple features such as fitting a spectral model to existing literature for given pulsars, estimating the flux density for a pulsar at a desired frequency and adding more spectral models to the repository. Even though this is a relatively new software, it has already been applied to other analyses. One such spectral analysis was done by Lee et al. (2022) for 22 radio pulsars using SKA-Low precursor stations. 21 out of the 22 pulsars showed a change in the spectral fit after the addition of the new low-frequency flux density measurements. A more extensive analysis using 893 radio pulsars is being undertaken by Swainston et al, 2023 (in prep).

This work uses the feature of **pulsar_spectra**, which enables us to include the flux density measurements from this work and compare the spectral fits before and after the addition. The flux density measurements from this work are more reliable as it is a direct measurement of the continuum radio flux density for the pulsars taken from the Stokes I image. However, we do have to take into account that the flux densities from the Stokes I images may be overestimated due to the blending of sources and hence introduce errors to the measurements. Figure 4.13 shows the comparison of the flux densities from this work to the literature and demonstrates that the flux densities from this work match well within the error limits of the flux densities in the literature. These low-frequency, reliable flux density measurements will be useful in filling up the gap in the measurements at the lower end of the frequency. Our study illustrates the meaningful utilization of image-based pulsar surveys conducted using the Murchison Widefield Array (MWA) for valuable scientific measurements and analysis of pulsar radio spectra. These insights serve as crucial inputs for informing both pulsar surveys and scientific endeavours planned with the Square Kilometer Array Low-Frequency (SKA-Low) telescope. The details of the results from this analysis are given in Section 4.3.4.

4.3 Results and discussion

4.3.1 Detection of known pulsars

Our image-based survey is generally expected to detect pulsars with high flux density irrespective of the DM of the pulsars. For MWA frequencies, the sensitivity for periodic searches significantly reduces above a DM of 250 pc cm^{-3}, without any compromise on the flux density sensitivity limit for the pulsar detections. In a simplified view, image-based and periodic searches, both, cover a unique area in the DM-flux space that can only be probed by one of them, while also overlapping in the bright and low DM pulsar regime, where both searches are effective. However, it depends on a combination of pulsar period and DM which is shown in Figure 4.7.

The Australian Telescope National Facility (ATNF) pulsar catalogue (v1.70 [1]; Manchester et al., 2005) comprises of about 3000 pulsars detected to date. Of the total population, 1000 pulsars are present in the 3dB (half power point) for the 12 observations processed for this work. Taking the local σ for the pulsar positions from Stokes I images and applying a flux density threshold of 25 mJy/beam (corresponding to 5σ detection for mean noise of 5 mJy/beam for Stokes I images), we evaluate that 85% (850) of the pulsars are below our detection threshold. As our work is focused on the dense region of the Galactic Plane, we also have to account for the pulsars that are present in supernova remnants (SNRs) which amounts to 4% (40) of the pulsars, leaving 11% (110) of the population which can be detected in image domain with the MWA Phase II sensitivity. Out of the 110 expected pulsar detections we were able to detect 66 pulsars in image-domain i.e. 60% of the expected number of detections. The non-detections can be either due to spectral turnover of the pulsars at low frequencies (Jankowski et al., 2018) which leads to reduced flux density. The other possible reason can be that the pulsars are in regions of diffused emission such as in pulsar wind

[1] https://www.atnf.csiro.au/research/pulsar/psrcat/

nebulae (PWN) or in SNRs that are not accounted for and may be excluded as extended sources (compactness criteria in Chapter 3). Apart from detections of the pulsars in the image domain, time-domain beamformed searches resulted in 17 more pulsar detections. The total number of pulsar detections in this survey is 83 shown in Figure 4.5, including 3 MSPs and 4 binary pulsars. In Figure 4.5, purple dots are the pulsars detected by both image-domain and time-domain searches, yellow dots are pulsars detected only in images and orange dots are the pulsars that are detected via periodic searches. For 14 pulsars, these are also the first low-frequency ($\leq$400 MHz) detections (shown in Table 2.3), and our flux density measurements can be helpful in more accurate spectral modelling of the pulsars. Some of the detections are discussed in detail in Section 4.3.2.

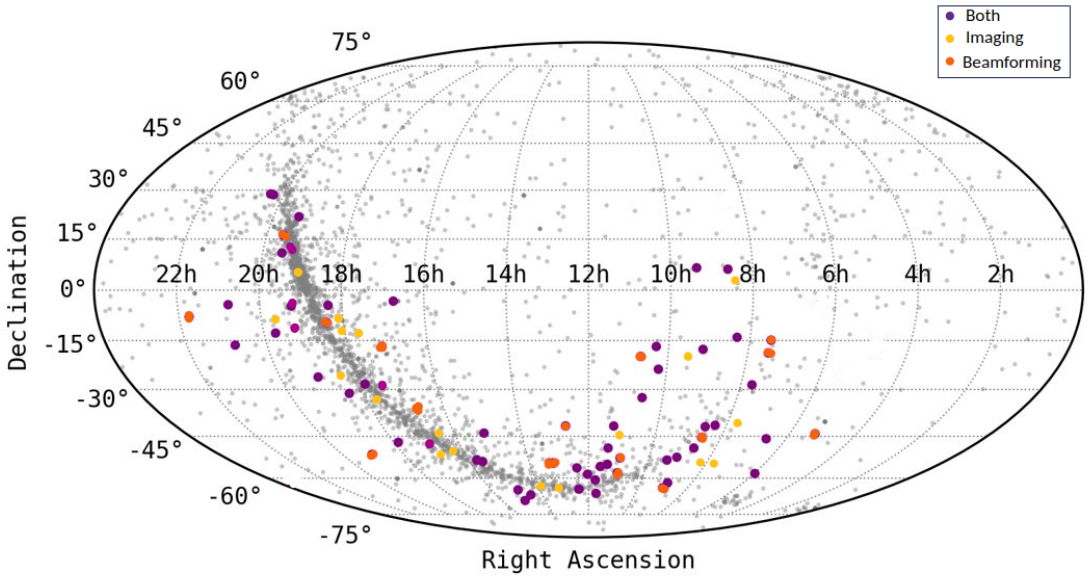

Figure 4.5: Distribution of known pulsars with colour dots showing pulsars detected in this work. Grey-filled circles are the all-sky distribution of known pulsars in the ATNF pulsar catalogue (Manchester et al., 2005). The purple-filled circles denote the pulsars that are detected by both periodicity searches and imaging. The yellow-filled circles are the pulsars that are detected only in imaging and the orange-filled circles are the pulsars detected only in periodicity searches.

PSRJ	Period (s)	DM ($pccm^{-3}$)	S_I (mJy)	S_{lit} (mJy)	Reference	α	S_V (mJy)
J0737-3039A	0.022	48.916	52±10	53±8	M	-1.86	
J0742-2822	0.166	73.728	154±33.6	168±8	X	-2	-15
J0820-1350	1.23	40.938	155±31	160±7	M	-2.2	
J0820-4114	0.5454	113.4	112 ±22	116±16	M	-1.8	
J0835-4510	0.089	67.721	997 ±199	1050±16	K	-0.9	
J0837+0610	1.273	12.864	300 ±55	286±13	M	-2.7	
J0837-4135	0.751	147.2	109 ±21	95±16	M	-1.64	
J0856-6137	0.96	95	85 ±17	85±9	M	-2.7	
J0907-5157	0.253	103.72	100 ±20	106±11	M	-0.5	
J0908-1739	0.401	15.879	54 ±10	62±6	K	-1.5	
J0922+0638	0.43	27.2986	117 ±21	100±13	M	-1.8	
J0924-5302	0.746	152.9	88 ±17	96±9	M	-2.16	
J1041-1942	1.386	33.777	60 ±12	49±7	S	-2	
J1057-5226	0.197	29.69	187 ±35	202±12	M	-0.95	
J1059-5742	1.18	108.7	39 ±7	49±10	S	-3.3	
J1116-4122	0.943	40.53	51 ±11	52±7	M	-1.2	
J1121-5444	0.535	204.7	92 ±17	101±15	M	-2.2	
J1136+1551	1.187	4.84	650 ±120	684±61	M	-1.1	-51
J1136-5525	0.364	85.111	30 ±6	34±6	S	-1.2	
J1141-6545	0.393	116.08	94 ±18	78±12	X	-2.7	
J1202-5820	0.452	145.41	73 ±14	88±11	S	-1.8	
J1224-6407	0.2164	97.686	80 ±16	89±9	S	-1.36	
J1312-5402	0.728	133	26 ±5	26±	S	-2.49	
J1430-6623	0.785	65.102	110 ±22	190±28	M	-0.8	
J1453-6413	0.179	71.248	629 ±120	684±23	M	-1.5	27
J1456-6843	0.263	8.613	657 ±130	738±21	M	-1.1	

Continued on next page

PSRJ	Period (s)	DM ($pccm^{-3}$)	S_I (mJy)	S_{lit} (mJy)	Reference	α	S_V (mJy)
J1507-4352	0.286	48.7	347 ±68	384±27	X	-2.1	
J1534-5334	1.36	24.82	726 ±145	705±22	X	-0.3	
J1544-5308	0.178	35.16	80 ±16	102±15	X	-1.71	
J1607-0032	0.421	10.6823	145 ±29	137±15	M	-1.9	
J1645-0317	0.387	35.7555	752 ±150	774±18	M	-2.6	
J1709-1640	0.653	24.891	102 ±20	271±18	X	-2	
J1731-4744	0.829	123.056	219 ±43	424±8	X	-0.8	
J1751-4657	0.742	20.4	187 ±37	411±10	X	-1.6	
J1752-2806	0.5625	50.372	2450 ± 40	2441±28	X	-1.7	
J1820-0427	0.598	84.435	386 ± 77	1035±120	X	-2.45	
J1823-3106	0.284	50.245	126 ± 25	105±15	X	-1.8	
J1825-0935	0.769	19.3833	106 ±21	612±40	X	-1.1	
J1900-2600	0.6122	37.994	262 ± 52	393±11	X	-1.21	
J1902-5105	0.0017	36.2505	95 ± 19	362±55	X	-3.12	
J1913-0440	0.825	89.385	120 ± 24	169±22	X	-2.6	
J1921+2153	1.33	12.443	2010 ± 100	2112±49	X	-1.9	
J1932+1059	0.226	3.18	450 ± 90	362±15	X	-1.7	-43
J1935+1616	0.358	158.521	200 ±40	106±9	X	-1.4	
J1943-1237	0.972	28.918	97 ±19	68±8	X	-2.4	
J2018+2839	0.557	14.1977	185 ±37	561±41	X	-2.3	
J2022+2854	0.343	24.63109	45 ± 9	323±48	X	-0.4	
J2046-0421	1.54	35.799	53 ±10	34±7	X	-1.7	
J2048-1616	1.961	11.456	102 ± 20	77±5	X	-1.7	16
J2145-0750	0.016	9.0008	295 ± 54	282±20	X	-1.94	

Continued on next page

PSRJ	Period (s)	DM ($pccm^{-3}$)	S_I (mJy)	S_{lit} (mJy)	Reference	α	S_V (mJy)

Table 4.2: This table shows the known pulsars detected in the GP survey in both imaging and beamforming searches. S_I is the mean flux density of the pulsars in Stokes I image from this work, S_V is the Stokes V for the pulsars that were detected in Stokes V image in this work and S_{lit} is the low-frequency flux density available in the literature: 'M' stands for MWA-image detection by Murphy et al. (2017), 'X' stands for MWA-incoherent beam detection by Xue et al. (2017), 'S' stands for MWA SMART survey detections by Bhat et al. (2023b) and 'K' stands for LOFAR detection by Kondratiev et al. (2016). α is the spectral index of the pulsars. α is calculated using the flux densities of the pulsars in MWA Stokes I image (154 MHz) and the RACS Stokes I image (888 MHz).

PSR Name	Period (s)	DM (pc cm^{-3})	S_I (mJy)	α	S_V (mJy)
J1231-6303	1.35	301	39 ± 8	-2	
J1527-5552	1.04	370.06	36 ± 7	-1.7	
J1600-5044	0.192	262.791	163 ± 27	-1.19	20
J1614-5048	0.231	582.4	145 ± 21	-2.16	
J1623-4256	0.36	295	45 ± 10	-2.35	
J1639-4604	0.264	258.91	89 ± 16	-2.4	
J1644-4559	0.455	478.66	227 ± 41	-2.9	
J1807-2715	0.827	312.98	28 ± 5	-3	
J1823-1115	0.279	428.59	65 ± 11	-1.52	
J1827-0958	0.245	430	28 ± 4	-2.56	
J1832-0827	0.64	300.869	66 ± 12	-0.8	
J1833-0559	0.483	346.7	53 ± 10	-1.44	
J1836-1008	0.562	316.98	81 ± 14	-2.98	
J1903+0135	0.729	245.167	60 ± 10	-2	
J1751-2737	0.00223	260	77 ± 15	-1.7	
J1748-3009	0.009	420.2	27 ± 5	-1.3	

Table 4.3: The known pulsars detected in the GP survey in only Stokes I images. The mean flux density of the pulsars from the Stokes I image from this work is denoted by S_I and the flux density from the Stokes V image is denoted by S_V. α refers to the spectral index of the pulsars. Only two of the pulsars, PSRs J1614-5048 and J1644-4559 have a previously recorded flux density below 300 MHz by Frail et al. (2016). For the 14 remaining pulsars, this is the first low-frequency detections below 300 MHz.

PSR Name	Period (s)	DM ($pccm^{-3}$)	S_{400} (mJy)	S_{1400} (mJy)	Spectral index
J0514-4408	0.32	15.122	-	-	-
J0600-5756	2.26	30	2.1	-	-
J0636-4549	1.98	26.31	-	0.1	-
J0729-1448	0.25	91.89	-	0.83	-1.7
J0729-1836	0.51	61.293	11.2	1.9	-1.7
J0842-4851	0.644	196.85	6.2	1.07	-1.78
J0902-6325	0.66	72.72	4.5	1.7	-
J1012-2337	2.51	22.51	4.1	0.135	-2.66
J1018-1642	1.804	48.82	5.1	0.7	-2
J1034-3224	1.15	50.75	41	8	-1.6
J1123-4844	0.244	92.915	8	1	-1.4
J1146-6030	0.273	111.68	17	3.2	-1.6
J1225-5556	1.018	125.835	5	0.3	-
J1240-4124	0.512	44.1	3.5	0.6	-
J1312-5402	0.728	133	15	0.78	-2.49
J1320-5359	0.279	97.1	18	2.1	-1.7
J2324-6054	2.34	14	4	1	-

Table 4.4: The known pulsars detected in the GP survey in only beamformed searches. It shows the names and parameters of the pulsars. Detailed analysis of these pulsars can be found in Xue et al. (2017) and Bhat et al. (2023b). As this work is mainly focused on the imaging aspect of pulsar searching, these pulsars are not included as part of the analysis done for this work.

If we plot the pulsars detected on the DM-flux density plane as shown in

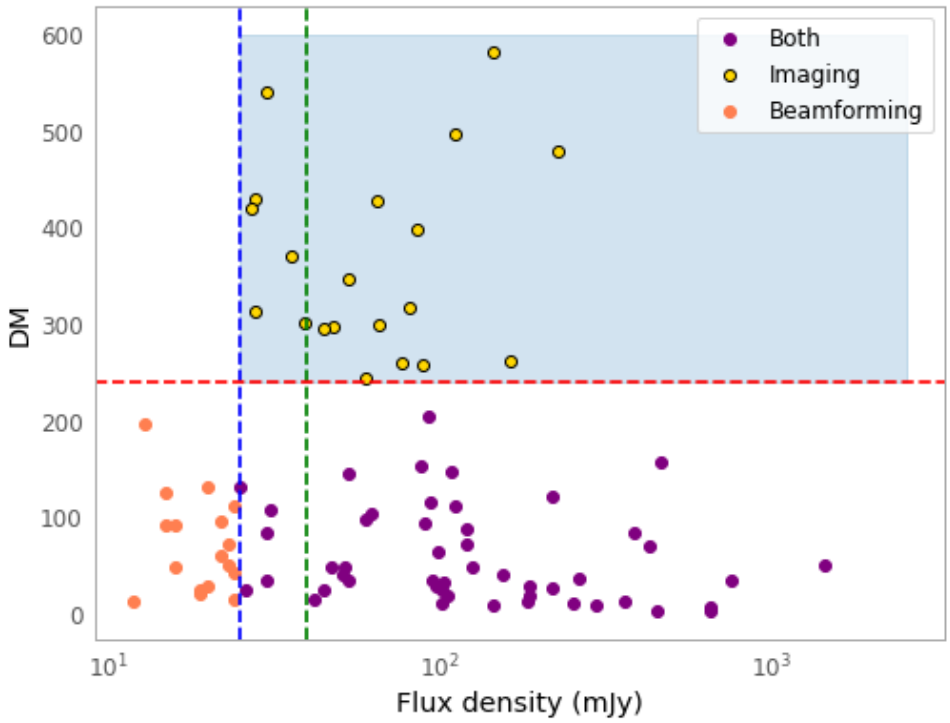

Figure 4.6: Known pulsars detected in this survey are shown in the DM-flux density plane. The purple-filled circles denote the pulsars that are detected by both periodicity searches and imaging. The yellow-filled circles are the pulsars that are detected only in imaging and the orange-filled circles are the pulsars detected only in periodicity searches. The blue and green dashed line indicates the mean flux density threshold for a 5σ detection of pulsars in Stokes image of mean RMS of 5 mJy/beam and 8 mJy/beam respectively. The two thresholds are taken based on the range of mean RMS of the Stokes I image from the observations. The red dashed line indicates the DM threshold beyond which periodicity searches become less sensitive due to the scattering and DM smearing of the pulses at low frequencies. The blue-shaded region is the parameter space that is exclusively available to image-based searches.

Figure 4.6, it is clearly visible that the different search methods are optimal in different parts of parameter space, and they overlap in the region of bright and low-DM pulsars. The purple dots denote the pulsars that are detected in both periodicity as well as imaging and as listed in Table 4.2. These are mainly bright, low DM pulsars which have the highest overlap between the two search methods. The yellow dots denote the pulsars that are detected only in Stokes I images as

listed in Table 4.3. These pulsars are mainly the high DM pulsars which are harder to detect via periodicity searches at low frequencies. The orange dots are the pulsars that are detected only in beamformed searches, the details of which are given in Table 4.4. These pulsars are faint and hence are below the detection threshold of Stokes images. The blue-shaded region is the parameter space that is exclusively available to image-based searches. Image-based searches, therefore, can be useful in detecting high DM or highly scattered pulsars that may be missed by periodic searches at low frequencies but they are sensitive primarily to very bright sources.

As the mean RMS for the observations ranges from 5 mJy/beam to 8 mJy/beam, the blue and green dashed line in Figure 4.6, indicates a flux density threshold of 25 mJy/beam and 40 mJy/beam for the sensitivity of image-domain searches for a 5σ detection of pulsars.

Obtaining a threshold for DM for periodicity searches is much more complicated as a DM cutoff is a complex relation between pulse broadening, frequency and period of the pulsar. Under the assumption of a pure Kolmogorov electron density spectrum (Armstrong et al., 1995a), a non-linear function between scattering timescale, DM and frequency is given as $\tau_d \propto DM^{-2.2}\nu^{-4.4}$. This affects pulsar searches at low frequencies, especially when the pulse broadening time is longer than the pulsar's spin period, leading to a loss in sensitivity of periodicity searches. Figure 4.7 shows the significant effect of pulse broadening (i.e. smearing due to scattering) at larger DMs for the MWA SMART survey (Bhat et al., 2023a). This is applicable to our work as we are using the same instrumental and processing parameters and observing frequency. The scatter broadening is also dependent on the line-of-sight and is larger in the Galactic Plane compared to off-Galactic Plane latitudes. Given that this work is focused on the Galactic Plane, pulse broadening needs to be taken into account when determining the DM cutoff. As shown in Figure 4.7, the pulse broadening is higher at larger DMs. At higher DMs, the pulse broadening times are $\gtrsim$300 ms for a line of sight towards

the Galactic Centre region at $|b| \lesssim 5°$, $l \gtrsim 330°$ or $l \lesssim 30°$, where one would expect such high DMs. Furthermore, DM smearing is also significant at low frequencies (154 MHz) and is ~ 10 ms at DM of ~ 250 pc cm^{-3} (Bhat et al., 2023a). Therefore, taking these effects into account we consider a virtual DM threshold of 250 pc cm^{-3} beyond which DM smearing and pulse broadening greatly affect the sensitivity of the search. This DM threshold is shown as a red dashed line in Figure 4.6.

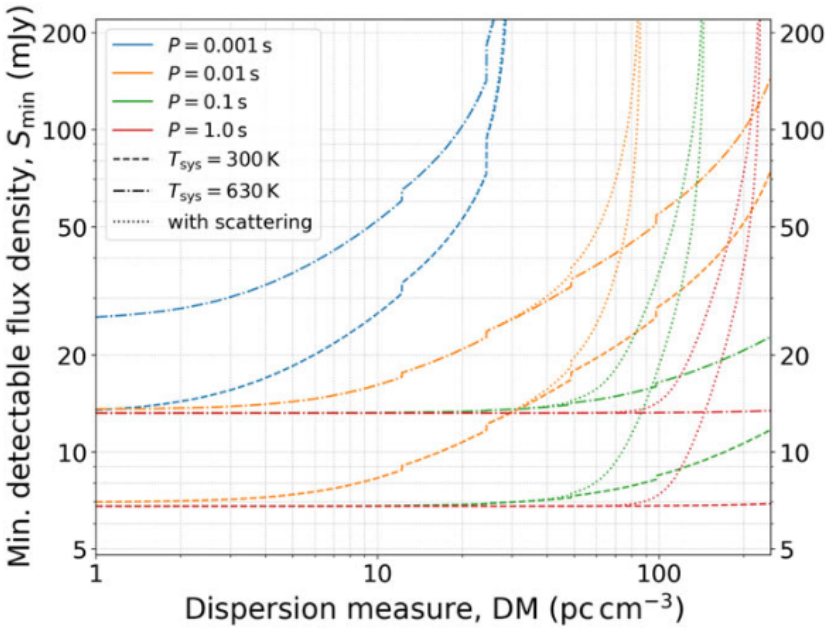

Figure 4.7: Minimum detectable flux density as a function of DM for the MWA SMART survey (Bhat et al., 2023a). The same can be applied to this work due to similar observational and processing parameters. This shows the sensitivity limits for 10-min integration time for different pulse periods, for two different T_{sys} (one for regions away from the Galactic Plane and the other for the mean in the plane excluding regions of Galactic Centre. The effect of pulse broadening is shown in the dotted lines (Bhat et al., 2004). The minimum pulsar flux density required for detection rapidly increases for pulsars beyond a DM of 250 $pc\ cm^{-3}$ due to the significant effect of pulse broadening, making it harder to detect such pulsars in periodicity searches.

The 66 pulsars detected in the image domain can be used to test the efficiency of the criteria described in Chapter 3 that are used to select the pulsar candidates. The efficiency of the criteria is determined based on the pulsar detections via each

criteria and is described in detail in Section 5.4.2 in Chapter 5.

4.3.2 Pulsar detections - Imaging vs. Beamforming

As mentioned earlier, both search methods are sensitive to certain areas of the DM-flux parameter space. Given that the total number of pulsar detections in this survey is 83, Figure 4.8 shows the percentages of the detections with the two search methods. It shows that more than half of the pulsar detections were by both the search methods and image-based searches seems to perform as well as beamformed searches for the Galactic Plane observations processed as part of this work.

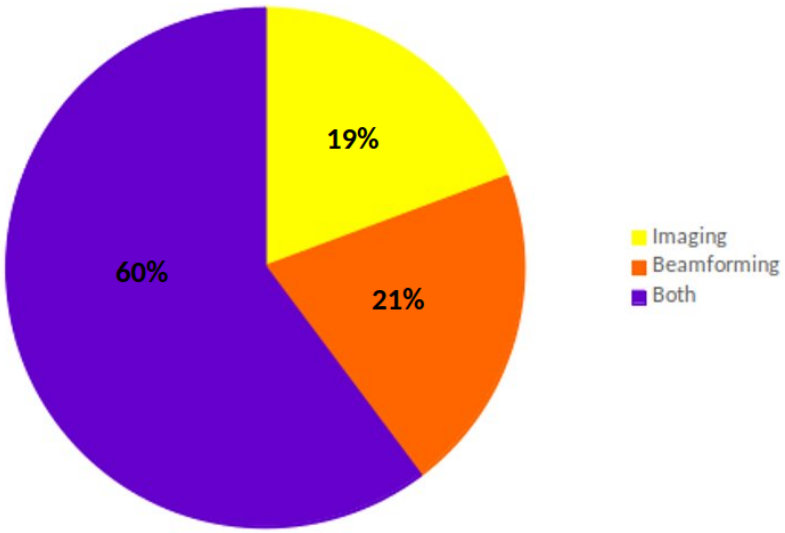

Figure 4.8: Percentages of the detections with the two search methods. 60% of pulsars were detected by both methods, while imaging is seen to perform as well as beamforming for the Galactic Plane observations.

60% of the total pulsar detections were done by both image-based as well as beamformed searches. An example of the detection of PSR J1141-6545 in both imaging and beamformed searches is shown in Figure 4.9. It is seen as a 75 mJy (13 σ) source in imaging and a 12σ PRESTO detection. The detection significance in both methods is comparable denoting that pulsars above our imag-

ing sensitivity are successfully detected at similar significance with beamformed detections.

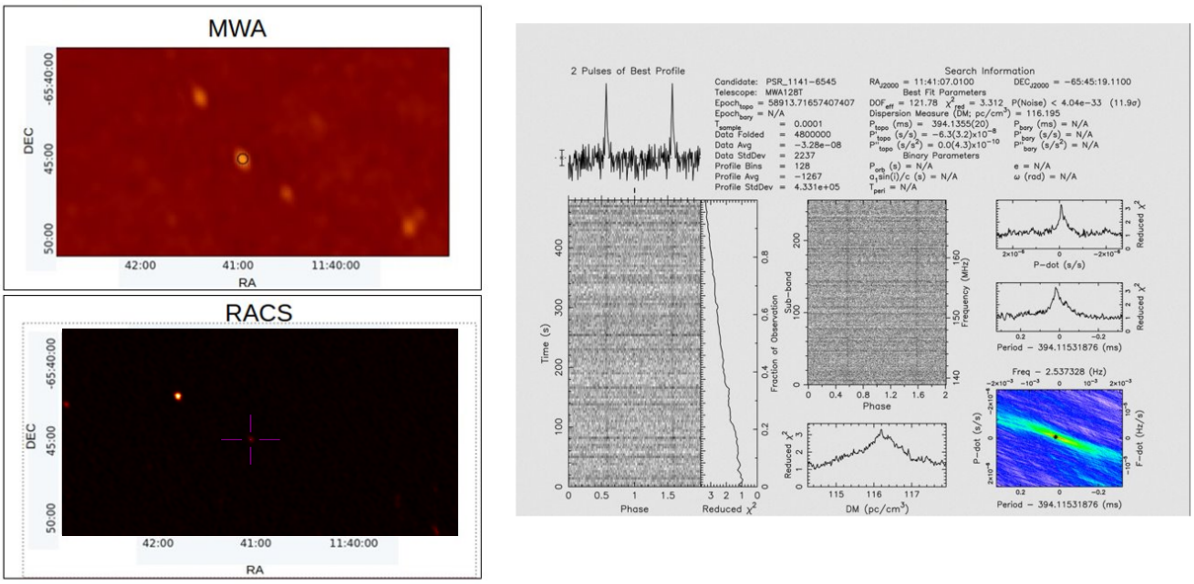

Figure 4.9: Detection of PSR J1141-6545 in both imaging (13σ) and beamformed (12σ) searches. It shows the detection of the pulsar as a continuum source in MWA and RACS images along with the PRESTO detection plot based on the MWA data. The significance of the detection is comparable for both methods.

However, for the highly scattered or high DM pulsars, image-based searches are more favourable. One such example of PSR J1823-1115 with a high DM of 428.59 pc cm^{-3} is shown in Figure 4.10. It shows the image-based detection of the pulsar in MWA as a 125 mJy (25σ) continuum source at the position of the pulsar as well as a detection in RACS Stokes I image. The beamformed search, however, did not result in any detection. The reason for the non-detection is possibly due to the highly scattered profile of the pulsar at lower frequencies when compared to higher frequencies. This scattered profile is demonstrated in Figure 4.11, which shows the available profiles of the pulsar at 410 MHz and 925 MHz, given in the European Pulsar Network (EPN) database. Due to the frequency dependence of scattering, we can expect the profile of this pulsar to be even more scattered at MWA frequency (185 MHz), making it harder to detect via

beamformed searches. Periodicity searches at higher frequencies, such as that of RACS (888 MHz) would be able to detect it more comfortably. This demonstrates the capability of image-based searches at low frequencies to detect similar pulsars having scatter-broadened profiles which may be missed by periodicity searches.

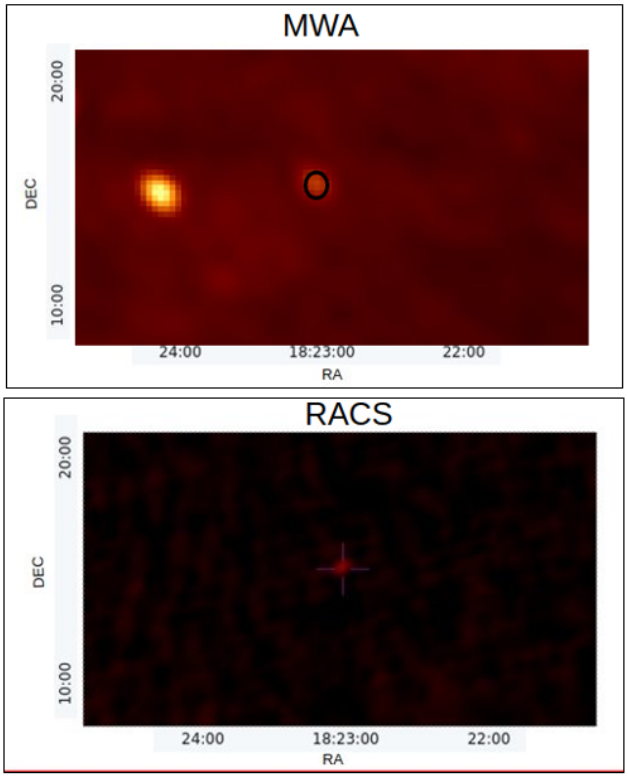

Figure 4.10: Image-based detection of PSR J1823-1115. It can be seen as a 125 mJy continuum source in the MWA image (25σ). The corresponding source in the RACS Stokes I image is also shown in the bottom panel.

Even though image-based searches are good for detecting high DM or highly scattered pulsars, the sensitivity of Stokes I images is still a limiting factor. This can be demonstrated by the example of detection of PSR J1320-5359 shown in Figure 4.12. This shows that the pulsar was detected at a high PRESTO detection significance of 33σ but was not seen as a continuum source in the MWA Stokes I image. The expected flux density of the pulsar at a frequency of 184 MHz is $\sim$ 15 mJy/beam, which is below our best 5σ detection threshold of 25 mJy/beam. Therefore, the sensitivity of MWA is a limiting factor in detecting fainter pulsars

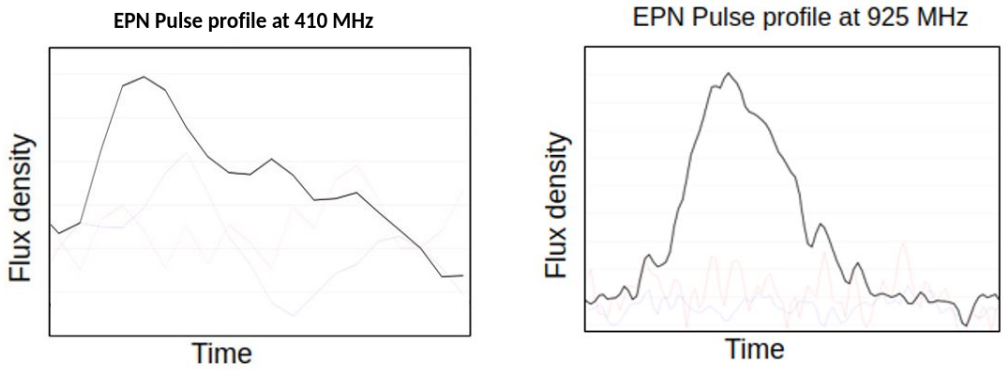

Figure 4.11: EPN pulse profile of PSR J1823-1115 at 410 MHz and 925 MHz. It can be seen that the profile is more scattered at lower frequencies which makes it more difficult to detect at lower frequencies.

in image domain searches. However, the SKA-Low with approximately 64 more antennas (better sensitivity) will be a significantly better instrument for image-based pulsar searches at low frequencies.

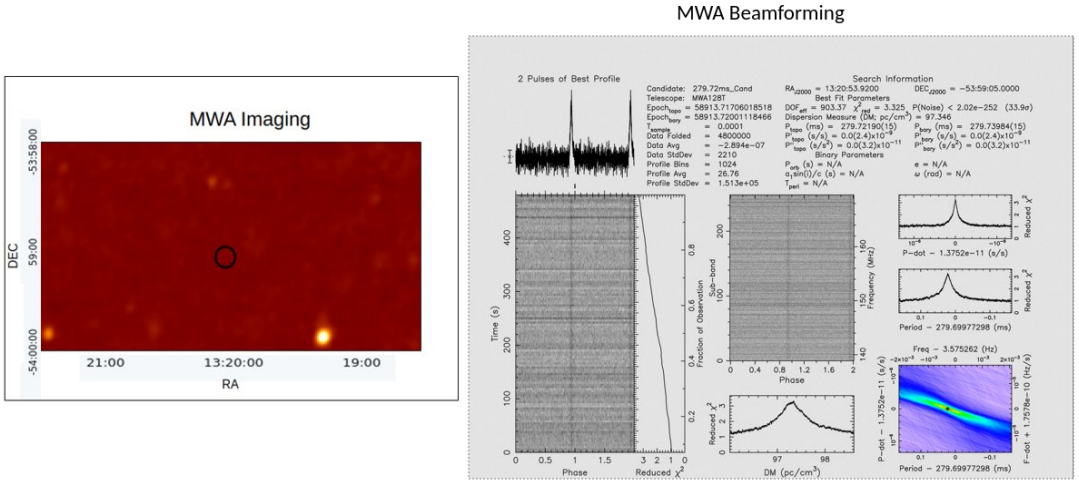

Figure 4.12: Beamformed detection of PSR J1320-5359. The pulsar was below the detection threshold for the MWA Stokes I image and hence is not detected in the image domain.

4.3.3 Comparison with literature

Figure 4.13 shows the flux densities of the pulsars detected in the image plane as part of this work compared to their flux densities from the literature. Sixty-eight of the pulsars in the sample that is detected have previously measured flux densities at low frequencies. The surveys by Murphy et al. (2017), Xue et al. (2017) and Bhat et al. (2023b) provide a good comparison as they were also performed with the MWA, while Frail et al. (2016) conducted the survey using the GMRT at 150 MHz which aligns well with our MWA band of 184 MHz.

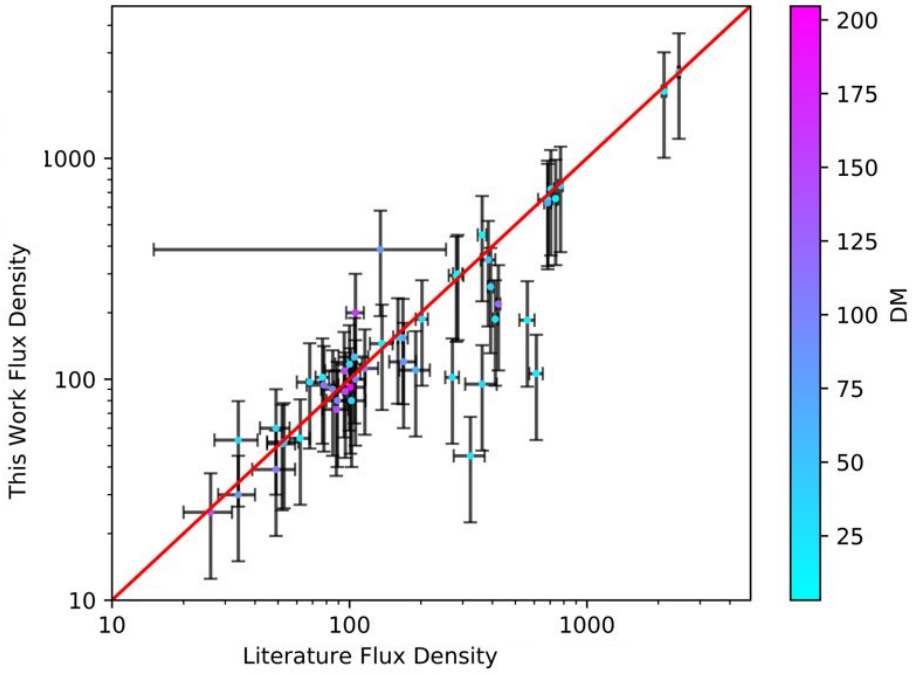

Figure 4.13: The comparison of pulsar flux density measurements in this work with the literature. A 1:1 line is shown in red and most of the data points are within error limits of the line. The disagreements may be due to scintillation of the pulsar at low frequencies or differences in the mean flux density measurement method.

Table 4.2 shows the flux density of the pulsars from Stokes I images that are detected in both imaging and beamforming searches and the recorded low-frequency fluxes from the literature. Eighteen pulsars were previously detected

by Murphy et al. (2017) using MWA images generated as part of the GLEAM survey (Wayth et al., 2015; Hurley-Walker et al., 2017), with the GLEAM sub-band centred at 151 MHz, which matches well with our central frequency of 185 MHz. 24 pulsars were previously detected in Xue et al. (2017) and six in Bhat et al. (2023b) using periodicity searches. One pulsar was previously detected by Kondratiev et al. (2016) using LOFAR observations and periodicity searches. For the pulsars detected only in the Stokes I image, shown in Table 4.3, only two pulsars were previously detected using the GMRT 150 MHz radio continuum survey (TGSS ADR, Frail et al., 2016). As can be seen in Figure 4.13, the flux densities measured in our work agree (within the errors) with these earlier surveys. However, it is important to note that the fluxes from the literature are from different instruments and observational setups. The low-frequency measurements are also more affected by scintillation than higher-frequency measurements and pulsars are also intrinsically variable which may lead to differences in measured flux densities on particular days. Moreover, flux densities may also vary depending on the detection method i.e. time domain detection using the radiometer equation to derive the flux density vs. image-based detections using the flux density of the sources directly from images. Hence, flux densities measured by different surveys and using different search methods may vary by an order of magnitude. Given this, the agreement of our flux density measurements with the earlier measurements (as shown in Figure 4.13) is good, and shows that MWA images can provide reliable flux density measurements despite being potentially prone to blending (due to spatial resolution of the MWA Phase II limited to $\sim$1 arcmin).

4.3.4 Spectral energy distributions

The exact nature of the pulsar emission is an open question even after decades of research. Studying the radio spectra of the pulsars provides clues to the mystery of their emission mechanism. However, these investigations are limited by

Spectral model	Acronym
Simple power law	SPL
Broken power law	BPL
Low frequency turn over	LFTO
Double turn over spectrum	DTOS
High frequency cut off	HFCO

Table 4.5: List of acronyms for the spectral fits used in spectral modelling analysis in this work.

the small number of flux density measurements, especially at frequencies below 400 MHz, which limits the accuracy of spectral modelling. The flux density measurements, especially the first low-frequency detections of pulsars in this work will be helpful in bridging the gap between the low and high-frequency flux density measurements and improve the study of their spectra.

For the 66 pulsars that are detected in the image-plane accurate flux density measurements can be obtained with 10% - 20% uncertainty depending on the position of the pulsar in the Stokes I image. Using the flux density measurements, we fitted spectra using the method described in the software, **pulsar_spectra** [2] (Swainston et al., 2022b) and attempted to investigate the change in the resulting spectral model, if any, upon addition of our low-frequency flux density measurements. The list of spectral fits used and the acronyms are given in Table 4.5

If we have two measurements for flux density for a pulsar, we can calculate a two-point spectral index but will not be producing a spectral fit. Therefore, in order to increase the reliability of the spectral fits produced, the software, **pulsar_spectra**, requires at least three data points for a simple power law fit and four or more data points for other spectral fits. The software does not produce any fits if the requirement is not met. Taking this threshold into consideration, out of the 66 pulsars, 63 had sufficient flux density measurements in the literature to produce the spectral fits without the addition of our work, one did not have

[2] https://github.com/NickSwainston/pulsar_spectra

enough measurements to fit the model without our data points and two did not have a sufficient number of data points to create a spectral fit even after the addition of our work. The lack of measurement data at frequencies below 400 MHz shows the need for more low-frequency campaigns to fill the gap in the literature. The reliable flux density measurement of pulsars with the MWA below 300 MHz will be useful in better spectral modelling of the pulsars. This is exemplified by the fact that 15 out of the 66 pulsars that were detected in Stokes I images changed the spectral models after the addition of our measurements as shown in Table 4.6.

Five pulsars changed from LFTO to BPL (Figure 4.14), two pulsars changed from SPL to HFCO (Figure 4.15), two pulsars changed from LFTO to DTOS (Figure 4.16) and one pulsar changed from SPL to LFTO (Figure 4.17). The remaining five pulsars changed models to equally or more complex ones (Figure 4.18). Most of the pulsars are seen to have a reliable fit.

For millisecond pulsars, the broken power law for PSR J0737-3039A and double frequency turnover spectra for PSR J2145-0750 are consistent before and after the addition of our low-frequency flux density measurement. For one of the millisecond pulsars, PSR J1902-5105, a simple power law fit was produced (Figure 4.19) only after the addition of our flux density measurement. This shows the importance of performing more flux density measurements at lower and intermediate frequencies, which will improve the spectral modelling of pulsars and help explain the emission mechanism behind them. Measuring flux densities at multiple epochs is also important for improving the reliability of these measurements with reduced effects of flux variability. However, for two of the millisecond pulsars, PSR J1751-2737 and J1748-3009, we were unable to produce a reliable spectral fit even with the addition of our low-frequency measurements as **pulsar_spectra** software requires at least three points for a simple power law fit and four or more for other spectral fits.

Even though **pulsar_spectra** provides reliable spectral fits, there can be dis-

PSRJ Name	Original model	New model
J0820-1350	LFTO	DTOS
J0820-4114	BPL	LFTO
J0907-5157	LFTO	BPL
J1121-5444	HFCO	LFTO
J1312-5402	SPL	LFTO
J1456-6843	LFTO	BPL
J1709-1640	HFCO	BPL
J1752-2806	DTOS	LFTO
J1913-0440	LFTO	BPL
J1932+1059	LFTO	DTOS
J2022+2854	LFTO	BPL
J2048-1616	LFTO	HFCO
J1600-5044	LFTO	BPL
J1807-2715	SPL	HFCO
J1827-0958	SPL	HFCO

Table 4.6: The list of pulsars whose spectral fits changed after the addition of the flux density measurements from this work. The original model is the spectral model without our work and the new model is the spectral model after the addition of our work. SPL stands for a simple power law, BPL is a broken power law, LFTO is a power law with low-frequency turn-over, HFCO is a power law with a high-frequency cut-off and DTOS is a double turn-over spectrum.

crepancies in the model fits due to several reasons. One of the reasons can be the lack or small number of measurements between 185 MHz and 1.4 GHz which may cause the fit to be less reliable. For example, the spectral fit for PSR J1827-0958 may be unreliable due to the lack of measurements between our flux density at 185 MHz and the measurements at higher frequencies as shown in Figure 4.20. The fits may also be skewed by underestimated error which can result from scintillation not being taken into account potentially increasing the measured flux density, especially at low frequencies.

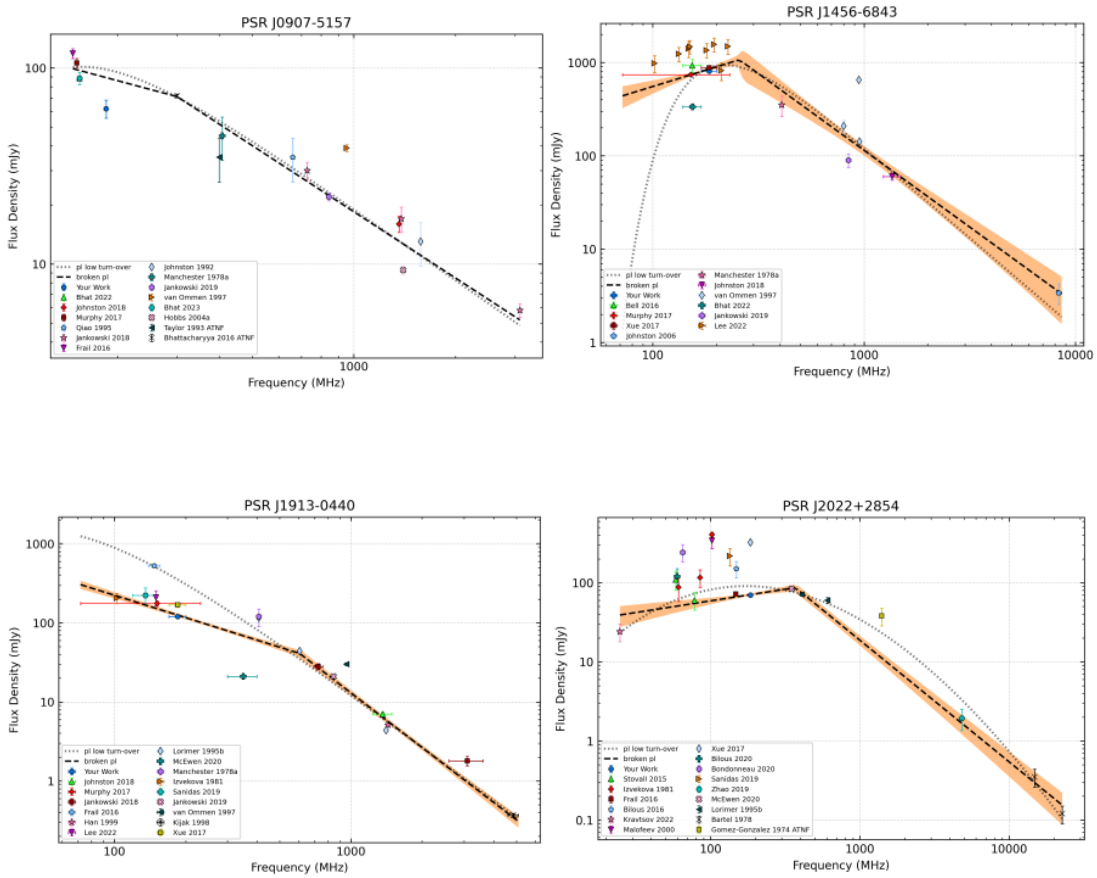

Figure 4.14: Spectral fits for the pulsars that changed fits from LFTO to BPL after the addition of our measurements.

4.3.5 The undetected pulsar population

Despite the detection of many known pulsars, there are many other which were not detected in imaging and periodic searches, that needs to be addressed. The non-detections in imaging can be attributed to either spectral turnover at low frequencies as highlighted by (Jankowski et al., 2018) or confusing the pulsars with other extended structures such as supernova remnants and pulsar wind nebulae near the Galactic Plane or the high noise confusion at the edge of the image. For periodic searches, the detection sensitivity is mainly affected by high scattering and scintillation which makes it harder to detect highly scattered pulsars and pulsars that tend to scintillate down making it fainter than the sensitivity

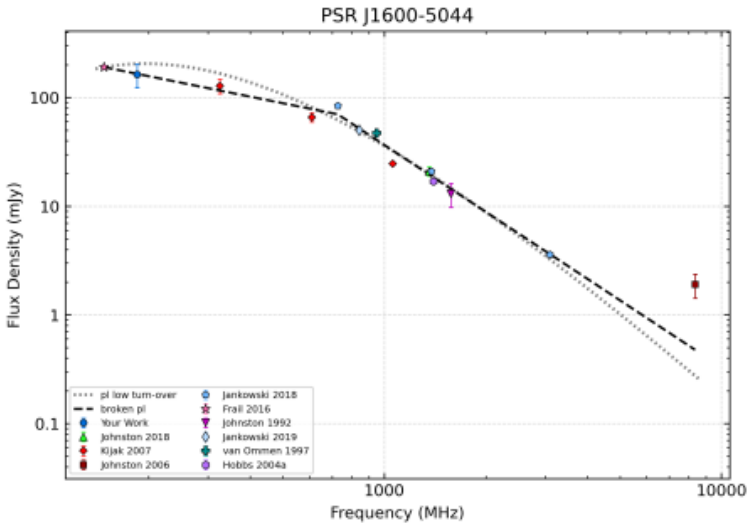

Figure 4.14: Spectral fits for the pulsars that changed fits from LFTO to BPL after the addition of our measurements.

threshold.

The sky brightness temperature at low radio frequencies (∼400 MHz) scales with frequency as $T_b \propto \nu^{-2.6}$ (Haslam et al., 1981), such that it becomes dominant at lower frequencies, making pulsar detections increasingly difficult. This affects both pulsed and imaging searches equally, with imaging searches also being affected by confusion and reduced image fidelity in the presence of bright Galactic HII regions and supernova remnants. The pulsar J1513-5908 is a good example of a bright pulsar confused by nearby bright, extended emission from supernova remnant, SNR G320.4-1.2 as shown in Figure 4.21.

The detectability at low frequencies is also affected by the spectral shape of the pulsar emission. Approximately 10% of the known pulsar population is shown to have spectral turnovers (Maron et al., 2000). The pulsar population that we expect to detect also has a number of pulsars with known spectral turnovers such as PSR J1644-4559 which has a turnover at 600 MHz (Jankowski et al., 2018). However, the lack of more accurate pulsar flux densities at low frequencies makes it difficult to confidently determine the behaviour of the pulsars at frequencies below 300 MHz.

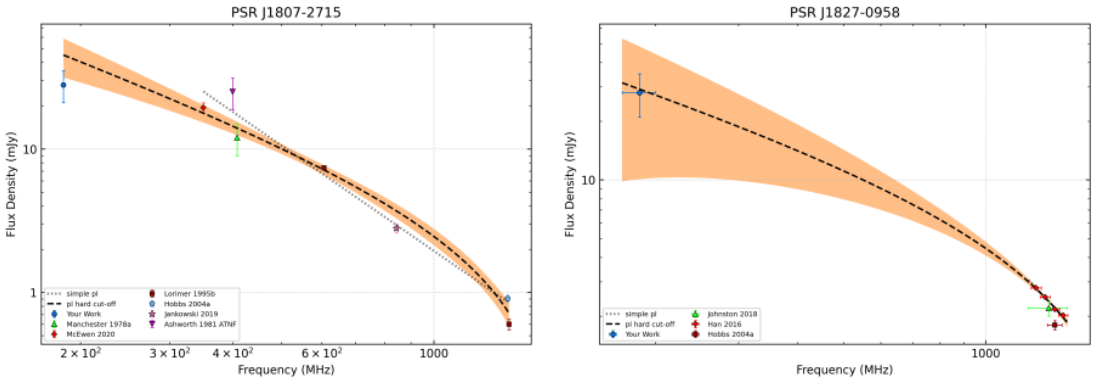

Figure 4.15: Spectral fits for the pulsars that changed fits from SPL to HFCO after the addition of our measurements.

For periodic searches, a factor that affects the detection of almost 40% of the Southern pulsar population is the rapid decline in sensitivity beyond DM $\sim$ 250 pc cm^{-3} for time series data at MWA-frequencies, which is due to scattering and interstellar scintillation. This will be discussed in detail in Section 5.4.4.

In summary, we conclude that the non-detections of the pulsars can be due to a combination of effects. There is clear evidence that the majority of the non-detections in the imaging plane are due to the increased confusion noise near the Galactic Plane and the low-frequency spectral turnover of the pulsars. The periodic search non-detections are a combination of factors such as reduced sensitivity at high DMs, scattering and scintillation.

4.4 Summary and Conclusion

We have identified 83 pulsars from the 12 MWA VCS observations covering the Galactic Plane. 66 of the pulsars are detected in wide-field MWA images due to their phase-averaged emission. The approach of imaging is complementary to pulsation studies because it is not affected by pulse scatter broadening or dispersion making it sensitive to pulsars that may have been missed by previous

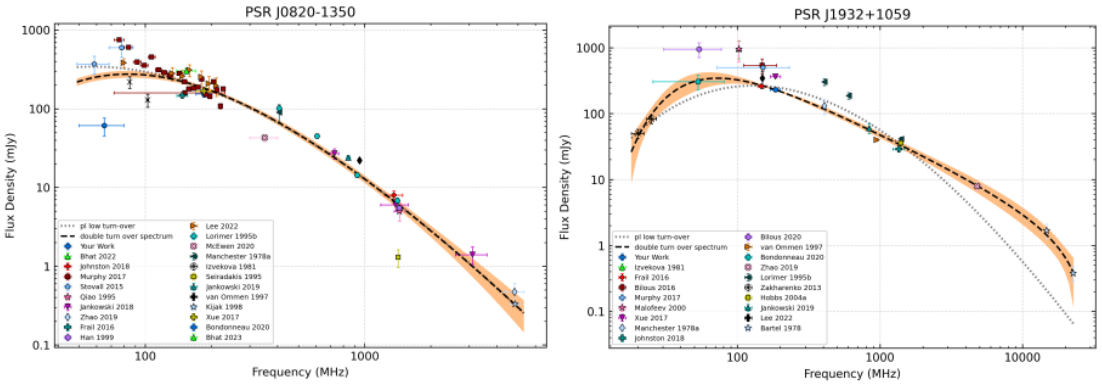

Figure 4.16: Spectral fits for the pulsars that changed fits from LFTO to DTOS after the addition of our measurements.

time domain searches. This work also explores the unique parameter space that is exclusively accessible to image-domain pulsar searches eg., bright, high DM pulsars which are hard to detect at low frequencies. We also presented the new low-frequency flux density measurements for 14 pulsars from the ATNF pulsar catalogue. These low-frequency flux density measurements can be helpful in better modelling the spectra of the pulsars and address questions about the origins of low-frequency spectral turnovers. We have carried out a preliminary spectral index study of our sample. We find that 15 pulsars change the spectral index model after the addition of our low-frequency measurement. However, these changes in the spectral index models may have been affected by the lack of measurements in intermediate frequencies such as 300 MHz or large fractional bandwidths of the existing measurements. Another factor that affects the spectral index model is the variability of the flux density measurements which may over or under-estimate the flux density measurement on a particular day.

Our identification of the pulsars was largely limited due to the sensitivity and the high confusion region near the Galactic Plane. The number of detections may also be affected by low-frequency spectral turnover for pulsars rendering them undetectable. We can conclude that a combination of all the effects is responsible

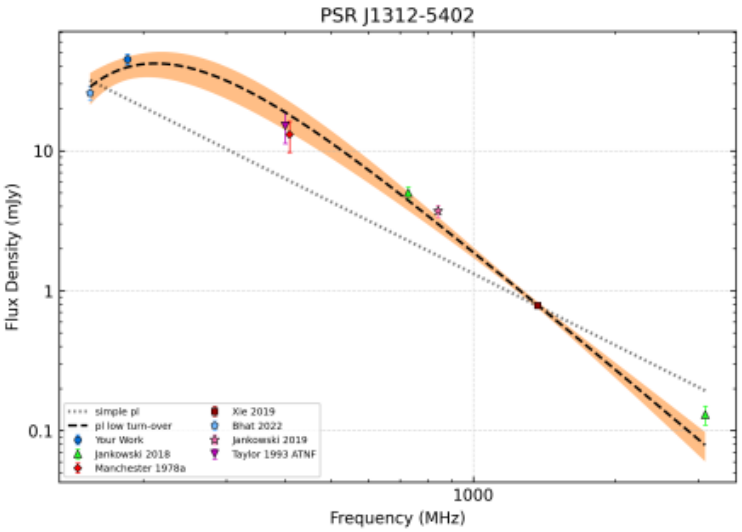

Figure 4.17: Spectral fits for the pulsar that changed fits from SPL to LFTO after the addition of our measurements.

for the pulsar non-detections in the image domain, while, time domain searches were mainly affected by scattering and scintillation. This work also emphasises the need for more flux density measurements at low frequencies i.e. including flux density measurements especially at multiple different epochs to better understand pulsar spectra, and the population of Southern sky pulsars and answer questions about their low-frequency spectral turnover.

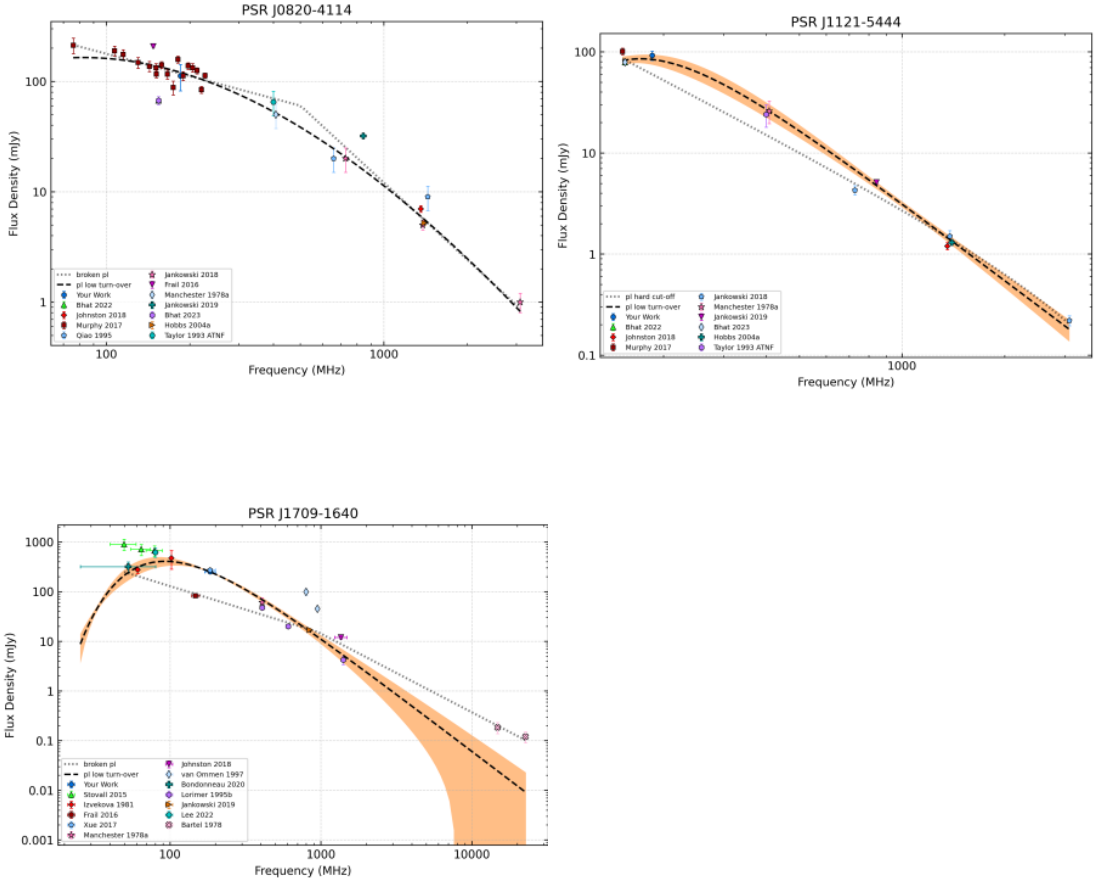

Figure 4.18: Spectral fits for the pulsars that changed to other less or more complicated fits after the addition of our measurements.

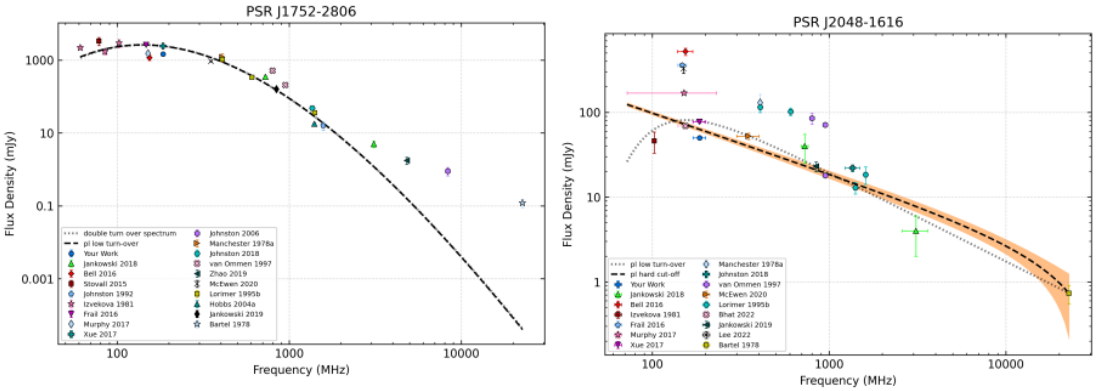

Figure 4.18: Spectral fits for the pulsars that changed to other less or more complicated fits after the addition of our measurements.

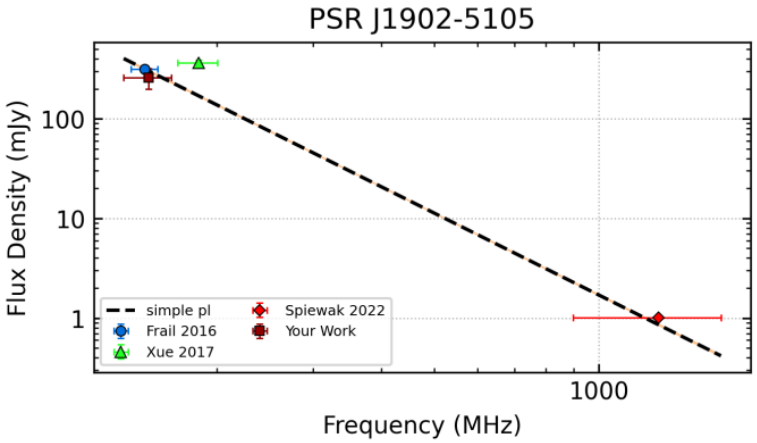

Figure 4.19: Simple power law fit for MSP J1902-5105. The red box shows the low-frequency flux density measurement from this work.

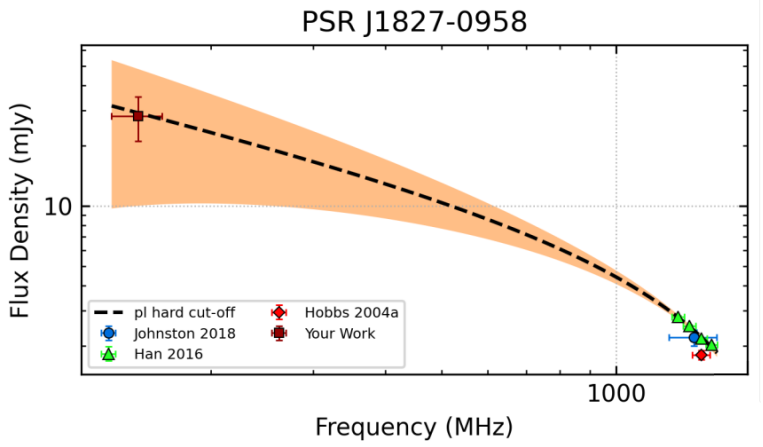

Figure 4.20: Broken power law fit for PSR J1827-0958 after the addition of the low-frequency flux density measurements from this work. The spectral fit is less reliable due to a lack of measurements between the low and high-frequency measurements.

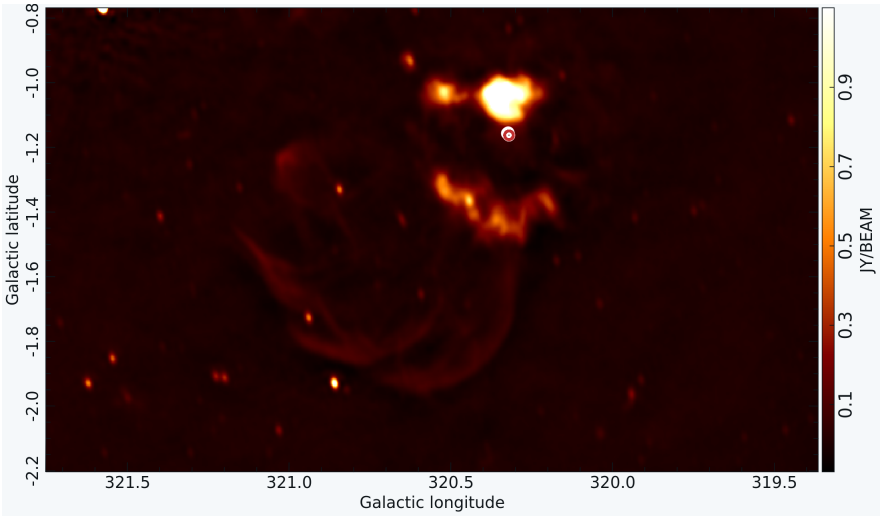

Figure 4.21: SNR G320.4-1.2 is shown in the middle of the image. The bright pulsar, PSR J1513-5908 is shown as a red dot amongst the diffuse emission of the supernova remnant. It is extremely hard to detect this pulsar in the image domain due to the source being confused by the bright, extended emission of its surroundings.

Chapter 5

Follow up of Galactic pulsar candidates

5.1 Introduction

Chapter 4 describes the image-based pulsar census using the 12 MWA VCS observations. The application of the image-based methodologies to these observations also resulted in a list of pulsar candidates satisfying the criteria. The main objective of this chapter is twofold:

(i) to verify if known pulsars are indeed identified by our criteria as the candidates. This is used to quantify the efficacy of the methodologies by calculating the ratio of the number of known pulsars identified by a given criterion to the number of pulsar candidates produced by the criteria.

(ii) to rank the candidates according to the number of criteria they satisfy and follow them up with the Parkes radio telescope and GMRT to search for pulsations.

The follow-up strategy has three main stages. All candidates were searched in MWA VCS data by beamforming the same observation the candidate was identified in the images. The 25 highest-ranked candidates (satisfying more than

one criteria) were searched for pulsations using only the Parkes Radio Telescope. The five highest ranked candidates that had a γ-ray or X-ray counterpart were followed up using imaging and phased-array (PA) mode of GMRT as well as the Parkes Radio Telescope. Given that these sources were extremely bright at the MWA frequencies (184 MHz), if they were indeed pulsars the pulsations can easily be detected with both Parkes as well as GMRT telescopes.

This chapter also focuses on the possibility that the sources we detect are indeed pulsars but not detectable due to due to various reasons, such as propagation effects or geometry of the emission. We also discuss the possibility of these sources belonging to other categories of radio sources or a completely new class of Galactic radio objects as discussed in Maan et al. (2018).

5.2 Candidate selection criteria

The candidate selection methodologies are based on pulsar properties such as steep spectrum, circular polarisation and variability (described in detail in Chapter 3). These can be applied to the source catalogues produced by source-finding software applied to our images for the observations to get a list of pulsar candidates. The detailed development and the testing of the methodologies can be found in 3. A brief description of them is given below. The methodologies described below are applied only to sources considered compact because pulsars are point sources and not extended. To select the compact sources, we use the criteria defined in Frail et al. (1994), such that the ratio of the integrated flux to the peak flux of the source in the Stokes I continuum image should be less than 1.5. This constraint allows for anomalous values of this ratio which can occur if a pulsar scintillates strongly during the observations.

A way by which pulsars can be distinguished from other radio sources is that they are typically steep spectrum. They have an average spectral index of -1.6 ± 0.2 (Jankowski et al., 2018), and can have a spectral index as steep as -4. Many pulsars have been discovered after noticing the steep spectra of

their counterparts in the continuum images. This has proven useful in detecting various interesting systems. For example, the discovery of pulsar PSR J1824-2452A in globular cluster (Lyne et al., 1987) or the first millisecond pulsar (Backer et al., 1982). Sensitive all-sky imaging surveys have been uncovering interesting new sources including ones with steep spectra. The TIFR GMRT Sky Survey (TGSS) at 147 MHz covering the Southern sky along with the NRAO VLA Sky Survey (NVSS) was used by de Gasperin et al. (2018) to produce a spectral index catalogue of almost 80% of the sky, confirming an excess of compact and steep spectrum sources in the GP as first indicated by De Breuck et al. (2000). This excess of steep spectrum sources is a compelling case to search for radio pulsars in the GP. In our GP survey, the first criterion selects sources that have a spectral index steeper than that of -1.2, calculated from the mean flux densities of the sources using the MWA Stokes I continuum image and Rapid ASKAP Continuum Source catalogue (RACS; McConnell et al., 2020; Hale et al., 2021).

For the second criterion, Stokes V continuum images are used to select sources with circular polarisation above a certain threshold. The details of the polarisation properties of pulsars can be found in Section 3.3.2. This threshold is determined after taking the instrumental leakage into consideration. Polarisation leakage can be present even when using the most advanced MWA primary beam model (Sokolowski et al., 2017) and can be handled by modelling the leakage pattern across the beam and subtracting it. After taking this approach, sources that have circular polarisation greater than 7% are selected. Compared to the sources in Stokes I, the number of sources in Stokes V is significantly smaller and hence results in a lower classical confusion limit. This is particularly beneficial in our case, as the GP has significantly high confusion noise in Stokes I images, which can be avoided by using Stokes V images. This is also helpful in getting a smaller number of candidates as the total number of sources in Stokes V images is comparatively smaller. This method was proven successful in recent discoveries of millisecond pulsars with a wide profile and high dispersion measure

(DM) by ASKAP (Kaplan et al., 2019), which was missed by traditional periodic searches. However, when selecting such sources, one needs to keep in mind that the instrument and consequently the data suffer from instrumental leakage which may result in false-positive candidates. In this work, we mitigate the instrumental leakage by modelling the leakage pattern across the MWA beam and then subtracting it as realised by Lenc et al. (2017). Sources present in both Stokes I and V continuum images are selected and the median leakage within a 5-degree radius for each source is calculated and then subtracted from the Stokes V flux density to suppress any residual leakage. This provides a more reliable estimate of the signal-to-noise ratio and the fractional polarisation of the sources. All sources above 7% fractional polarisation threshold are selected as pulsar candidates (Lenc et al., 2018, 2017).

The third criterion used to select pulsar candidates in this work relies on searching for time variability. As we have images at short timescales for the whole observation, this method probes a detection parameter space where periodicity searches may not perform well. This method is effective, especially for low frequencies, where sources are affected by scattering and dispersion lowering the sensitivity of periodic searches. For example, this method of detecting transients has been producing interesting candidates in the ASKAP Variables and Slow Transients (VAST) Pilot project (Banyer et al., 2012) and the LOFAR Transients key science project (Swinbank et al., 2015). In this work, we probe diffractive scintillation specifically by generating light curves of possible variable sources at timescales of 5min, 1min and 30sec. Variability statistics such as modulation index (m) and significance (χ^2) are used to select the most variable sources when compared to its surroundings (Bell et al., 2016a). The details of the statistical equations used are described in detail in Chapter 3. A threshold of 20% for modulation index and significance of 5 is determined such that we limit the number of resulting pulsar candidates to a manageable number (less than 1000) to follow up as well as not get a huge number of false positives. All the shortlisted

candidates are followed up using the very same MWA VCS observations to search for periodic pulsations.

Combining the three criteria is also performed in order to rank the candidates according to the number of criteria they satisfy and therefore more probable to be real pulsars. A subset of the highly ranked candidates are followed up using the Parkes radio telescope (30 candidates). Five of the candidates that have counterparts at other wavelengths were also followed up using the GMRT as well as the Parkes radio telescope as described in Section 5.3.1.

5.3 Classes of selected candidates

Apart from the known pulsar population, we also detect three main and three subcategories of candidates, totalling to 1132 candidates that could not be associated with any known pulsars. The three main categories of candidates after the application of criteria described in Section 5.2 are steep spectrum, circularly polarised and variable. These are then combined together to generate a list of candidates that satisfy more than one criterion which forms the subcategories.

Figure 5.1 shows the distribution of the spectral index of the candidates that are selected from the first criteria, i.e., steep spectrum sources. As shown in Figure 5.1, we select sources that have a spectral index steeper than -1.2 and the majority of the candidates occupy the right side of the plot which agrees well with the currently known pulsar population. However, there are pulsars such as PSR J1237-6725, which has a spectral index of -4.48 (Manchester et al., 2005), showing that the range of pulsar spectral indexes is quite broad. In our steep spectrum candidate sample of $\sim$ 1000 sources, we have $\sim$ 5 ultra-steep spectrum sources with spectral indexes that are all steeper than -4.5.

The second category is the sources that show circular polarisation after the application of the criteria as mentioned in Section 5.2. The cutoff of circular polarisation (7%) is taken after the subtraction of the mean of the leakage from nearby sources. We have 150 sources that show fractional circular polarisation

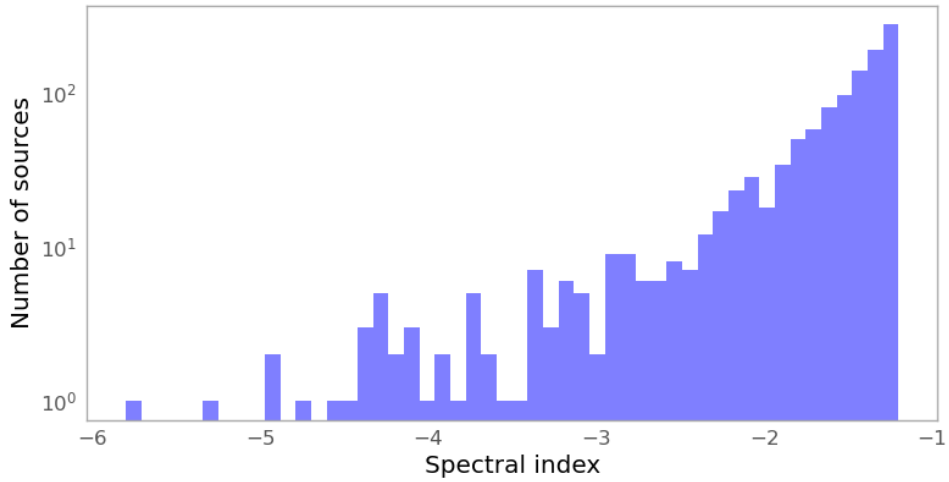

Figure 5.1: Distribution of spectral index of the sources selected on the basis of steep spectrum criteria. A majority of the sources comply with the general spectral index distribution of known pulsars. There are $\sim$ 20 sources that are at the highly negative end of spectral indexes. These can be real sources or errors in spectral index calculation due to some of the sources having variable flux density or blended with other sources.

above 7 %. The number of sources in the circular polarisation criterion is less than that of the other two and results in a lower classical confusion limit. The third category of sources is variable and selected based on the criteria defined in Section 5.2. After the application of the statistical metric of modulation index and χ^2 value cutoff, we obtain 200 candidates that show variability. A variety of the light curves generated are given in Figure 5.2. The discarded light curves generally look like a) and b) in Figure 5.2 and generally do not show any variability. The light curves that we take into consideration for our work are light curves that show sources that increase in flux density in a short timescale and then decrease in flux density in Figure 5.2(c)) and light curves that show a "flaring" activity i.e. there is a sharp increase in flux density in a very short timescale in Figure 5.2(d)).

The three main categories are then combined together to form subcategories, namely steep spectrum and variable, steep spectrum and circularly polarised, variable and circularly polarised and sources that satisfy all three criteria. All the selected sources are then ranked and followed up using MWA data as well as

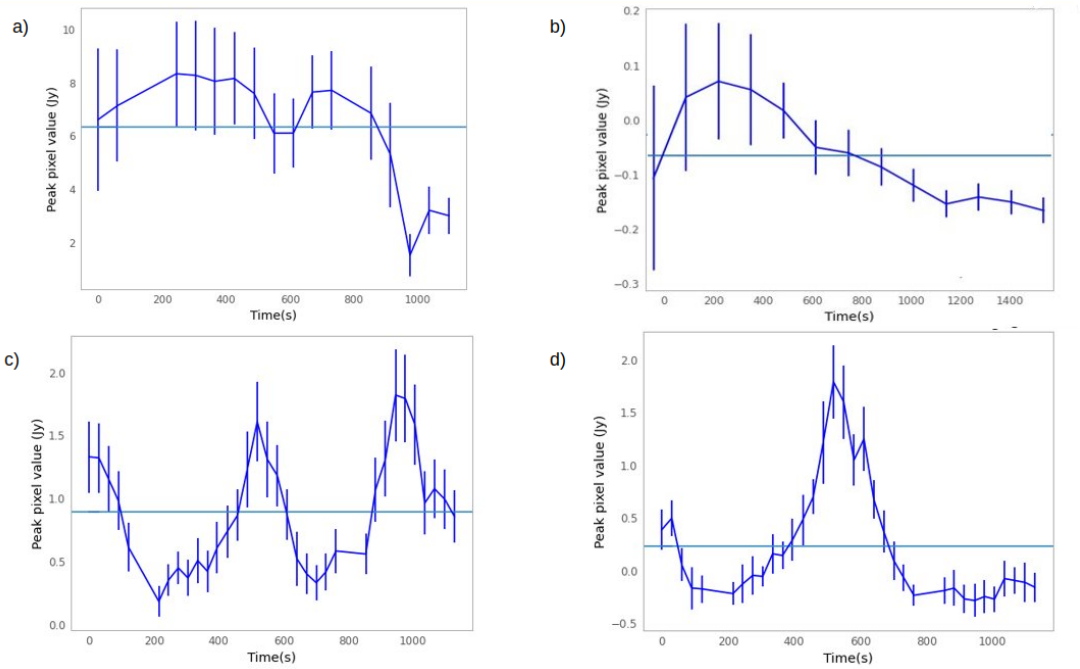

Figure 5.2: This panel shows the different light curves that are generated as part of the variability criteria. The light blue line is the mean flux density of a source. The error bar is the standard deviation of the noise close to the source. Figures a) and b) are time-varying RFI and noise respectively and do not show any significant variability other than the occasional rise and decline in flux density within the error limits. Figure c) shows an intermittent source that seems to have a rise and then decline and then followed by a rise in flux density. Figure d) shows a rapid increase in flux density and then a sharp decrease. Figures c) and d) are good candidates for variable sources and are selected for further analysis.

using other telescopes such as Parkes Radio Telescope and the Giant Metrewave Radio Telescope (GMRT), as discussed in Section 5.3.1.

MWA follow-up of the candidates did not result in any detection of periodic pulsations. The details of the GMRT and the Parkes follow up are discussed below. Even though we have moderate number of candidates (in the orders of 100s), it is still a considerable amount of candidates to be followed up using other telescopes. So in order to select the candidates we rank them with regards to the number of criteria they satisfy. For example, candidates that satisfy all three criteria are ranked the highest, compared to the ones that satisfy only one criterion. We do acknowledge and discuss the inadequacies in this combination

of criteria in Section 5.4.2.

5.3.1 Follow up of five candidates with the Parkes and GMRT telescope

25 candidates, shown in Table 5.1 are followed up using Parkes Radio telescope.

Five out of the 30 candidates are also followed up using the GMRT telescope. Five candidates as shown in Table 5.2 selected as per the selection criteria described in Section 5.2 were followed up using the GMRT and Parkes radio telescope. Three of the candidates have a counterpart in the Fermi Large Area Telescope 4th source catalogue (4FGL, Abdollahi et al., 2020). We used a cross-matching radius of 10 arcmin, which is similar to the localisation error of these sources in the Fermi catalogue. Even though we have used the 10 arcmin radius, the candidate was only selected as interesting if it lied within the Fermi (and X-ray) error ellipse. This was determined by comparing the given error ellipse and the distance of our candidate source from the Fermi/X-ray source. If our candidate was outside the error ellipse, it was not chosen as an interesting source for follow up. This association of Fermi sources with four of our MWA candidates is very encouraging as many millisecond pulsars (MSPs) have been discovered by targeted radio searches of Fermi sources. Similar image-based and pulsar searches of Fermi sources using the uGMRT have been done leading to the discovery of 6 MSPs and one normal pulsar (Frail et al., 2016). The other two sources have an X-ray source associated with them and are part of the ROSAT All-Sky Survey Faint Source Catalogue (Voges et al., 2000). The association of our radio source with an X-ray source suggests that these sources can potentially be young pulsars being produced in a supernova and emitting in both radio and X-ray frequencies. All the candidates have a steep spectrum and are variable on timescales of 60 seconds.

RA	Dec	α	CP (%)	Variability (%)
19:17:45	-19:21:26	-1.6	7.5	7
19:31:18	-15:57:46	-1.5	7.2	10
19:12:08	-8:04:18	-1.3	8.3	8
18:50:53	-14:00:47	-1.4	7	10
19:34:47	-5:53:35	-1.3	7.4	2
18:43:41	-11:13:22	-1.6	2	20
18:58:03	+03:13:28.19	-1.5	5	24
20:15:06	+16:22:52.61	-3.5	1	32
17:27:51	-8:43:51	-1.2	2	40
18:11:37	-9:01:09	-1.3	1	20
17:42:11	-15:17:24	-3.9	6	29
18:03:41	-11:26:59	-1.5	5	23
18:58:03	-4:33:10	-1.4	7	34
18:51:59	-4:31:33	-1.9	4	42
19:51:41	-4:20:21	-1.4	2	27
17:30:33	-4:22:27	-1.2	7	48
17:43:47	-5:12:33	-1.4	5	23
17:52:39	-5:13:51	-2.7	2	21
17:25:04	-4:35:12	-1.6	4	30
20:06:56	+14:00:06.61	-2.1	2	22
20:15:20	+13:55:26.53	-1.3	1	20
18:57:11	-21:34:14	-1	7.8	22
17:17:00	-21:22:01	-1.1	7.2	20
19:07:53	-21:30:46	-0.9	8.1	31
18:52:25	-21:32:14	-1	8	30

Table 5.1: Candidates followed up using the Parkes Radio Telescope. The first two columns gives the RA and Dec of the candidates. α is the spectral index of the candidates, CP is the circular polarisation percentage and variability is the modulation percentage of the candidates. All candidates with α steeper than -1.2, CP more than 7% and modulation index more than 20% are selected.

MWA Name	RACS SRC ID	$S_{\rm RACS}$ (mJy)	$S_{\rm MWA}$ (mJy)	Spectral index α	Association
GPM 1850-11	1856-12A_4133	11.467	118	-1.6	4FGL J1850.8-1105
GPM 1811-14	1806-12A_1457	7.796	54	-1.4	4FGL J1811.7-1442
GPM 1744-13	1741-12A_2898	21.082	138	-1.3	4FGL J1742.2-1229
GPM 1849-11	1856-12A_4518	3.959	63	-2.0	1RXS 184929.0-113638
GPM 1838-13	1831-12A_1971	4.72	43	-1.6	1RXS J183844.8-131344

Table 5.2: Details of the five candidate pulsars followed up with GMRT and Parkes. The 185-MHz flux density corresponds to the peak flux density of the source as recorded by the source-finding software. The spectral index is calculated using the peak flux density of the sources in MWA (150 MHz) and RACS (888 MHz) frequencies. The first three sources have an association with a Fermi γ-ray counterpart within Fermi error ellipses (Abdollahi et al., 2020). The last two sources have an associated X-ray source in ROSAT All-Sky Survey Faint Source Catalogue (Voges et al., 2000) within 10 arcmin of the source position in the MWA image.

The observation with the Parkes Radio Telescope used the ultra-wideband receiver that operated from 704 - 4032 MHz. The total integration time for the observations for each source was 15 minutes. A test pulsar, PSR J1852-2610, was also observed as part of every observation to ensure that the observational setup has no issues as well as to use the pulsar detection as a measure of the sensitivity that we reach with our observations. The detection of the pulsar is shown in Figure 5.3.

As the sources were known to vary, they were followed up on two different days, separated by a day in the middle. The beamformed data was used to search for pulsations. The pulsar searching software, PRESTO (Ransom, 2001) was used for search, with DMs of up to $\sim$ 1000 pc cm^{-3}. An acceleration search was also performed up to Fourier bins of $\sim$ 300 m s^{-2}. As the pulsars were steep spectra, and therefore expected to be brighter at the lower band of Parkes, the data was split into multiple bands and the search was performed with the same parameters. The details of the principles governing the search procedure

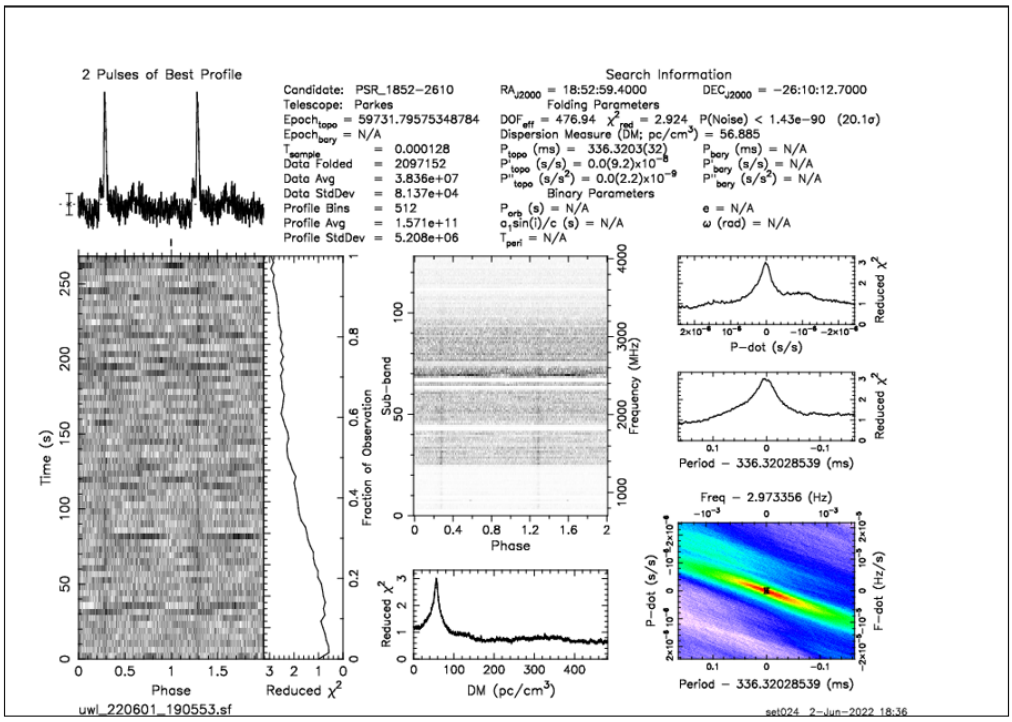

Figure 5.3: Successful Parkes detection of PSR J1852-2610. This ensures that there were no issues with the observational setup of the observation.

are described in Section 2.6.

For the GMRT follow-up of the five candidates, concurrent observations in the imaging and phased-array (PA) mode were performed, in Band 3 (250-500 MHz). This band was chosen as this is the frequency closest to MWA frequency and hence ideal for confirmation of these candidates as pulsars. The PA beam mode yields high-fidelity detection of pulsar profiles and helps us determine whether the sources are new pulsars or not. The high time resolution imaging with the uGMRT helps us to verify detections in uGMRT Stokes images, and improve their localisation accuracy. For the PA beam mode, we made use of $\sim$ 10 - 12 antennas located within the central square. The PA beam consisting of the central square antennas provides $\sim$ 50% of the full array sensitivity, which is adequate for good quality detection of the sources as pulsars, given the sources being extremely bright in MWA Stokes I images. We made use of the 2048 channel mode with 655.56 μs resolution of the GWB pulsar backend. The PA beam recording was

done in the total intensity mode.

For continuum imaging, we recorded visibilities in the standard 2.68-second mode of the wide-band correlator, which we was used in the 200-MHz mode, while switching between the target and the phase calibrator after every source. In order to verify astrometry and to cross-check any residual ionospheric or other calibration-dependent offsets, we also made a short (∼20 minutes) observation of a nearby bright pulsar, PSR J1857-1027, with a DM of 108.9 pc cm^{-3} and S_{350} of 12 mJy. The detection of the pulsar in imaging and PA mode is shown in Figure 5.4 and 5.5 respectively, which assures us that the quality of the data was satisfactory.

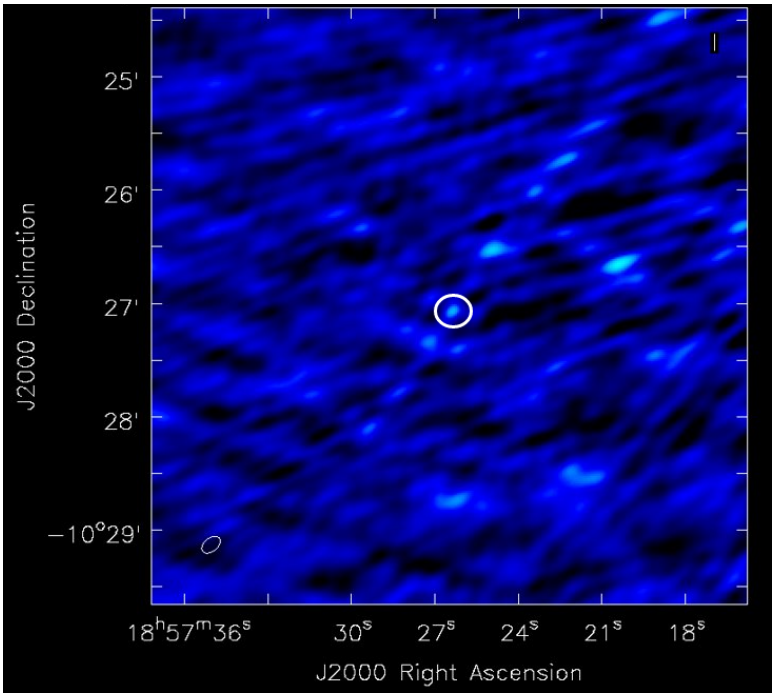

Figure 5.4: Successful GMRT imaging detection of PSR J1857-1027 showing that the observational setup has no issues during the PA mode observation.

The continuum data from the GMRT was first processed to form Stokes I images to determine the nature of the sources. The details of the processing are described in 2.7.2. The PA mode data was then searched for pulsations using the principles described in 2.6 and pulsar processing software, PRESTO (Ransom, 2001).

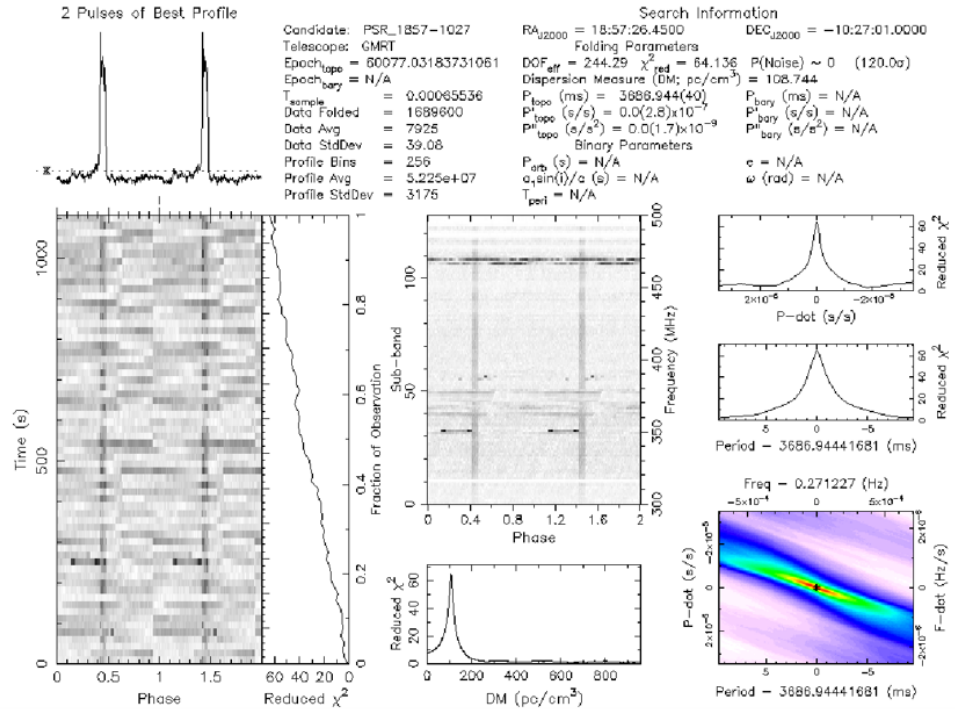

Figure 5.5: Successful GMRT detection of PSR J1857-1027. This ensures the observational setup has no issues during the PA mode observation. The pulsar is marked in a white circle.

5.4 Results and discussion

5.4.1 Parkes and GMRT follow up

We were not able to detect any pulsations from the pulsar candidates using the Parkes Radio Telescope. Using the detection of the test pulsar shown in Figure 5.3, we were able to determine the sensitivity of our observations to be down to 0.2 mJy. The possible reasons for the non-detections can be that the pulsations were undetectable due to the variable nature of the candidates. Another possible reason can be that the pulse profiles at high frequencies such as that of Parkes Radio Telescope were too scattered and therefore, undetectable. These sources can possibly not be pulsars but some other radio sources that share common properties of pulsars. The various interpretation of the sources is discussed in detail in Section 5.4.3.

The five candidates followed up with GMRT, when imaged turned out to be extended or double radio sources. Table 5.3 shows the RMS achieved for the Stokes I images for the five sources. Given that the GMRT images were able to reach down to μJy level sensitivity and the extended nature of the sources we are certain that these five sources are not pulsars.

MWA Name	RMS (μJy)	Source in GMRT
GPM 1850-11	140	Double
GPM 1811-14	260	Extended
GPM 1744-13	990	Double
GPM 1849-11	280	Extended
GPM 1838-13	300	Extended

Table 5.3: RMS achieved for GMRT image for five sources. The nature of the source in the GMRT image is also given in the last column.

Three of them as shown in Figure 5.6 are extended sources with a compact core and a tail-like structure. Figure 5.7 shows the two sources that turned out to be double sources. Given the extended nature of the sources, it is highly unlikely that the sources are pulsars. More investigation using existing multi-wavelength catalogues and follow-up observations of these sources are needed to confirm the nature of the sources.

We deduce that these sources were selected as compact candidates from the MWA images due to the low spatial resolution of MWA and ASKAP, which leads to double and extended sources to look like single compact sources, i.e. blending multiple sources into one. This may also lead to a higher flux density of these blended sources and hence an incorrect estimation of the spectral index. This can be avoided by checking in other catalogues and images, as is done in this work with the GMRT for these sources to determine whether an MWA source is truly compact or not. Even though these sources are not pulsars, they can be other

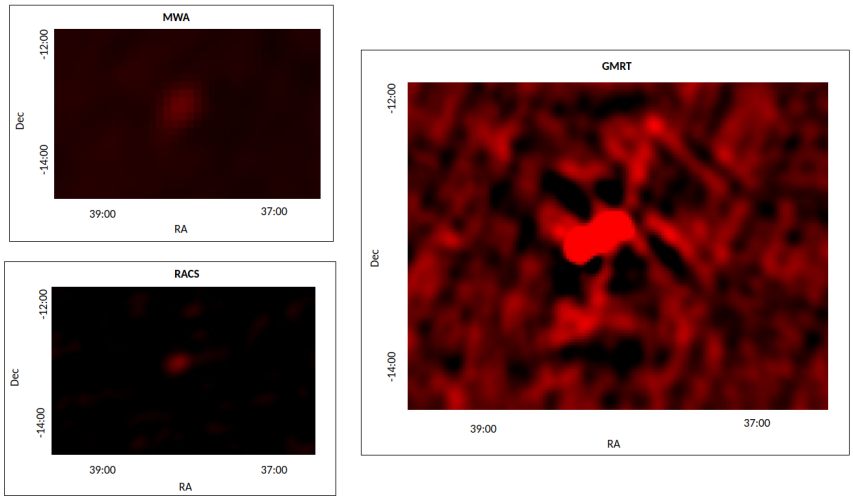

(a) GPM 1838-13

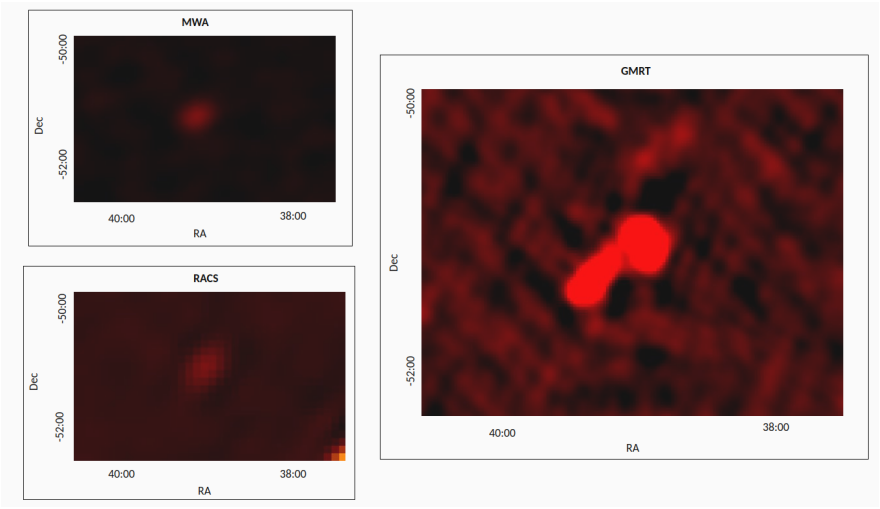

(b) GPM 1811-14

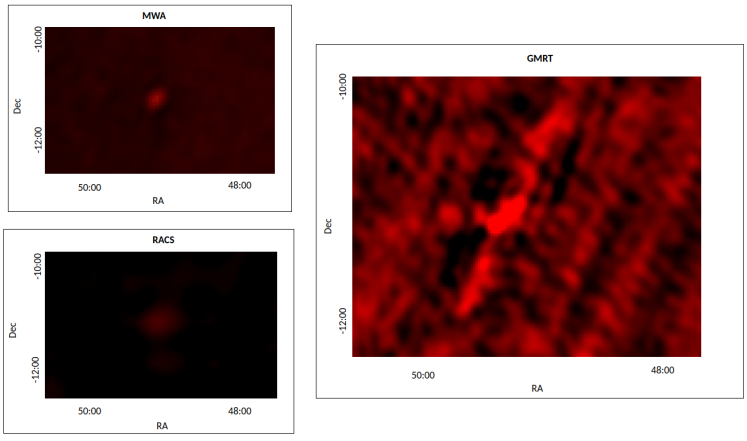

(c) GPM 1849-11

Figure 5.6: Cutout of images from Stokes I image from MWA, RACS and GMRT for the sources that turned out to be extended sources when observed with GMRT.

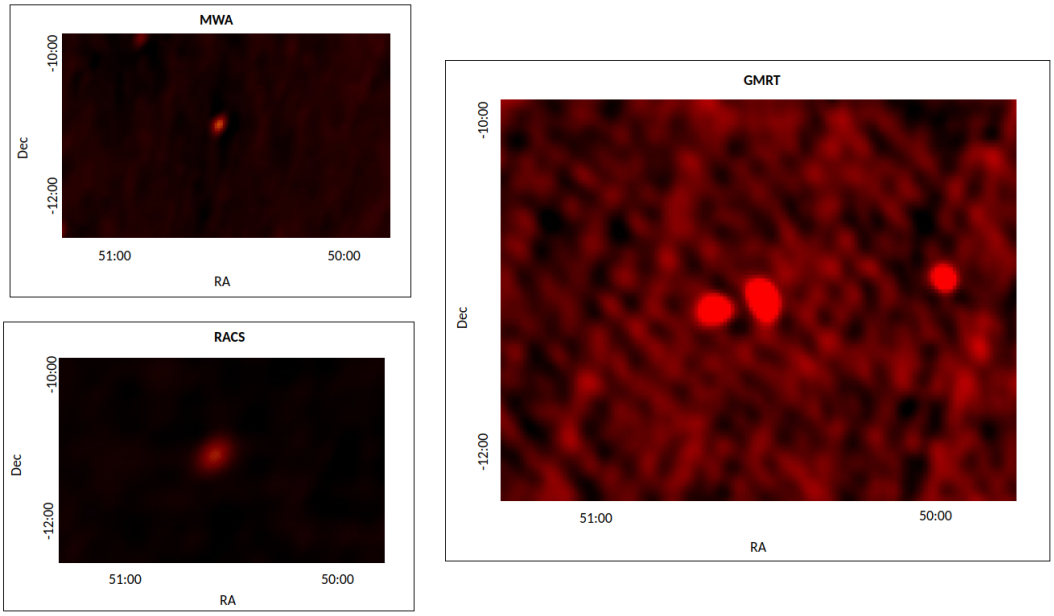

(a) GPM 1850-11

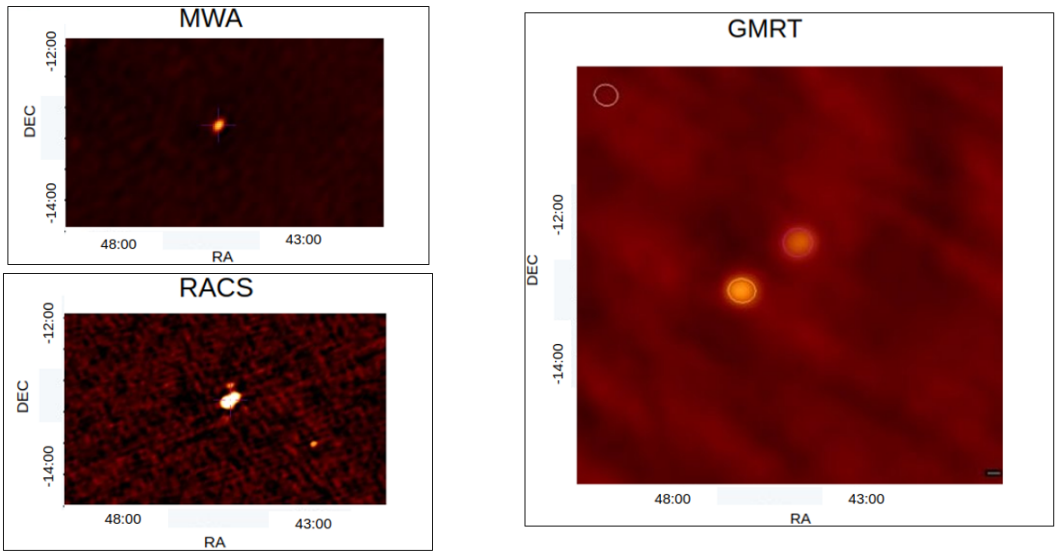

(b) GPM 1744-13

Figure 5.7: Cutout of images from Stokes I image from MWA, RACS and GMRT for the sources that turned out to be double sources when observed with GMRT.

extended sources such as AGN, radio galaxies etc., which is discussed in Section 5.4.3.

5.4.2 Efficiency of the criteria

The pulsars detected in the image domain can be used as an efficiency marker for the developed criteria. One way of doing this is by comparing the number of pulsars that are detected by the different criteria and comparing them to the number of candidates that each criterion selects. This method can help us understand the balance between actual pulsar detections and the number of false positives we get and improve the criteria such that we do not have numerous false positives when compared to actual detections.

Table 5.4 shows the number of candidates and the pulsars that were selected by each criterion before the criteria were combined. The table also shows the efficiency of each criterion when the number of candidates and pulsars are compared. The spectral index criterion works the best when compared to the other two criteria, detecting 50 pulsars and a manageable number of candidates (less than 1000) for follow-up. The circular polarisation criterion was able to detect six pulsars as candidates and therefore shows the potential of circular polarisation surveys to detect pulsars that may be missed by other criteria. The variability criterion was able to detect two pulsars. There are possible reasons for the low efficiency of the variability criterion. One of them can be that the pulsars detected in this survey do not vary on the timescales that our variability criterion is probing and makes them undetectable. As diffractive scintillation is the main cause of variability of the pulsars in our timescale of minutes it is most applicable to low-DM pulsars. Given that this work is focused on the GP, it is unlikely that the variability criterion will be performing to its full potential due to the dominant population of high-DM pulsars (order of 100s in the Galactic Plane).

Table 5.5 shows the candidates and the pulsars detected when the criteria are combined. The combination results in a reduction in the number of candidates.

Four pulsars were detected by the combined criteria of steep spectrum and circular polarisation and two with the combined criteria of steep spectrum and variability. The other combinations do not yield any pulsar detections. Even though the combination of the criteria reduces the number of candidates, one has to be careful while combining the criteria. This is because it may happen that the combination of the criteria can excise good pulsar candidates that do not satisfy more than one criterion. This discrepancy in selecting candidates when combined criteria are applied arises mainly from the less understanding of the criteria. For example, the circular polarisation criteria may not be extremely reliable due to less reliable beam model leading to inadequate leakage characterisation.

Overall, we conclude that the steep spectrum criterion is better than the other two when a combination of criteria is not done to select pulsar candidates. Circular polarisation has its own advantage of being less affected by confusion noise and can be useful in detecting pulsars that may be missed in Stokes I image due to increased noise. However, not all pulsars have circular polarisation and for some of the pulsars, the mean circular polarisation is zero due to sign flip. Variability criterion will be most fruitful if used for detecting low DM pulsars that are affected by diffractive scintillation. When criteria are combined, the combination of steep spectrum and circular polarisation works better than the other combination and has the highest efficiency. In an ideal case, one would follow up on all candidates, but due to the constraints of telescope time and computational costs, combining the criteria to rank the candidates is the best way to reduce the number of follow-up candidates and select the best possible candidates for future work.

Criterion	Candidates	Pulsars amongst candidates	Efficiency %
Spectral index	1000	50	5
CP	150	6	4
Variability	200	2	1

Table 5.4: Table showing the efficiency of the criteria without combination. It shows the candidates that each criterion selects and the corresponding pulsars that are selected. The last column shows the efficiency percentage for each of the criteria. Spectral index criteria perform better than the other two criteria.

Combined Criteria	Candidates	Pulsars amongst candidates	Efficiency %
Spectral index + CP	45	4	8
Spectral index + Variability	100	2	2
CP + Variability	15	-	-

Table 5.5: Table showing the efficiency of the combined criteria. It shows the candidates selected by each combined criterion along with the corresponding pulsars detected. The final column indicates the efficiency percentage for each criterion.

5.4.3 Interpretation of the pulsar candidates

Given that none of our candidates was confirmed as a pulsar, the natural question to follow is what could be the reasons for the non-detections and if these sources

are not pulsars, what could they be? Earlier pulsation searches of similar kind (Damico et al., 1985; Crawford et al., 2000; Kaplan et al., 2000b) based on the X-ray, optical and infrared counterparts, concluded that most of their sources were extragalactic. However, these radio sources can belong to a wide variety of objects or maybe a new class of objects being discovered through radio imaging surveys. In the following subsections, we discuss the different classes that these radio sources may belong to based on their characteristics.

5.4.4 Pulsar interpretation

Though we did not detect any pulsations from the compact sources, the steep spectrum, high degree of circular polarisation and variability make the sources compelling pulsar candidates. If we assume that the sources are indeed pulsars, there are possible effects that could prevent detection of them as pulsars and can be broadly divided into three categories: propagation effects, 3D spatial and emission geometry of the pulsars and the orbital components of the system. In the following subsections, we discuss if these scenarios can explain the non-detections of the underlying pulsar population in the sources we detected in our work as pulsar candidates.

5.4.4.1 Propagation effects

One of the many propagation effects that may hinder detection is scattering in the ionised interstellar medium (ISM). Scattering that occurs in the ionised interstellar medium causes a broadening of individual pulses emitted by pulsars. This broadening effect is heavily influenced by the observing frequency and DM of the source and becomes more pronounced at lower frequencies and higher DMs. In certain cases, depending on the observing frequency and DM, the scatter-broadened pulse width could become as wide as, or even wider than the pulse period, making detection of pulsations impossible (due to reduced signal-to-noise ratio). For example, the non-detection of sources with steep spectra and high

circular polarisation (10% - 20%) as pulsars can be attributed to the pulses being scatter broadened (Hyman et al., 2021a).

To investigate the effect scattering would have on our sources, we calculate the maximum Galactic DM if these sources were at the edge of our Galaxy using electron density models by Yao et al. (2017) and Cordes (2004), hereafter referred to as YMW16 and NE2001 respectively. The average expected DM for the sources according to both the models is more than 250 pc cm^{-3}. At low frequencies such as that of the MWA (185 MHz), the scattering timescale is expected to be $\sim$ 1 s and for that of Parkes frequencies (700 MHz) is $\sim$ 1 ms. It means that for a source to be detected as a pulsar should have a period comparable to or longer than the scattering timescale at the particular frequencies. Otherwise, our time-domain searches would be affected by scattering and lead to the non-detection of pulsations.

Diffractive scintillation can be another possible propagation effect that may have caused our non-detections. We can calculate a scintillation bandwidth in MHz using equation 1.10 (Kolmogorov scaling dependence, Hallbäck et al., 1996):

$$\Delta\nu_{scint} \simeq 11\nu_c^{4.4} d^{-2.2}, \tag{5.1}$$

where ν_c is the central observing frequency in GHz, and d is the source distance in kpc. If the sources are at the edge of the Galaxy, the scintillation bandwidth is significantly smaller than that of our observing bandwidth for both MWA and Parkes and hence diffractive scintillation may not be a potential impediment to detection. However, we should note that it does not take into account the large degree of variability in the scintillation bandwidth as a function of the position of the source in the sky. We calculated the predicted scintillation bandwidth for all our sources and concluded that their non-detections are not likely to be caused by scintillation effects.

We performed pulsation searches in the time series up to DM = 1000 pc cm^{-3}, which is more than the NE2001 and YWM16 predicted DM when the sources are

at the edge of the Galaxy. Hence it is not possible for dispersive smearing to make pulses of these sources undetectable. Given the high flux densities of the source, they are likely to be nearby objects and, hence, unaffected by dispersive smearing.

5.4.4.2 3D spatial and emission geometry

The observed periodic signals from pulsars are caused by the misalignment of their rotation and magnetic axes, as well as the beaming of radio emission around the latter. It has been seen that these axes may approach alignment with age, on typical timescales of 10^7 years (Tauris & Manchester, 1998). If the magnetic inclination angle approaches but remains larger than the half-opening angle of the radio beam, then the main observable effect would be an increase in the pulse duty cycle. As the overall flux is spread out over more bins and harmonic summing in the Fourier domain search becomes less effective, detecting periodic signals with large duty cycles becomes harder for periodic pulsar searches. Less than 1% of known pulsars have pulse widths wider than half their rotation periods. For periods longer than 100ms, only a few pulsars such as PSR J1732-3131 (Maan et al., 2012) have intrinsic emission that spans a significant fraction of the period. So, it may be a possibility that our sources are large duty-cycle pulsars due to the near alignment of their rotation and magnetic axes. Probing such a scenario where the pulsed flux density is only a few per cent of the total observed emission would require significantly deeper observation to confirm these sources as new pulsars.

When the magnetic inclination angle is comparable to or smaller than the half-opening angle of the radio beam, a significant portion of the radio emission would appear as continuous emission, which is different from the typical pulse shape for most pulsars. For a nearly aligned rotator, this variation is expected to cause modulation in the observed flux density for the pulse period. In some pulsars such as PSR J0218+4232, only a part of the radio flux is pulsed with

a large duty cycle (Navarro et al., 1995). Therefore, if our sources were nearly aligned rotators then detecting these sources as pulsars where the flux that is pulsed is only a few percent of the total observed emission would be difficult. Deeper observations would be required to probe such a scenario.

5.4.4.3 Orbital components of the system

The detection of pulsars in tight and relativistic binary systems is difficult due to the signals experiencing varying Doppler shifts depending on the orbital phase. As we have searched for acceleration up to 300 m s^{-2} in both our MWA and Parkes observation, it is sufficient to detect all currently known relativistic double neutron star binaries. However, it might be that our search was not sensitive to orbital periods shorter than that of an hour. To date, the shortest binary detected is in a 75-minute orbit binary pulsar, PSR J1653-0158 (Nieder et al., 2020), with no detections of such systems with no orbital periods lower than that. Hence, a system with an orbital period shorter than an hour is extremely rare and an insufficient acceleration search is not likely to be a reason for pulsar non-detection.

5.4.4.4 Other factors

Pulsar signals at low DM have a possibility of getting flagged as RFI. For several of our Parkes follow-up observations, a significant amount of data needed to be flagged due to RFI and there is a possibility of removal of low-DM pulsars during the RFI excision process.

If some of these sources are RRATS (McLaughlin et al., 2006), or intermittent or nulling pulsars, it may happen that the follow-up observations to confirm the pulsar nature of the sources were ill-timed. It means that the sources were not active at the time of observation and hence were not detected. We can potentially increase the chances of the detection of these sources by longer follow-up observations in the future and commensal observations with the MWA and Parkes Radio Telescope.

5.4.5 Other transients

If these sources are not pulsars, they may still be some other categories of transients such as magnetars, X-ray binaries or tidal disruption events. In this section we discuss the possibility of a subset of our candidates falling into this category.

Magnetars: Magnetars are neutron stars in which a strong magnetic field is the main energy source. They are generally characterised by their circular polarisation and variability and have an X-ray counterpart. Magnetars typically are sources that do not have a steep spectrum. Taking these characteristics into consideration, 1% of our candidate sources fall into the category of magnetars. Searching archival observations of telescopes such as MWA, GMRT, and VLA to detect the sources can help in constraining the period derivative and understanding more about the properties and emission mechanism of the sources. Similar work has been done by Hurley-Walker et al. (2023) leading to the detection of ultra-long period magnetar repeating since 1988.

X-ray binaries: X-ray binaries are a common population towards the GP (Hailey et al., 2018) and can have circular polarisation and show variability which is consistent with a subset of our candidates (less than 1% of candidate sources). The extremely steep spectrum sources are inconsistent with the expectations of the production of a steady jet such as from low-mass X-ray binaries (LMXBs) (Fender, 2006). As LMXBs are hard to detect in radio frequencies as they are much fainter than their X-ray counterpart, there are only a few NS LMXBs detected in radio (Tudor et al., 2017; Gusinskaia et al., 2020). Crossmatching these sources with radio catalogues at higher frequencies would be helpful in confidently attributing them to the category of X-ray binaries.

Gamma ray bursts (GRB) afterglow and other extragalactic transients: The short variability timescales ($\sim$ minutes) for our work rule out sources such as GRB afterglows ($\sim$days, Frail et al., 2000), supernovae ($\sim$days, Dubner & Giacani, 2015) and tidal disruption events ($\sim$months, Gezari, 2021).

5.4.6 Stellar interpretation

One of the possibilities is that some of our candidates are stellar objects such as flare stars or magnetic cataclysmic variable stars (CVs). This interpretation is applicable to sources that are moderately bright and either circularly polarised or variable.

Flaring is a common characteristic of magnetically active stars and is driven by reconnection events that convert magnetic energy to particle kinetic energy and bulk plasma motion. Candidates that are moderately bright and show high circular polarisation could possibly be flare stars. However, there are various avenues that one needs to explore before confirming such an interpretation. Previous detection of polarised flares from UV Ceti by Lynch et al. (2017b) shows evidence that MWA can detect polarised flares from UV Ceti-like flare stars. Lynch et al. (2017b) states that the polarisation behaviour is due to a highly inclined magnetic axis. If any of our sources that satisfy the above criteria is a UV Ceti-like flare star, we can estimate its brightness temperature at a typical MWA frequency of 184 MHz and determine if it is driven by coherent or incoherent emission. Equation: $S_\nu = 2k_B T_b \left(\frac{\nu}{c}\right)^2 \left(\frac{l}{d}\right)^2$ from Dulk (1985) can be used to determine the brightness temperature for a UV Ceti like flare star, where k_B is the Boltzmann constant, T_b is the brightness temperature of the emission at a frequency ν, c is the speed of light, l is the size of the source and d is the distance to the source.

The brightness temperature of an incoherent synchrotron emission by inverse Compton scattering is $< 10^{12}$ K. (Dulk, 1985). Brightness temperature greater than this number can be explained by coherent emission mechanisms such as plasma emission or electron cyclotron maser (ECM; Treumann, 2006) emission. Even though our variable sources show flare-like behaviour as shown in Figure 5.8, they possess very low circular polarisation (7-20 %) as opposed to the previously reported circular polarisation of flare stars which are as high as 70 % (Lynch et al., 2017b). Low circular polarisation of the sources that show flares can be

explained when the multiple pulsations of the sources are blended into one pulse resulting in a reduced circular polarisation. Therefore, it is highly unlikely that our sources are indeed flare stars. Further optical and infrared investigation of the sources is required to confirm the origin of such flaring activity.

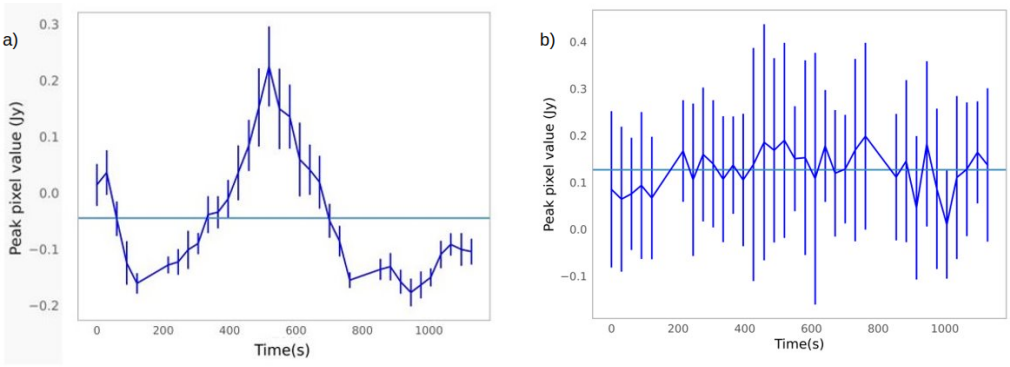

Figure 5.8: Figure a) shows a flare-like activity for a source when compared to a non-variable source within a 3-degree radius as shown in Figure b). In Figure a) we can clearly see a rise and then decline in the flux of a source signifying a flare-like behaviour.

Another stellar object category that may be applicable to our sources is magnetic cataclysmic variables (CVs). This is most relevant to sources that are bright and variable in timescales of minutes (5% of our candidates). In particular dwarf nova-type cataclysmic variable stars, nova like systems show variability in timescales between 1min and 5min. These systems have an outbursts and interval phase, such that a constant flux density is maintained in the interval phase with a sudden change in flux, by several orders of magnitude seen in the outburst phase. Similar phenomena is seen in novalike variable RX Andromedae with a significant rise in flux density in 4 minutes (Coppejans et al., 2016). Such emission is non-thermal and is consistent with synchrotron or coherent emission (Coppejans, 2015). An example lightcurve of such an outburst is shown in Figure 5.9, varying on a timescale of 5 min for the whole observation. Figure 5.9, (b) is the reference light curve for a non-variable source that is near the variable source. This is a check that this variation is not due to processing error or imaging artifact.

A stellar-like interpretation, especially CV-type variability is applicable to $\sim$

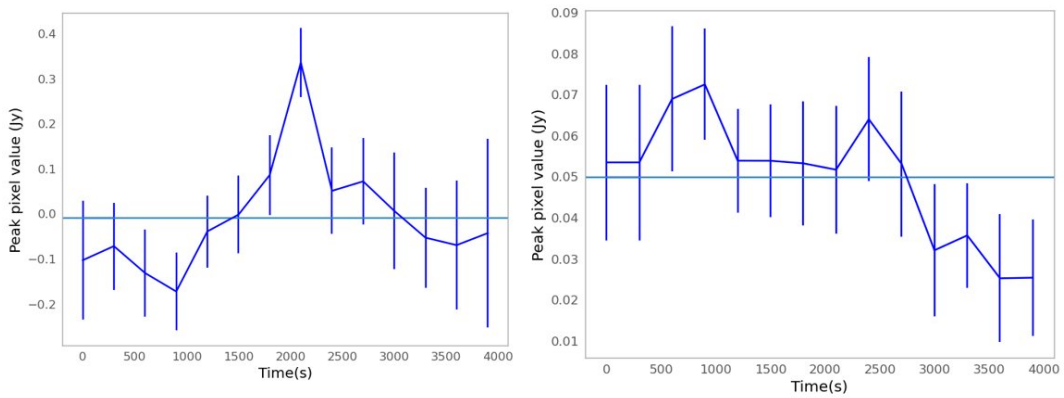

Figure 5.9: Figure a) shows the variable nature of a source undergoing a gradual rise and fall in flux density similar to that for cataclysmic variable (CVs) when compared to a non-variable source near it as shown in Figure b).

5% of our sources and can be further confirmed by leveraging archival optical and infrared catalogues. The occurence of CVs in MHz radio frequencies is an unexplored space mainly due to observational bias as they are not typically bright at these radio frequencies. hence, searching these candidate sources in archival observations would be helpful in gaining further insight into the kind of emission and help narrow down this down.

5.4.7 Extrinsic effects

Extrinsic effects are applicable to candidates picked up by the variability criterion. As the variability timescales probed by our methodology is seconds to minutes, refractive interstellar scintillation (RISS) cannot be the cause of such variability as RISS can cause variability on timescales of weeks to months for radio sources (Lyne & Rickett, 1968). Due to the unknown distance to sources, the expected variability for refractive scintillation is less than 10% and decreases further with increasing distance (Cordes, 1978). Given that we select sources that modulate more than 20%, on timescales of minutes, none of our variable candidates can be explained by refractive scintillation as the timescale of variation for refractive scintillation is $\sim$ weeks to months.

Alternatively, we can consider if the observed emission can be caused by other forms of extrinsic variability or possibly a combination of extrinsic and intrinsic effects. For example, some radio sources can undergo extreme scattering events (ESE, Fiedler et al., 1987; Bannister et al., 2016) in which the emission is lensed by the plasma in the intervening medium. This could explain the low or even no circular polarisation observed in some of the variable candidates. In such a case, the radio light curve variability could be caused due to propagation effects while the polarisation is intrinsic to the source. However, given that ESE's have been seen at GHz frequencies (Fiedler et al., 1987) and the timescales of flux density variations for such ESEs are $\sim$ weeks it is highly unlikely or even impossible that any of our candidates are effects of ESEs.

Another effect that can give rise to such variability is gravitational lensing or plasma lensing. For example, a star with an active region could have different parts of that region magnified or demagnified which could increase the flux in some parts of the observations relative to other bands and give rise to highly polarised emission. Multiple of these events are difficult to explain unless we have multiwavelength observations during the bright states of such a system to better characterise the light curve of these sources and confidently determine their nature to be a cause of extrinsic effects.

These speculations can be further confirmed by exploiting archival observations to validate the variability of the sources. Further information on longer timescales regarding the variability of the sources would be useful in characterising the sources.

5.4.8 Galactic Centre Rotating Transient like objects

As our observations focus on the GP, some of the sources are located near the Galactic centre and hence can be interpreted as Galactic Centre Rotating Transient (GCRT). GCRTs are a group of unclassified radio sources located towards the Galactic centre, with three of such objects detected so far (Hyman et al., 2005,

2021b). Some of the characteristics of the previously detected GCRT sources are shared with some of our candidate sources. For instance, GCRT J1742-3001 has a spectral index of ≤ -2 and the spectral index for GCRT J1745-3009 has a varying spectral index from -4 to -13. The spectral index for a subset of our sources vary from -5 to -1.2 which matches quite well with the recorded spectral index values of the previously mentioned GCRTs. The flux density of a subset of our very bright sources is $\sim$ 200 mJy to almost as bright as 400 mJy at 150 MHz, which is comparable to the extrapolated flux density of GCRT J1745-3009 ($\sim$400 mJy). GCRT J1745-3009 is thought to be a coherent emitter based on very rapid variability ($\sim$ mins) which is consistent with the variability timescales of our sources (2 sources). A variability light curve along with a reference light curve of a non-variable source within 3 arcmin of the variable source is given in Figure 5.10.

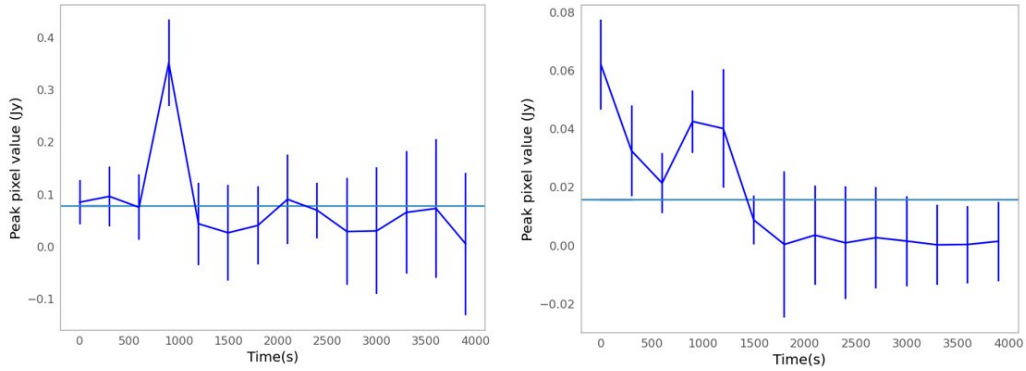

Figure 5.10: Figure a) shows the light-curve of a source from a non-zero flux density rising to a high flux density value and then declining to the previous state which is consistent with the variable nature of GCRTs. Figure b) shows a non variable source within 3 arcmin of the source of interest.

Some properties of GCRTs do not fully match with that of our candidate sources, namely circular polarisation. However, most of our candidates have much lower circular polarisation (10%) than typically observed in GCRTs (e.g. GCRT J1745-3009 have 100% circular polarisation). However, the exact nature and properties of GCRTs are not well understood due to a small sample known so

far. So, discarding this interpretation on the basis of circular polarisation is not justified, and we can still consider candidates near the Galactic Centre which are very bright, have steep spectrum, show circular polarisation and are variable as possible candidate GCRTs. Further multi-wavelength monitoring of such sources is needed to limit conclusions based on their temporal properties and determine if all GCRTs share a common origin.

5.4.9 Other radio objects

A large number of the steep spectrum sources can possibly be Active Galactic Nuclei (AGN). This is mainly applicable to sources that are steep spectrum and/or have rapid variability ($\sim$ seconds) and do not have circular polarisation. This category may be applicable to almost 70% of the sample in our candidate source list. AGNs make a huge percentage of bright sources in Stokes I images at MWA frequencies and hence a lot of our bright sources could be AGNs. Using available catalogues of sources at multiple wavelengths to rule out other possibilities such as pulsars, transients, and magnetars are required to confirm these sources as background AGN.

5.5 Summary and Conclusion

We have presented an image-based GP survey using MWA VCS data to detect pulsar candidates via image-based methodologies described in Chapter 3. We verified the detection of 83 known pulsars (see Chapter 4) and a list of candidates with pulsar-like properties such as steep spectrum, polarisation and variability. These candidates were then ranked according to the number of criteria they satisfied and were then searched for pulsations in the MWA data. The highly ranked candidates were then followed up with the Parkes Radio telescope, along with a subset of them being followed up with the Giant Metrewave Radio Telescope (GMRT).

The detections of known pulsars were used to test the efficiency of the criteria and their combinations. On comparing the number of pulsars amongst the candidates to the total number of candidates for each criterion we see that the steep spectrum criterion works better than the other criteria and combining steep spectrum with circular polarisation criteria shows better results than the other combinations. Circular polarisation is useful to detect the pulsars that are being missed by other criteria while variability is most applicable to low-DM pulsars that are affected by diffractive scintillation.

Given that none of the candidates was confirmed as a pulsar, there are several other possible interpretations. If they are still considered pulsars, several factors such as propagation effects, emission geometry and maybe aligned or near aligned rotators. We also explore the possibility of these candidates being other radio objects. Almost 70% ($\sim$ 1000 sources) of our candidate sample can be possible foreground AGNs. Around 5% ($\sim$ 50 sources) of the candidates can possibly be magnetic cataclysmic variables and further gamma-ray follow-up needs to be done to confirm the nature. Even though, 3% ($\sim$ 30 sources) show flaring activity the low circular polarisation (7-20%) makes them less likely to be flare stars unless their pulsations are blended leading to the case of low circular polarisation. A small subset of sources ($\sim$1%, 15 sources), that are circularly polarised and variable can be magnetars or X-ray binaries. However, these two categories do not apply to steep spectrum candidate sources at all. Steep spectrum sources that lie near the Galactic Centre, and satisfy all three criteria, which is the case for a very small subset of sources ($\sim$ 0.1%, 2 sources) could fall into the category of a GCRT. We also rule out the possibility of our variable candidates being caused by ESEs, tidal disruption events and supernovae as the variability timescales of these events are longer than what was probed in this work. An interesting possibility is that these sources we detect are not any of the above classifications but rather a new population of Galactic radio sources that share similar properties as pulsars but lack pulsations as first suggested by Maan et al. (2018). Overall, a large

number of interpretations is possible for these sources which can be confirmed by further deep follow-up of the sources with existing and upcoming telescopes.

Even though we detect interesting sources with the present state-of-the-art instruments, there are still areas of improvement required. The predominant factor affecting the detection of pulsars in the image domain with the MWA is sensitivity. This will not be a limiting factor in the future with telescopes such as the Square Kilometre Array (SKA) which will be much more sensitive in all-sky surveys. The low spatial resolution of the MWA also makes it hard to distinguish between truly compact sources and pseudo-compact sources (multiple sources blended into one). With the RACS mid and high frequency in the future, which will have better spatial resolution than the MWA, it will be easier to excise sources blended in MWA images but resolved in RACS images. This will be useful in detecting true compact sources and also prevent blending of the sources and accurately determine their spectral index. Even with the best beam model and calibration that exists for the MWA, improvements in the characterisation of the leakage exist which can be improved by using better beam model and calibration techniques. This will be useful in detecting sources with high circular polarisation which may be new pulsars. Future strategic observations such as observing the same patch of sky with observations separated by a few days will be helpful in targeting the sources that vary on the timescales of days or even weeks. Future large-scale surveys with more sensitive instruments having more sensitivity, better spatial resolution and leakage characterisation with a strategic observing campaign will be beneficial to detect any missed foreground pulsars or characterise the new emerging population of Galactic radio sources.

Chapter 6

Discussion and conclusion

6.1 Summary

The primary goal of this research was to demonstrate a complementary, image-based path to pulsar discovery and investigate its potential application to existing (MWA) and future (SKA-Low) low-frequency radio telescopes. Pulsars have been studied extensively over the last few decades and have proven instrumental in testing theories of general relativity and probing various areas of physics like nano-Hertz gravitational waves. Discovering more pulsars emitting at low radio frequencies is crucial to further our understanding of their spectral properties and emission mechanisms. The MWA VCS, operating at low frequencies of 70-300 MHz, along with its data processing flexibility provided a perfect opportunity to develop and test such image-based pulsar searches that can lead to the discoveries of new pulsars with existing and future instruments. Devising image-based techniques for identifying potential pulsars, which can later be confirmed using beamformed data, has the potential to expedite the entire process of discovering pulsars. The use of image-based searches to find pulsar candidates can decrease the number of tied-array beams needed, thus enhancing the efficient use of computational resources. Despite a factor of ~ 4 loss in sensitivity for image-based searches when compared to periodic searches, the pursuit of pulsar candidates

within images sourced from the MWA VCS allows us to investigate a broader range of parameters. This broader exploration could result in the detection of pulsars that might have been missed by high-frequency surveys, including those with steep spectra, unique binary systems, or pulsars obscured in high-resolution time-series data due to propagation effects. Additionally, image-based searches are crucial for exploring parameter regions that are inaccessible to traditional beamformed searches with the MWA, particularly those involving high dispersion measures.

Chapter 3 describes the imaging pipeline and the methodologies developed, as part of this work to detect pulsar candidates. The imaging pipeline was tested on four MWA VCS observations to produce full Stokes images, reaching an average RMS of 5 mJy/beam. This work was the first attempt at producing full Stokes images using the MWA VCS data and opened up new opportunities for the detection of pulsars. The Stokes I and V images from the four observations were used to develop and validate the three methodologies based on pulsar properties such as steep spectrum, circular polarisation and variability. Method I (steep spectrum) and method II (circular polarisation) were able to detect 50% of the known pulsars while method III (variability) was tested on a small number of test sources all of which were successfully retrieved after the application of the methodologies. The testing of the methodologies also resulted in a list of candidates that were beamformed and searched for pulsations using the very same MWA VCS data. However, we were not able to detect any pulsations. A combination of the criteria was also investigated to reduce the number of candidates and increase the confidence that the candidate may indeed be a pulsar. It is important to exercise caution when combining criteria, as there's a potential risk of overlooking interesting sources that may not fulfil multiple criteria simultaneously. Overall, the study successfully identified over 50% of the expected pulsars for each criterion, along with novel pulsar candidates. As image-based pulsar searches are a relatively new approach the success of the methodologies with the

MWA, is helpful in informing the need for similar image-based pulsar surveys with SKA-Low.

The imaging pipeline and the developed methodologies described in Chapter 3 were then applied to 12 MWA VCS observations covering the dense region of the Galactic Plane, to perform one of the most sensitive image-based pulsar searches using MWA VCS data to date. This work led to the detection of 83 known pulsars shown in Figure 6.1 and a list of promising pulsar candidates. As seen in Figure 6.1, most of the detections are in the main island of the pulsar population while also having a few detections of MSPs. This shows that imaging detections are not biased towards one type of pulsar population. Chapter 4 discusses the known pulsar detections and presents flux density measurements of these pulsars based on Stokes I images and demonstrates the significance of image-based flux density measurements for improving spectral modelling of pulsars. Out of the 83 pulsar detections, the work mainly focuses on the 66 pulsars that were detected through their averaged emission in wide-field MWA images. This image-based approach complements periodicity searches, as it remains unaffected by pulse scatter broadening or dispersion effects, enabling the discovery of pulsars that might have been overlooked by previous time domain searches. Improvements required for the detection of new pulsars in the image domain with the MWA are discussed in Section 6.2. Moreover, this work emphasizes the distinct parameter space that image-domain pulsar searches can exclusively access as shown in Figure 4.6. This includes pulsars with high dispersion measures (DM) and scattering, which can be challenging to detect at low frequencies using periodicity searches.

These flux density measurements include the first low-frequency flux density measurements for 14 pulsars. We conducted an initial investigation into the spectral indices of our sample and observed that our low-frequency measurements altered the spectral index model for 15 pulsars. Nevertheless, it's worth noting that these changes in spectral index models could be influenced by the absence of measurements at intermediate frequencies, or by the substantial frac-

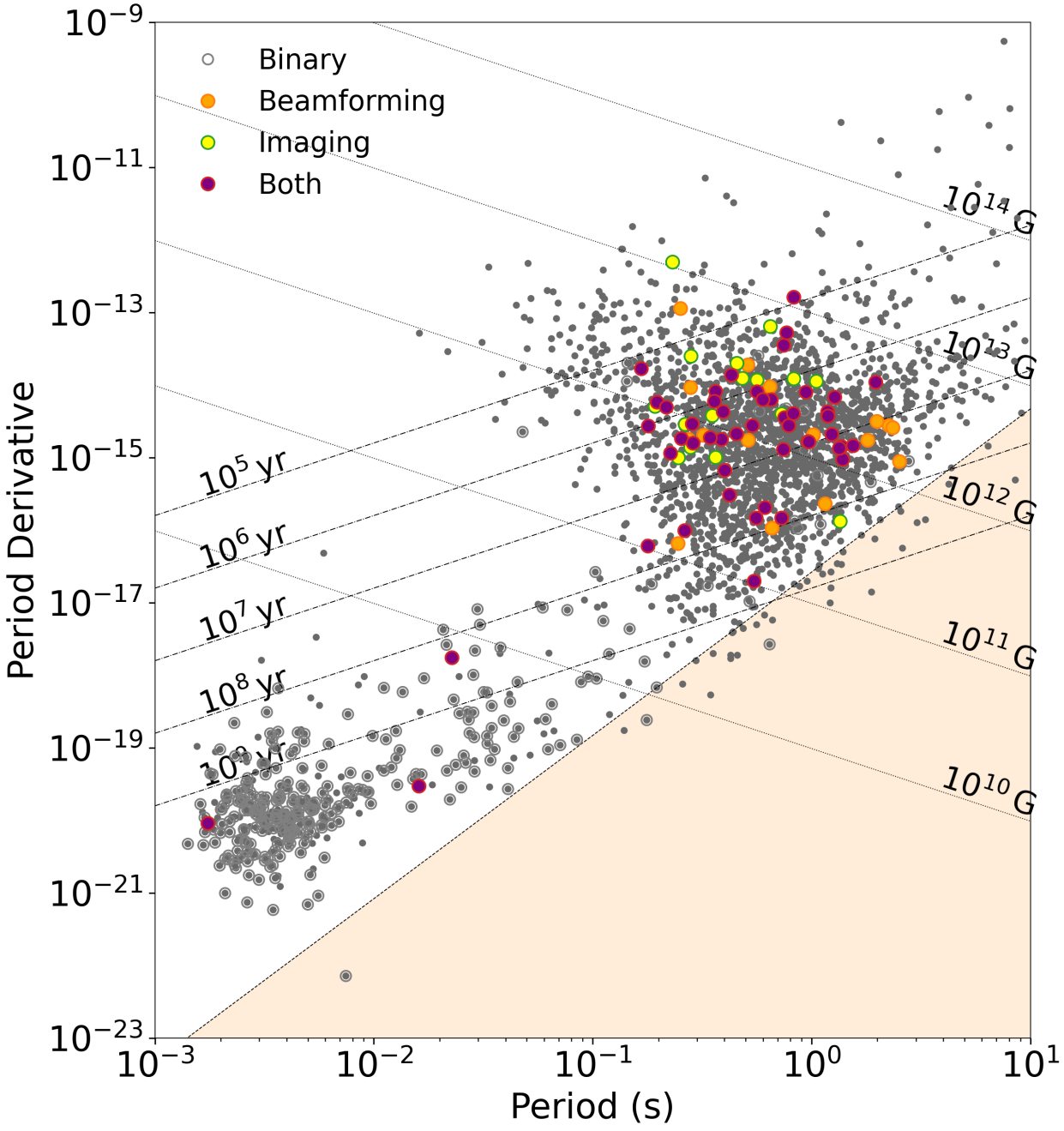

Figure 6.1: P-$\dot{\text{P}}$ diagram with the pulsars detected in this work shown in coloured dots. Purple dots are the pulsars detected in both beamforming and imaging, yellow are the pulsars that are detected in only imaging and orange are the pulsars detected in only beamformed searches.

tional bandwidth of existing measurements. Furthermore, the variability in flux density measurements due to scintillation can also impact spectral index modelling, potentially leading to over or underestimations on specific days. Overall, these measurements contribute to refining pulsar spectral models and addressing inquiries about the origins of low-frequency spectral turnovers.

Along with the pulsar detections, the work focused a Galactic Plane imaging survey, which resulted in 1350 pulsar candidates having one or more pulsar-like properties. The known pulsars among the candidates allowed us to evaluate the efficacy of individual criteria and their combinations. The assessment indicated that the steep spectrum criterion outperformed the others (5% efficiency), and the combination of circular polarisation and steep spectrum criteria, exhibited superior results than other combinations (8% efficiency). Circular polarisation proved valuable in identifying pulsars that might be overlooked by other criteria, while variability was most relevant for low-dispersion measure (DM) pulsars influenced by diffractive scintillation. All the pulsar candidates were followed up using MWA VCS data and searched for pulsations. The candidates were ranked based on the number of criteria they satisfied. The 30 most promising candidates were followed up using the Parkes (Murriyang) Radio telescope and five candidates were also observed with the Giant Metrewave Radio Telescope (GMRT).

Although none of the candidates were definitively confirmed as pulsars, various alternative explanations are plausible. If they are pulsars, their non-detections could be explained due to propagation effects, emission geometry, and potentially aligned or closely aligned rotators. We also examined the possibility of these candidates being other radio objects. Roughly 80% (around 1000 sources) of the candidate sample could be background active galactic nuclei (AGNs). Approximately 5% (around 50 sources) could be magnetic cataclysmic variables, warranting gamma-ray follow-up for confirmation. Although around 3% (approximately 30 sources) exhibited flaring activity, their low circular polarisation (7-20%) makes them less likely to be flare stars—unless their pulsations are

blended, leading to reduced circular polarisation. A smaller subset of sources (about 1%, 15 sources), displaying circular polarisation and variability, might belong to the magnetar or X-ray binary categories. In exceptional cases, steep spectrum sources located near the Galactic Centre that satisfy all three criteria (an extremely small subset of sources, approximately 0.1%, 2 sources) could fall into the Galactic Centre Radio Transients (GCRT) category. We ruled out the possibility of our variable candidates being attributed to ESEs, tidal disruption events, or supernovae, given the longer variability timescales of these phenomena compared to our study. An intriguing possibility is that the sources we've detected do not fall into any of the above classifications but could potentially constitute a novel population of Galactic radio sources, sharing properties with pulsars but lacking detectable pulsations, as proposed by Maan et al. (2018). In essence, a wide array of interpretations is feasible for these sources. Their confirmation will necessitate improved classification schemes using existing catalogues and archival observations and in-depth follow-up observations with existing and forthcoming telescopes.

6.2 Future improvements to image-based pulsar surveys

While we've identified compelling pulsar candidates using state-of-the-art instruments, there are still improvements that are required. The chief factor limiting pulsar detection in the image domain with the MWA is sensitivity. Existing telescopes such as Australian SKA Pathfinder Telescope (ASKAP), GMRT etc. with its advanced technology and increased sensitivity are proving useful in further facilitating the groundwork for future image-based pulsar search efforts. Furthermore, future telescopes like the Square Kilometre Array (SKA) are poised to alleviate this limitation by offering significantly enhanced sensitivity for all-sky surveys. Additionally, MWA's relatively low spatial resolution presents challenges

in distinguishing between genuinely compact sources and those that appear compact due to the blending of multiple sources together. The blending of the sources is more prominent in observations that have the Galactic Plane passing through the primary beam, leading to a higher density of sources in the Stokes I images. The blending of the sources leads to a higher flux density measurement and hence a steeper spectral index than what it should be. This means that our spectral index criterion may select sources that are not steep spectrum but blended with other sources, leading to false positives. A part of this problem can be solved using the RACS-Low catalogue (at 888 MHz), using ASKAP which has a better resolution than MWA. However, it is still not completely successful in determining whether a source is a real compact source. The forthcoming RACS mid and high-frequency surveys are anticipated to offer improved spatial resolution compared to MWA, enabling more accurate differentiation of compact sources and alleviating blending issues. Using the RACS mid and high catalogues will essentially lead to refining the criterion of steep spectrum and help in reducing the false positives.

While we were able to account for leakage up to 7%, further improvements would be required to probe sources with lower levels of circular polarisation. Despite having the best available beam model and calibration, there is room for enhancing leakage characterization through improved beam models and calibration techniques that would be helpful in reducing the effect of leakage. This would be especially advantageous in detecting weakly circular polarisation sources, which could potentially be new pulsars and improvement of our circular polarisation criterion.

Given that all of the pulsar candidates that we detect in this work are from individual observations, selecting more than one archival observation that covers the same patch of sky more than once would be useful in improving the confidence of the detections of pulsar candidates. This will also be helpful in probing variability timescales on the scales of hours and even days and months. This

would be a significant improvement in our criterion of variability and increase the parameter space that we probe in this work.

Future large-scale surveys equipped with more sensitive instruments boasting enhanced sensitivity, superior spatial resolution, and leakage characterization, coupled with strategic observing campaigns, hold the potential to uncover overlooked foreground pulsars or to shed light on the emerging population of Galactic radio sources.

6.3 Conclusion

The main objective of this study was to explore the significance of image-based searches at low frequencies for identifying new pulsars using existing and upcoming telescopes. The detection of known pulsars showed the use of such searches and highlighted the parameter space that is exclusively available to image-based searches. It also highlighted the importance of low-frequency flux density measurements in the spectral modelling of the pulsars and reported the first low-frequency flux density measurements for 14 pulsars.

This study also demonstrated the capability of the image-based methodologies leveraging pulsar observables as criteria for selecting pulsar candidates. Steep spectrum criteria proved to be a useful method to detect pulsars. However, combining the criteria was done in order to reduce the number of candidates, which may not always be optimal. All the pulsar candidates were searched for pulsations using MWA VCS data, while a subset of candidates were followed up using the Parkes (Murriyang) Radio Telescope and GMRT. Even though we were unable to detect any new pulsars in this pilot survey, it provided us with insights with regard to the improvements required for the future. With SKA-Low on the horizon, sensitivity will no longer be a limiting factor for all-sky imaging surveys. The issue of spatial resolution which causes pseudo-compact sources can be resolved by using the upcoming RACS-mid and high catalogues and the SKA-Low in the future. Improvements in the beam model of the MWA and better calibration

techniques will be helpful in better characterising the polarisation leakage. These improvements will help in revisiting and improving our methodologies of selecting pulsar candidates leading to less number of candidates and false positives.

Overall, this work establishes image-based searches and methodologies as a complementary method to periodicity searches, to detect pulsars and highlights the parameter space that is exclusively accessible to image-based searches leading to pulsar detection that may have been missed by previous periodicity searches. It also shows the importance of more low-frequency flux density measurements of pulsars and the improvements in spectral modelling with the help of these measurements. This work encourages more image-based pulsar surveys at low frequencies which will provide deeper insights into pulsar spectra, the Southern sky pulsar population, and the enigma of low-frequency spectral turnovers. The success of this preliminary endeavour underscores the potential of image-based techniques for detecting low-frequency pulsar candidates, enhancing future pulsar detection efficiency not only for the MWA but also for the SKA-Low.

Appendices

Appendix A

Appendix Title

A.1 COTTER

The COTTER software, developed by Offringa et al. (2015), is a pre-processing pipeline designed specifically for the processing of MWA data. It consists of several stages outlined as below:

1. Detection and flagging of RFI in cross-correlations is done using AOFLAGGER (Offringa et al., 2012b).

2. UV-FITS files or CASA measurement sets are created from the raw correlator files.

3. Bandpass corrections are then implemented and calibrated for the change in phase lengths.

4. Phase tracking is applied to the sky location that we are interested in.

5. Missing or incorrect data is flagged.

6. Finally, the visibilities are averaged in time, frequency or both to reduce

the data volume.

A.2 Stokes I images of the observations

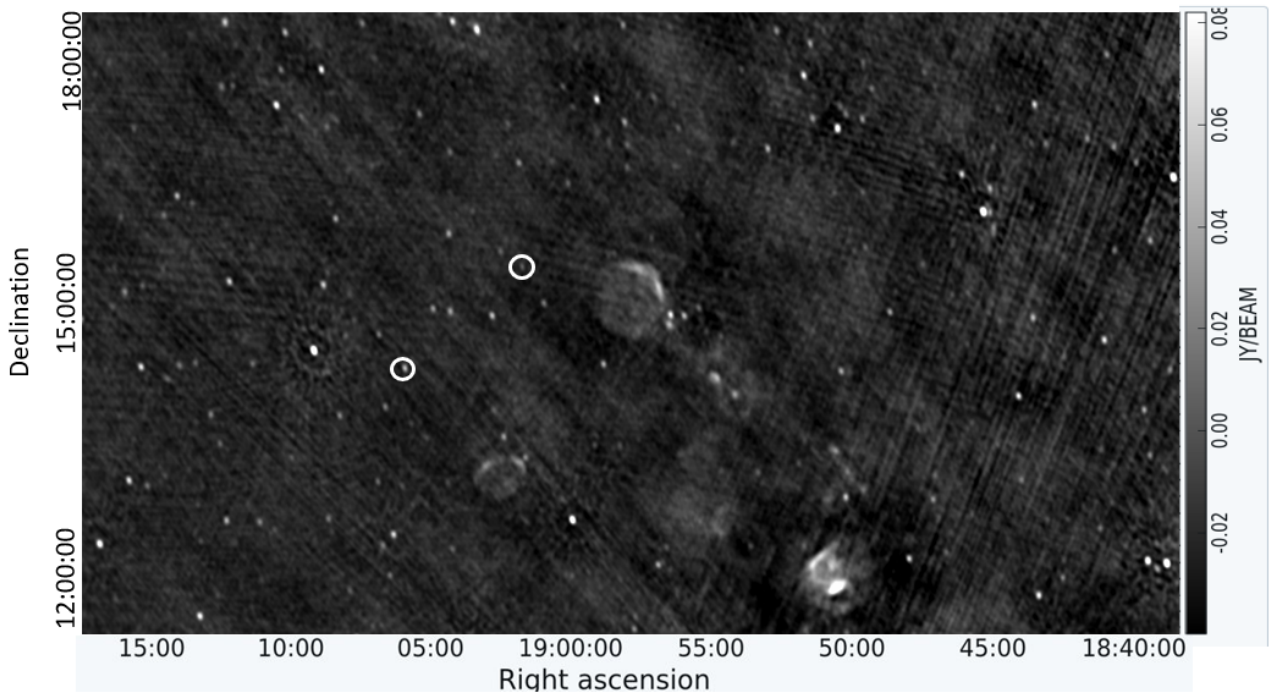

Figure A.1: Obs A, mean rms of 8 mJy/beam, number of pulsars detected is 4, number of sources is 1094

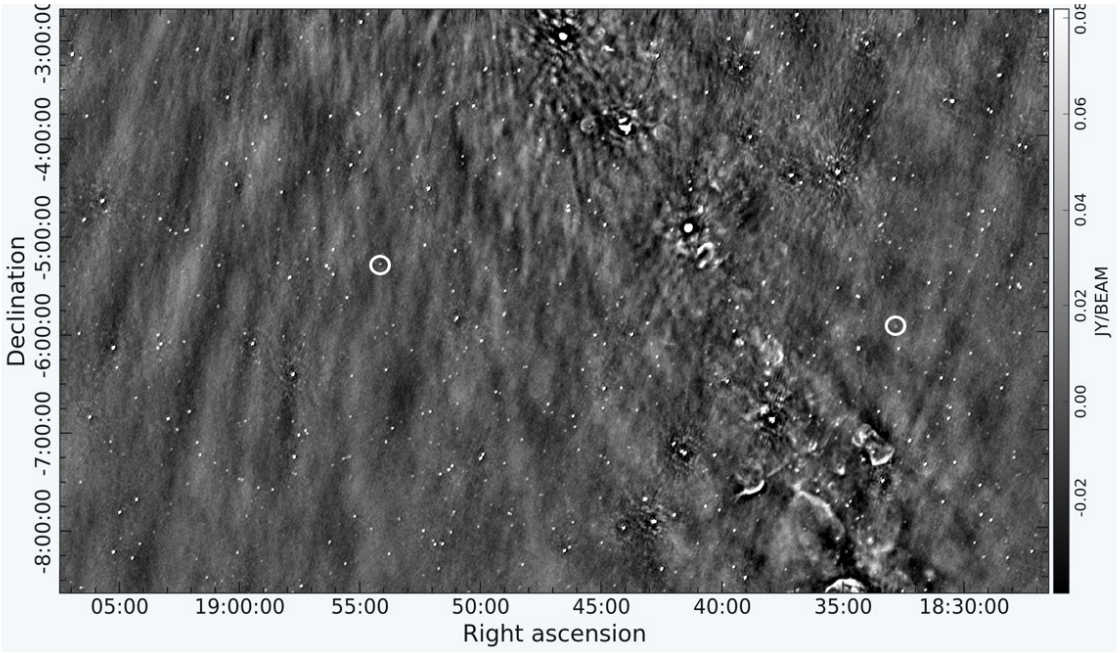

Figure A.1: Obs B, mean rms of 5 mJy/beam, number of pulsars detected is 7, number of sources is 9490

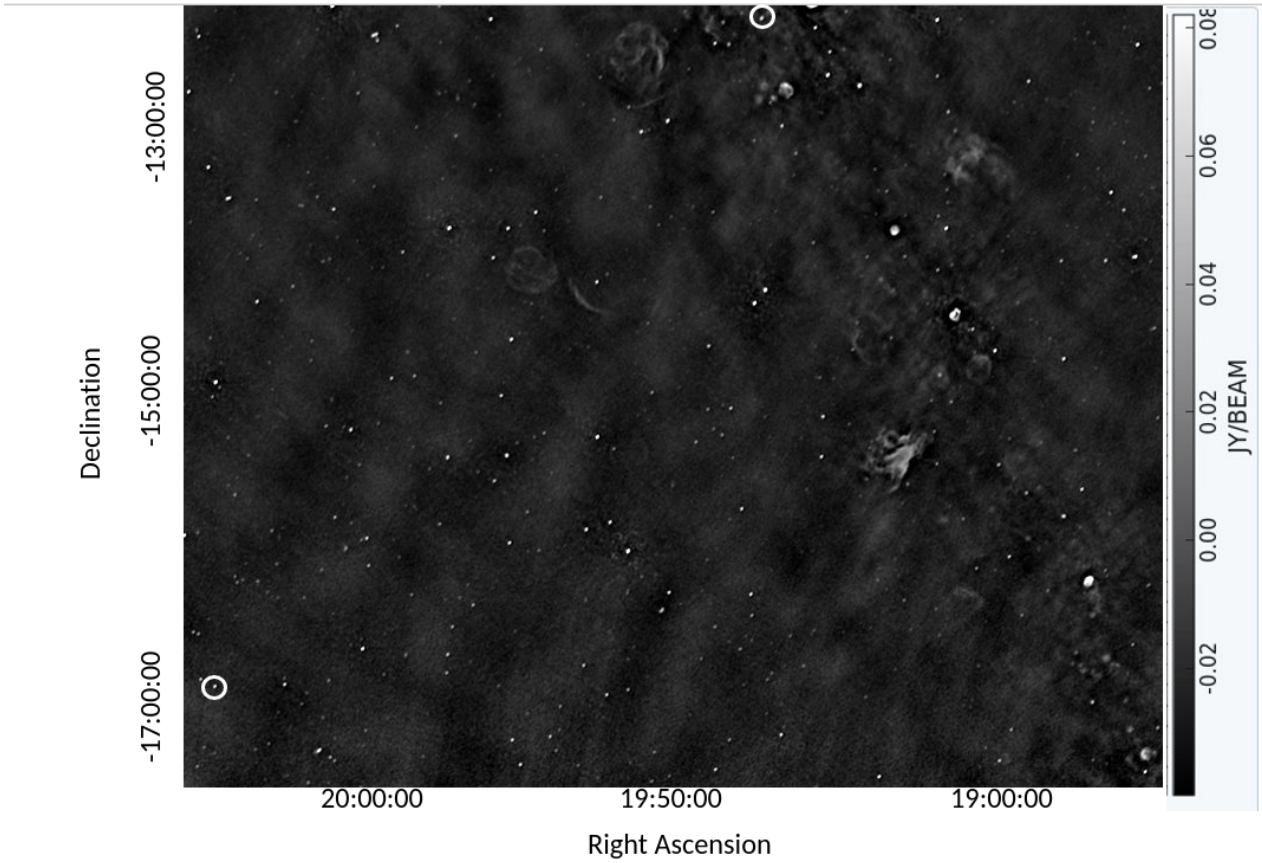

Figure A.1: Obs C, mean rms of 5 mJy/beam, number of pulsars detected is 7, number of sources is 9459

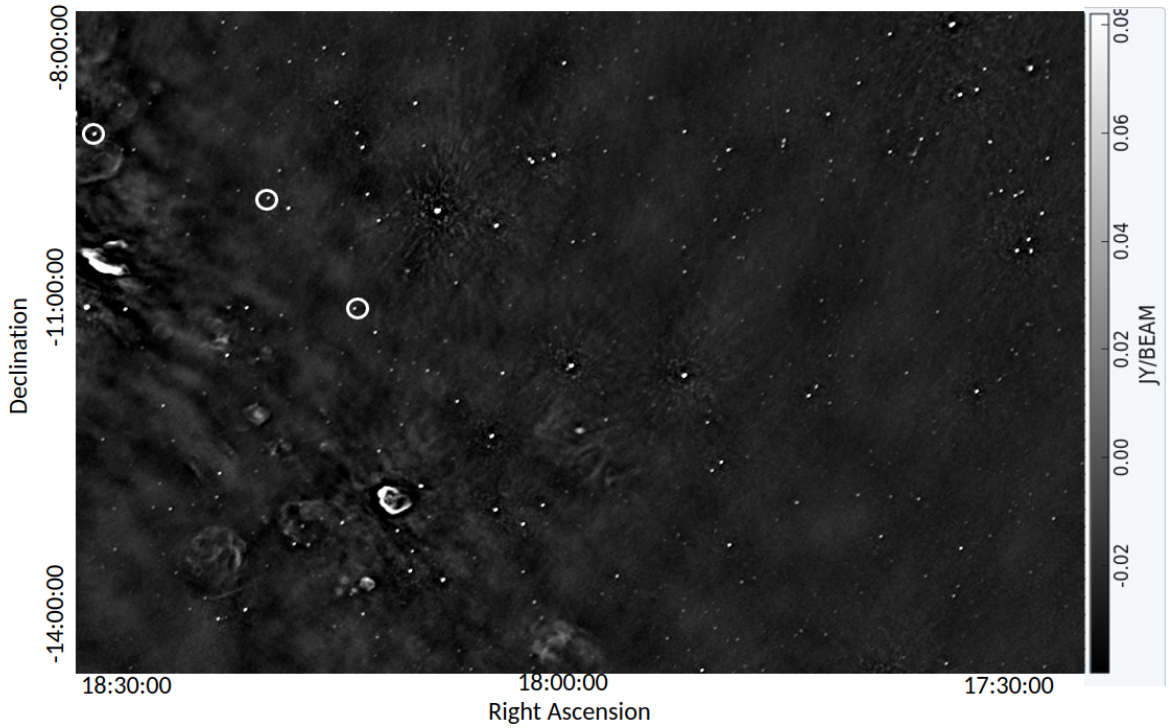

Figure A.1: Obs D, mean rms of 6 mJy/beam, number of pulsars detected is 6, number of sources is 4296

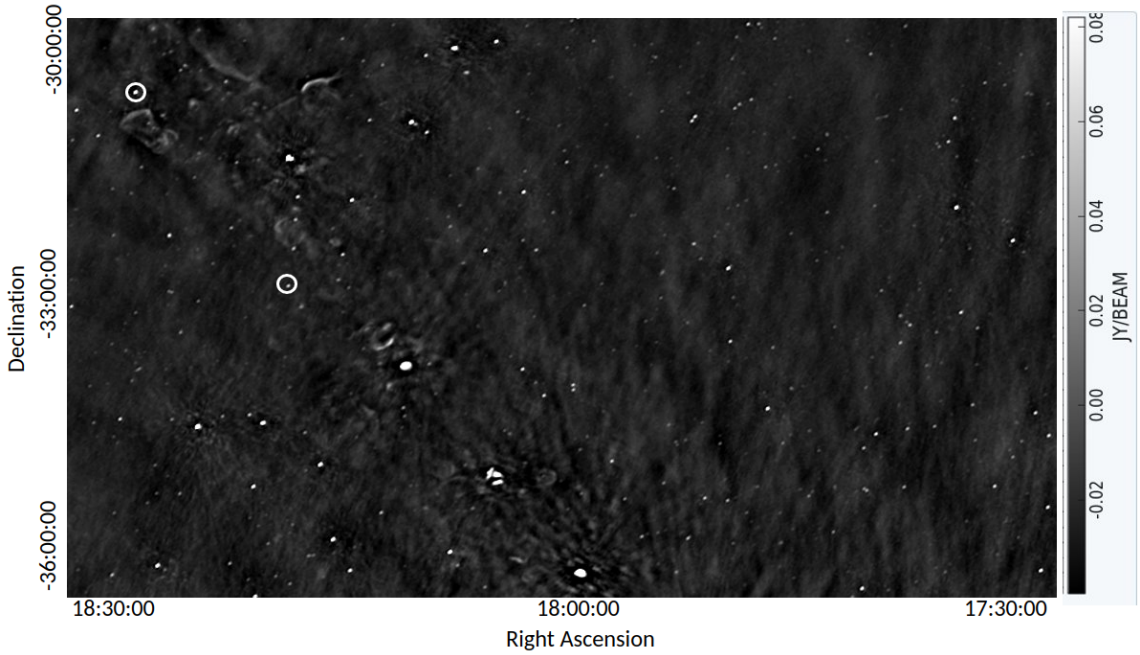

Figure A.1: Obs E, mean rms of 6 mJy/beam, number of pulsars detected is 6, number of sources is 4126

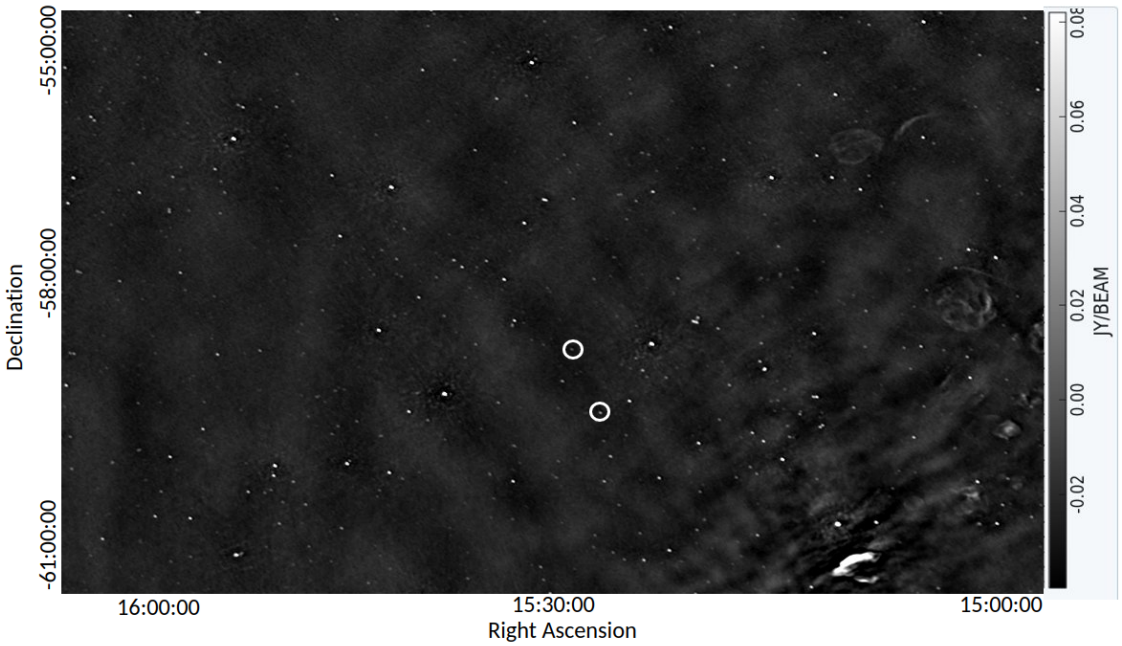

Figure A.1: Obs F, mean rms of 5 mJy/beam, number of pulsars detected is 8, number of sources is 5388

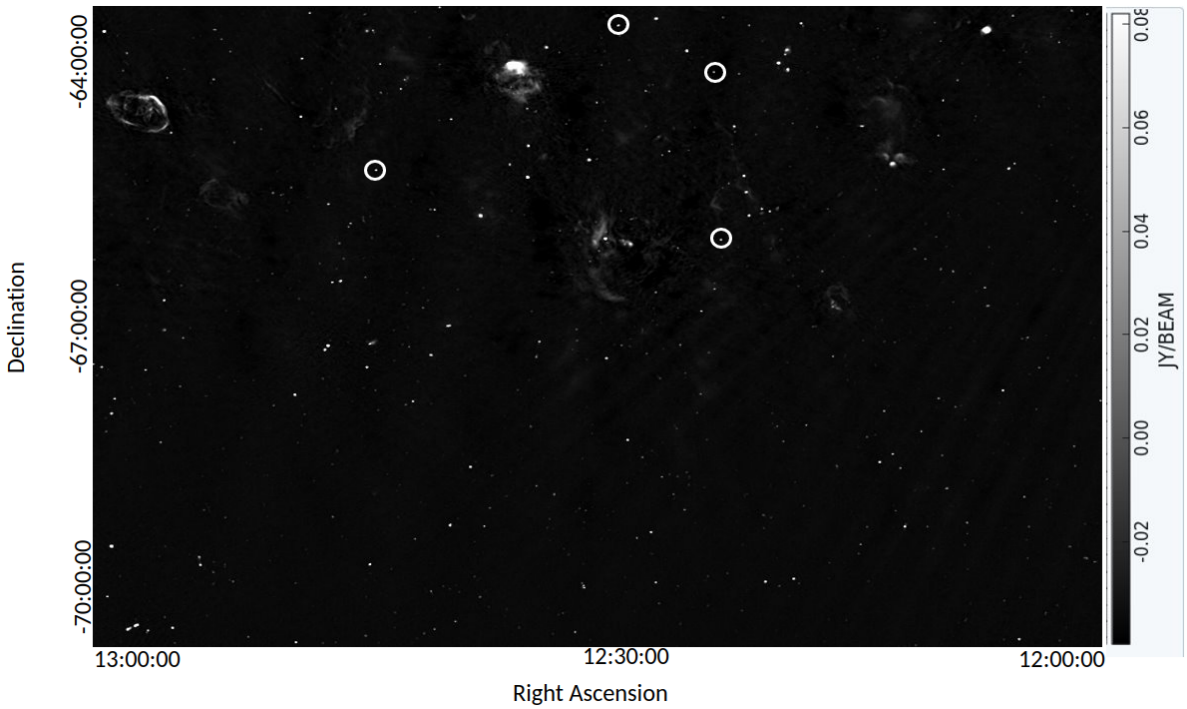

Figure A.1: Obs G, mean rms of 5 mJy/beam, number of pulsars detected is 12, number of sources is 9453

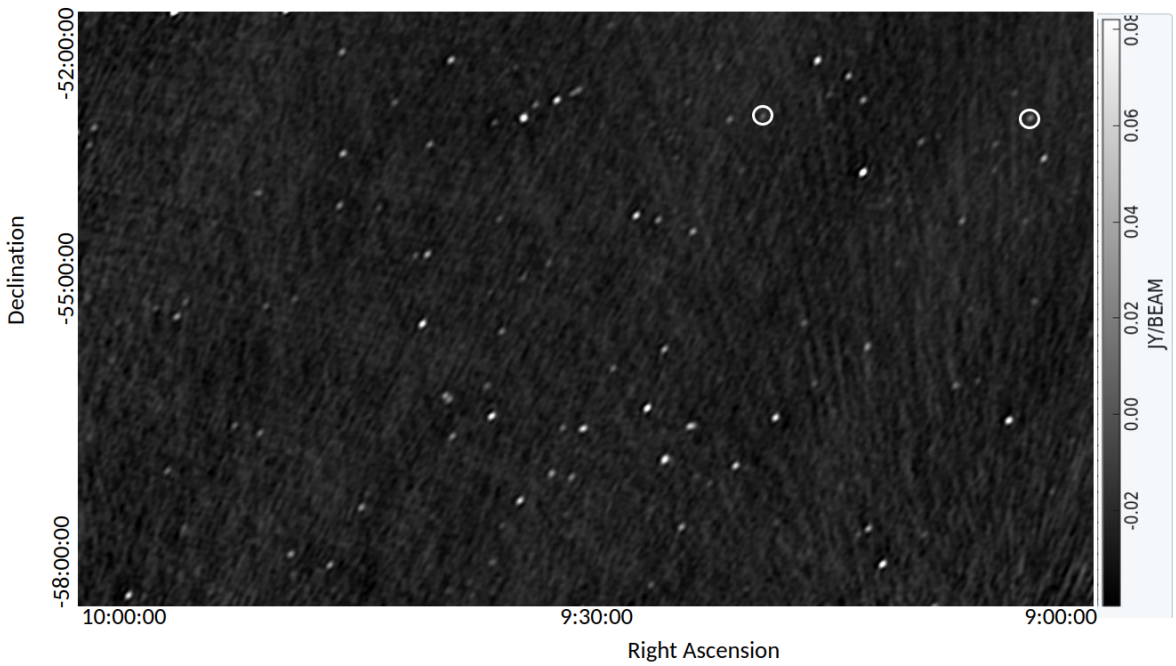

Figure A.1: Obs H, mean rms of 6 mJy/beam, number of pulsars detected is 7, number of sources is 1002

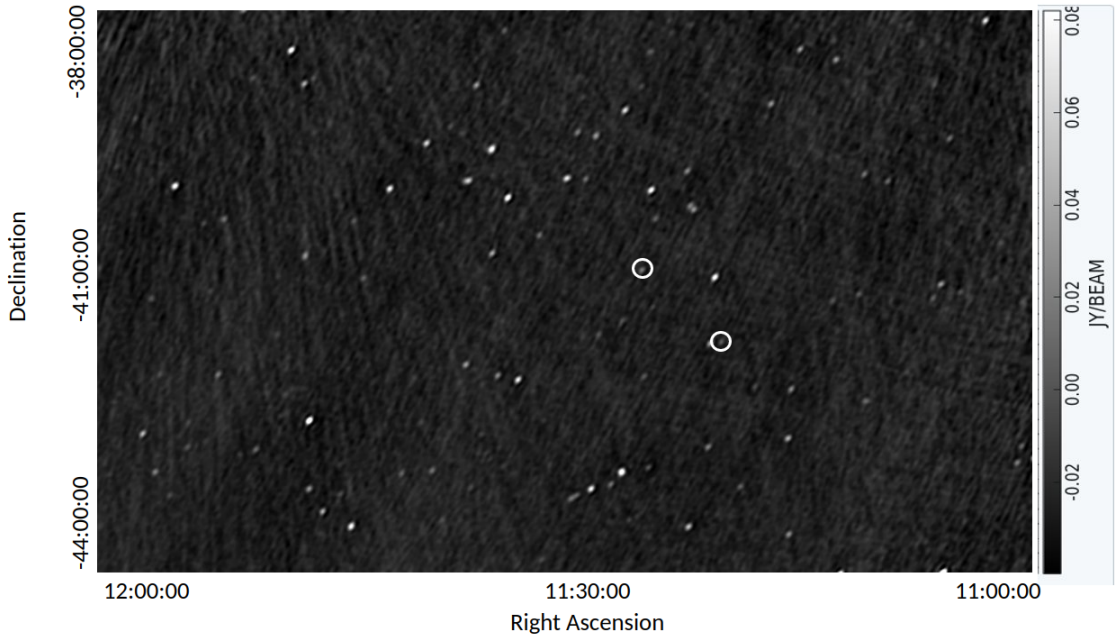

Figure A.1: Obs I, mean rms of 5 mJy/beam, number of pulsars detected is 8, number of sources is 1035

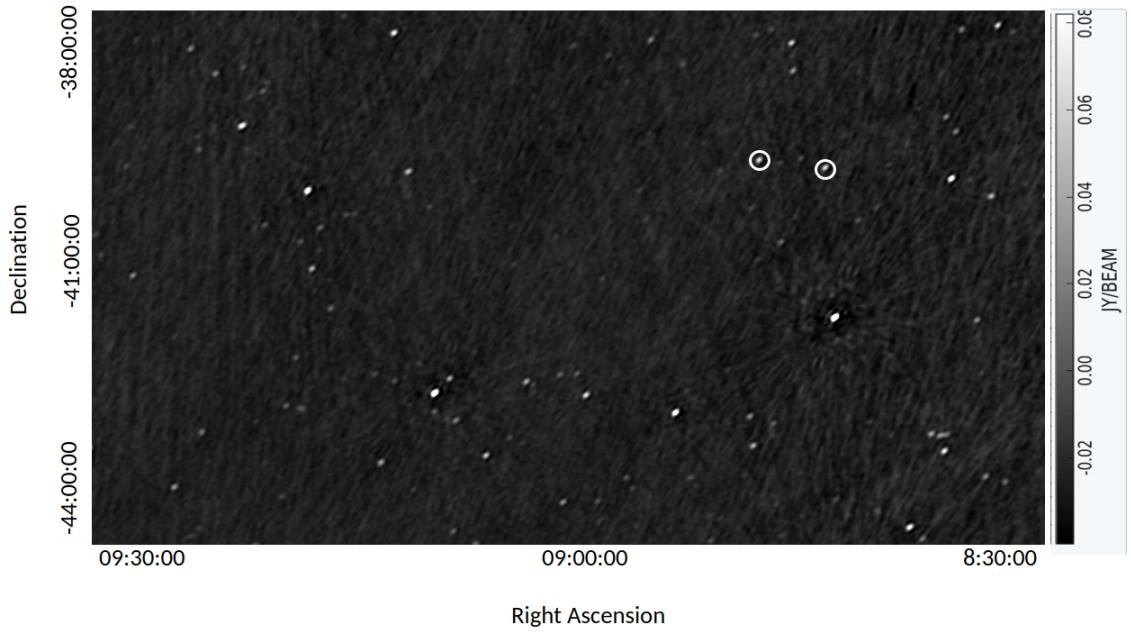

Figure A.1: Obs J, mean rms of 5 mJy/beam, number of pulsars detected is 6, number of sources is 1028

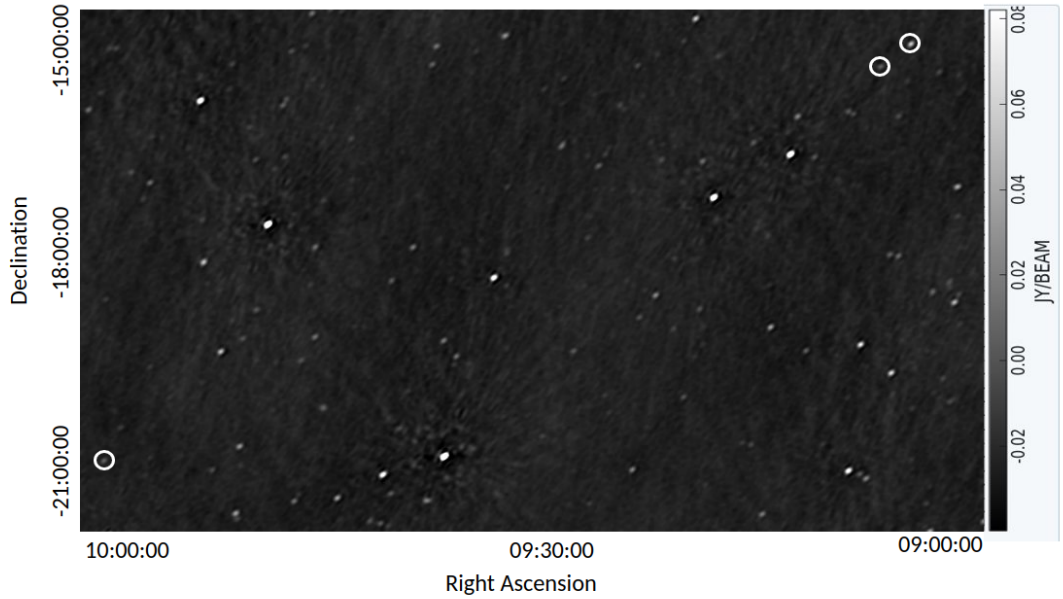

Figure A.1: Obs K, mean rms of 5 mJy/beam, number of pulsars detected is 9, number of sources is 3626

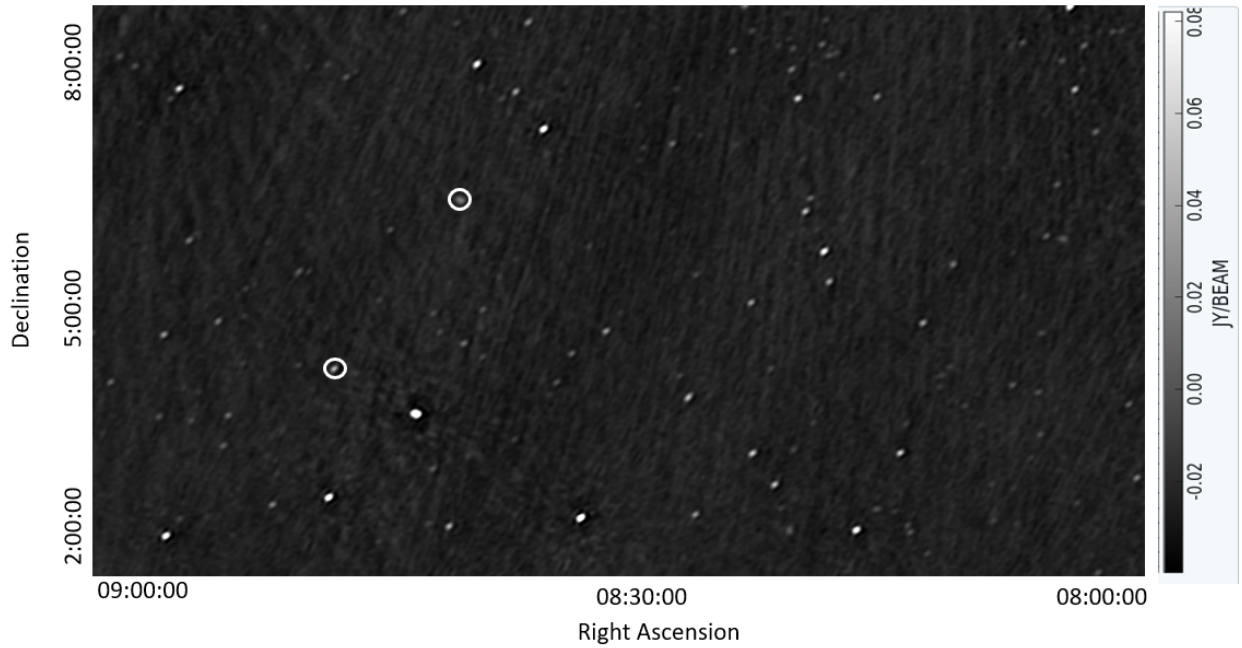

Figure A.1: Obs L, mean rms of 8 mJy/beam, number of pulsars detected is 3, number of sources is 968

Appendix B

Copyright Information

I, Susmita Sett, have outlined in the table below the contribution of the co-author to Chapter 3 of this thesis, "Methodologies to detect pulsars in high time resolution images using the Murchison Widefield Array", which is a reproduction of an already published work by Sett et al. (2023), accepted in Publications of the Astronomical Society of Australia, DOI:10.1017/pasa.2022.59

	Conception and Design	Acquisition of Data and Method	Data Conditioning and Manipulation	Analysis and Statistical Method	Interpretation and Discussion
S.Sett	✔	✔	✔	✔	✔
S.Sett Acknowledgment: I acknowledge that these represent my contribution to the above research output and I have approved the final version. Signed:					
N.D.R Bhat	✔	✔		✔	✔
N.D.R Bhat Acknowledgment: I acknowledge that these represent my contribution to the above research output and I have approved the final version. Signed:					
M.Sokolowski	✔		✔	✔	✔
M.Sokolowski Acknowledgment: I acknowledge that these represent my contribution to the above research output and I have approved the final version. Signed:					
E.Lenc		✔	✔	✔	✔
E.Lenc Acknowledgment: I acknowledge that these represent my contribution to the above research output and I have approved the final version. Signed:					

Bibliography

S. Abdollahi, et al. (2020). 'Fermi Large Area Telescope Fourth Source Catalog'. *The Astrophysical Journal Supplement Series* **247**(1):33.

J. G. Ables & R. N. Manchester (1976). 'Hydrogen-line absorption observations of distant pulsars.'. *Astronomy and Astrophysics* **50**:177–184.

G. Agazie, et al. (2023). 'The NANOGrav 15 yr Data Set: Evidence for a Gravitational-wave Background'. *The Astrophysical Journal Letters* **951**(1):L8.

M. A. Alpar, et al. (1982). 'A new class of radio pulsars'. *Nature* **300**(5894):728–730.

J. W. Armstrong, et al. (1995a). 'Electron Density Power Spectrum in the Local Interstellar Medium'. *The Astrophysical Journal* **443**:209.

J. W. Armstrong, et al. (1995b). 'Electron Density Power Spectrum in the Local Interstellar Medium'. *The Astrophysical Journal* **443**:209.

W. Baade & F. Zwicky (1934). 'Remarks on Super-Novae and Cosmic Rays'. *Physical Review* **46**(1):76–77.

D. C. Backer (1970). 'Pulsar Nulling Phenomena'. *Nature* **228**(5266):42–43.

D. C. Backer, et al. (1982). 'A millisecond pulsar'. *Nature* **300**(5893):615–618.

K. W. Bannister, et al. (2016). 'Real-time detection of an extreme scattering event: Constraints on Galactic plasma lenses'. *Science* **351**(6271):354–356.

J. Banyer, et al. (2012). 'VAST: A Real-time Pipeline for Detecting Radio Transients and Variables on the Australian SKA Pathfinder (ASKAP) Telescope'. In P. Ballester, D. Egret, & N. P. F. Lorente (eds.), *Astronomical Data Analysis Software and Systems XXI*, vol. 461 of *Astronomical Society of the Pacific Conference Series*, p. 725.

S. D. Bates, et al. (2013). 'The pulsar spectral index distribution'. *Monthly Notices of the Royal Astronomical Society* **431**(2):1352–1358.

A. P. Beardsley, et al. (2019). 'Science with the Murchison Widefield Array: Phase I results and Phase II opportunities'. *Publications of the Astronomical Society of Australia* **36**:e050.

M. E. Bell, et al. (2016a). 'Time-domain and spectral properties of pulsars at 154 MHz'. *Monthly Notices of the Royal Astronomical Society* **461**(1):908–921.

M. E. Bell, et al. (2016b). 'Time-domain and spectral properties of pulsars at 154 MHz'. *Monthly Notices of the Royal Astronomical Society* **461**(1):908–921.

N. D. R. Bhat, et al. (2004). 'Multifrequency Observations of Radio Pulse Broadening and Constraints on Interstellar Electron Density Microstructure'. *The Astrophysical Journal* **605**(2):759–783.

N. D. R. Bhat, et al. (2014). 'The Low-frequency Characteristics of PSR J0437-4715 Observed with the Murchison Wide-field Array'. *The Astrophysical Journal Letters* **791**(2):L32.

N. D. R. Bhat, et al. (2023a). 'The Southern-sky MWA Rapid Two-metre (SMART) pulsar survey—I. Survey design and processing pipeline'. *Publications of the Astronomical Society of Australia* **40**:e021.

N. D. R. Bhat, et al. (2023b). 'The Southern-sky MWA Rapid Two-metre (SMART) pulsar survey—II. Survey status, pulsar census, and first pulsar discoveries'. *Publications of the Astronomical Society of Australia* **40**:e020.

D. Bhattacharya & E. P. J. van den Heuvel (1991). 'Formation and evolution of binary and millisecond radio pulsars'. *Physics Reports* **203**(1-2):1–124.

A. V. Bilous, et al. (2016). 'A LOFAR census of non-recycled pulsars: average profiles, dispersion measures, flux densities, and spectra'. *Astronomy and Astrophysics* **591**:A134.

G. S. Bisnovatyi-Kogan & B. V. Komberg (1974). 'Pulsars and close binary systems'. *Soviet Astronomy* **18**:217.

J. D. Bowman, et al. (2013). 'Science with the Murchison Widefield Array'. *Publications of the Astronomical Society of Australia* **30**:e031.

D. S. Briggs (1995). 'High Fidelity Interferometric Imaging: Robust Weighting and NNLS Deconvolution'. In *American Astronomical Society Meeting Abstracts*, vol. 187 of *American Astronomical Society Meeting Abstracts*, p. 112.02.

M. Caleb, et al. (2022). 'Discovery of a radio-emitting neutron star with an ultra-long spin period of 76 s'. *Nature Astronomy* **6**:828–836.

F. Camilo (2002). 'Review of deep radio surveys for young pulsars'. In *34th COSPAR Scientific Assembly*, vol. 34, p. 2054.

F. Camilo, et al. (2006a). 'Transient pulsed radio emission from a magnetar'. *Nature* **442**(7105):892–895.

F. Camilo, et al. (2006b). 'Transient pulsed radio emission from a magnetar'. *Nature* **442**(7105):892–895.

S. Chandrasekhar (1931). 'The Maximum Mass of Ideal White Dwarfs'. *The Astrophysical Journal* **74**:81.

K. Chen & M. Ruderman (1993). 'Pulsar Death Lines and Death Valley'. *The Astrophysical Journal* **402**:264.

B. G. Clark (1999). 'Coherence in Radio Astronomy'. In G. B. Taylor, C. L. Carilli, & R. A. Perley (eds.), *Synthesis Imaging in Radio Astronomy II*, vol. 180 of *Astronomical Society of the Pacific Conference Series*, p. 1.

M. A. Clark, et al. (2013). 'Accelerating radio astronomy cross-correlation with graphics processing units'. *International Journal of High Performance Computing Applications* **27**:178–192.

D. Coppejans (2015). 'Cataclysmic Variables are significant radio emitters'. In *The Golden Age of Cataclysmic Variables and Related Objects - III (Golden2015)*, p. 15.

D. L. Coppejans, et al. (2016). 'Dwarf nova-type cataclysmic variable stars are significant radio emitters'. *Monthly Notices of the Royal Astronomical Society* **463**(2):2229–2241.

J. M. Cordes (1978). 'Observational limits on the location of pulsar emission regions.'. *The Astrophysical Journal* **222**:1006–1011.

J. M. Cordes (2002). 'Pulsar Observations I. – Propagation Effects, Searching Distance Estimates, Scintillations and VLBI'. In S. Stanimirovic, D. Altschuler, P. Goldsmith, & C. Salter (eds.), *Single-Dish Radio Astronomy: Techniques and Applications*, vol. 278 of *Astronomical Society of the Pacific Conference Series*, pp. 227–250.

J. M. Cordes (2004). 'NE2001: A New Model for the Galactic Electron Density and its Fluctuations'. In D. Clemens, R. Shah, & T. Brainerd (eds.), *Milky Way Surveys: The Structure and Evolution of our Galaxy*, vol. 317 of *Astronomical Society of the Pacific Conference Series*, p. 211.

J. M. Cordes & T. J. W. Lazio (2003). 'NE2001. II. Using Radio Propagation Data to Construct a Model for the Galactic Distribution of Free Electrons'. *arXiv e-prints* pp. astro–ph/0301598.

T. J. Cornwell, et al. (2005). 'W Projection: A New Algorithm for Wide Field Imaging with Radio Synthesis Arrays'. In P. Shopbell, M. Britton, & R. Ebert (eds.), *Astronomical Data Analysis Software and Systems XIV*, vol. 347 of *Astronomical Society of the Pacific Conference Series*, p. 86.

T. J. Cornwell, et al. (2008). 'The Noncoplanar Baselines Effect in Radio Interferometry: The W-Projection Algorithm'. *IEEE Journal of Selected Topics in Signal Processing* **2**(5):647–657.

F. Crawford, et al. (2000). 'A Search for Submillisecond Pulsations in Unidentified FIRST and NVSS Radio Sources'. *The Astronomical Journal* **119**(5):2376–2381.

S. Dai, et al. (2016). 'Detecting pulsars with interstellar scintillation in variance images'. *Monthly Notices of the Royal Astronomical Society* **462**(3):3115–3122.

N. Damico, et al. (1985). 'A search of steep-spectrum radio sources for millisecond pulsars.'. *Publications of the Astronomical Society of Australia* **6**(2):174–176.

C. De Breuck, et al. (2000). 'A sample of 669 ultra steep spectrum radio sources to find high redshift radio galaxies'. *Astronomy and Astrophysics Supplement Series* **143**:303–333.

F. de Gasperin, et al. (2018). 'A radio spectral index map and catalogue at 147-1400 MHz covering 80 per cent of the sky'. *Monthly Notices of the Royal Astronomical Society* **474**(4):5008–5022.

G. Dubner & E. Giacani (2015). 'Radio emission from supernova remnants'. **23**:3.

G. A. Dulk (1985). 'Radio emission from the sun and stars.'. *Annual Review of Astronomy and Astrophysics* **23**:169–224.

R. C. Duncan & C. Thompson (1992). 'Formation of Very Strongly Magnetized Neutron Stars: Implications for Gamma-Ray Bursts'. *The Astrophysical Journal Letters* **392**:L9.

A. Einstein (1915). 'Die Feldgleichungen der Gravitation'. *Sitzungsberichte der Königlich Preussischen Akademie der Wissenschaften* pp. 844–847.

R. Fender (2006). 'Jets from X-ray binaries'. In *Compact stellar X-ray sources*, vol. 39, pp. 381–419.

R. L. Fiedler, et al. (1987). 'Extreme scattering events caused by compact structures in the interstellar medium'. *Nature* **326**(6114):675–678.

D. A. Frail, et al. (1994). 'Shock-excited Maser Emission from the Supernova Remnant W28'. *The Astrophysical Journal Letters* **424**:L111.

D. A. Frail, et al. (2016). 'Pulsar candidates towards Fermi unassociated sources'. *Monthly Notices of the Royal Astronomical Society* **461**(1):1062–1067.

D. A. Frail, et al. (2018). 'An image-based search for pulsars among Fermi unassociated LAT sources'. *Monthly Notices of the Royal Astronomical Society* **475**(1):942–954.

D. A. Frail, et al. (2000). 'A 450 Day Light Curve of the Radio Afterglow of GRB 970508: Fireball Calorimetry'. *The Astrophysical Journal* **537**(1):191–204.

S. Gezari (2021). 'Tidal Disruption Events'. *Annual Review of Astronomy and Astrophysics* **59**:21–58.

N. K. Glendenning (1992). 'Limiting rotational period of neutron stars'. **46**(10):4161–4168.

T. Gold (1968). 'Rotating Neutron Stars as the Origin of the Pulsating Radio Sources'. *Nature* **218**(5143):731–732.

T. Gold (1969). 'Rotating Neutron Stars and the Nature of Pulsars'. *Nature* **221**(5175):25–27.

J. A. Green, et al. (2009). 'The 6-GHz multibeam maser survey - I. Techniques'. *Monthly Notices of the Royal Astronomical Society* **392**(2):783–794.

Y. Gupta (2002). 'Pulsars and the ISM'. In A. Pramesh Rao, G. Swarup, & Gopal-Krishna (eds.), *The Universe at Low Radio Frequencies*, vol. 199, p. 363.

Y. Gupta, et al. (2017). 'The upgraded GMRT: opening new windows on the radio Universe'. *Current Science* **113**(4):707–714.

N. V. Gusinskaia, et al. (2020). 'Quasi-simultaneous radio and X-ray observations of Aql X-1 : probing low luminosities'. *Monthly Notices of the Royal Astronomical Society* **492**(2):2858–2871.

C. J. Hailey, et al. (2018). 'A density cusp of quiescent X-ray binaries in the central parsec of the Galaxy'. *Nature* **556**(7699):70–73.

C. L. Hale, et al. (2021). 'The Rapid ASKAP Continuum Survey Paper II: First Stokes I Source Catalogue Data Release'. *Publications of the Astronomical Society of Australia* **38**:e058.

M. Hallbäck, et al. (1996). *The Basics of Turbulence Modelling*, pp. 81–154. Springer Netherlands, Dordrecht.

J. L. Han, et al. (2009). 'Polarization Observations of 100 Pulsars at 774 MHz by the Green Bank Telescope'. *The Astrophysical Journal Supplement Series* **181**(2):557–571.

J. L. Han, et al. (2021). 'The FAST Galactic Plane Pulsar Snapshot survey: I. Project design and pulsar discoveries'. *Research in Astronomy and Astrophysics* **21**(5):107.

P. J. Hancock, et al. (2012). 'Compact continuum source finding for next generation radio surveys'. *Monthly Notices of the Royal Astronomical Society* **422**(2):1812–1824.

P. J. Hancock, et al. (2018). 'Source Finding in the Era of the SKA (Precursors): Aegean 2.0'. *Publications of the Astronomical Society of Australia* **35**:e011.

C. G. T. Haslam, et al. (1981). 'A 408 MHz all-sky continuum survey. I - Observations at southern declinations and for the North Polar region.'. *Astronomy and Astrophysics* **100**:209–219.

G. Hellbourg, et al. (2014). 'Reference antenna-based subspace tracking for RFI mitigation in radio astronomy'. In *Signal and Information Processing (GlobalSIP*, pp. 1286–1290.

J. W. T. Hessels, et al. (2008). 'The GBT350 Survey of the Northern Galactic Plane for Radio Pulsars and Transients'. In C. Bassa, Z. Wang, A. Cumming, & V. M. Kaspi (eds.), *40 Years of Pulsars: Millisecond Pulsars, Magnetars and More*, vol. 983 of *American Institute of Physics Conference Series*, pp. 613–615.

A. Hewish, et al. (1968). 'Observation of a Rapidly Pulsating Radio Source'. *Nature* **217**(5130):709–713.

G. Hobbs, et al. (2020). 'An ultra-wide bandwidth (704 to 4 032 MHz) receiver for the Parkes radio telescope'. *Publications of the Astronomical Society of Australia* **37**:e012.

J. A. Högbom (1974). 'Aperture Synthesis with a Non-Regular Distribution of Interferometer Baselines'. *Astronomy and Astrophysics Supplement Series* **15**:417.

A. W. Hotan, et al. (2014). 'The Australian Square Kilometre Array Pathfinder:

System Architecture and Specifications of the Boolardy Engineering Test Array'. *Publications of the Astronomical Society of Australia* **31**:e041.

F. Hoyle, et al. (1964). 'Electromagnetic Waves from Very Dense Stars'. *Nature* **203**(4948):914–916.

P. J. Huber (1964). 'Robust Estimation of a Location Parameter'. *The Annals of Mathematical Statistics* **35**(1):73 – 101.

R. A. Hulse & J. H. Taylor (1975). 'Discovery of a pulsar in a binary system.'. *The Astrophysical Journal Letters* **195**:L51–L53.

B. Humphreys & T. J. Cornwell (2011). 'Analysis of Convolutional Resampling Algorithm Performance'.

N. Hurley-Walker, et al. (2017). 'GaLactic and Extragalactic All-sky Murchison Widefield Array (GLEAM) survey - I. A low-frequency extragalactic catalogue'. *Monthly Notices of the Royal Astronomical Society* **464**(1):1146–1167.

N. Hurley-Walker, et al. (2023). 'A long-period radio transient active for three decades'. *Nature* **619**(7970):487–490.

S. D. Hyman, et al. (2021a). 'Two extreme steep-spectrum, polarized radio sources towards the Galactic bulge'. *Monthly Notices of the Royal Astronomical Society* **507**(3):3888–3898.

S. D. Hyman, et al. (2021b). 'Two extreme steep-spectrum, polarized radio sources towards the Galactic bulge'. *Monthly Notices of the Royal Astronomical Society* **507**(3):3888–3898.

S. D. Hyman, et al. (2019). 'A Search for Pulsars in Steep-spectrum Radio Sources toward the Galactic Center'. *The Astrophysical Journal* **876**(1):20.

S. D. Hyman, et al. (2005). 'A powerful bursting radio source towards the Galactic Centre'. *Nature* **434**(7029):50–52.

H. T. Intema, et al. (2017). 'The GMRT 150 MHz all-sky radio survey. First alternative data release TGSS ADR1'. *Astronomy and Astrophysics* **598**:A78.

P. Janagal, et al. (2023). 'PSR J0026-1955: A curious case of evolutionary subpulse drifting and nulling'. *Monthly Notices of the Royal Astronomical Society* **524**(2):2684–2697.

F. Jankowski, et al. (2018). 'Spectral properties of 441 radio pulsars'. *Monthly Notices of the Royal Astronomical Society* **473**(4):4436–4458.

S. Johnston & M. Kerr (2018). 'Polarimetry of 600 pulsars from observations at 1.4 GHz with the Parkes radio telescope'. *Monthly Notices of the Royal Astronomical Society* **474**(4):4629–4636.

P. B. Jones (2020). 'Source of circular polarization in radio pulsars'. *Monthly Notices of the Royal Astronomical Society* **498**(4):5003–5008.

D. L. Kaplan, et al. (2000a). 'Radio Morphologies and Spectra of Compact Radio Sources with the Steepest Spectra'. *The Astrophysical Journal Supplement Series* **126**(1):37–62.

D. L. Kaplan, et al. (2000b). 'The Steep Spectrum Pulsar Population'. In M. Kramer, N. Wex, & R. Wielebinski (eds.), *IAU Colloq. 177: Pulsar Astronomy - 2000 and Beyond*, vol. 202 of *Astronomical Society of the Pacific Conference Series*, p. 35.

D. L. Kaplan, et al. (2019). 'Serendipitous Discovery of PSR J1431-6328 as a Highly Polarized Point Source with the Australian SKA Pathfinder'. *The Astrophysical Journal* **884**(1):96.

E. F. Keane (2018). 'Pulsar Science with the SKA'. In P. Weltevrede, B. B. P. Perera, L. L. Preston, & S. Sanidas (eds.), *Pulsar Astrophysics the Next Fifty Years*, vol. 337, pp. 158–164.

J. Kijak, et al. (2007). 'Turn-over in pulsar spectra around 1 GHz'. *Astronomy and Astrophysics* **462**(2):699–702.

J. Kocz, et al. (2010). 'Radio Frequency Interference Removal through the Application of Spatial Filtering Techniques on the Parkes Multibeam Receiver'. *The Astronomical Journal* **140**(6):2086–2094.

V. I. Kondratiev, et al. (2016). 'A LOFAR census of millisecond pulsars'. *Astronomy and Astrophysics* **585**:A128.

V. M. Kontorovich & A. B. Flanchik (2013). 'High-frequency cutoff and change of radio emission mechanism in pulsars'. *Astrophysics and Space Science* **345**(1):169–175.

R. Kothes, et al. (2018). 'A Radio Continuum and Polarization Study of SNR G57.2+0.8 Associated with Magnetar SGR 1935+2154'. *The Astrophysical Journal* **852**(1):54.

M. Kramer, et al. (2006). 'A Periodically Active Pulsar Giving Insight into Magnetospheric Physics'. *Science* **312**(5773):549–551.

M. I. Large, et al. (1968). 'A Pulsar Supernova Association?'. *Nature* **220**(5165):340–341.

J. M. Lattimer & A. Yahil (1990). 'Research in nuclear astrophysics: Stellar collapse and supernovae'. Technical Progress Report, 1 Dec. 1989 - 30 Nov. 1990 State Univ. of New York, Stony Brook. Dept. of Earth and Space Sciences.

K. D. Lawson, et al. (1987). 'Variations in the spectral index of the galactic radio continuum emission in the northern hemisphere.'. *Monthly Notices of the Royal Astronomical Society* **225**:307–327.

C. P. Lee, et al. (2022). 'Spectral analysis of 22 radio pulsars using SKA-Low precursor stations'. *Publications of the Astronomical Society of Australia* **39**:e042.

E. Lenc, et al. (2017). 'The Challenges of Low-Frequency Radio Polarimetry: Lessons from the Murchison Widefield Array'. *Publications of the Astronomical Society of Australia* **34**:e040.

E. Lenc, et al. (2018). 'An all-sky survey of circular polarization at 200 MHz'. *Monthly Notices of the Royal Astronomical Society* **478**(2):2835–2849.

L. Levin, et al. (2018). 'Pulsar Searches with the SKA'. In P. Weltevrede, B. B. P. Perera, L. L. Preston, & S. Sanidas (eds.), *Pulsar Astrophysics the Next Fifty Years*, vol. 337, pp. 171–174.

D. R. Lorimer & M. Kramer (2004). *Handbook of Pulsar Astronomy*.

D. R. Lorimer, et al. (1995). 'Multifrequency flux density measurements of 280 pulsars'. *Monthly Notices of the Royal Astronomical Society* **273**(2):411–421.

B. Y. Losovsky (2022). 'The specifics of pulsar radio emission'. *Open Astronomy* **31**(1):189–197.

R. V. E. Lovelace, et al. (1968). 'Pulsar NP 0532 Near Crab Nebula'. *International Astronomical Union Circulars* **2113**:1.

C. Lynch, et al. (2017a). 'MWA targeted campaign of nearby, flaring M dwarf stars'. MWA Proposal id.2017A-02.

C. R. Lynch, et al. (2017b). '154 MHz Detection of Faint, Polarized Flares from UV Ceti'. *The Astrophysical Journal Letters* **836**(2):L30.

A. Lyne, et al. (2010). 'Switched Magnetospheric Regulation of Pulsar Spin-Down'. *Science* **329**(5990):408.

A. G. Lyne, et al. (1987). 'The discovery of a millisecond pulsar in the globular cluster M28'. *Nature* **328**(6129):399–401.

A. G. Lyne & B. J. Rickett (1968). 'Radio Observations of Five Pulsars'. *Nature* **219**(5161):1339–1342.

Y. E. Lyubarskii & S. A. Petrova (1998). 'Refraction of radio waves in pulsar magnetospheres'. *Astronomy and Astrophysics* **333**:181–187.

Y. Maan, et al. (2012). 'Pulsed radio emission from the Fermi-LAT pulsar J1732-3131: search and a possible detection at 34.5 MHz'. *Monthly Notices of the Royal Astronomical Society* **425**(1):2–7.

Y. Maan, et al. (2018). 'A Search for Pulsars in Steep Spectrum Radio Sources'. *The Astrophysical Journal* **864**(1):16.

I. F. Malov (1979). 'On the nature of the low-frequency dropoff in pulsar spectra'. *Soviet Astronomy* **23**:205.

R. N. Manchester, et al. (2005). 'The Australia Telescope National Facility Pulsar Catalogue'. *The Astronomical Journal* **129**(4):1993–2006.

R. N. Manchester, et al. (2001). 'The Parkes multi-beam pulsar survey - I. Observing and data analysis systems, discovery and timing of 100 pulsars'. *Monthly Notices of the Royal Astronomical Society* **328**(1):17–35.

R. N. Manchester & J. H. Taylor (1972). 'Parameters of 61 Pulsars'. *Astrophysical Letters* **10**:67.

O. Maron, et al. (2000). 'Pulsar spectra of radio emission'. *Astronomy and Astrophysics Supplement Series* **147**:195–203.

D. N. Matsakis, et al. (1997). 'A statistic for describing pulsar and clock stabilities.'. *Astronomy and Astrophysics* **326**:924–928.

D. McConnell, et al. (2020). 'The Rapid ASKAP Continuum Survey I: Design and first results'. *Publications of the Astronomical Society of Australia* **37**:e048.

P. M. McCulloch, et al. (1983). 'A radio pulsar in the Large Magellanic Cloud.'. *Nature* **303**:307–308.

M. A. McLaughlin, et al. (2006). 'Transient radio bursts from rotating neutron stars'. *Nature* **439**(7078):817–820.

J. P. McMullin, et al. (2007). 'CASA Architecture and Applications'. In R. A. Shaw, F. Hill, & D. J. Bell (eds.), *Astronomical Data Analysis Software and Systems XVI*, vol. 376 of *Astronomical Society of the Pacific Conference Series*, p. 127.

S. J. McSweeney, et al. (2017). 'Low-frequency Observations of the Subpulse Drifter PSR J0034-0721 with the Murchison Widefield Array'. *The Astrophysical Journal* **836**(2):224.

B. W. Meyers, et al. (2017). 'Spectral Flattening at Low Frequencies in Crab Giant Pulses'. *The Astrophysical Journal* **851**(1):20.

D. A. Mitchell, et al. (2008). 'Real-Time Calibration of the Murchison Widefield Array'. *IEEE Journal of Selected Topics in Signal Processing* **2**(5):707–717.

T. Murphy, et al. (2017). 'Low-Frequency Spectral Energy Distributions of Radio Pulsars Detected with the Murchison Widefield Array'. *Publications of the Astronomical Society of Australia* **34**:e020.

R. L. Mutel & D. H. Morris (1988). *Properties of stellar magnetospheres deduced from radio observations of close binaries*, vol. 143, p. 283.

R. Nan (2006). 'Five hundred meter aperture spherical radio telescope (FAST)'. *Science in China: Physics, Mechanics and Astronomy* **49**(2):129–148.

J. Navarro, et al. (1995). 'A Very Luminous Binary Millisecond Pulsar'. *The Astrophysical Journal Letters* **455**:L55.

L. Nieder, et al. (2020). 'Discovery of a Gamma-Ray Black Widow Pulsar by GPU-accelerated Einstein@Home'. *The Astrophysical Journal Letters* **902**(2):L46.

A. R. Offringa, et al. (2012a). 'Post-correlation filtering techniques for off-axis source and RFI removal'. *Monthly Notices of the Royal Astronomical Society* **422**(1):563–580.

A. R. Offringa, et al. (2012b). 'Post-correlation filtering techniques for off-axis source and RFI removal'. *Monthly Notices of the Royal Astronomical Society* **422**(1):563–580.

A. R. Offringa, et al. (2014a). 'WSCLEAN: an implementation of a fast, generic wide-field imager for radio astronomy'. *Monthly Notices of the Royal Astronomical Society* **444**(1):606–619.

A. R. Offringa, et al. (2014b). 'WSCLEAN: an implementation of a fast, generic wide-field imager for radio astronomy'. *Monthly Notices of the Royal Astronomical Society* **444**(1):606–619.

A. R. Offringa, et al. (2015). 'The Low-Frequency Environment of the Murchison Widefield Array: Radio-Frequency Interference Analysis and Mitigation'. *Publications of the Astronomical Society of Australia* **32**:e008.

S. A. Olausen & V. M. Kaspi (2014). 'VizieR Online Data Catalog: The McGill magnetar catalog (Olausen+, 2014)'. *VizieR Online Data Catalog* p. J/ApJS/212/6.

J. R. Oppenheimer & G. M. Volkoff (1939). 'On Massive Neutron Cores'. *Physical Review* **55**(4):374–381.

S. M. Ord, et al. (2015). 'The Murchison Widefield Array Correlator'. *Publications of the Astronomical Society of Australia* **32**:e006.

S. M. Ord, et al. (2010). 'Interferometric Imaging with the 32 Element Murchison Wide-Field Array'. **122**(897):1353.

S. M. Ord, et al. (2019). 'MWA tied-array processing I: Calibration and beamformation'. *Publications of the Astronomical Society of Australia* **36**:e030.

J. P. Ostriker & J. E. Gunn (1971). 'Do Pulsars Make Supernovae?'. *The Astrophysical Journal Letters* **164**:L95.

F. Pacini (1968). 'Rotating Neutron Stars, Pulsars and Supernova Remnants'. *Nature* **219**(5150):145–146.

A. Parsons, et al. (2012). 'A Sensitivity and Array-configuration Study for Measuring the Power Spectrum of 21 cm Emission from Reionization'. *The Astrophysical Journal* **753**(1):81.

E. S. Phinney & S. R. Kulkarni (1994). 'Binary and Millisecond Pulsars'. *Annual Review of Astronomy and Astrophysics* **32**:591–639.

J. Pritchard, et al. (2021). 'A circular polarization survey for radio stars with the Australian SKA Pathfinder'. *Monthly Notices of the Royal Astronomical Society* **502**(4):5438–5454.

V. Radhakrishnan & D. J. Cooke (1969). 'Magnetic Poles and the Polarization Structure of Pulsar Radiation'. *Astrophysical Letters* **3**:225.

S. M. Ransom (2001). *New search techniques for binary pulsars*. Ph.D. thesis, Harvard University.

L. Rawley, et al. (1987). 'Millisecond Pulsar Rivals Best Atomic Clock Stability'. In *Proceedings of the Eighteenth Annual Precise Time and Material Interval (PTTI) Applications and Planning Meeting. A meeting held at the DuPont Plaza Hotel*, pp. 453–466.

C. J. Riseley, et al. (2020). 'The POlarised GLEAM Survey (POGS) II: Results from an all-sky rotation measure synthesis survey at long wavelengths'. *Publications of the Astronomical Society of Australia* **37**:e029.

C. J. Riseley, et al. (2018). 'The POlarised GLEAM Survey (POGS) I: First results from a low-frequency radio linear polarisation survey of the southern sky'. *Publications of the Astronomical Society of Australia* **35**:e043.

J. Roy, et al. (2010). 'A real-time software backend for the GMRT'. *Experimental Astronomy* **28**(1):25–60.

S. Sanidas, et al. (2019). 'The LOFAR Tied-Array All-Sky Survey (LOTAAS): Survey overview and initial pulsar discoveries'. *Astronomy and Astrophysics* **626**:A104.

P. A. G. Scheuer (1968). 'Amplitude Variations in Pulsed Radio Sources'. *Nature* **218**(5145):920–922.

F. R. Schwab & W. D. Cotton (1983). 'Global fringe search techniques for VLBI'. *The Astronomical Journal* **88**:688–694.

S. Sett, et al. (2023). 'Image-based searches for pulsar candidates using MWA VCS data'. *Publications of the Astronomical Society of Australia* **40**:e003.

N. Shibazaki, et al. (1989). 'Does mass accretion lead to field decay in neutron stars'. In Columbia Univ., Physics of Systems Containing Neutron Stars 9 p. (SEE N90-22467 15-89).

A. Skrzypczak, et al. (2018). 'Meterwavelength Single-pulse Polarimetric Emission Survey. IV. The Period Dependence of Component Widths of Pulsars'. *The Astrophysical Journal* **854**(2):162.

C. Sobey, et al. (2022). 'Searching for pulsars associated with polarised point sources using LOFAR: Initial discoveries from the TULIPP project'. *Astronomy and Astrophysics* **661**:A87.

C. Sobey, et al. (2015). 'LOFAR discovery of a quiet emission mode in PSR B0823+26'. *Monthly Notices of the Royal Astronomical Society* **451**(3):2493–2506.

M. Sokolowski, et al. (2017). 'Calibration and Stokes Imaging with Full Embedded Element Primary Beam Model for the Murchison Widefield Array'. *Publications of the Astronomical Society of Australia* **34**:e062.

M. Sokolowski, et al. (2020). 'Calibration database for the Murchison Widefield Array All-Sky Virtual Observatory'. *Publications of the Astronomical Society of Australia* **37**:e021.

D. H. Staelin & I. Reifenstein, Edward C. (1968). 'Pulsating Radio Sources near the Crab Nebula'. *Science* **162**(3861):1481–1483.

L. Staveley-Smith, et al. (1996). 'The Parkes 21 CM multibeam receiver'. *Publications of the Astronomical Society of Australia* **13**(3):243–248.

G. G. Stokes (1851). 'On the Composition and Resolution of Streams of Polarized Light from different Sources'. *Transactions of the Cambridge Philosophical Society* **9**:399.

K. Stovall, et al. (2016). 'Timing of Five PALFA-discovered Millisecond Pulsars'. *The Astrophysical Journal* **833**(2):192.

A. Sutinjo, et al. (2015). 'Understanding instrumental Stokes leakage in Murchison Widefield Array polarimetry'. *Radio Science* **50**(1):52–65.

N. A. Swainston, et al. (2022a). 'pulsar_spectra: A pulsar flux density catalogue and spectrum fitting repository'. *arXiv e-prints* p. arXiv:2209.13324.

N. A. Swainston, et al. (2022b). 'pulsar_spectra: A pulsar flux density catalogue and spectrum fitting repository'. *Publications of the Astronomical Society of Australia* **39**:e056.

G. Swarup, et al. (1991). 'The Giant Metre-Wave Radio Telescope'. *Current Science* **60**:95.

J. D. Swinbank, et al. (2015). 'The LOFAR Transients Pipeline'. *Astronomy and Computing* **11**:25–48.

C. M. Tan, et al. (2018). 'LOFAR Discovery of a 23.5 s Radio Pulsar'. *The Astrophysical Journal* **866**(1):54.

T. M. Tauris & R. N. Manchester (1998). 'On the Evolution of Pulsar Beams'. *Monthly Notices of the Royal Astronomical Society* **298**(3):625–636.

J. Taylor, Joseph H. (1991). 'Millisecond pulsars: nature's most stable clocks.'. *IEEE Proceedings* **79**:1054–1062.

A. R. Thompson (2017). *Interferometry and Synthesis in Radio Astronomy*, chap. 15, pp. 767–771. John Wiley Sons, Ltd.

A. R. Thompson, et al. (2001). *Interferometry and Synthesis in Radio Astronomy, 2nd Edition.*

C. Thompson & R. C. Duncan (1993). 'Neutron Star Dynamos and the Origins of Pulsar Magnetism'. *The Astrophysical Journal* **408**:194.

S. J. Tingay, et al. (2013a). 'The Murchison Widefield Array: The Square Kilometre Array Precursor at Low Radio Frequencies'. *Publications of the Astronomical Society of Australia* **30**:e007.

S. J. Tingay, et al. (2013b). 'The Murchison Widefield Array: The Square Kilometre Array Precursor at Low Radio Frequencies'. *Publications of the Astronomical Society of Australia* **30**:e007.

S. E. Tremblay, et al. (2015). 'The High Time and Frequency Resolution Capabilities of the Murchison Widefield Array'. *Publications of the Astronomical Society of Australia* **32**:e005.

R. A. Treumann (2006). 'The electron-cyclotron maser for astrophysical application'. **13**(4):229–315.

V. Tudor, et al. (2017). 'Disc-jet coupling in low-luminosity accreting neutron stars'. *Monthly Notices of the Royal Astronomical Society* **470**(1):324–339.

J. M. Uson & W. D. Cotton (2008). 'Beam squint and Stokes V with off-axis feeds'. *Astronomy and Astrophysics* **486**(2):647–654.

P. H. van Cittert (1934). 'Die Wahrscheinliche Schwingungsverteilung in Einer von Einer Lichtquelle Direkt Oder Mittels Einer Linse Beleuchteten Ebene'. *Physica* **1**(1):201–210.

M. P. van Haarlem, et al. (2013). 'LOFAR: The LOw-Frequency ARray'. *Astronomy and Astrophysics* **556**:A2.

J. P. W. Verbiest, et al. (2021). 'Pulsar Timing Array Experiments'. In *Handbook of Gravitational Wave Astronomy*, p. 4.

W. Voges, et al. (2000). 'Rosat All-Sky Survey Faint Source Catalogue'. *International Astronomical Union Circulars* **7432**:3.

A. von Hoensbroech & H. Lesch (1999). 'A transition from linear to circular polarization in pulsar radio emission'. *Astronomy and Astrophysics* **342**:L57–L61.

Y. Wang, et al. (2022). 'Discovery of PSR J0523-7125 as a Circularly Polarized Variable Radio Source in the Large Magellanic Cloud'. *The Astrophysical Journal* **930**(1):38.

R. B. Wayth, et al. (2015). 'GLEAM: The GaLactic and Extragalactic All-Sky MWA Survey'. *Publications of the Astronomical Society of Australia* **32**:e025.

R. B. Wayth, et al. (2018). 'The Phase II Murchison Widefield Array: Design overview'. *Publications of the Astronomical Society of Australia* **35**:e033.

N. Wex (2014). 'Testing Relativistic Gravity with Radio Pulsars'. *arXiv e-prints* p. arXiv:1402.5594.

A. Wolszczan & D. A. Frail (1992). 'A planetary system around the millisecond pulsar PSR1257 + 12'. *Nature* **355**(6356):145–147.

M. Xue, et al. (2017). 'A Census of Southern Pulsars at 185 MHz'. *Publications of the Astronomical Society of Australia* **34**:e070.

J. M. Yao, et al. (2017). 'A New Electron-density Model for Estimation of Pulsar and FRB Distances'. *The Astrophysical Journal* **835**(1):29.

F. Zernike (1938). 'The concept of degree of coherence and its application to optical problems'. *Physica* **5**(8):785–795.

B. Zhang, et al. (2000). 'Radio Pulsar Death Line Revisited: Is PSR J2144-3933 Anomalous?'. In *American Astronomical Society Meeting Abstracts #195*, vol. 195 of *American Astronomical Society Meeting Abstracts*, p. 133.03.

P. Zhou, et al. (2019). 'Spatially resolved X-ray study of supernova remnants that host magnetars: Implication of their fossil field origin'. *Astronomy and Astrophysics* **629**:A51.